Factors influencing the thermal insulation potential of different thermal barrier coating systems

Germain Boissonnet

ÉCOLE DOCTORALE EUCLIDE

Université de La Rochelle

Laboratoire des Sciences de l'Ingénieur pour l'Environnement – LaSIE (UMR-CNRS 7356)

THÈSE DE DOCTORAT

présentée par :

Germain BOISSONNET

Soutenance prévue le 21 mars 2019
pour l'obtention du grade de Docteur de l'Université de La Rochelle

Discipline : Sciences des Matériaux

Facteurs influençant la capacité d'isolation thermique de différents systèmes de revêtements « barrière thermique »

Composition du jury :

Rapporteurs :	
Dr. HDR Vladislav KOLARIK	Institut Fraunhofer ICT (Allemagne)
Pr. Francisco Javier VELASCO LOPEZ	Université Carlos III (Espagne)
Examinateurs :	
Dr. Luc BIANCHI	Safran Aircraft Engines
Dr. Maël MOLLARD	AIRFRANCE Industries
Pr. Michel VILASI	Université de Lorraine
Directeurs de thèse :	
Pr. Gilles BONNET	Université de La Rochelle
Pr. Fernando PEDRAZA	Université de La Rochelle

TABLE OF CONTENTS

INTRODUCTION

In aeronautical gas turbine engines, the metallic materials employed in the hottest section are subject to very high pressure and velocity hot gases. In order to reduce the temperature at the surface of the metal substrate, thermal barrier coatings (TBCs) are employed in combination with an inner cooling system. These coating systems delay the onset of thermally induced failures by reducing the temperature and the oxidation rate of the metal substrate. Despite some of these coatings are currently fabricated by e.g. solution precursor plasma spray (SPPS) and suspension plasma spray (SPS), most of the yttria-stabilized zirconia (YSZ) TBCs are elaborated either by plasma-spray (PS) or by electron-beam physical vapour deposition (EB-PVD), depending on the specific requirements of the different engine parts. Unlike bulk materials, the heat transport through these coatings is related to both the intrinsic attributes of the material and the coating properties (composition, microstructure and thickness). As the evaluation of TBCs lifetime is critical for engine service span, understanding the evolution of TBC's insulation ability in such harsh environments is key from both the scientific and technological perspectives.

In addition, new issues arise due to the current limitations of material temperature and coatings efficiencies when one considers the need to increase the gas temperature of turbine engines for reduction of fuel consumption and increased performances. In the hottest section of the turbine, the high-pressure turbine (HPT), the current coatings might not be protective enough to cope with the rise in temperature, hence creating a need to develop new solutions. Similarly, in the low-pressure turbine (LPT), the materials might need additional protection and insulation as their surface temperature will also increase.

For the HPT section, different studies thus focus on finding new processing and low-thermal conductivity oxides to invent coatings that would replace the current columnar YSZ TBCs of aeronautical turbines. However, the complexity and diversity of these properties arising from the plurality of TBCs make it difficult to establish universal insulation–property relationships and the dynamic evolution of microstructure and properties during service offers additional challenges to microstructural characterization as well as lifetime prediction. In addition, the applicability and repeatability of the techniques for thermal conductivity measurements have a significant effect on the accuracy of the obtained results and, thus, on the reliable description

of microstructure-property relationships. Lowering the thermal conductivity of TBCs depends then on the understanding of the relationship between the insulation ability and the properties of the coating. The second challenge, arising from the need to extend the thermal protection to the LPT section, is to find a solution that also considers economic limitations. On an industrial scale, the extrapolation of the TBCs from the HPT section to the LPT is not a viable solution as EB-PVD and plasma spray processes are complex and require costly pieces of equipment and are thus too expensive.

Therefore, this dissertation is structured following two main axes. Firstly, based on current PS and EB-PVD coatings, the study seeks to provide a better comprehension on the relationships between the intrinsic properties of the current TBCs and their thermal insulation capacity in order to give reliable tools for the development of future coatings. The second part of the work focuses on the study of an alternative solution to create a TBC from a cost-effective and environmentally friendly process through the slurry route. Further details of the strategy and the structure of the dissertation are given in chapter I.

I. STATE OF THE ART AND BACKGROUND OF THE STUDY

Table of contents

1. Materials and coatings for gas turbines

The present work is related to the field of gas turbines and their components which are subject to aggressive conditions in different environments at high temperature. In this way, the gas turbines and their associated features will be reviewed in this chapter.

1.1 Gas turbine

Gas turbines have long been used in energy and aeronautical sectors. In utility power plants, the fuel is converted into electricity through heat transfer. Such heat is transferred to e.g. steam (steam power plants), molten nitrates (solar concentration plants), etc. In contrast, the modern aeronautical gas turbines burn fuel to produce exhaust gas that thrust the civil and military aircrafts. Since the present study focuses on high-temperature coatings for aero-engines, the specifics of jet engines will be further developed with respect power generation gas turbines. These engines comprise three primary sections that are mounted on the same shaft: the compressor, the combustion chamber and the turbine (**Figure I.1**).

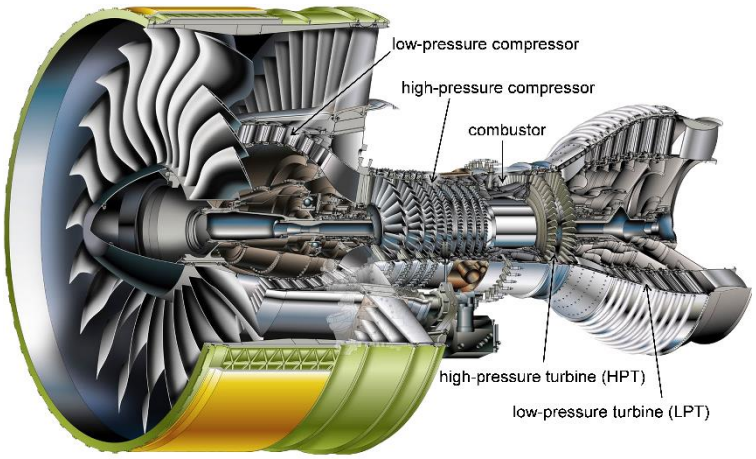

Figure I.1 *– Gas turbine engine [1].*

The compressor is constituted of multiple stages of rotating and stationary blades (called rotors and stators, respectively) of decreasing length through which the air is compressed. The compressed air is then mixed with fuel and ignited into the combustion chamber under constant pressure conditions. The hot combustion gases produced are directed through the turbine where they rapidly expand, involving faster rotation of the shaft which will draw in and compress more air to maintain a continuous combustion. Finally, the gases leaving the turbine at

intermediate pressure and temperature are accelerated through a nozzle (exhaust pipe) to reach a velocity greater than the free stream velocity, which produces thrust.

In the combustion chamber of such engines, the temperature can raise up to about 1930°C and the temperature at the entrance to the turbine (the turbine inlet temperature: TIT) can be as high as 1650°C [2]. However, the TIT cannot currently exceed about 1100°C because of material limitations. Therefore, only part of the compressed air is burned in the combustion chamber and the remainder being used to cool down the turbine. Due to these severe conditions, the structure of the engine is optimized in order to withstand the combined effect of gas temperature, pressure and velocity by using a combination of cooling schemes and appropriate materials, which are designed in accordance with the limitations of service conditions and economic standpoint.

1.2 Materials for the gas turbine

The resistance of materials under service conditions is the main limitation for increasing the overall performance of the jet engines. Indeed, higher temperatures of the hot gases in the turbine allow increasing the overall yield of the engine, hence, to decrease the consumption of fuel and the associated costs while simultaneously releasing fewer greenhouse gases. However, such increase in temperature brings about much higher thermal stresses and further degradation. Consequently, progresses in materials science have been paramount over the past years to find adequate compositions and fabrication methods to get materials with high elevated temperature strength to weight ratio. Currently, a wide spectrum of high-performance materials – steels, titanium alloys and superalloys – (***Figure I.2***) is used for the construction of gas turbines, depending on the properties needed in the different parts of the engine.

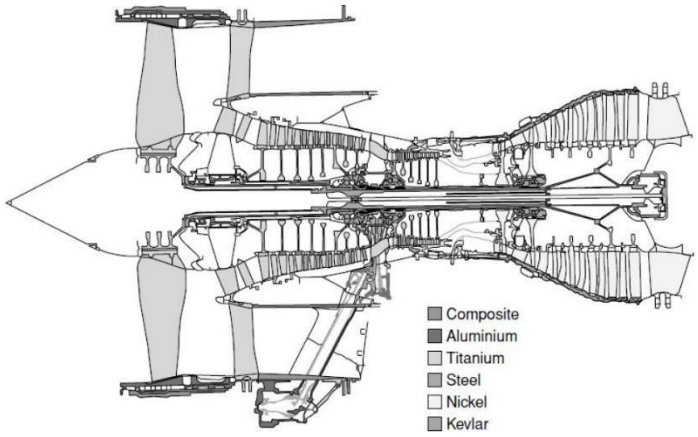

Figure I.2 *– Materials in use in the Rolls Royce Trent 800 engine [3].*

Other materials like ceramics, composites and intermetallics are also used in some engines. Nevertheless, superalloy materials are still the main material of choice for the hottest section components.

1.2.1 Superalloys

Iron (Fe), cobalt (Co) and nickel (Ni) based alloys have been well developed for industrial applications and each of them possesses specific properties depending on its metallic base and alloying elements. Iron based alloys are meant for lower temperature range and are therefore not suitable for aeronautical turbines: only Ni and Co-based alloys can be used for high temperature applications. However, Ni-based superalloys are generally preferred to Co for turbine design due to a higher specific modulus. Nonetheless, Co-based alloys possess a resistance to combustion gas higher than that of Ni and can be used for combustor components [3, 4].

1.2.1.1 Nickel-based superalloys

The structure of Ni-based alloys relies on the coherence between two major phases: FCC (L_{12} type) γ'-Ni_3X [X = Al, Ti, Ta] cuboidal precipitates embedded in a FCC γ-Ni matrix (***Figure I.3***). Other adding elements (Cr, Co, Mo, W, Nb, V and Hf) provide higher resistance to temperature stresses and structural strengthening by the formation of carbides at the grain boundaries.

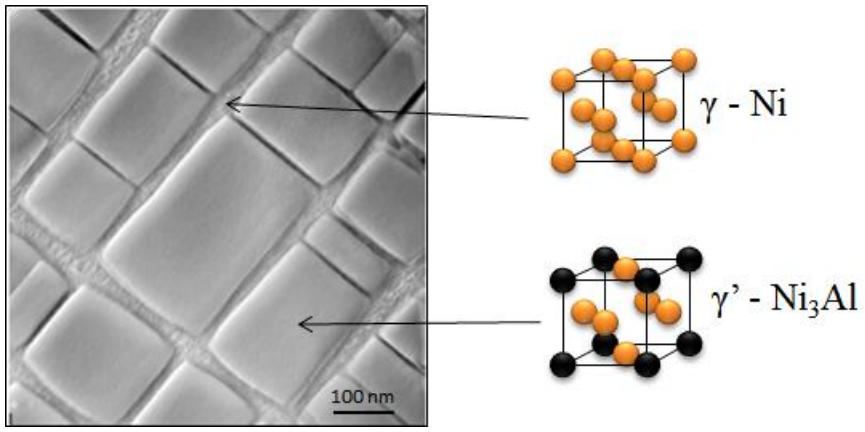

Figure I.3 *– Microstructure of a nickel-based superalloy γ/γ' [3].*

Further increase of the strengthening can be done by the control of the volume ratio of the γ/γ' phases, the size of the precipitates and the interstice of the γ'-cuboidal precipitates into the γ matrix to reduce the parametric mismatches [5, 6, 7]. Also, a refinement of the structure of

the superalloys allows delaying the initiation of cracking during service conditions. However, these alloying elements may also form detrimental phases upon service conditions called Laves and "Topologically Close-Packed" (TCP) phases. These TCP phases display different shapes (platelets, needles or bulky) depending on their composition and microstructure and consume the alloying elements which causes the reduction of mechanical properties by embrittlement.

The chemical composition has been enhanced with the addition of different elements, e.g. Re and Ru. Simultaneously, the crystalline structure has also evolved through improved casting processes. Indeed, conventionally casted materials resulting in EQ microstructures (EQ: equiaxed) have been progressively replaced by DS materials (DS: directionally solidified) which permitted to obtain grains parallel to the axis of the turbine blade. Such microstructure gives a better creep strength due to the absence of grain boundaries perpendicular to the direction of the main stress. Afterwards, the addition of a grain selector coupled to a proper heat treatment allowed the achievement of a single crystal structure (SX). Such SX often corresponds rather to a single-grained bi-phased material (γ/γ') than to a real single crystal. By shedding the grain boundaries, the ductility at high temperature and the creep strength are considerably improved in addition with the fact that crack propagation is reduced.

However, despite these chemical and structural evolutions, the Ni-based superalloys tend to reach a maximum of material performances and corrosion resistance at temperatures around 900°C. In contrast, the temperature in the combustion chamber and in the turbine are higher than 900°C and protective and thermal barrier coatings must be used to increase the mechanical and oxidation resistance of the superalloys.

1.3 The thermal-barrier coating system

The thermal-barrier coating system is a multi-layered and multifunctional material assembly that enables the complete system to operate at temperatures near or above the melting temperature of the substrate in a highly oxidizing combustion environment (**Figure I.4**). It includes two layers that combine the roles of oxidation, corrosion and thermal protection at the same time: the bond coating (BC) and the thermal barrier coating (TBC).

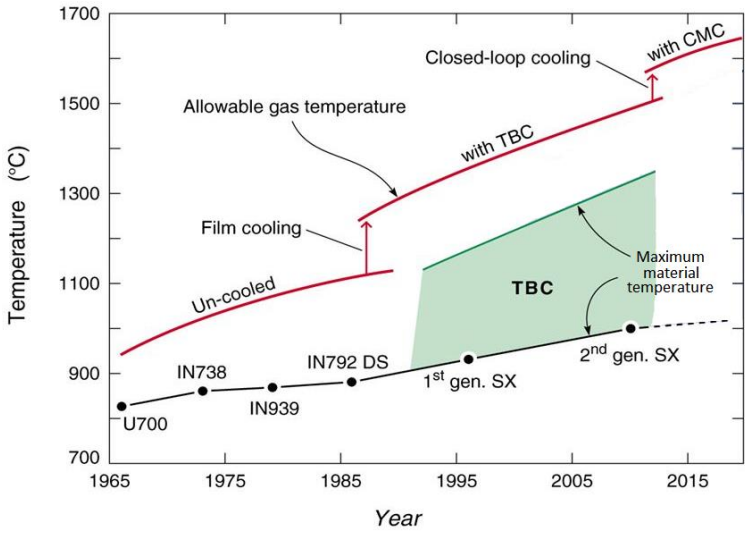

Figure I.4 *– Progression of temperature capabilities of Ni-based superalloys and thermal barrier coating material over the past 50 years [8].*

1.3.1 The bond coating

The bond coating (BC) is an intermetallic (or mixed metallic and intermetallic) interlayer that was originally developed in order to protect the substrate from oxidation and corrosion. Aluminide-type coatings based on NiAl and overlay coatings of the NiCoCrAl-group are considered as the standard systems for oxidation protection while diffusion chromides and overlays of CoNiCrAl materials are preferably used for hot corrosion protection [3, 9]. As the operating temperature in the turbine has increased over the years, fuels have become cleaner, materials have evolved and, thus, the environmental coatings have become multifunctional. Currently, the interlayer is expected to provide resistance to type II and type I hot corrosion, to be resistant to high-temperature oxidation in the hottest sections, to permit the adhesion of the thermal barrier coating, to provide an environmental protection if the TBC spalls off and to minimize interdiffusion and transformations at the interface with the substrate [10].

1.3.1.1 Structure and functionality of bond coatings

The thickness of the bond coating varies between 30-100 µm depending on the processing approach and the desired service time. The chemical complexity of such coatings is due to the need to adapt to thermomechanical and thermochemical properties of the system.

As the bond coating is deposited on Ni-based substrate and is supposed to form chromia or alumina films for environmental protection, the main constituents of this kind of coatings are Ni, Cr and Al. The different phases of the different combinations of these elements can be

predicted using a Ni-Al-Cr ternary diagram (**Figure I.5**). For an approximate equal level of Ni and Al, the β phase (B2) is formed and coatings that primarily comprise this phase are known as "nickel aluminide" coatings or "platinum aluminides" if additional Pt is present. The β phase could also be combined with the FCC γ'-Ni_3Al (Ll_2) to form the basis of "MCrAlY" coatings (where M refers to Ni, Co or both). Several emerging coatings are composed of γ'-Ni_3Al with some level of γ-Ni. However, during the high temperature exposures upon service, the bond-coat structure evolves, resulting in phase transformations and/or migration of the elements that could be detrimental to system performance [10].

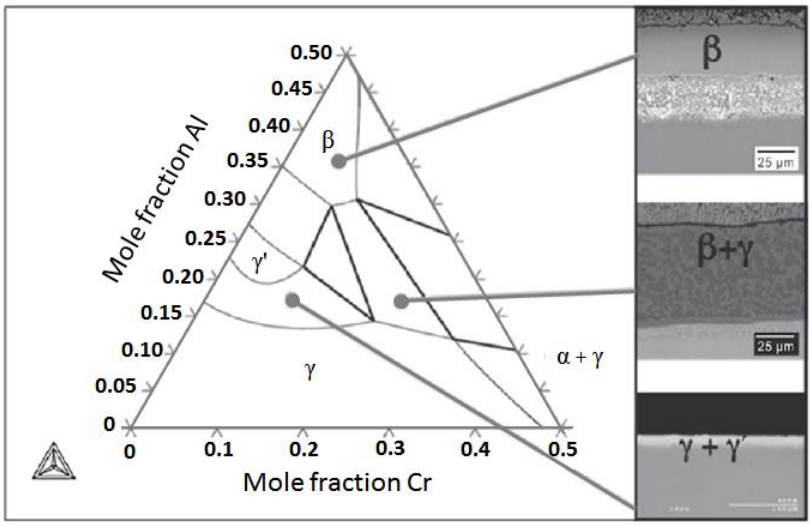

Figure I.5 *– Ternary Ni-Al-Cr phase diagram predicted by Calphad method, and approximate compositions of three different bond coating classes shown in SEM micrographs on the right [10].*

The bond coating needs to act as an environmental barrier for the substrate because the outer thermal barrier coating is permeable to oxygen and also because the bond coating itself can be exposed to the aggressive environment when local or full spallation of the top coat occurs. Therefore, the ability of this layer to form a protective oxide is one of the primary requirements and most of the intermetallics currently used contain enough Al to promote the formation of a dense α-Al_2O_3 layer at the interface between the bond coating and the thermal barrier coating. This thin layer is referred to the thermally grown oxide (TGO) and its properties must be in accordance with its multifunctional purpose. Firstly, the TGO needs to have a relatively slow growth rate and to be resistant to degradation by any corrosive species that might reach its surface. In order to achieve this protective requirement, the bond coating must act as a chemical reservoir for TGO formation as well as a diffusion barrier or diffusion sink for the refractory

elements of the substrate that may degrade the BC properties or the TGO/BC interface adhesion. Moreover, due to the given operating temperature of service and stresses associated with the severe thermal transient characteristics of the turbine, the BC also needs to be thermodynamically compatible with both the ceramic thermal barrier and the BC to prevent – or at least limit – the degradation of the mechanical properties that maintain the assembly [10].

1.3.1.2 Coating application and processing paths

In addition to their functional requirements, the coatings must be applied using processes that are cost effective, capable of providing the required thickness and chemical homogeneity on components of complex geometry. They also must be compatible with the other processes or thermal operations required for component fabrication, e.g. TBC deposition. The challenge of delivering ever-increasing coating functionality while maintaining robust and cost-effective manufacturing processes has led to a wide variety of coating processes that could be broadly classified in two categories: diffusion or overlay coatings.

Diffusion coatings, particularly aluminide coatings, result from the interdiffusion between an aluminium source and the elements of the substrate. There are two major types of processes: pack aluminizing and long-range vapour-phase transport techniques, e.g. vapour-phase aluminizing (VPA) and chemical vapour deposition (CVD) [11].

For the pack cementation process, the component to aluminise is embedded into a cement composed of an inert matrix (alumina sand), a halide salt activator (e.g., AlF_3 or NH_4F), and aluminium sources that can be Al or alloys, e.g. CrAl, CoAl, NiAl. The whole system is put into a furnace and heated to 650-1200°C in an inert atmosphere. The halide activator transports the Al from the source to the surface of the component where it decomposes, releasing aluminium that diffuses into the substrate. Control of the activity of the reaction is done using different sources and temperatures, allowing the control of the intermetallic phases obtained.

The long-range vapour-phase processes employ a gas phase for the transport and deposition of Al. In VPA, the aluminium source is usually composed of donors (CrAl, CoAl, NiAl and Ti_2AlC-TiAl) and halide activators (e.g., AlF_3 or NH_4F, NaF). In CVD, the Al source is injected in the heated furnace as a precursor gas in a non-oxidizing carrier gas. The precursor is obtained directly from a tank source ($AlCl_3$) or by using anhydrous halide (HCl or HF) reacting with an aluminium donor to form volatile halide salts ($AlCl_3$ or AlF_3).

Additional performance can be obtained by adding other elements to the diffusion coating such as Cr, Si, Hf, Zr, Y and Pt. These elements increase the resistance against hot corrosion

(Cr, Si, Pt), cyclic oxidation and improve TBC adhesion (Hf, Zr and Pt). One of the most used enhanced aluminides that permits to improve both environmental resistance and TBC adhesion is the platinum-modified nickel aluminide (NiPtAl). While diffusion aluminides are still considered as the standard for internal coatings, outer coatings can be also applied using overlay processes.

Overlay coatings allow the formation of more complex coatings on a wide range of thicknesses due to the absence of constraints relative to diffusion. In this way, MCrAl-family coatings can be deposited by numerous processes that differ from degrees of coating density and process-induced oxidation.

Electron-beam physical vapour deposition (EB-PVD) allows to deposit high quality (dense and clean) MCrAls that can easily contain reactive elements of addition (e.g., Hf, Y, Zr and Si) that could otherwise be easily tied up with oxygen under non-inert atmosphere. However, the EB-PVD technique requires expensive equipment and maintenance and is thus limited to relatively small components. Vacuum (VPS) and low-pressure plasma spray (LPPS) are lower-cost alternatives to thermally sprayed coatings and are thus broadly used, in particular LPPS. However, they remain relatively expensive because of the need of a vacuum chamber. Due to the limitations encountered with processes under vacuum atmosphere, atmospheric plasma spray (APS) techniques are preferred in some cases with inert-gas shrouded plasma spray or high-velocity oxy-fuel (HVOF). New techniques have also been developed for atmospheric deposition of dense coatings. These techniques, known as advanced combustion high-velocity air fuel (HVAF) and cold-gas dynamic spraying (cold spray), use reduced temperature of the particles with increased velocity of the spray to obtain coatings with limited oxidation of the most reactive elements. Recent technological advances have been made with hybridization of different deposition mechanisms that allows the combination of the advantages of different processes.

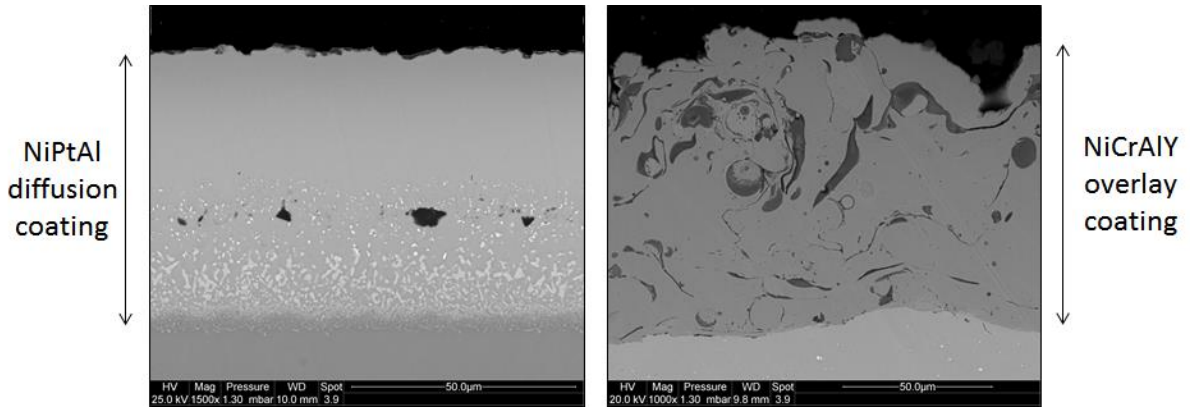

Figure I.6 *– Examples of bond coatings: (left) NiPtAl diffusion coating deposited by physical vapour deposition process and (right) NiCrAlY coating deposited by atmospheric plasma spraying.*

1.3.2 The thermal barrier coating

The top surface coating of the thermal barrier system is a refractory-oxide ceramic, known as thermal barrier coating (TBC), which is applied on the metallic parts in the hottest sections of the gas-turbine engines. Originally, TBCs were introduced to extend the useful life of stationary engine parts such as the combustor, but the technological improvements for design and functionality of the TBCs allowed their application in rotating blades afterwards. However, as the temperature in the gas-turbine engine has increased over the years, the TBCs became critical and entered in the classic design of hot components, comprising the combustor, stationary guide vanes, rotating blades, blade outer-air seals and shrouds in the high-pressure section behind the combustor as well as in afterburners in the tail section of jet engines. Associated with the internal cooling of the components, the coating enables the engine to operate at greater temperatures, which can be close to the melting temperature of the metallic materials (**Figure I.7**).

Typically made of 7 wt. % Y_2O_3-stabilized ZrO_2 (7YSZ) ceramics, these coatings have to fulfil a wide panel of requirements. Along with their primary role of thermal insulation, the TBCs need to have strain compliance to minimize thermal-expansion mismatch stresses with the underlying parts on thermal fluctuations. They also need to reflect the radiant heat from the hot gas, to have a good thermodynamic stability on the whole range of service temperature, possess good chemical compatibility with the underlying TGO (Al_2O_3) and to present sufficient chemical and physical resistance (see §3.2) due to the aggressive oxidizing and polluted environment that can reach maximum pressures of 40 bars (in the combustion chamber) and

maximum gas velocities exceeding Mach 1 (~1230 km/h) for maximum temperatures up to 1300°C [8].

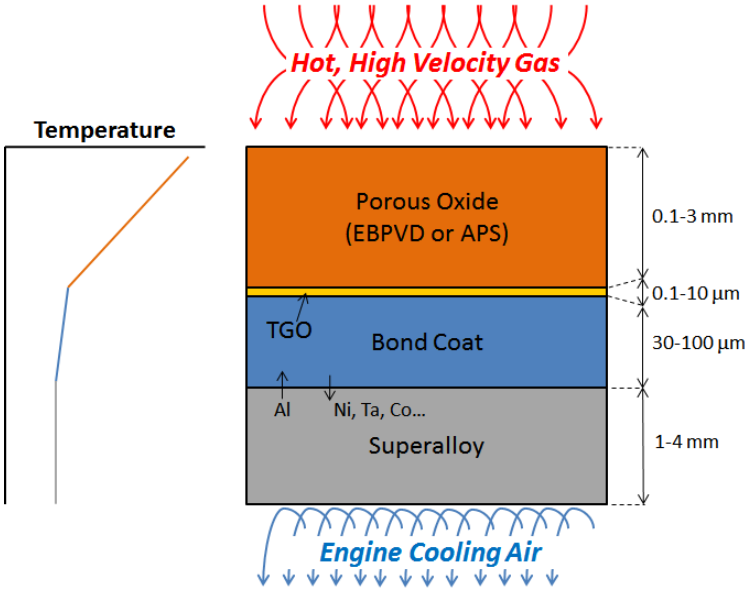

Figure I.7 *– Schematic illustration of the multilayer nature of the thermal-barrier coating system [8].*

The compositions of 7YSZ coatings (7 wt. % Y_2O_3) have been empirically chosen based on their low thermal conductivity, high melting point, resistance to sintering, a capability to deposit constant composition, and resulting in long life TBCs. Zirconia possesses three crystallographic phases: monoclinic (m), tetragonal (t) and cubic (c) whose transformations depend on temperature (**Figure I.8**).

$$m\text{-}ZrO_2 \underset{950\ °C}{\overset{1170\ °C}{\rightleftharpoons}} t\text{-}ZrO_2 \overset{2370\ °C}{\rightleftharpoons} c\text{-}ZrO_2$$

Figure I.8 *– Allotropic phases equilibrium of zirconia under atmospheric pressure [12].*

As the temperature in the turbine fluctuates between RT and ~1300°C, zirconia can undergo a transition between t-ZrO_2 and m-ZrO_2, which is a reversible martensitic transformation. This transformation is quasi-instantaneous and causes an important modification of the volume of the cell from 4 to 5 % (**Figure I.9**) [12]. This transformation generates major internal stresses that can lead to the ruin of the coating. The addition of yttria stabilizes a tetragonal phase of zirconia (metastable tetragonal phase t') that arises from a

reversible ferro-elastic transformation, allowing the switch from one tetragonal variant to the other when stressed. As a result, the 7YSZ possesses high fracture toughness, hence leading to a good resistance to impact, erosion and spallation without major changes in the cell-volume.

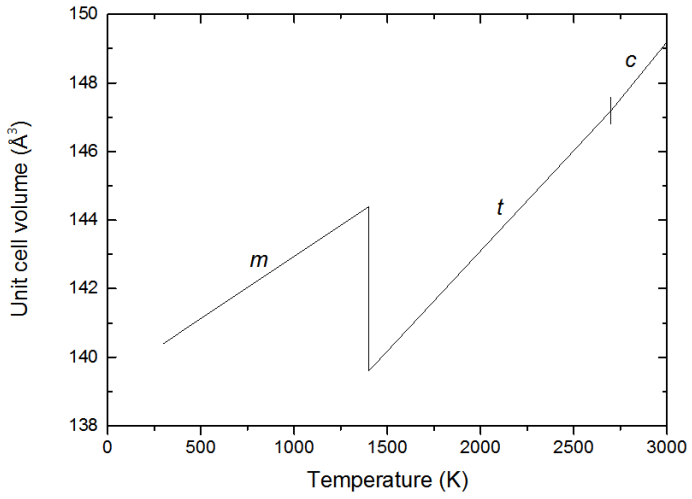

Figure I.9 *– Unit cell volume evolution of zirconia upon heating [12].*

Because of its refractory nature, the YSZ material possesses a melting point close to 2700 °C and requires ultra-high temperature materials processing capabilities. Currently, YSZ TBCs are deposited using air plasma-spraying (APS) or electron-beam physical vapour deposition (EB-PVD). For jet engines, the low-cost APS coatings are usually used for stationary components whereas EB-PVD TBCs are used to cope with more demanding hot-section parts in jet engines such as blades and vanes. These techniques allow the deposition of coatings (generally from 100 µm to 1 mm thick –and even more-) containing 10-30 % porosity. Porosity reduces the already low intrinsic thermal conductivity of YSZ by an additional 100-150%. As a result, the conductivity of the EB-PVD coatings is about half (45 to 65 %) of that of the bulk while the APS coatings have thermal conductivities of just about 20 % of the bulk. In addition to porosity of various shapes and sizes, many other defects like interfaces of different shapes and lengths contribute to lower the thermal conductivity. The amount and type of defects depend on the coating process. **Figure I.10** shows an example of the different defects that can be encountered in the two different processes. These defects also impart compliance to these coatings, which permits to the ceramic to accommodate the strains arising between the ceramic coating and the metal substrate (or bond coating) due to the differences of thermal expansion coefficients [13-16].

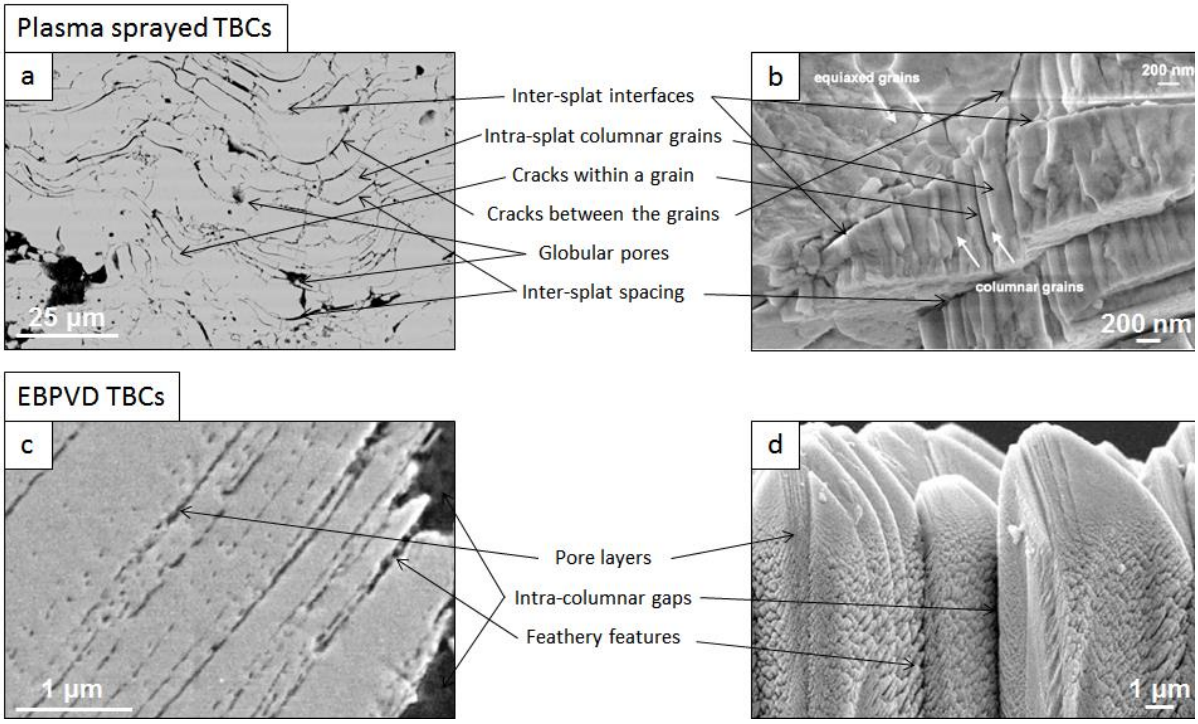

Figure I.10 *– Microstructures and defect components of atmospheric plasma sprayed (APS) and electron-beam physical vapour (EB-PVD) deposition thermal barrier coatings. (a,c) polished cross sections; (b,d) fractured cross-sections [13-16]*

Each of these coatings presents different advantages that are discussed hereafter. However, due to the constant need to increase temperature of service, new techniques and coatings are being pursued to increase the temperature that could be used with the metallic components of gas-turbine engines.

1.3.2.1 State-of-the-art processes for deposition of YSZ coatings

Atmospheric plasma spray deposition consists in the deposition of molten micro-sized particles using the energy of an arc-plasma to melt and accelerate them in the direction of the substrate to coat (**Figure I.11**). When reaching the substrate, the impacting particles form micro-splats which undergo rapid solidification. The resulting spray-deposited layer is the assembly of the splats that form a “brick-wall” structure. Typical powder particles in the range of 10-100 µm give splats of a few microns thick and of 100-150 µm in diameter. Under atmospheric conditions, most particles solidify independently, resulting in a chaotic assembly of the deposited microstructure that consists of splat-interfaces and unfilled regions that create the characteristic porosity.

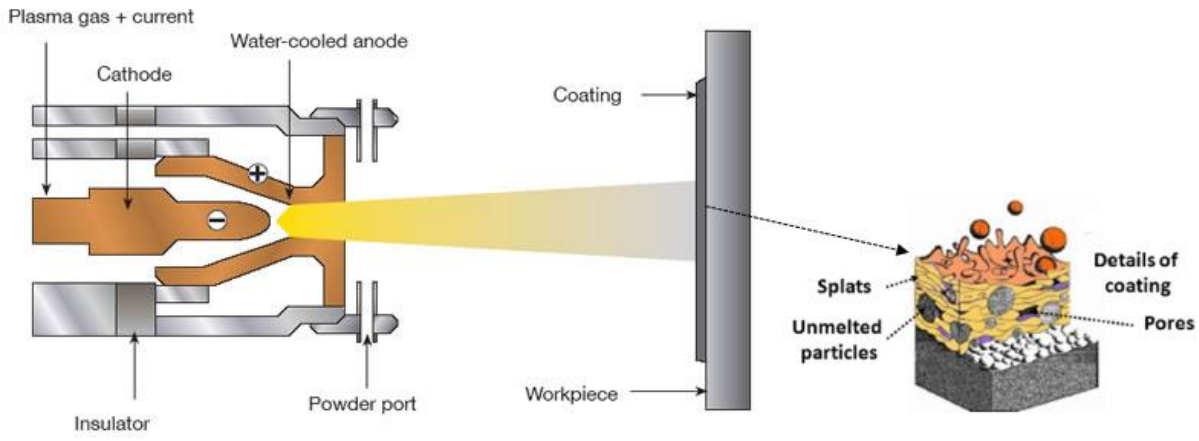

Figure I.11 *– Schematics of atmospheric plasma spray (APS) deposition process for thermal barrier coatings (TBCs) and resulting "brick wall" structure [17].*

In such process, the elaboration parameters are paramount for the resulting coating microstructure. In turn, the microstructure governs the thermal conductivity and stress compliance of the coatings. In this way, both the feedstock powder and the spray device play a major role in the nature of the deposit build-up, hence in the extrinsic microstructural character (porosity and interfaces) and in the intrinsic metallurgical properties of the material (grain size, texture, cracks, phase evolution and stability). In the recent years, progress has been made in the understanding on the impact of process parameters on the microstructure, hence on the performances of the coatings [18, 19, 20]. For example, the process parameters modify the amount and type of defects in a very significant way for YSZ. Steady progress has been made in the macroscopic quantification of the structure-property relationship (porosity-thermal conductivity relations) and in the underlying fundamentals on the generation of defects [20, 21]. These developments allow better monitoring and control of the desired properties of the coatings.

Electron beam physical vapour deposition processing relies on evaporation of the ceramic material. A highly energetic electron beam allows the melting and the evaporation of the ceramic ingots within a vacuum chamber and the pre-heated substrate is placed in the vapour cloud where the vaporised ceramic deposits on the substrate at rates of μm/min. The part to be coated is rotated in the vacuum chamber for homogeneous deposition on all sides. Due to the formation of the coating from a vapour phase combined with surface diffusion, shadowing and crystallographic growth selection, a columnar structure of the TBC is obtained. The microstructural features of EB-PVD YSZ coatings like shape and size of the columns, porosity

and the microstructural feature referred to "feather arms", are highly connected to the parameters of the process (**Figure I.12**).

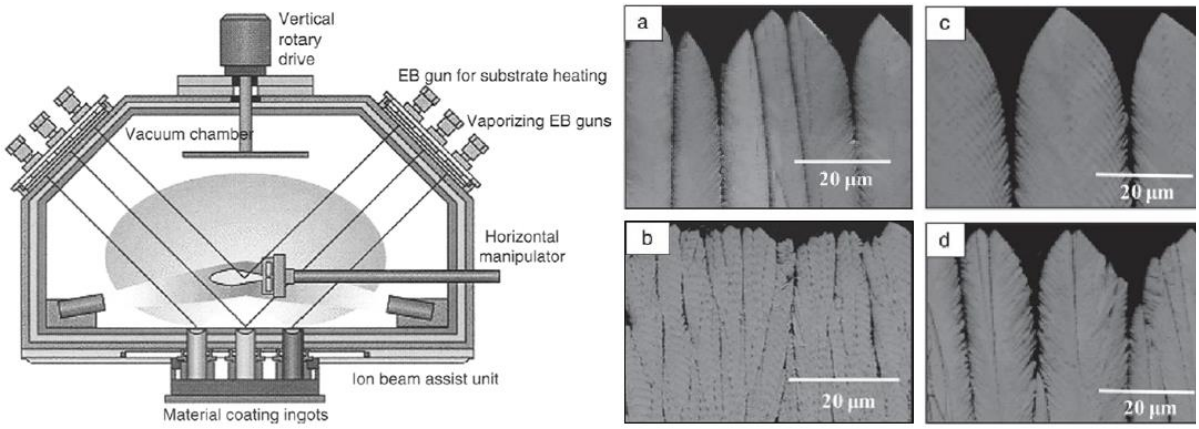

Figure I.12 *– A schematic of electron-beam physical vapour deposition (EB-PVD) processing. (a-d) are SEM micrographs showing cross-sections of different shapes of column obtained by varying the parameters of the process [13].*

All such features have a direct impact on the mechanical and thermal properties of the coatings. The main advantages of EB-PVD coatings is the columnar structure that provides a high strain tolerance and pseudo-plasticity compared with plasma sprayed coatings. Compared to APS YSZ coatings, the EB-PVD layers present higher erosion resistance, smoother surface finish (aerodynamic advantages) and do not obstruct the cooling holes of the blades upon processing. However, EB-PVD leads to higher cost, higher thermal conductivity of the coatings and limits in chemical tailoring due to vapour pressure issues.

1.3.2.2 Alternative coating processing and materials

Both EB-PVD and APS coatings are currently used in mainstream TBC manufacturing and offer different advantages in terms of compliance and thermal conductivity due to their specific structures. However, other processes and materials could be used in order to further improve the existing systems.

Some processes use enhanced plasma technology to create new type of coatings that differs in their microstructure and characteristics. By modifying the temperature of atmospheric plasma spraying, it is possible to obtain segmented cracked TBCs [22, 23]. By increasing the temperature of deposition, the rapid quench that the coating undergoes allows to obtain large microscale cracking (i.e. so-called segmentation cracks or dense vertical cracks) (**Figure I.13a**). However, the density of segmentation cracks occurs at the expense of micro-porosity. This is

related to the increase in temperature of the substrate and of the deposition parameters. In turn, the wetting temperature between overlaid splats is also increased and the number of splat interfaces decreases. Although the segmentation cracks lead to higher compliance to stress than the conventional APS YSZ coatings, the reduction of porosity induces a higher thermal conductivity.

Another process similar to APS uses suspension or solution precursors (suspension plasma spraying –SPS– and solution precursor plasma spraying –SPPS–) instead of micro-particles powder as alternative feedstock for plasma spray (**Figure I.13b**) [24, 25]. The use of a suspension or a solution allows the deposition of nano-droplets to form hybrid microstructures that combine the low conductivity of conventional APS coatings with the segmented cracks that impart in-plane compliance. As the deposited splats show very small dimensions (diameters from 0.2 to 6 μm and thicknesses of 20-300 nm), the number of inter-splat interfaces increases, which leads to low thermal conductivity. Because of the inherent low inertial mass of such small particles requires approaching the plasma to the substrate. Therefore, the increased temperature brings about the same phenomenon of vertical cracking observed for segmented cracked TBCs.

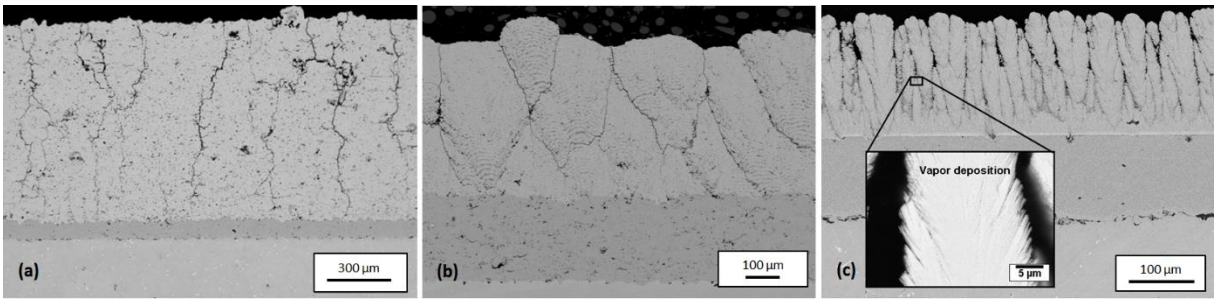

Figure I.13 *– SEM micrographs of alternative plasma spray techniques: (a) atmospheric plasma spray segmented cracked structure, (b) suspension plasma sprayed (SPS) coating and (c) plasma spray physical vapour (PSPVD) deposited coating [26, 27, 28].*

Originally developed as very low-pressure plasma spray (VLPPS), plasma spray physical vapour deposition (PSPVD) is currently an investigated technique that use the plasma in order to vaporise the feedstock material which will be deposited on the hot substrate in a way akin to PVD but at higher rates (**Figure I.13c**) [29, 30]. The microstructures, thermal conductivities and in-plane compliance are similar to those obtained by EB-PVD depending on the selected parameters of deposition.

Other deposition processes from aqueous precursors followed by a heat treatment to obtain TBCs (i.e. sol-gel and slurry routes) are being developed due to their multiple advantages compared to PVD methods. As a matter of fact, their relative low cost combined to the ease of use and the versatility that they offer present a non-negligible appeal.

The **sol-gel route** is a synthesis technique that allows obtaining high purity materials at relatively low temperature. The synthesis under liquid conditions allows tailoring the homogeneity, the stoichiometry, the crystalline structure and the size of the compounds synthesised. This method is based on the transformation of a liquid phase, the sol, into a semi-solid phase, the gel, by means of successive chemical reactions (hydrolysis and condensation).

The different deposition techniques that could be associated with such process (spray-coating, dip-coating and spin-coating), using the sol as a precursor, allow coating surfaces of pieces of different shapes and sizes. Metastable *t'*-YSZ coatings using the sol-gel route and the dip-coating technique have been achieved at relatively low temperature (700°C) due to the homogeneity of the precursor into the sol and the small grain size of the gel [31]. Due to the versatility of the sol-gel route and by tailoring the different parameters of the synthesis and the composition of the coatings, it is possible to obtain mechanical resistance equivalent to that of EB-PVD coatings and to functionalise them with additive elements to make them more resistant to corrosion [32] and to enhance their thermal insulation capacity [33].

The **slurry route** is a technique that uses a suspension of insoluble particles mixed in a liquid phase to coat the substrates like a painting. However, this technique is not widespread in the aero domain yet, except for repairing. Recent works have been though conducted in order to elaborate a complete thermal barrier system in a single-step process using aluminium micro-particles slurry [34, 35, 36]. The slurry is deposited on the surface of the material to coat and forms a layer composed of micro-particles of aluminium. After a proper thermal treatment, the aluminium diffuses into the substrate to form an additive layer (the bond coating) associated with a "foam" of emptied alumina shells on the top of it (the TBC), a thin alumina TGO being obtained at the interface between them (**Figure I.14**). Like the sol-gel route, the slurry technique is very versatile, and a wide variety of properties can be obtained by modifying the parameters of application. The technique and its relative features will be further discussed in section 4.

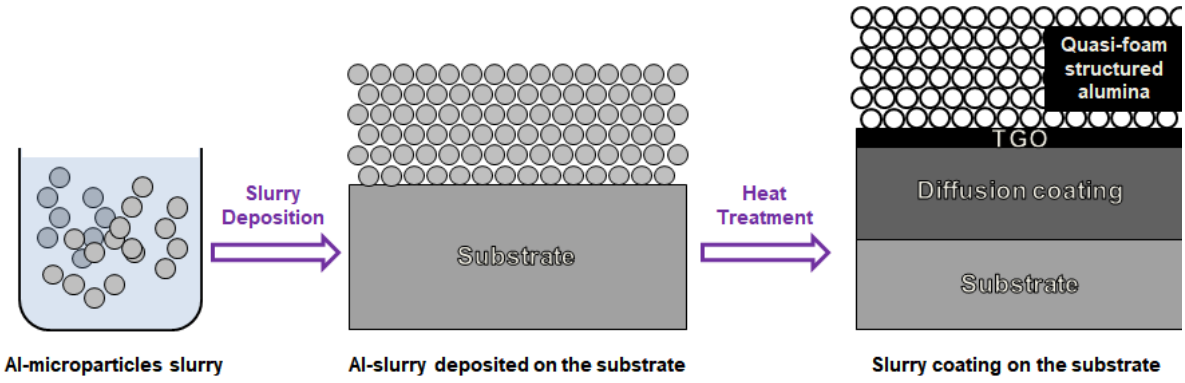

Figure I.14 *- Schematics of the formation of a thermal barrier coating using a slurry containing Al microparticles.*

2. Heat transfer mechanisms

Thermal insulation is the main role attributed to thermal barrier system. Therefore, the understanding of the mechanisms of heat transfer is a matter of importance to understand how the TBCs protect the materials from hot gases in the aero-engines and what is the role of the different features that compose the system (coating design, microstructure and chemistry) for providing thermal protection. The thermal conductivity is used to represent the thermal transport property of solids but unlike bulk materials, the thermal conductivity of TBCs is significantly affected by both the intrinsic properties of the materials and the extrinsic features of the system (microstructural defects, oxidation and temperature).

After a brief description of the general theory on heat transport, the case of thermal barrier system will be discussed for further understanding of the role of each feature on the overall thermal conductivity.

2.1 General theory

The theory of heat transfer has been widely described in the literature [37-40] and only a brief description is given hereafter.

In the case of crystalline solids, the heat energy can be transferred through electrons, lattice waves (phonons) and electromagnetic waves (photons). The total thermal conductivity (λ) is the sum of the three contributions is given by equation (I.1) in its general form:

$$\lambda = \frac{1}{3}\sum_{j=1}^{N} C_{p_j} v_j \, l_j \qquad \text{(I.1)}$$

where C_p is the specific heat at constant pressure, N is the total number of energy carriers, v is the velocity of a given carrier (group velocity if the carrier is a wave), and l is the corresponding mean free path (the mean path length where the particle or wave is free of interaction with any obstacle).

Concerning the **electronic contribution**, only electrons that do not interact with the crystal lattice are able to transfer energy. This type of electrons is only present in metals and partly in metal alloys, especially at high temperature. The electronic contribution of thermal conductivity λ_e is proportional to the product of the temperature and the electron mean free path, with v_e being independent of temperature. The electron mean free path has two components: the residual mean free path, which is related to the scattering of electrons by defects, and the intrinsic mean free path, which is related to the scattering of electrons by lattice vibrations. Only the intrinsic mean free path is dependent on the temperature.

The **lattice thermal conduction**, or heat energy transport by phonons, occurs in all type of solids. At low temperature, the component of thermal conductivity related to heat transport by phonons, λ_{ph}, is proportional to exp(T*/T) – where T* is the characteristic temperature of the material. T* is generally proportional to the Debye temperature – at low temperature and becomes proportional to 1/T as the temperature increases. λ_{ph} may also be expressed as:

$$\lambda_{ph} = \frac{1}{3} \int C_v \rho v l_p \tag{I.2}$$

where C_v is the specific heat capacity at constant volume, ρ is the density and l_p is the mean free path for scattering of phonons.

The heat energy transport by **photon conduction**, or radiation, especially occurs at high temperatures in materials that are transparent to infrared radiation, such as ceramics. The radiative component of thermal conductivity, λ_r, may be expressed as:

$$\lambda_r = \frac{16}{3} \sigma_s n^2 l_r T^3 \tag{I.3}$$

where n is the refractive index, l_r the mean free path for photon scattering (defined as the path length over which the intensity of radiation will be reduced by a factor of 1/e), and σ_s is the Stefan-Boltzman constant that relates temperature and scattering of a black body. In the harmonic approximation, a heat source will create vibrations in the form of phonons which will move through the sample to deposit their energy at the other end of the sample. Since there is nothing within the harmonic model to inhibit the flow of phonons, the thermal conductivity will

be infinite in value. Experimentally, it is found that the thermal conductivity decreases upon heating. As a matter of fact, in real crystal structures, a scattering of phonons occurs due to their interaction with lattice imperfections like vacancies, dislocations, grain boundaries, atoms of different masses and other phonons. Phonon scattering may also occur due to ions and atoms of different ionic radius as they locally distort the bond length and might create elastic strain fields in the lattice. The mean free path of the phonon is then proportional to the mean free path associated with each type of possible interaction of the real crystal structure where the lattice structure and the strain fields are the major contributors to it.

Based on an empirical expression, the contribution of **thermal conduction of a constrained gas** depends on the molecular mean free path of the gas l_g, which is proportional to T/P for ideal gas behaviour. The thermal conductivity of a gas λ_g, in a constrained channel of length d_v can be expressed as:

$$\lambda_g = \frac{\lambda_g^0}{1+\mathrm{BT}/(d_v P)} \tag{I.4}$$

Where λ_g^0 is the unconstrained conductivity of the gas at the temperature concerned and B is a constant which depends on the gas type (λ_g), on the solid surface material, the surface roughness and gas-solid interactions [41, 42].

2.2 Application to TBCs

The intrinsic features of the bulk materials determine the heat transport mechanisms. In solids, heat can be transported by phonons and free electrons at room temperature. In ceramics like YSZ coatings, phonons play the dominant role in heat transfer due to the lack of free electrons. In contrast, the electron mechanism of heat transport plays the dominant role for the metallic bond coating or substrate.

However, the extrinsic characteristics (temperature, pressure, microstructural defects and design) also play an important role in thermal transport, i.e. thermal conductivity of thermally sprayed materials is substantially reduced from that of their bulk counterpart and can reach a value from 90 % to 10 % of the bulk conductivity.

2.2.1 Radiative heat transfer

Considering the temperature of the environment, photon heat transport (radiation) will also occur. In an aeronautical engine, the TBCs that protect the substrate from the hot gas receive radiations which can be classified into two categories: far-field and near-field radiation. The

far-field radiation comes from the combustion gas whose temperature is about 1930°C [2]. However, this far-field radiation makes a small contribution as the hot combustion gas have finite thickness and limited opacity leading to a reduced emissivity. Near-field radiation comes from the layer of cooler gas, around 1200°C, adjacent to the surface of the ceramic top coat. The surface is then at the same temperature as this gas layer and emits radiations that can be transmitted through the ceramic layer, thanks to its partial transparency to infra-red radiation. This near field radiation contributes to the thermal conductivity and may considerably affect it at elevated temperature. **Figure I.15** shows the temperature dependent thermal conductivity of YSZ coatings.

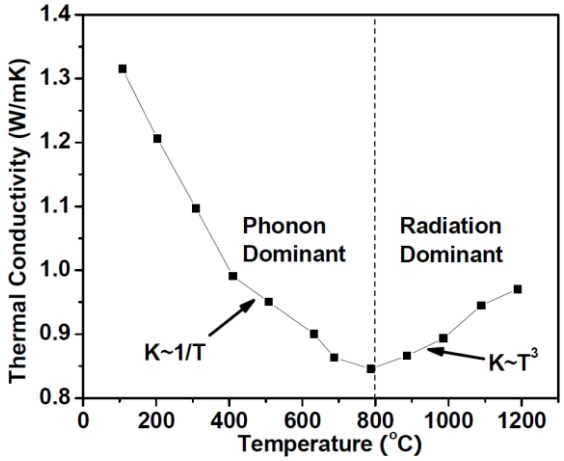

Figure I.15 *- Temperature dependent thermal conductivity of YSZ coating [43]*

From room temperature to 800°C, the heat transport in YSZ ceramic is mostly generated by phonon conduction and decreases due to scattering of phonons whose contribution increases with temperature. The component of thermal conductivity related to heat transport by phonons is then proportional to 1/T. As the temperature increases, the photon conduction becomes more dominant which results in an elevation of the thermal conductivity proportional to T^3. The contribution from radiation also depends on the radiation scattering lengths, which increases as the grain structure coarsens and inter-splat contact area increases.

2.2.2 Effect of microstructural defects

Although there are significant effects of extrinsic temperature and intrinsic attributes of the materials composing the thermal barrier system on thermal conductivity, the extrinsic microstructural defects arising from deposition process and transformations over time are determinant to the thermal transport of the system.

For ceramic coatings, the microstructural defects like grain boundaries, impurities and porosities are the main contributors to the reduction of thermal conductivity as they lead to significant phonon scattering. The grain size only influences the mean free path at low temperature and the crystal structure plays a more determinant role to the mean free path than the grain size. By adding yttria to zirconia, the lattice structure is locally modified, ion vacancies are introduced, and local strain fields are generated due to the large size of dopants. Such large concentration of defects also changes the vibrational modes from pure phonons in undoped and monoclinic zirconia to a variety of other modes in yttria-stabilized zirconia [44]. This results in lower phonon scattering length and, thus, in lower thermal conductivity.

Some studies on thermally sprayed coatings demonstrated that the most influencing extrinsic features that reduce thermal transport are the porosities and interfaces of the coatings because of their major role in phonon/photon scattering [21, 45, 46]. In the case of sprayed YSZ coatings, the microstructural defects consist of three types of pores: interlamellar pores – that result from the build-up of micro-splats – microcracks – that result from the stress relief after coating deposition – and globular pores – that are due to a lack of complete filling. These three types of pores fall into different ranges of size distribution. It has been shown that the thermal conductivity is strongly dependent on the pore morphology and porosity [47, 48]. As a matter of fact, the thermal conductivity of a gas inside a pore has a strong influence on the overall heat transfer and the temperature/pressure conditions may significantly affect its conductivity [49]. Convective heat transfer can be neglected between interconnected pores because the minimum size of pore required for convection to be significant is very high compared to the actual pore size [49]. **Figure I.16** summarises the different mechanisms of heat transfer through a zirconia-based plasma-sprayed TBC.

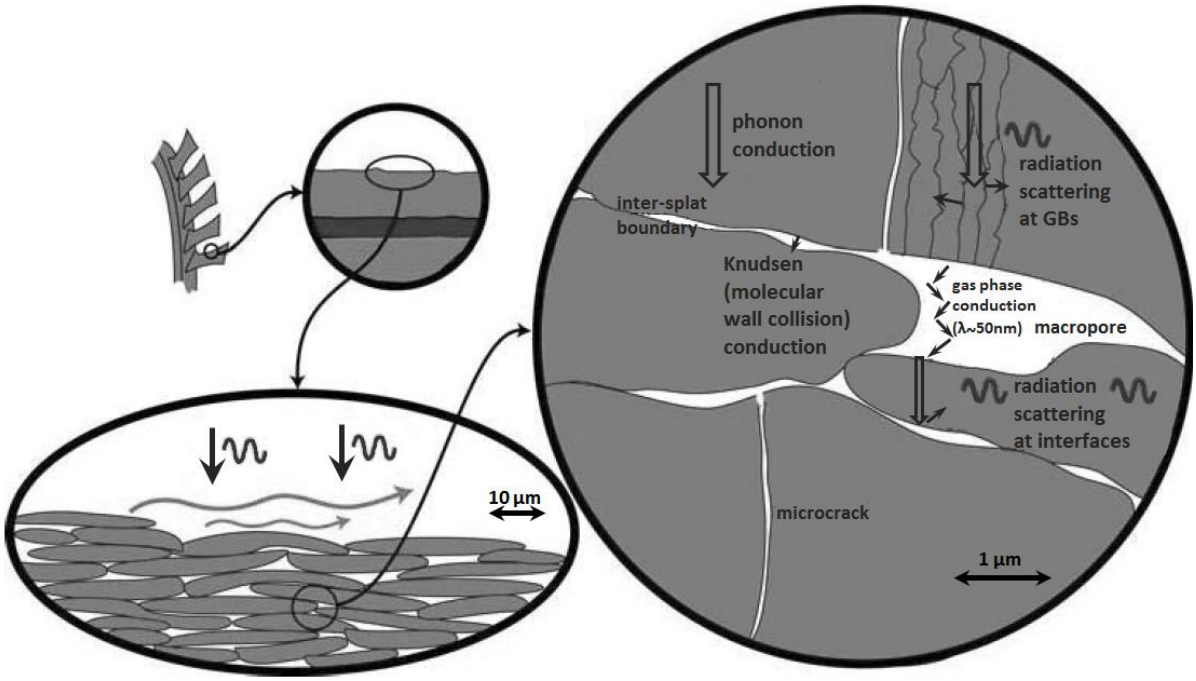

Figure I.16 *- A schematic representation of heat transfer mechanisms in zirconia-based plasma-sprayed TBCs [49].*

For metallic coatings, the extrinsic effects on thermal conductivity include the microstructural defects and the oxidation that occurs during spraying process (**Figure I.17**). In this way, their size and distribution and, thus, their contribution to the thermal conductivity will depend on the spraying processing. Also, impurities like copper or tungsten (particles coming from the electrodes of the torch for plasma spray coatings) or sand blasted particles (surface preparation) may be encountered in some cases. Depending on their concentration, distribution and size, their effects on thermal conductivity can be neglected.

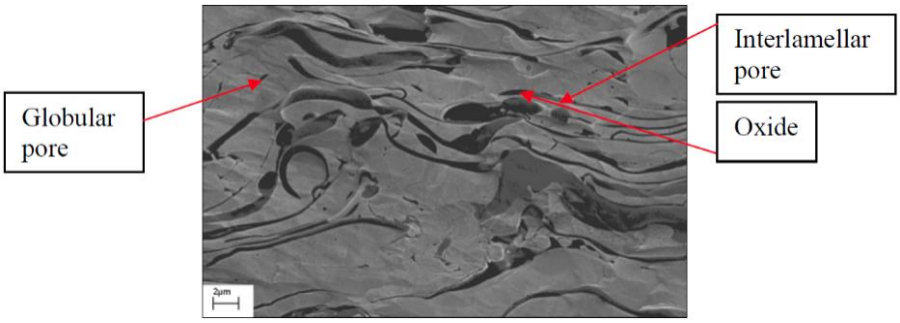

Figure I.17 *- Microstructural defects and oxide in sprayed metallic NiAl coating [50].*

3. Degradation mechanisms of TBC system

Due to the severe conditions of the gas turbine where the system operates, TBCs are prone to degradation over time that may reduce the life-time service. As a matter of fact, these degradations may have a direct impact on the mechanical behaviour of the system but may also reduce the thermal insulation capacity of the TBC that will also lead to a reduction of the life-time of the system. The different TBC failure mechanisms have been thoroughly reviewed by Evans et al. [51]. They can be differentiated into *intrinsic mechanisms*, due to the evolution of the system itself – in the conditions of temperature, pressure and gas composition of the environment – and *extrinsic mechanisms* generated by external factors. **Figure I.18** summarises the main mechanisms of intrinsic and extrinsic degradation that might be seen by the TBC system.

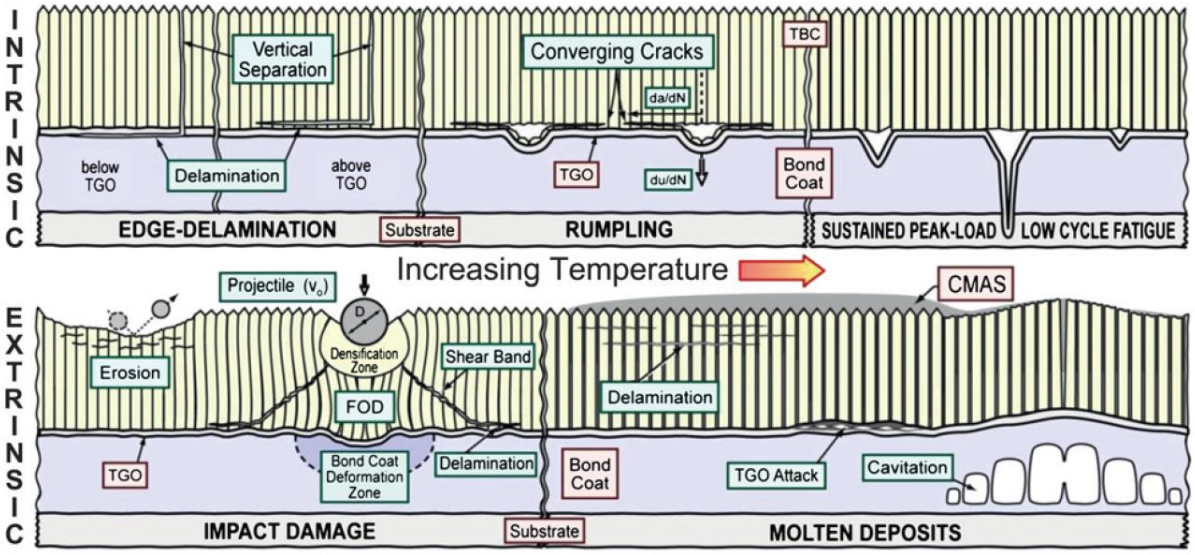

Figure I.18 *– Summary of failure mechanisms typical of current thermal barrier coatings [52].*

3.1 Intrinsic degradation

As the TBC systems are exposed to high temperatures coupled to harsh environments and thermal cyclic conditions, they may undergo inherent microstructural and chemical modifications. Among these degradations, the major effect on the lifetime of the systems is attributed to the TGO growth. Nevertheless, sintering is not to be neglected as it might lead to a drastic reduction of the insulation ability of the coating and thus, to a faster degradation of the system.

3.1.1 Edge-delamination, rumpling, buckling…

It is to be highlighted that the most severe constraints are imposed on the bond coating whose primary function is to provide the Al reservoir to form a protective α-Al_2O_3 oxide while anchoring the ceramic top coat without reacting with it. The TGO is expected to remain elastic at high temperature and not to creep excessively to prevent "rumpling" or cavitation on thermal cycling (see **Figure I.18**) that can lead to local spallation at the TBC interface. However, the ceramic coating being permeable to oxygen (TBC microstructures are highly defective with porosity and cracks and YSZ is an oxygen conductor). Therefore, the oxidation of the bond coating cannot be fully prevented (**Figure I.19**). Although the Al_2O_3 is the slowest growing oxide at high temperatures, thickening cannot be avoided and over a critical thickness failure of the system occurs. This critical thickness can be understood as the maximum stored elastic strain energy that the film can withstand before exceeding its fracture resistance. The two main contributions to the stress in the TGO are associated with the growth strain as new oxide is formed (thickening and lateral expansion) and with the mismatch stress generated by the differences of thermal expansion coefficient of the substrate and the oxide through cooling.

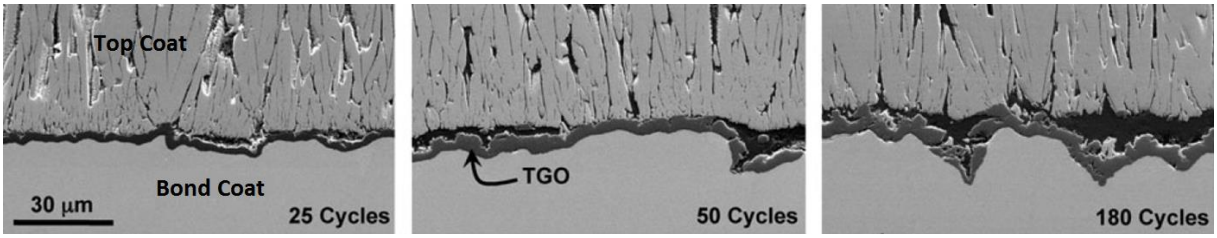

Figure I.19 *– Cross-sectional SEM images showing the progression of thermally grown oxide (TGO) thickening and the evolution of local interface separations in a EB-PVD 7YSZ TBC [8].*

3.1.2 Sintering

During exposure at high temperatures, the gaps between fine cracks and pores sinter together at discrete contact points, leading to a reduction of the global porosity rate and number of interfaces (**Figure I.20**). This sintering is known to reduce the TBC mechanical performances [53, 54, 55]. It may also contribute to a decrease in thermal resistance due to the loss of phonon-scattering defects, i.e. fine porosities of feather-like EB-PVD coatings [56, 15] and microcracks or lamellar interspaces of plasma sprayed TBCs [49, 57, 15]. As a result, the thermal conductivity increases. Such sintering is driven by both in-plane stress within the coating and the surface energy of the zirconia $-\gamma_{TBC} = 1\ J.m^{-2}$ [55]. Moreover, the sintering of the TBC is also associated with an increase of the Young's modulus of the ceramic coating,

which in turn promotes high in-plane stresses within the coating during thermal cycling that result in delamination [55].

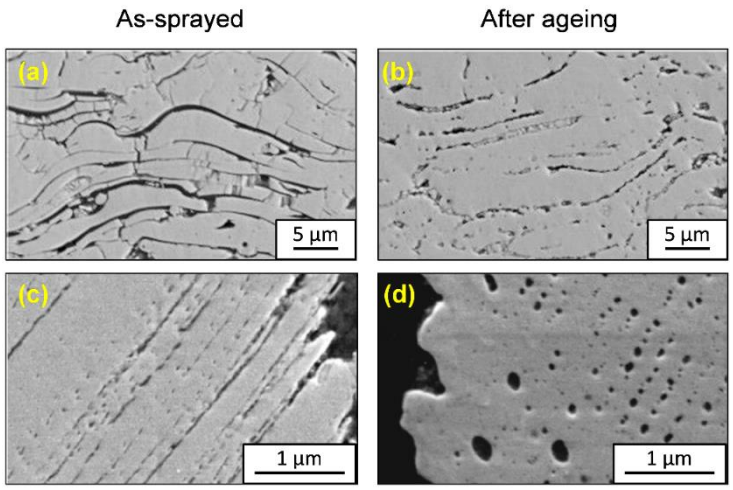

Figure I.20 *– SEM micrographs showing polished cross-sections of (a,b) APS YSZ coatings and (c,d) EB-PVD PYSZ coatings in the (a,c) as-sprayed conditions and after (c) 1100 °C - 200h and (d) 1200°C - 500h [15, 58].*

3.2 Extrinsic degradation

Upon service, the TBCs are also exposed to degradations that originate from their environment. Indeed, the intake air of the engines may contain different kinds of particles and impurities (e.g. sodium –from NaCl-, sulphur – from SO_2-), and the fuel may also contain diverse damaging impurities like vanadium or sulphur. The ingested particles move at a high velocity and, being submitted to the high temperature of the engine, can lead to different mechanisms of degradation.

3.2.1 Impact damage

Erosion by impinging particles is a concern that is more pronounced on EB-PVD than on APS TBCs. Since EB-PVD TBCs are the designated coatings for turbine blades, the hot gas stream to which they are subjected implies greater impact velocities and higher impact angles, which make the erosion problem a possible life-limiting problem. Previous works showed that the erosion of such TBCs resulted from a number of distinct mechanisms depending on the particle impact energy (related to particle size, density and velocity), the particle temperature (solid or semi-molten state of the particle), and the microstructure of the coating [59]. Three modes on the different types of damage mechanisms have been observed for erosion of EB-

PVD TBCs and could be singled out based on their criticality. However, these mechanisms are not mutually exclusive, and a certain degree of overlap is possible due to the various nature of particles impacting the coatings.

3.2.1.1 Mode I – erosion (lateral cracking/near surface cracking)

This erosion mode indicates individual columns cracking at the top 20 µm of the surface of the TBC induced by small particles with low energy (**Figure I.21**). Material loss is observed when a certain number of neighbouring columns have been impacted and cracked.

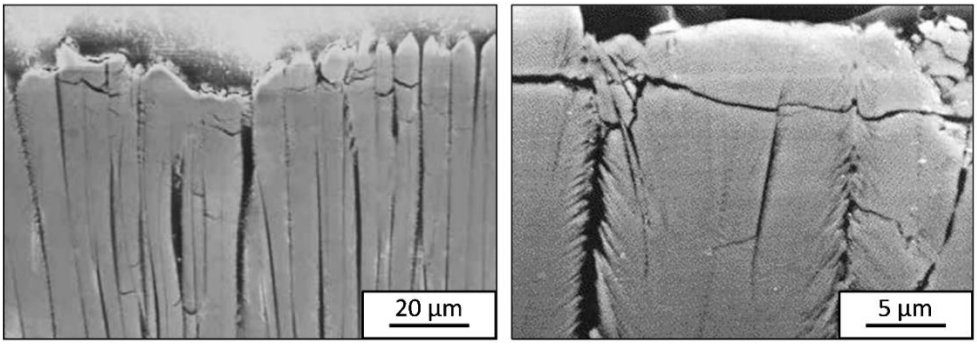

Figure I.21 *– Cross-sectional SEM micrographs of eroded EB-PVD TBCs [59, 60]*

3.2.1.2 Mode II – compaction damage

This mode is an intermediate damage mechanism between small particles erosion and foreign object damage (FOD), where compaction of the EB-PVD TBC columns is observed but neither the near surface cracking of Mode I nor the large plastic deformation of Mode III (FOD) are involved. This compaction (**Figure I.22**) results from the surface impact of low energy particles on the highly porous columns where cracking does not occur.

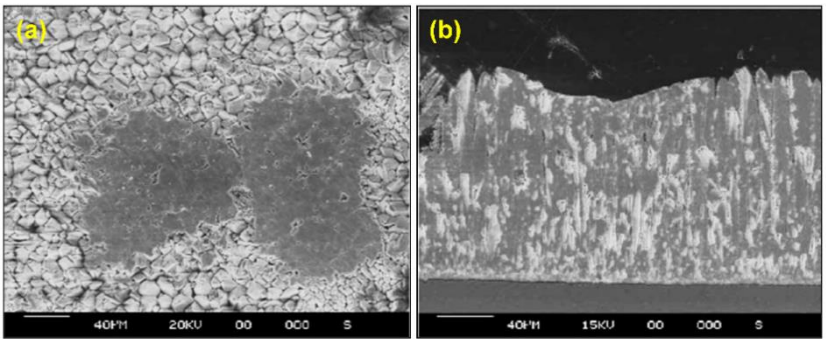

Figure I.22 *- Micrographs of single impact Mode II compaction damage showing compaction of the coating, note the absence of cracking: (a) top view; (b) cross-section view [59].*

3.2.1.3 Mode III – foreign object damage (FOD)

FOD occurs when large particles with low and intermediate velocities, or smaller particle with higher velocities, hit the TBCs, leading to significant deformation of the columns that may propagate to the substrate. This mode is subdivided into two other types according to their effect on the coating. The first one is the classically accepted mechanism that results in a large deformation of the coating with the associated densification bending and cracking of the columns (**Figure I.23a**). The second one rather involves a significant buckling of adjacent columns and plastic deformation at elevated temperatures without any significant degree of cracking (**Figure I.23b**).

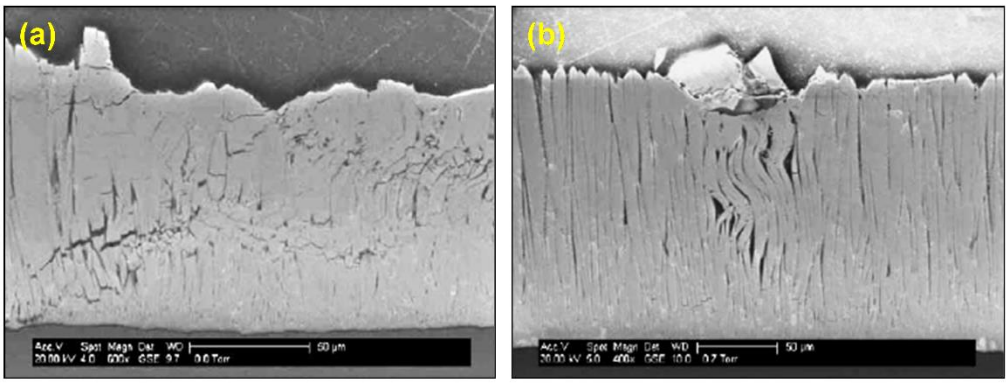

Figure I.23 *- SEM micrographs illustrating FOD in EB PVD TBCs: (a) Type 1; (b) Type 2 [59].*

These degradations may induce a progressive (or sudden) spallation of the TBC, hence reducing the life time of the system. Impact damages are due to solid (or semi-molten) particles that are ingested in the turbine engine. However, some of these particles may reach the TBCs molten, which leads to other degradation modes.

These different impact damages bring about changes in the thermal conductivity as they change the structural properties of the coatings. Whereas cracks formation or erosion leads to local loss of the coating, compaction damages can therefore also conduct to densification and, thus, to the loss of the porosity responsible for thermal insulation.

3.2.2 Molten deposits

Among the different sources of identified failures of yttria-stabilized zirconia (YSZ) -based thermal barrier coatings (TBCs) [8], the infiltration of siliceous molten deposits, also known as Calcium-Magnesium-Alumino-Silicates (CMAS), are a matter of concern [10]. In the hot-gas path and at peak temperatures, CMAS deposit yields a glassy melt that can penetrate the porous

structure of ceramic coatings due to its low viscosity [61, 62, 63]. This penetration of the melt within the coating, slowed due to the inherent temperature gradient across the coating thickness, degrades the in-plane compliance of the structured ceramic, further leading to delamination processes upon thermal cycling [64, 65]. Moreover, it has been shown that CMAS can chemically interact with the YSZ material, leading again to structural modifications but also to phase transformations. Thus, CMAS related damages could be classified as thermomechanical or thermochemical aspects.

3.2.2.1 Thermomechanical degradation

Once the siliceous debris deposited on the hot parts start to melt, the infiltration of the molten mixture begins thanks to a great wettability and to the capillaries formed by the columns for EB-PVD coatings (**Figure I.24**) or the porous network of APS coatings. Due to the temperature gradient throughout the TBC, the melt keeps infiltrating till it reaches a cooler depth that lowers its viscosity. After cooling, the zone of the TBC where CMAS has penetrated and solidified cannot release the elastic strain energy stored in the coating, which becomes the driving force for the delamination and spalling of the TBC. The progressive delamination of the ceramic leads to a loss in its insulating capacity. As a result, the temperature at the metal interface is increased, hence the oxidation rate and the activation modes of failure, e.g. rumpling or cavitation [8].

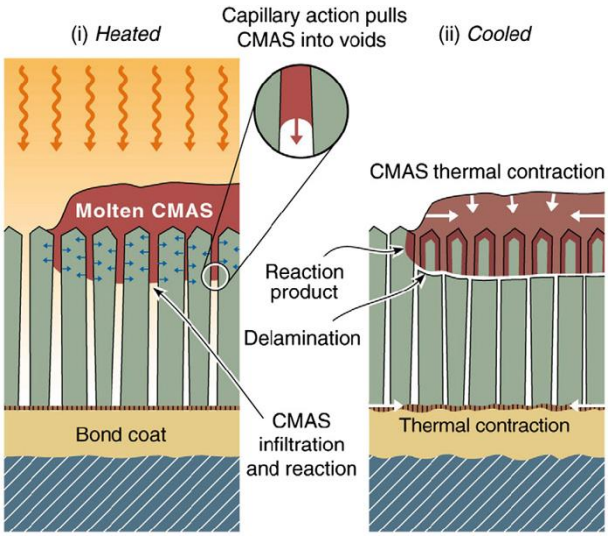

Figure I.24 *– A schematic representation of molten CMAS penetration in an EB-PVD TBC and resulting spallation upon cooling [66].*

Recent work has also shown that chemical interactions between CMAS and the TGO may lead to delamination along the TGO or promote creep cavitation in the bond coating wherein the delamination crack path would propagate within the metal [67].

Moreover, infiltration of the CMAS melt in the void spaces of the coating causes an effect similar to sintering that few studies proved to result in a decline of the insulation capacity of TBCs [68, 69].

3.2.2.2 Thermochemical degradation

Even if *t'*-YSZ is unlikely to meet the long-term requirements for advanced engines due to inherent limitations in its phase stability above 1200°C, the thermochemical interactions of CMAS with the *t'*-YSZ TBCs are an important matter in understanding the mechanisms of chemical interactions and developing alternative coatings since CMAS nominally attacks all oxides of interest for thermal barriers.

A way to understand the chemical interactions is based on the knowledge of the chemical composition of the molten deposits. However, their composition varies a lot and depends on the different sources that provide the siliceous minerals as well as other engine-originating sources of oxides due to erosion. **Figure I.25** gathers different compositions of mineral sources and examples of engine deposits already encountered compared to model CMAS used in laboratory. Another important fact is that the melts infiltrating the TBCs do not necessarily have the same compositions as that of the deposits on the surface of the coatings, probably indicating a partial melt of these deposits. The infiltrated CMAS were reported to possess similar composition despite the different compositions of the deposits. However, the diversity of reaction products with the *t'*-YSZ could indicate that small variations of CMAS compositions may have very different impacts on the coatings. Recent studies have reported that the composition of CMAS could be classified depending on a "*basicity index*" that correlates the compositions to a degree of severity on the corrosion of the coatings [70].

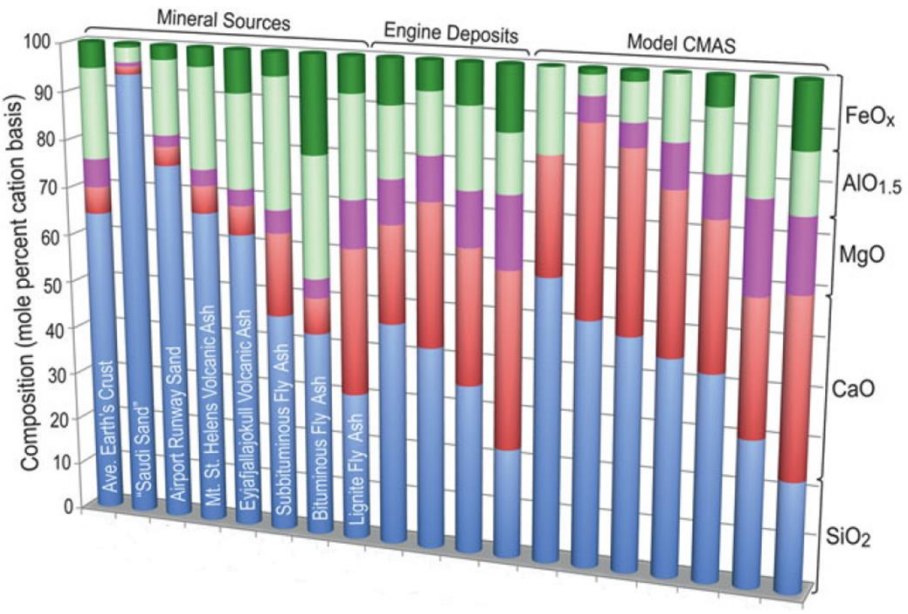

Figure I.25 *– Concentration of predominant oxides in the composition of calcium-magnesium alumino-silicates, grouped by examples of sources of siliceous debris, compositions reported for actual deposits in engines, and model compositions used in laboratory investigations of the problem. [71]*

The mechanism of interactions between the siliceous melt and the oxide of the coatings is that of a dissolution/re-precipitation. The oxide of the coating dissolves in the siliceous melt and re-precipitates in one or more crystalline phases upon saturation [14]. However, when the temperature is above the melting point of CMAS, the penetration of the melt can lead to different interactions with the surrounding TBC. When the amount of CMAS is large, the *t'*-YSZ is dissolved and re-precipitates as Y-lean ZrO_2 (that can transform to monoclinic on cooling) or as a fully stabilized Y-rich ZrO_2 depending on the amount of alumina content of the melt [14, 72]. In contrast, the diverse compositions of CMAS can lead to various complex oxides as $Ca_2ZrSi_4O_{12}$, $ZrSiO_4$ and even produce tetragonal YSZ [73, 74]. The destabilization of the t' phase that results from the depletion of Y in the ceramic matrix may provoke an increase in heat transport as it has been demonstrated that the thermal conductivity of YSZ is also dependent of the Y content [75]. Kakuda et al. investigated the effect of amorphous CMAS infiltration on the thermal properties and heat transport of plasma-sprayed (APS) coatings using phase of photo-thermal emission analysis (PopTea) and observed a rise in both volumetric heat capacity and thermal conductivity of the coating upon infiltration [69].

4. Motivations and objectives of the study

4.1 Statement of the problems

Considering the need to increase the gas temperature of turbine engines for reduction of fuel consumption and increased performances, new issues arise due to the current limitations of material temperature and coatings efficiencies. In the hottest section of the turbine (HPT), the current coatings will not be protective enough to cope with the rise in temperature, hence creating a need to develop new solutions. Similarly, the materials of the LPT section might need additional protection as their surface temperature will increase.

For the HPT section, studies thus focus on finding new processing and low-conductivity oxides to perform coatings that would replace the current columnar YSZ TBCs. As the evaluation of TBCs life time is critical for engine service span, understanding the evolution of TBC's insulation ability, which is directly related to the coating intrinsic properties (composition, microstructure and thickness), is a key challenge for the future of TBCs. Lowering the thermal conductivity of TBCs is then dependent on the understanding of the relationship between the insulation ability and the properties of the coating.

However, the complexity and diversity of these properties arising from the plurality of TBCs make it difficult to establish universal insulation–property relationships and the dynamic evolution of microstructure and property during service offers additional challenges to microstructural characterization as well as lifetime prediction. In addition, the applicability and repeatability of the techniques for thermal conductivity measurements have a significant effect on the accuracy of the obtained results and thus, on the reliable description of microstructure-property relationships.

The second challenge, arising from the need to extend the thermal protection to the LPT section, is to find a solution that also considers economic limitations. On an industrial scale, the extrapolation of the TBCs from the HPT section to the LPT is not a viable solution as EB-PVD and plasma spray processes are complex and thus very expensive.

4.2 Summary of the Proposed Strategy

To address the different issues outlined in the above section, this dissertation is structured following two main axes. Firstly, based on current APS and EB-PVD coatings, the dissertation seeks to provide a better comprehension on the relationships between the intrinsic properties of

the current TBCs and their thermal insulation capacity in order to give reliable tools for the development of future coatings. The second part of the work focuses on the study of an alternative solution to create a TBC from a cost-effective and environmentally friendly process through the slurry route.

4.2.1 Evaluation of the relationships between intrinsic properties and insulation capacity of APS and EB-PVD YSZ coatings

Understanding the evolution of TBC's insulation ability over ageing depends on the comprehension of the degradation mechanisms that could affect the thermal transport properties. For instance, an obvious loss of the thermal insulation potential of the coatings occurs via a reduction in thickness of the coating by spallation or erosion. Microstructural changes such as sintering, crack formation, delamination, filling of pores by infiltrating molten glass can also modify the heat transport properties. In addition, chemical changes like phase transformations of the stabilized-tetragonal phase due to CMAS corrosion could also alter the thermo-physical properties and hence must be considered. Plasma-sprayed (PS) and EB-PVD TBCs possess very different microstructures and thus, must be studied separately to understand how their microstructure affects heat transport and how ageing affects the microstructure-thermal insulation relationships.

As previously mentioned, some studies have focused on the impacts of time and temperature that result in modifications of the structure of PS TBCs via sintering and oxidation, and on the associated relative changes of thermo-physical properties [76, 77, 78, 79]. However, most of these studies have only focused on the ceramic coating itself while the evolutions of the other components of the thermal barrier coating system have been neglected. For instance, the development of the thermally grown oxide (TGO) and the growth of cracks in the ceramic due to thermal cycling may also play a role in the overall protection potential of TBCs. Furthermore, the CMAS-related degradation mechanisms that are susceptible to increase heat transport through the TBCs by filling the pores or by chemical transformations have been only demonstrated in a few studies [68, 69].

For EB-PVD coatings, some studies dealt with the impact of the thickness and the columnar morphology of the coatings on the associated heat transport properties [80, 81]. However, very few investigations were conducted to understand the influence of ageing on the heat conduction of these coatings [15, 82, 83]. For the interaction of these columnar coatings with molten

CMAS, the studies were mostly conducted to understand the degradation mechanisms [84, 63, 66] and none can be found on the impact on the thermal transport properties.

To deepen our understanding on the relation between the properties of heat transport and the evolution of the TBC system for both coatings upon ageing, the discussion has been separated in two chapters (III and IV). The first one (chapter III) focus on PS TBC systems and intends to shed light on the microstructural and chemical changes arising from exposure to high temperature with or without CMAS deposit to show how the related transformations could affect the heat conduction. Chapter IV is thus focused on the same issues but for EB-PVD TBC systems.

Finally, the last part (chapter V) describes the mechanisms of formation and the properties that offer the alternative TBCs made from the slurry route whose challenges are discussed hereafter.

4.2.2 Thermal barrier coating made from the slurry route

4.2.2.1 Presentation of the PARTICOAT concept

The formation of a complete thermal barrier coating using the slurry technique (presented in 1.3.2.2) appears to be a convincing alternative for protection of materials of the LPT section due to its relative low cost and ease of application. The University of La Rochelle was involved in the European project “PARTICOAT” (2008-2012) [86] whose purpose was to obtain a complete thermal barrier coating in a single-step process from Al-microparticles in water-based slurries.

Studied **under pure argon**, on a pure Ni substrate first [34] and then extrapolated to Ni-based superalloys [87, 88] and iron-based alloys [89], the mechanism of formation was found to involve self-propagating high-temperature synthesis (SHS), combustion synthesis [88] as depicted on **Figure I.26** for a Ni-based substrate. The surface of the Al microparticles get oxy-hydroxylated in the aqueous slurry at room temperature [90]. Upon curing of the slurry, thickening and oxidation of the surface shell occurs by dehydration [91]. As the temperature gets closer to the melting point of Al, the oxide shells of the microparticles start to crack due to internal build-up pressure and release the molten Al toward the substrate. Then, an exothermic reaction occurs, leading to a fast melting of the remaining Al that progressively dissolve the Ni of the substrate to form Al-rich intermetallics [88, 92]. When Al stops flowing from the particles, solid state diffusion occurs between the Ni substrate and Al-rich coating to form a

Ni_2Al_3 layer. An annealing heat treatment at high temperature, i.e. 1000-1100°C, is necessary to transform the Al-rich layer into the β-NiAl phase.

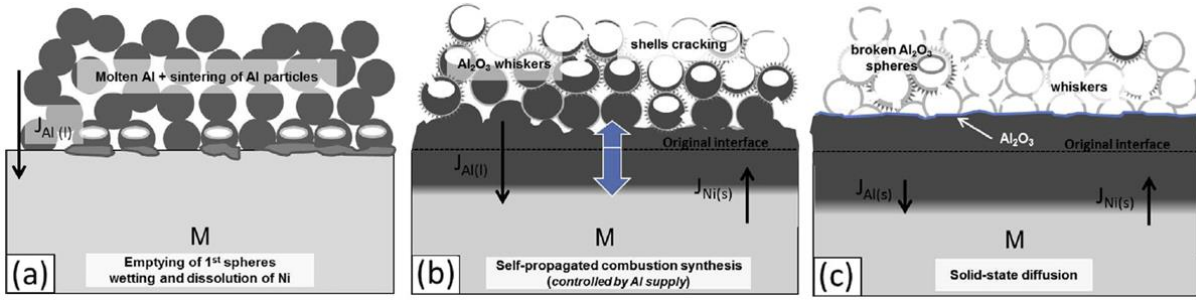

Figure I.26 *– Mechanisms of formation of the thermal barrier system on a metal substrate proposed by Bouchaud et al. [92].*

At the same time, the shells of the Al microparticles start to oxidize and sinter on top of the diffusion layer to form a ceramic foam coating. The resulting coating was shown to provide thermal insulation when measuring the temperature difference between the surface heated with a butane flame and the back side of the sample. The preliminary laser flash measurements also demonstrated a significant decrease of the thermal conductivity of this thermal barrier coating system with hollow alumina spheres [35, 93]. However, the annealing of these coatings conducted in Ar resulted in very thin alumina shells. Therefore, the grit blasting with alumina sand at different angles showed poor erosion resistance of these coatings. Therefore, further work was needed to strengthen this ceramic foam.

4.2.2.2 Oxidation of the Al microparticles: influence of oxidizing atmosphere

A recent study pointed out the importance of the annealing conditions on the formation of hollow alumina from the Al microparticles [91]. The composition of the atmosphere was found to play a prime role for finding the balance between releasing the Al towards the substrate and oxidizing the shells to obtain the hollow spheres [94, 95]. As the release of the Al from the oxide shells was associated with the simultaneous peripheral oxidation of the spheres and the expansion of the Al core due to the increase in temperature upon heating [91, 96], the thickening of the shells was found dependent on the oxidizing capacity of the atmosphere and the flow rate of Al through the cracks. Moreover, the mechanisms of oxidation that were first proposed by Levitas et al. [97, 98, 99, 100] were shown to be different depending on the particle size (i.e. nano- or micro-sized).

For micro-sized particles, the initial amorphous alumina shell grew until it reached the critical thickness of 4-5 nm [95, 101, 102] which crystallized into γ-Al_2O_3 around 550°C, prior to Al melting [94, 95, 103, 104]. Due to the higher density of the γ-Al_2O_3 phase compared to the amorphous oxide, the shrinkage of the oxide led to a cracked layer that could be healed through the exposure of metallic Al to the atmosphere [96]. Then, as temperature increases, metallic Al could diffuse through the cracks depending on the pressure build-up of the Al melt and the resistance of the mechanical strength of the shell [96, 97, 100]. During the final stage of annealing at high-temperature performed to transform the Al-rich layer into β-NiAl, the γ-Al_2O_3 was fully converted into the α-Al_2O_3 [94, 104]. This oxide transformation is accompanied with a volume shrinkage of about 13.8 % that was proposed as the responsible for the formation of cracks and pores in the shells [96].

The mechanisms of formation of this slurry coating presented in Ar [34, 88] were also studied under air [87] but did not focus on providing both the diffusion coating and the ceramic foam. As a matter of fact, only a recent study showed the difficulty to obtain this duality in a single step process on pure Ni substrate [105]. Tailoring the temperature and the atmosphere of the treatment was outlined in this study to be essential for the formation of adherent top foam with thicker shells while diffusing enough Al towards the substrate to form the aluminide coating. **Upon annealing in flowing Ar**, only a partial crystallization of the amorphous shell occurred before the melting of Al. With the Ni substrate, melting of the Al was accelerated by the combustion synthesis but the O_2 partial pressure of the atmosphere was not sufficient to thicken the shells before the diffusion of the Al towards the substrate. Consequently, the resulting shells presented thin walls with a low sintering. However, **under a flow of synthetic air**, the annealing was shown to heal rapidly the γ-Al_2O_3 shell causing the Al to be kept in the particles. Only large particles were able to release the Al due to a greater amount of liquid Al that generates greater stresses within the oxide shell. Further heating to high temperature leaded to the γ-Al_2O_3 to α-Al_2O_3 transition while the Al left in the shells slowly flowed through the cracks and was rapidly oxidized to form thicker walls. In this case, due to the very oxidative atmosphere, the Ni substrate developed oxides that formed a barrier to the diffusion of Al, thus resulting in heterogeneity in the aluminide coating.

4.2.2.3 Strategy to enhance the slurry coating performances

The idea proposed in this study is to obtain both aluminide coating and thick shells using a hybrid treatment in which a change from an inert atmosphere to an oxidative atmosphere is operated at intermediate temperature. The first steps of the heat treatment will be performed

under Ar to allow enough aluminium to diffuse in the substrate. Then, a switch to synthetic air should provoke the fast oxidation of the remaining Al to thicken the shells. Water vapour will be also studied as an alternative to synthetic air for the oxidative atmosphere as it was demonstrated to result in shell oxidation in a different way compared to air [91].

The mechanisms of formation of the coatings using the described hybrid heat treatment will be discussed in the first part of chapter V. In the second part of this chapter, the resulting coatings will be mechanically tested, and their thermal insulation capacity measured via the laser-flash technique and compared with the state-of-the-art YSZ TBCs.

4.2.3 Structure of the dissertation

The structure of the dissertation is summarized in **Figure I.27**. Firstly, chapter II describes the methods used to characterize the microstructural and chemical modifications of the studied TBC systems and the details of the techniques used for the determination of their thermal insulation potential. The experimental methods for the elaboration of the slurry TBCs will be also described. Then, in the first part of the dissertation that gathers the APS and EB-PVD coatings, the scientific publications from 1 to 4 will attempt to deepen our understanding on the relation between the properties of heat transport and the evolution of the TBC system resulting from ageing of the state-of-the-art coatings. The second part describes the mechanisms of formation and the properties that offer the alternative TBCs made from the slurry route and gathers the articles 5 and 6. Conclusions on the work presented in these articles are summarized in chapter VI.

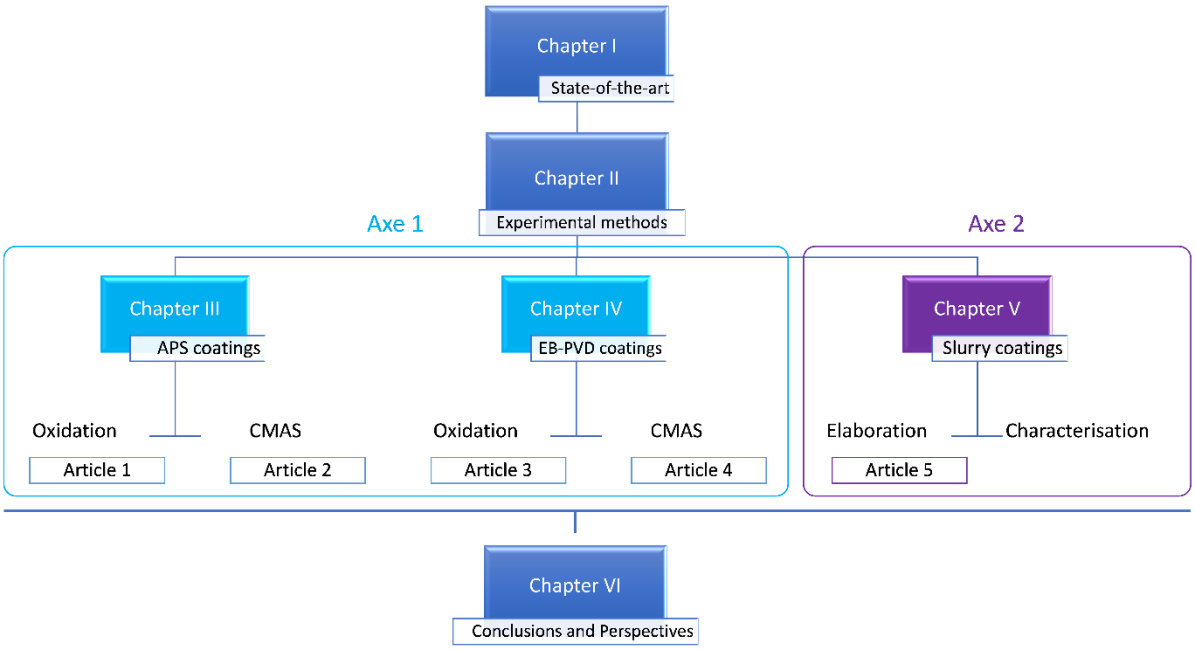

Figure I.27 *– Summary of the dissertation's structure with the associated scientific articles per chapter.*

List of articles:

1. *Evolution of Thermal Insulation of Plasma-Sprayed Thermal Barrier Coating Systems with Exposure to High Temperature, accepted in Journal of the European Ceramic Society, 2019, DOI: 10.1016/j.jeurceramsoc.2019.01.026*

2. *Thermal insulation of CMAS (Calcium-Magnesium-Alumino-Silicates)- attacked plasma-sprayed thermal barrier coatings.*

3. *Phase Stability and Thermal Insulation of YSZ and Erbia-Yttria co-doped Zirconia EB-PVD Thermal Barrier Coating Systems.*

4. *Thermal Insulation of YSZ and Erbia-Yttria co-doped Zirconia EB-PVD Thermal Barrier Coating Systems after CMAS attack.*

5. *Development of thermal barrier coating systems from Al microparticles. Part I: Influence of processing conditions on the mechanisms of formation.*

6. *Development of thermal barrier coating systems from Al microparticles. Part II: Characterisation of mechanical and thermal transport properties.* ***In preparation****.*

5. References

1. Airplane Flying handbook (**2004**) U.S. Government Printing Office, Washington D.C.: U.S. Federal Aviation Administration FAA-8083-3A.
2. N. Eliaz, G. Shemesh, R.M. Latanision, *Hot Corrosion in gas turbine components*, Engineering Failure Analysis 9, **2002**, 31-43.
3. R.C. Reed, *The Superalloys: fundamentals and applications*, Cambridge University Press, **2006**.
4. C.T. Sims, N.S. Stoloff, W.C. Hagel, *Superalloys II*, Wiley, **1987**.
5. P. Caron, T. Khan, *Evolution of Ni-based superalloys for single crystal gas turbine blade applications*, Aerospace Science and Technology. 3, **1999**, 513-523.
6. J.J. Jackson, M.J. Donachie, R.J. Henricks, M. Gell, *The effect of volume percent of fine γ' on creep in DS Mar-M200 + Hf*, Metallurgical Transactions A8, **1977**, 1615-1620.
7. A.M. Ges, O. Fornaro, H.A. Palacio, *Coarsening behaviour of a Ni-base superalloy under different heat treatment conditions*, Material Science and Engineering A458, **2007**, 96-100.
8. D.R. Clarke, M. Oechsner, N.P. Padture, *Thermal-barrier coatings for more efficient gas-turbine engines*, MRS Bulletin 37, **2012**, 891-898.
9. J.R. Nicholls, *Advances in Coating Design for High-Performance Gas Turbines*, MRS Bulletin 28, **2003**, 659-670.
10. T.M. Pollock, D.M. Lipkin, K.J. Hemker, *Multifunctional coating interlayers for thermal-barrier systems*, MRS Bulletin 37, **2012**, 923-931.
11. F. Pedraza, C. Tuohy, L. Whelan and A.D. Kennedy, *High Quality Aluminide and Thermal Barrier Coatings Deposition for New and Service Exposed Parts by CVD Techniques*, Materials Science Forum 461-464, **2004**, 305-312.
12. E.H. Kisi, C.J. Howard, *Crystal Structure of Zirconia Phases and Their Inter-Relation,* Key Engineering Materials 153-154, **1998**, 1-36.
13. S. Sampath, U. Schulz, M.O. Jarligo, S. Kuroda, *Processing Science of Advanced Thermal-Barrier Systems*, MRS Bulletin 37, **2012**, 903-910.
14. S. Krämer, J. Yang, C. G. Levi, *Thermochemical interaction of thermal barrier coatings with molten CaO–MgO–Al_2O_3–SiO_2 (CMAS) deposits*, Journal of the American Ceramic Society 89[10], **2006**, 3167-3175.

15. H.J. Rätzer-Scheibe, U. Schulz, *The thermal behavior of CMAS-infiltrated thermal barrier coatings*, Surface & Coatings Technology 201, **2007**, 7880-7888.
16. G. Di Girolamo, A. Brentari, E. Serra, *Some recent findings on the use of SEM-EDS in microstructural characterisation of as-sprayed and thermally aged porous coatings: a short review*, AIMS Materials Science 3[2], **2016**, 404-424
17. A.M. Philpot (Hard Chrome) Ltd, *Plasma Spraying*, web page visited on October 10th **2017** at http://www.amphardchrome.co.uk/plasma-spraying.php.
18. S. Kuroda, T.W. Clyne, *The quenching stress in thermally sprayed coatings*, Thin Solid Films 200, **1991**, 49-66.
19. A. Vaidya, V. Srinivasan, T. Streibl, M. Friis, W. Chi, S. Sampath, *Process maps for plasma spraying of yttria-stabilized zirconia: An integrated approach to design, optimization and reliability*, Materials Science and Engineering, A 497, **2008**, 239.
20. T. Nakamura, Y. Liu, *Determination of nonlinear properties of thermal sprayed ceramic coatings via inverse analysis*, International Journal of Solids and Structures 44, **2007**, 1990-2009.
21. W. Chi, S. Sampath, and H. Wang, *Microstructure-Thermal Conductivity Relationships for Plasma-Sprayed Yttria-Stabilized Zirconia Coatings*, Journal of the American Ceramic Society 91[8], **2008**, 2636-2645.
22. H.B. Guo, R. Vaßen, D. Stöver, *Atmospheric plasma sprayed thick thermal barrier coatings with high segmentation crack density*, Surface and Coatings Technology 186[3], **2004**, 353-363.
23. H.B. Guo, H. Murakami, S. Kuroda, *Effect of Hollow Spherical Powder Size Distribution on Porosity and Segmentation Cracks in Thermal Barrier Coatings*, Journal of the American Ceramic Society 89[12], **2006**, 3797-3804.
24. J. Karthikeyan, C.C. Berndt, J. Tikkanen, S. Reddy, H. Herman, *Plasma spray synthesis of nanomaterial powders and deposits*, Materials Science and Engineering, A 238, **1997**, 275-286.
25. T. Bhatia, A. Ozturk, L. Xie, E. Jordan, B. Cetegen, M. Gell, X. Ma, N. Padture, *Mechanisms of Ceramic Coating Deposition in Solution-Precursor Plasma Spray*, Journal of Material Research Society 17, **2002**, 2363-2372.
26. N. Curry, K. Van Every, T. Snyder, N. Markocsan, *Thermal Conductivity Analysis and Lifetime Testing of Suspension Plasma-Sprayed Thermal Barrier Coatings*, Coatings *4*[3], **2014**, 630-650.

27. N. Curry, K. Van Every, T. Snyder, J. Susnjar, S. Bjorklund, *Performance Testing of Suspension Plasma Sprayed Thermal Barrier Coatings Produced with Varied Suspension Parameters*, Coatings *5*[3], **2015**, 338-356.
28. Jülich Forschungszentrum, http://www.fz-juelich.de/, web page visited on October 10th, **2018**.
29. A. Hospach, G. Mauer, R. Vassen, D. Stover, *Columnar-Structured Thermal Barrier Coatings (TBCs) by Thin Film Low-Pressure Plasma Spraying (LPPS-TF)*, Journal of Thermal Spray Technology 20[1-2], **2011**, 116-120.
30. A. Guignard, G. Mauer, R. Vassen, D. Stöver, *Deposition and characteristics of submicrometer-structured thermal barrier coatings by suspension plasma spraying*, Journal of Thermal Spray Technology 21, **2012**, 416-424.
31. C. Viazzi, J-P. Bonino, F. Ansart, A. Barnabé, *Structural study of metastable tetragonal YSZ powders produced via a sol-gel route*, Journal of Alloys and Compounds 452, **2008**, 377-383.
32. G. Pujol, doctoral thesis, *Elaboration par voie sol-gel de nouvelles barrières thermiques architecturées présentant des propriétés contre l'infiltration des oxydes CMAS (Ca, Mg, Al, Si) - Etude de la réparabilité de systèmes endommagés*, Université Toulouse III Paul Sabatier, Toulouse, France, **2014**.
33. J. Fenech, M. Dalbin, A. Barnabe, J.P. Bonino, F. Ansart, *Sol-gel processing and characterization of (RE-Y)-zirconia powders for thermal barrier coatings*, Powder Technology 208, **2011**, 480-487.
34. F. Pedraza, M. Mollard, B. Rannou, J. Balmain, B. Bouchaud, G. Bonnet, *Potential thermal barrier coating systems from Al microparticles. Mechanisms of coating formation on pure nickel*, Material Chemistry and Physics 134, **2012**, 700-705.
35. M. Mollard, *Elaboration de systèmes barrière thermique par barbotine. Comportement du nickel et de ses superalliages revêtus en oxydation cyclique à haute température*, doctoral thesis, Université de La Rochelle, France, **2012**.
36. B. Rannou, *Slurry coatings from aluminium microparticles on Ni-based superalloys for high-temperature oxidation protection*, doctoral thesis, Université de La Rochelle, France, **2012**.
37. M.T. Dove, *Structure and Dynamics an Atomic View of Materials,* Oxford (Oxford University Press), **2003**. 356 pp. ISBN 0-19-850677-5.

38. R. Siegel and J.R. Howell, Thermal Radiation Heat Transfer, 1st ed., McGraw-Hill, New York, **1972**.
39. R. Berman, *Thermal Conduction in Solids*, Clarendon, Oxford, **1976**.
40. P.G. Klemens and R.K. Williams, *Thermal Conductivity of Metals and Alloys*, International Metals Reviews 31, **1986**, 197-215.
41. L.B. Loeb, *The Kinetic Theory of Gases*, McGraw-Hill, New York, **1934**.
42. R. McPherson, *A Model for the Thermal Conductivity of Plasma- Sprayed Ceramic Coatings*, Thin Solid Films 112, **1984**, 89-95.
43. Weiguang Chi, *Thermal Transport Properties of Thermally Sprayed Coatings*, doctoral thesis, Stony Brook University, **2007**.
44. D.R. Clarke, S. Phillpot, *Thermal barrier coating materials*, Materials Today, June **2005**, 22-29.
45. L. Lu, F-C. Wang, Z. Ma, and Q-B. Fan, *Anisotropic effect of splat interface on thermal conductivity of plasma sprayed YSZ coating*, Surface and Coatings Technology 235, **2013**, 596-602.
46. K. Torkashvand, E. Poursaeidi, and J. Ghazanfarian, *Experimental and numerical study of thermal conductivity of plasma-sprayed thermal barrier coatings with random distributions of pores*, Applied Thermal Engineering 137, **2018**, 494-503.
47. A. Kulkarni, Z. Wang, T. Nakamura, S. Sampath, A. Goland, H. Herman, J. Allen, J. Ilavsky, G. Long, J. Frahm and R. W. Steinbrech, *Comprehensive microstructural characterization and predictive property modeling of plasma-sprayed zirconia coatings*, Acta Materialia 51[9], **2003**, 2457-2475.
48. Z. Wang, A. Kulkarni, S. Deshpande, T. Nakamura and H. Herman, *Effects of pores and interfaces on effective properties of plasma sprayed zirconia coatings*, Acta Materialia 51[18], **2003**, 5319-5334.
49. I.O. Golosnoy, *Heat Transfer Through Plasma-Sprayed Thermal Barrier Coatings in Gas Turbines: A Review of Recent Work*, Journal of Thermal Spray Technology 18[5-6], **2009**, 809-821.
50. S. Deshpande, S. Sampath and H. Zhang, *Mechanisms of oxidation and its role in microstructural evolution of metallic thermal spray coatings - Case study for Ni-Al*, Surface & Coatings Technology 200, **2006**, 5395-5406.

51. A.G. Evans, D.R. Mumm, J.W. Hutchinson, G.H. Meier, F.S. Pettit, *Mechanisms controlling the durability of thermal barrier coatings*, Progress in Materials Science 46, **2001**, 505-553.
52. A.G. Evans, D.R. Clarke, C.G. Levi, *The influence of oxides on the performance of advanced gas turbines*, Journal of the European Ceramic Society 28[7], **2008**, 1405-1419.
53. R.G. Wellman, J.R. Nicholls, *On the effect of ageing on the erosion of EB-PVD TBCs*, Surface and Coatings Technology 177-178, **2004**, 80-88.
54. X. Zhao, X. Wang, P. Xiao, *Sintering and failure behaviour of EB-PVD thermal barrier coating after isothermal treatment*, Surface and Coatings Technology 200, **2006**, 5946-5955.
55. A.C.F. Cocks, N.A. Fleck, *Constrained sintering of an air-plasma-sprayed thermal barrier coating*, Acta Materialia 58, **2010**, 4233-4244.
56. A. Flores Renteria, B. Saruhan, U. Schulz, H.-J. Raetzer-Scheibe, J. Haug, A. Wiedenmann, *Effect of morphology on thermal conductivity of EB-PVD PYSZ TBCs*, Surface and Coatings Technology 201, **2006**, 2611-2620.
57. L. Lu, F.-C. Wang, Z. Ma, Q.-B. Fan, *Anisotropic effect of splat interface on thermal conductivity of plasma sprayed YSZ coating*, Surface and Coatings Technology 235, **2013**, 596-602.
58. N.A. Fleck, A.C.F. Cocks, S. Lampenscherf, *Thermal shock resistance of air plasma sprayed thermal barrier coatings*, Journal of the European Ceramic Society 34, **2014**, 2687-2694.
59. R.G. Wellman, M.J. Deakin, J.R. Nicholls, *The effect of TBC morphology on the erosion rate of EB PVD TBCs*, Wear 258, **2005**, 349-356.
60. R.G. Wellman, J.R. Nicholls, *Some observations on erosion mechanisms of EB PVD TBCS*, Wear 242, **2000**, 89-96.
61. M.P. Borom, C.A. Johnson, L.A. Peluso, *Role of environmental deposits and operating surface temperature in spallation of air plasma sprayed thermal barrier coatings*, Surface and Coatings Technology 86-87, **1996**, 116-126.
62. J.L. Smialek, *The chemistry of Saudi arabian sand: a deposition problem on helicopter turbine airfoils*, NASA Technical Memorandum, **1991**.

63. W. Braue, *Environmental stability of the YSZ layer and the YSZ/TGO interface of an in-service EB-PVD coated high-pressure turbine blade*, Journal of Material Sciences, **2009**, 1664-1675.
64. A.G. Evans, J.W. Hutchinson, *The mechanics of coating delamination in thermal gradients*, Surface and Coatings Technology 201, **2007**, 7905-7916.
65. S. Krämer, S. Faulhaber, M. Chambers, D.R. Clarke, C.G. Levi, J.W. Hutchinson, A.G. Evans, *Mechanisms of cracking and delamination within thick thermal barrier systems in aero-engines subject to calcium-magnesium-alumino-silicate (CMAS) penetration,* Materials Science and Engineering A 490, **2008**, 26-35.
66. H. Zhao, C.G. Levi, H.N.G. Wadley, *Molten silicate interactions with thermal barrier coatings*, Surface and Coatings Technology 251, **2014**, 74-86.
67. V. Tolpygo, *Vapor-Phase CMAS-Induced Degradation of Adhesion of Thermal Barrier Coatings*, Oxidation of Metals 88, **2017**, 87-96.
68. J. Wu, H.-B. Guo, Y.-Z. Gao, S.-K. Gong, *Microstructure and thermo-physical properties of yttria stabilized zirconia coatings with CMAS deposits*, Journal of the European Ceramic Society 31, **2011**, 1881-1888.
69. T.R. Kakuda, C.G. Levi, T.D. Bennett, *The thermal behavior of CMAS-infiltrated thermal barrier coatings*, Surface and Coatings Technology 272, **2015**, 350-356.
70. M. Craig, N.L. Ndamka, R.G. Wellman, J.R. Nicholls, *CMAS degradation of EB-PVD TBCs: The effect of basicity*, Surface and Coatings Technology 270, **2015**, 145-153.
71. C.G. Levi, J.W. Hutchinson, M-H. Vidal-Sétif, C.A. Johnson, *Environmental degradation of thermal barrier coatings by molten deposits*, MRS Bulletin 37, **2012**, 932-941.
72. A. Aygun, A.L. Vasiliev, N.P. Padture, X. Ma, *Novel thermal barrier coatings that are resistant to high-temperature attack by glassy deposits*, Acta Materiala 55, **2007**, 6734-6745.
73. A.D. Gledhill, K.M. Reddy, J.M. Drexler, K. Shinoda, S. Sampath, N.P. Padture, *Mitigation of damage from molten fly ash to air-plasma-sprayed thermal barrier coatings*, Material Sciences and Engineering A 528, **2011**, 7214-7221.
74. M.-P. Bacos, J.-M. Dorvaux, S. Landais, O. Lavigne, R. Mévrel, M. Poulain, C. Rio, M.-H. Vidal-Sétif, *Performance and Degradation Mechanisms of Thermal Barrier Coatings for Turbine Blades: a Review of Onera Activities*, Aerospace Lab: The ONERA Journal, issue 3, **2011**.

75. J.-F. Bisson, D. Fournier, M. Poulain, O. Lavigne, R. Mévrel, *Thermal conductivity of yttria–zirconia single crystals, determined with spatially resolved infrared thermography*, Journal of the American Ceramic Society 83[8], **2000**, 1993-1998.
76. F. Cernushi, L. Lorenzoni, S. Ahmaniemi, P. Vuoristo, and T. Mäntylä, *Studies of the sintering kinetics of thick thermal barrier coatings by thermal diffusivity measurements*, Journal of European Ceramic Society 25, **2005**, 393-400.
77. Y. Tan, J.P. Longtin, and S. Sampath, *Effect of the Starting Microstructure on the Thermal Properties of As-Sprayed and Thermally Exposed Plasma-Sprayed YSZ Coatings*, Journal of the American Ceramic Society 92[3], **2009**, 710-716.
78. Y. Tan, V. Srinivasan, T. Nakamura, S. Sampath, and P. Bertrand, *Optimizing Compliance and Thermal Conductivity of Plasma Sprayed Thermal Barrier Coatings via Controlled Powders and Processing Strategies*, Journal of Thermal Spray Technology 21[5], **2012**, 950-962.
79. N. Curry, N. Markocsan, L. Ostergren, X-H. Li, and M. Dorfman, *Evaluation of the Lifetime and Thermal Conductivity of Dysprosia-Stabilized Thermal Barrier Coating Systems*, Journal of Thermal Spray Technology 22[6], **2013**, 864-872.
80. A.F. Renteria, B. Saruhan, U. Schulz, H.-J. Raetzer-Scheibe, J. Haug, A. Wiedenmann, *Effect of morphology on thermal conductivity of EB-PVD PYSZ TBCs*, Surface & Coatings Technology 201, **2006**, 2611-2620.
81. H.-J. Rätzer-Scheibe, U. Schulz, T. Krell, *The effect of coating thickness on the thermal conductivity of EB-PVD PYSZ thermal barrier coatings*, Surface and Coatings Technology 200, **2006**, 5636-5644.
82. A. Azzopardia, R. Mévrel, B. Saint-Ramonda, E. Olsonc, K. Stiller, *Influence of aging on structure and thermal conductivity of Y-PSZ and Y-FSZ EB-PVD coatings*, Surface and Coatings Technology 177-178, **2004**, 131-139.
83. T.R. Kakuda, A.M. Limarga, T.D. Bennett, D.R. Clarke, *Evolution of thermal properties of EB-PVD 7YSZ thermal barrier coatings with thermal cycling*, Acta Materialia 57, **2009**, 2583-2591.
84. S. Krämer, J. Yang, C. G. Levi, *Thermochemical interaction of thermal barrier coatings with molten $CaO–MgO–Al_2O_3–SiO_2$ (CMAS) deposits*, Journal of the American Ceramic Society 89[10], **2006**, 3167 – 3175.
85. H. Zhao, C.G. Levi, H.N.G.Wadley, *Molten silicate interactions with thermal barrier coatings*, Surface and Coatings Technology 251, **2014**, 74-86.

86. Particoat - Homepage, web page visited on October 31st, **2017** at http://www.particoat.eu/

87. X. Montero, M. Galetz, M. Schütze, *A single step process to form in-situ an alumina foam/aluminide TBC system for alloys in extreme environments at high temperatures*, Surface and Coatings Technology 206, **2011**, 1586-1594.

88. M.C. Galetz, X. Montero, M. Mollard, M. Günthner, F. Pedraza, M. Schütze, *The role of combustion synthesis in the formation of slurry aluminization*, Intermetallics 44, **2014**, 8-17.

89. V. Kolarik, R. Roussel, M. Juez Lorenzo, H. Fietzek, *Factors influencing the formation of a diffusion zone and the adherence of the top coat of high temperature coatings from micro-sized spherical aluminium particles*, Materials at High Temperatures 29[2], **2008**, 89-94.

90. B. Rannou, F. Velasco, S. Guzmán, V. Kolarik, F. Pedraza, *Aging and thermal behavior of a PVA/Al microspheres slurry for aluminizing purposes*, Material Chemistry and Physics, **2012**, 360-365.

91. F. Pedraza, R. Podor, *Influence of annealing conditions on the formation of hollow Al_2O_3 microspheres studied by in situ ESEM*, Materials Characterization 113, **2016**, 198-206.

92. B. Bouchaud, B. Rannou, F. Pedraza, *Slurry aluminizing mechanisms of Ni-based superalloys incorporating an electrosynthesized ceria diffusion barrier*, Materials Chemistry and Physics 143, **2013**, 416-424.

93. F. Pedraza, G. Boissonnet, B. Fernandez, B. Bouchaud, R. Podor, *Synthesis and related properties of low conductivity TBCs with hollow alumina microspheres*, 43rd ICMCTF (25-29 April **2016**), San Diego (USA).

94. M.A. Trunov, M. Schoenitz, X. Zhu, E.L. Dreizin, *Effect of polymorphic phase transformations in Al_2O_3 film on oxidation kinetics of aluminum powders*, Combustion and Flame 140, **2005**, 310-318.

95. B. Rufino, F. Boulc'h, M.-V. Coulet, G. Lacroix, R. Denoyel, *Influence of particles size on thermal properties of aluminium powder*, Acta Materialia 55, **2007**, 2815-2827.

96. S. Hasani, M. Panjepour, M. Shamanian, *The oxidation mechanism of pure aluminum powder particles*, Oxidation of Metals 78, **2012**, 179-195.

97. V.I. Levitas, B.W. Asay, S.F. Son, M. Pantoya, *Mechanochemical Mechanism for Fast Reaction of Metastable Intermolecular Composites Based on Dispersion of Liquid Metal*, Journal of Applied Physics 101, **2007**, 1-20.
98. V.I. Levitas, B.W. Asay, S.F. Son, M.L. Pantoya, *Melt Dispersion Mechanism for Fast Reaction of Nanothermites*, Applied Physics Letters 89, **2006**, 1-3.
99. V.I. Levitas, M.L. Pantoya, K.W. Watson, *Melt Dispersion Mechanism for Fast Reaction of Aluminum Particles: Extension for Micron Scale Particles and Fluorination*, Applied Physics Letters 92, **2008**, 1-3.
100. V.I. Levitas, *Mechanochemical Mechanism for Reaction of Aluminum Nano- and Micron-scale Particles*, Philosophical Transactions of the Royal Society A 371, **2013**, 1-14.
101. A.A. Firmansyah, K. Sullivan, K.S. Lee, Y.H. Kim, R. Zahaf, M.R. Zachariah, D. Lee, *Microstructural Behavior of the Alumina Shell and Aluminum Core Before and After Melting of Aluminum Nanoparticles*, Journal of Physical Chemistry C 116, **2012**, 404-411.
102. L.P.H. Jeurgens, W.G. Sloof, F.D. Tichelaar, E.J. Mittemeijer, *Structure and morphology of aluminium-oxide films formed by thermal oxidation of aluminium*, Thin Solid Films 418, **2002**, 89-101.
103. B. Rufino, M.V. Coulet, R. Bouchet, O. Isnard, R. Denoyel, *Structural changes and thermal properties of aluminium micro- and nano-powders*, Acta Materialia 58, **2010**, 4224-4232.
104. K. Wefers, C. Misra, *Oxides and hydroxides of aluminum*. ALCOA Technical Paper No. 19, Rev. ALCOA Laboratories, Pittsburgh (**1987**).
105. B. Grégoire, doctoral thesis, Functionalization of Aeronautical Thermal Barrier Coatings Elaborated by Slurry, University of La Rochelle, France, **2017**.

II. MATERIALS AND METHODS

Table of contents

1. Materials of study

Three different types of thermal barrier coatings were investigated in this work: the air plasma-spray (APS) and electron-beam physical vapour deposition (EB-PVD) yttria-stabilized zirconia (YSZ) coatings and the Al slurry coatings. These coatings were either provided by our partners (Safran Aircraft Engines – France and SR Technics Airfoil Services – Ireland) or produced in the laboratories where the study was conducted (SENTi – Cranfield University (UK) and LaSIE –Université de La Rochelle (FR)). The substrates employed include pure Ni, Ni-based and Co-based superalloys, whose nominal compositions are presented in **Table II.1**.

Table II.1 *– Nominal composition (wt. %) of the substrate materials.*

	Ni	Co	Cr	Mo	W	Ta	Ti	Al	Fe	Mn	Other (<0.5)
AM1 (SX)	Bal.	6.0	8.0	2.0	6.0	9.0	1.2	5.2	-	-	-
Hastelloy X	Bal.	1.5	22.0	9.0	0.6	-	-	-	18.5	0.5	Si, C
Haynes 188	22.0	Bal.	22.0	-	14.0	-	-	-	3.0	1.25	La, B, C
Inconel 600	Bal.	-	15.5	-	-	-	-	-	8.0	0.5	Cu, Si, C
Pure Ni	Bal.	-	-	-	-	-	-	-	-	-	-

AM1, Haynes 188 and Hastelloy X superalloys were the substrates of the plasma-sprayed and EB-PVD coatings provided by Safran Aircraft Engines (France) while Inconel 600 was the substrate of the APS coatings provided by SR Technics Airfoil Services (Ireland). Inconel 600 was also used as a substrate material for the deposition of EB-PVD YSZ coatings at the SENTi laboratory in Cranfield University (UK). In addition, a pure Ni substrate was used as a model material of Ni-based superalloys to study the mechanisms of formation of thermal barrier coating systems made from the slurry route. The samples were cut from Ø12.7 mm^2 cylindrical rods with a Struers Secotom-50 cutting machine to obtain samples of ~2.0 mm thickness. The process for the elaboration of the slurry coatings is described in the next section.

The APS and EB-PVD YSZ thermal barrier coatings are presented hereafter while the Al-slurry TBCs will be presented in §2.

1.1 APS coatings

Table II.2 provides general information on the APS coatings supplied by Safran Aircraft Engines (France) and SR Technics Airfoil Services (Ireland). For all the samples, MCrAlY bond coatings (BC) were deposited prior to YSZ ceramic coatings. The deflector-APS (DFL_APS), combustion chamber-APS (CC_APS) and injector-APS (INJ_APS) samples (10

x 10 mm^2) were cut from aeronautical engine parts while the laboratory samples were made using metallic plates as substrates for coating deposition and cut afterwards. The CC_APS and INJ_APS samples were cut from serviced components of the combustion chamber and injectors, respectively. The IN_APS samples were used for the thermal ageing tests in laboratory conditions because of their greater availability (see §3).

Table II.2 *– Samples of the study coated with APS YSZ.*

Sample	Type	Substrate	Bond coating	Ceramic coating
AM1_APS1	lab sample, as-deposited	AM1	NiCrAlY HVOF, 40 ±12 µm	feedstock METCO 204 NS-G; 110 ±7 µm
AM1_APS2	lab sample, as-deposited	AM1	NiCrAlY HVOF, 15 ±5 µm	feedstock METCO 204 NS-G; 430 ±15 µm
DFL_APS	*deflector*, as-deposited	Haynes 188	NiCoCrAlY HVOF, 130 ±9 µm	feedstock METCO 204 NS-G; 330 ±12 µm
IN_APS	lab sample, as-deposited	Inconel 600	NiCrAlY HVOF, 72 ±5 µm	feedstock PRAXAIR ZRO-113/114; 230 ±10 µm
AM1_APSmf	lab sample, as-deposited	Hastelloy X	NiCrAlY HVOF, 15 ±7 µm	feedstock SPM 2000; 90 ±9 µm
CC_APS	*combustion chamber*, aged	Haynes 188	NiCoCrAlY, HVOF, 135 ±8 µm	feedstock METCO 204 NS-G; 190 ±6 µm
INJ_APS	*Injectors*, aged	Haynes 188	NiCoCrAlY, HVOF, 70 ±11 µm	feedstock METCO 204 NS-G; 450 ±8 µm

Freestanding coatings were also used for thermal measurements and ageing tests in order to isolate their contribution to the heat transport compared with the full system (TBC, BC and substrate). The freestanding coatings were obtained from the IN_APS samples by chemically dissolving the oxide interface between the bond coating and the YSZ TBC in a 20 vol. % HCl aqueous solution.

The samples were prepared with a square shape (10 x 10 mm^2) for the laser flash measurements. This preparation was usually made prior to the ageing tests or to the elaboration of the freestanding coatings because of the brittleness of the ceramic coatings.

1.2 EB-PVD coatings

The columnar coatings made of YSZ were either provided by Safran Aircraft Engines (France) on AM1 substrate in the form of Ø24 mm coupons or were elaborated during a three-month stay at the Surface Engineering and Nanotechnology Institute (SENTi) in Cranfield University (UK), with the collaboration of Pr. John Nicholls and Dr. Christine Chalk. The

elaboration of such coatings is one of the specialities of the SENTi laboratory, which is well known for its expertise in this domain.

Prior to the deposition of the ceramic coatings, the Inconel 600 plates provided by SR Technics Airfoil Services (Ireland) were cut into 11 x 10 x 2 mm^3 samples using an ATM GmbH Brilliant 220 cut-off machine. Then, the samples were grit blasted to give a clean and repeatable surface state before the elaboration of an Al diffusion coating via Chemical Vapour Deposition (CVD). After aluminizing, the samples were grit blasted again and cleaned before being placed in the EB-PVD reactor (**Figure II.1a**). They were then pre-heated to 860°C to grow a thin alumina scale (TGO) prior to the deposition of the YSZ. Finally, the temperature in the thermal enclosure was raised till ~1050°C and the atmosphere set to a low vacuum pressure (1.10^{-2} mbar) with a controlled atmosphere of Ar/O_2 (10/90 %), to compensate the possible loss of oxygen when evaporating the ingot (**Figure II.1b**) at a 2.2 $\mu m.min^{-1}$ rate. Three different batches were realised to obtain the coatings. Two batches were made using the state-of-the-art YSZ composition (ZrO_2 – 8 wt. % Y_2O_3) and the third one was made using an Er-doped composition (ZrO_2 – 4wt. % Y_2O_3 – 4 wt. % Er_2O_3).

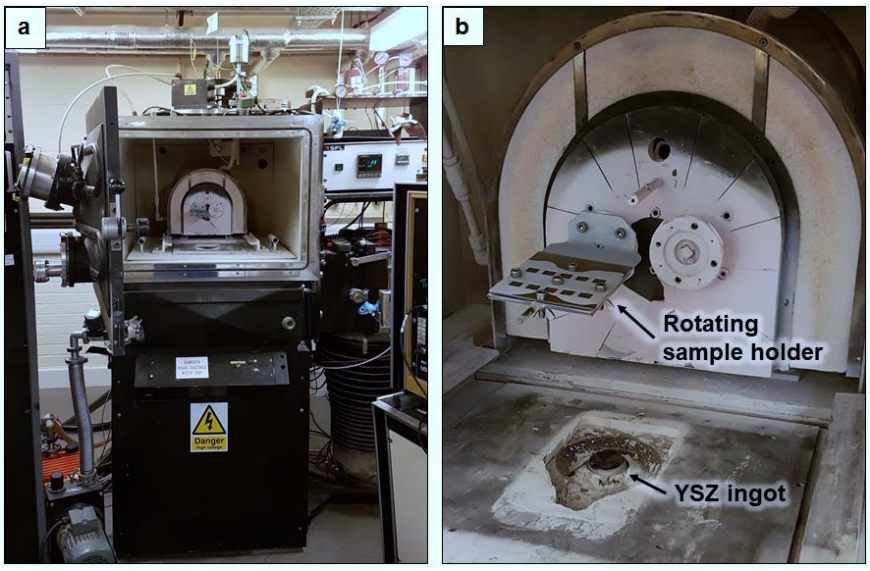

Figure II.1 *– Samples of the study coated with APS YSZ.* ***a****) EB-PVD coater and* ***b****) thermal enclosure showing the locations of the YSZ ingot and the sample holders.*

Table II.3 provides the main features of the EB-PVD coatings coming from the three different batches made at the SENTi laboratory of Cranfield University, as well as those of the samples provided by Safran Aircraft Engines.

Table II.3 *– Samples of the study coated with EB-PVD coatings.*

Sample	Type	Substrate	Bond coating	Ceramic coating
AM1_EBPVD	lab sample, as-deposited	AM1	PtAl diffusion coating, 34 ± 2 µm	ZrO_2-8wt.%Y_2O_3 130 ± 4 µm
IN_EBPVD1	lab sample, as-deposited	Inconel 600	Al diffusion coating, 30 ± 5 µm	ZrO_2-8wt.%Y_2O_3 130-180 µm
IN_EBPVD2	lab sample, as-deposited	Inconel 600	Al diffusion coating, 30 ± 5 µm	ZrO_2-8wt.%Y_2O_3 150-200 µm
IN_EBPVD-Er	lab sample, as-deposited	Inconel 600	Al diffusion coating, 30 ± 5 µm	ZrO_2-8wt.%Y_2O_3-4wt.%Er_2O_3 120-160 µm

The IN_EBPVD samples show a wide range of thicknesses since they were individually fixed on sample holders and were not all located at the same distance from the source of deposition (see **Figure II.2a**). Moreover, slight differences of column orientation were observed depending on the position of the samples on the rotating holder (see **Figure II.2b**).

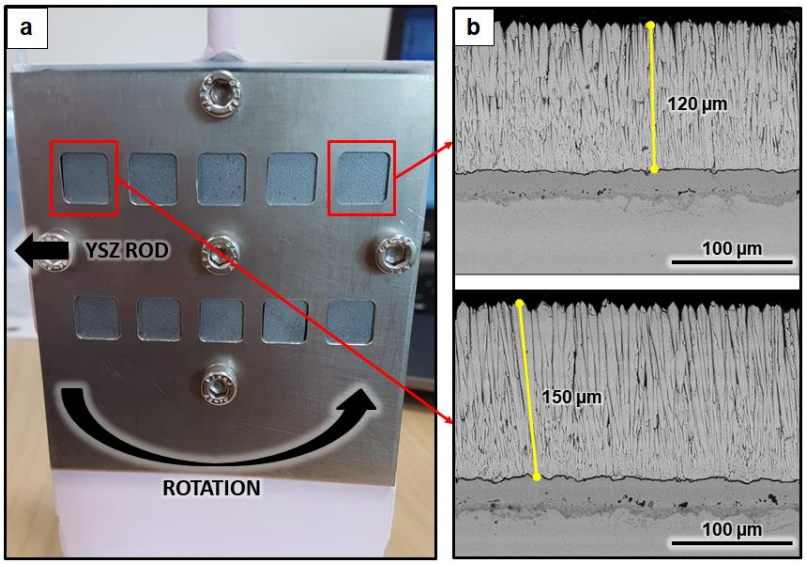

Figure II.2 *– **a**) sample holder showing the relative place of the samples in the furnace and **b**) the consequences on the resulting coatings.*

2. Elaboration of the slurry coatings

The slurry coatings developed in this study were based on the environmentally-friendly compositions developed during the European project PARTICOAT [1] and were elaborated following the sequence hereafter. Firstly, the samples to be coated were mechanically ground using a P180 grade SiC paper and successively cleaned in milliQ water and ethanol. This preparation was demonstrated to be necessary to get a good coverage of the slurry during spraying and a sufficient contact of the microparticles with the metallic substrate, required during the heat treatment. Then, after the preparation of the slurry, the liquid mixture was deposited by air brush and dried for at least 1h in ambient air. Finally, the fresh coatings were annealed at high temperature to form the desired coatings.

2.1 Composition and preparation of the slurries

The different slurries prepared for this study were composed of Al metallic powders, an organic binder (polyvinyl alcohol: PVA) and deionised water as a solvent. First, the PVA was mixed in deionized water at a 1/10 weight ratio and dissolved at approximately 80°C for 1h under magnetic stirring. The rheological behaviour and ageing of this solution was studied by Rannou et al. who showed its stability to at least 9 days [2]. However, the slurries were systematically prepared and sprayed the same day to ensure a good reproducibility of the spraying process. Finally, the Al powders were mixed with the aqueous solution in a pill box to a 45/65 weight ratio, which was previously shown to give the appropriate rheological properties to be sprayed [3].

2.2 The Al metallic powders

Two different Al powders (homogeneous size – HS, and dispersed size – DS) were selected to investigate the impact of particle size and distribution on the formation and adherence of the obtained TBC. Their main features are given in **Table II.4**. Both types of Al powders were elaborated by the wire electrical explosion (WEE) and passivated prior to shipping [4]. However, despite the similar composition determined via EDS, Al_HS and Al_DS exhibited different surface morphologies (see micrographs **Figure II.3**) and the Al_HS looked more oxidized. In addition, the sizes of the particles were measured using SEM micrographs for comparison with the data given by the suppliers. The Al_DS powders exhibited a mean diameter of ~3 µm while the theoretical D50 was given to be 5-7 µm. The mean diameter of

Al_HS powders were measured to be ~8 µm. The size distribution of both particles is also plotted on **Figure II.3** and the Al_DS particles showed a more dispersed particle diameter (Al_**D**ispersed **S**ize) than the Al_HS (Al_**H**omogeneous **S**ize).

Table II.4 *– Characteristics of the Al powders investigated in this study.*

Powders	Supplier (reference)	Theoretical size (µm)			Experimental composition	
		D10	D50	D90	Al	O
Al_DS	Hermillon (ULT-0665)	>2	5-7	<15	97 ± 1 wt.%	3 ± 1 wt.%
Al_HS	Sibthermochim (0911-35)	-	-	<20	96 ± 1 wt.%	4 ± 1 wt.%

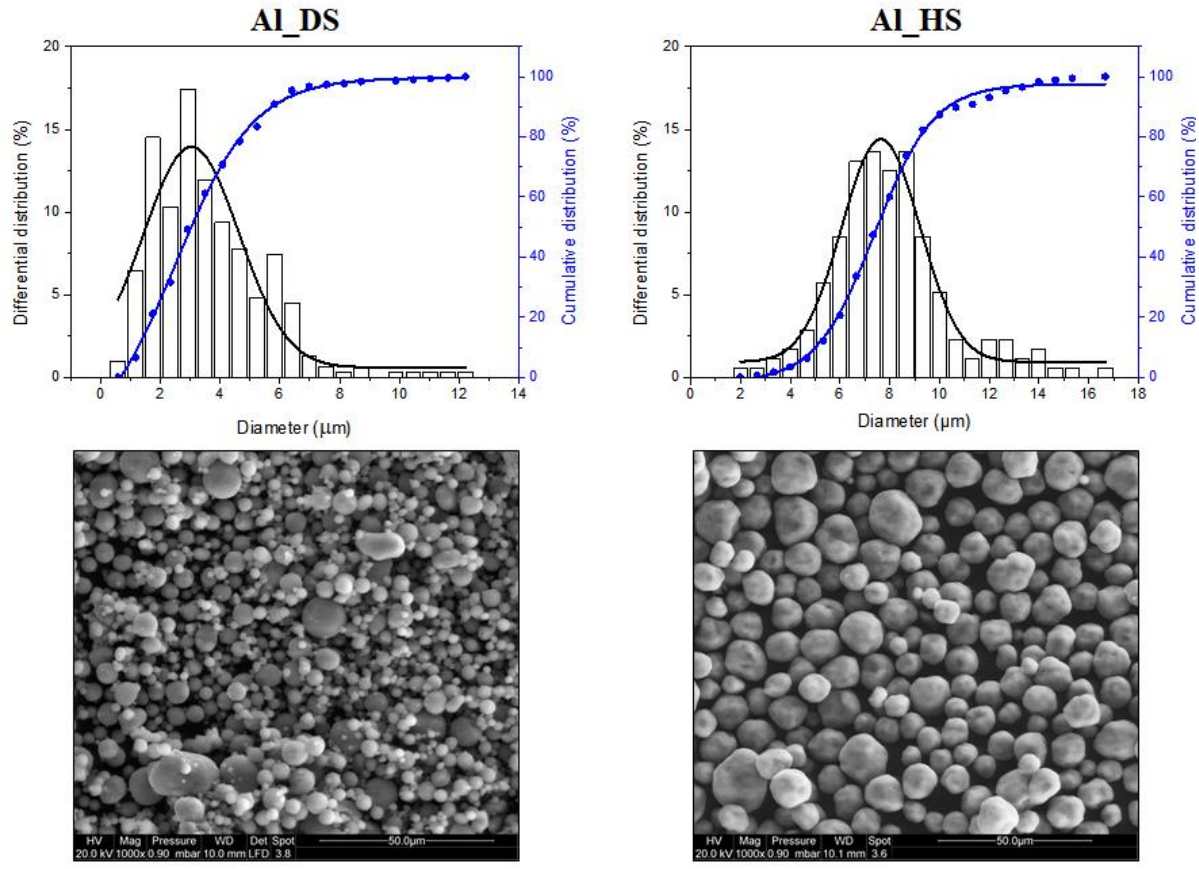

Figure II.3 *– Size dispersion and SEM images of the Al powders investigated in the study.*

2.3 Deposition by air brush

The deposition of the as-prepared slurry was performed using an AZTEK A4709T air brush with a nozzle of Ø 0.5 mm. The samples to coat were placed on a target that rotated at a constant

speed of 1 rpm. The distance between the nozzle and the samples was fixed to 10 cm. After spraying, the samples were dried at room temperature on a flat surface for one hour before being weighed using a 10^{-4} g precision balance. For consistency of the results, the input pressure for the deposition was fixed to 1.3 bar to obtain 9 ±1 mg.cm^{-2} of dry slurry on the Ø12.7 mm samples.

2.4 Heat treatments

After being dried overnight at room temperature, the samples were heat treated in the different atmospheres discussed in chapter I, using thermobalances to record the evolution of the mass of the samples along the heat treatment. A SETARAM TGA 92 thermobalance with a 10^{-6} g accuracy was used for the heat treatment in Ar and synthetic air, while a SETARAM Setsys Evo 1750 (10^{-6} g accuracy) was used for the treatment using water vapour. The water vapour was created using the SETARAM Wetsys module and transferred to the bottom of the thermal enclosure of the thermobalance via a heated transfer pipe.

The heat treatments were based on the one proposed in the PARTICOAT project which was briefly introduced in chapter I. The heat treatment consisted of three consecutive steps at 400°C, 700°C and 1100°C for 1, 2 and 2 h, respectively. The 1 hour-step at 400°C was used to dehydroxylate the particles and remove the organic binder from the pre-dried slurry coatings. Then, the melting of the Al and its diffusion towards the substrate was realised via the 700°C step. The 2 h at this temperature were shown to be sufficient to release the Al of the particles under inert Ar atmosphere. The same duration of 2 h was thus selected for the treatments under oxidizing atmosphere for comparison purposes. Finally, the step at 1100°C was used to promote the transformation of the Al oxides into the α-alumina phase and to enhance the major outward diffusion of Ni to form the final aluminide coating. This final step duration was also fixed at 2 hours for comparison with the PARTICOAT treatment. The heating and cooling ramps were conducted at 5°C.min^{-1} for the standard full heat treatment while a 50°C.min^{-1} cooling ramp was used when the observation of the microstructure at intermediate time was required.

3. Ageing of the TBCs

To investigate the effect of ageing of the different thermal barrier coating systems on their thermal insulation potential, isothermal and cyclic oxidation as well as CMAS corrosion tests were performed to induce microstructural and chemical evolutions.

3.1 Isothermal oxidation

Isothermal exposure of complete systems (TBC/BC/substrate) and of freestanding coatings (for APS YSZ coatings) were conducted in air at 1100°C in a PYROX furnace. For the APS YSZ coatings, the samples were removed from the hot furnace at different times (50, 150, 250 and 500 h). The EB-PVD coating samples were all maintained for 500 h at 1100°C and then cooled down to room temperature at a 5°C.min^{-1} rate.

3.2 Cyclic oxidation

To approach the conditions encountered in gas turbine engines, cyclic oxidation tests were conducted in a DELTA THERMIQUE cycle rig at 1100°C in air, the cycles being performed automatically. Each cycle consisted in maintaining the samples for 1 h in the hot furnace, then to perform a rapid cooling step of 15 minutes under pulsed air. The tests were carried out on complete systems (TBC + BC + substrate) till 500 cycles using the IN_APS samples. The samples were weighed when removed from the rig for characterization after 50, 100, 250 and 500 cycles.

3.3 CMAS corrosion

Preliminary CMAS corrosion tests were carried out at the Fraunhofer-ICT Institute (Germany) in collaboration with Dr. Vladislav Kolarik in order to assess the mechanisms of interaction (dissolution of YSZ material and kinetics of penetration at temperature) of a specific CMAS composition (see **Table II.5**) with our PS coatings. Specific CMAS corrosion tests using smaller quantities of deposits were carried out during a three month stay in Cranfield University (UK) in collaboration with Pr. John Nicholls and Dr. Christine Chalk. The CMAS mixture was deposited on the samples prior to a heat treatment to create the melt that penetrates the porous coatings and chemically interacts with the material.

The same CMAS mixture, whose composition is given in **Table II.5** was used for the corrosion tests. This composition was drawn from previous studies conducted by Aygun et al.

[5] and is close to the model CMAS composition used in other studies [6]. The individual oxide powders were mixed in deionized water to form a thick paste which was put into Pt-10Rh crucibles and heated a first time at 1400°C for 4 h. The resulting glassy melt was crushed in a mortar, re-melted for 4 h at 1400°C to improve the glass homogeneity and crushed again till the desired powders were obtained.

Table II.5 *– Average composition of the model CMAS measured via EDS (mol. %).*

CaO	MgO	Al_2O_3	SiO_2	Fe_2O_3
36	6	5	52	1

The resulting powders were mixed with milliQ water to a 50/50 weight ratio before spraying on the samples. A schematic representation of the experimental set up is given in **Figure II.4**. The samples to coat were weighed using a 10^{-5} g precision balance prior to CMAS deposition. Then, pre-heating at 80°C was performed to help the adhesion of the CMAS by evaporating the water once the spray in contact with the surface of the sample. Thus, short spray pulses were successively applied with intermediate re-heating and weighing of the samples, till the desired mass of deposited CMAS was obtained.

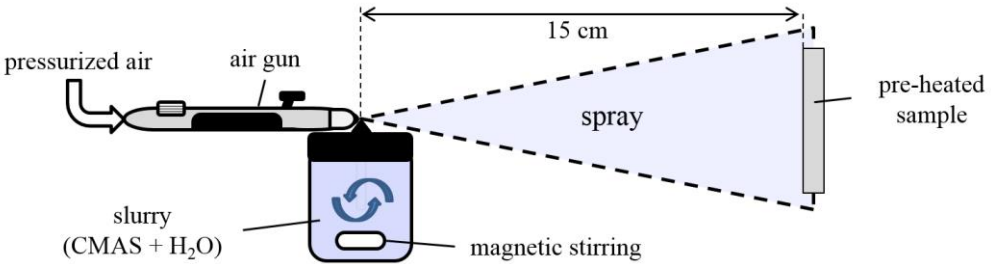

Figure II.4 *– Schematic representation of the set-up used for CMAS deposition.*

First, the tests were conducted to investigate the kinetics of penetration of the CMAS melt into the coatings. Therefore, thick deposits of ~20 $mg.cm^{-2}$ were applied on the surface of plasma-sprayed TBC and different durations of heat treatment were investigated. The samples were placed in a furnace at room temperature and heated till 1250°C, above the melting point of the mixture (observed with DSC), and were removed after 15 and 30 min, 1 and 2 h. **Figure II.5** shows that after only 15 minutes, the CMAS has almost penetrated the whole thickness of the 320 µm YSZ coating (till the red line) by infiltration through the pores, hence provoking

the sintering of the micro-pores. Moreover, the CMAS melt started to saturate the TBC (till the blue line) through the dissolution of the YSZ material, hence resulting in the loss of the initial microstructure of the coating. In order to isolate the sintering effect of the CMAS from this type of exaggerated degradation, smaller quantities were deposited. The different deposited masses of CMAS powders are gathered in **Table II.6**. These deposits were made on freestanding YSZ plasma-sprayed coatings coming from the IN_APS samples as well as on the EB-PVD coatings of IN_EBPVD2 and IN_EBPVD-Er samples.

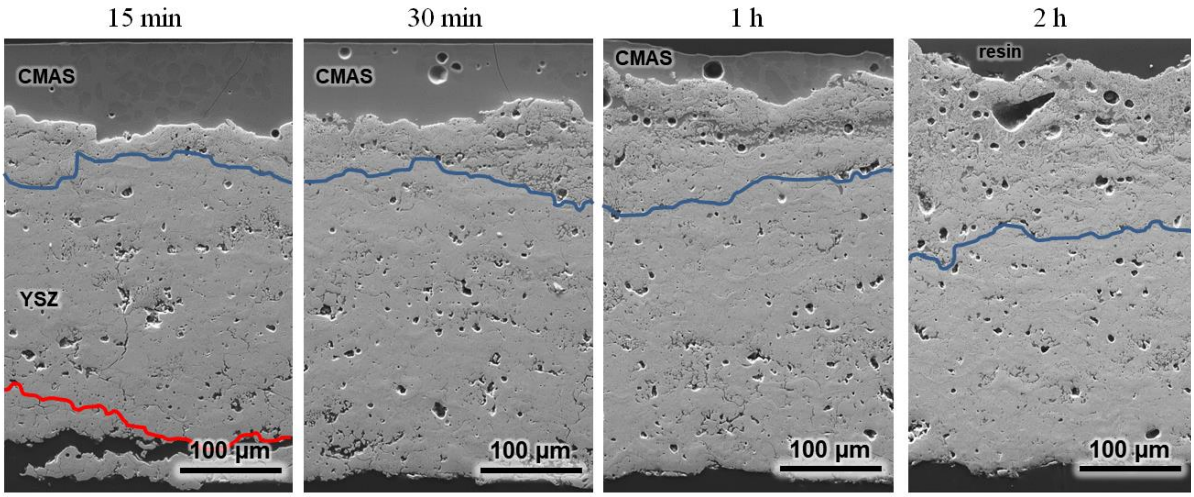

Figure II.5 *– Plasma-sprayed coatings with 20 mg.cm^{-2} of CMAS after exposure to 1250°C.*

Table II.6 *– Table of the samples with CMAS deposits.*

Samples	***CMAS deposits (mg.cm^{-2})***				
	0.25	*0.50*	*1.00*	*3.00*	*5.00*
Freestanding APS ~320 µm	√	√	√	√	√
IN_EBPVD2 ~200 µm	√	-	√	-	√
IN_EBPVD-Er ~150 µm	√	-	√	-	√

After deposition of the CMAS powders, the samples were put in a muffle furnace at 1275°C and were annealed for 1 h. Then, the microstructure and the thermal insulation potential of the samples were analysed.

4. Characterization methods

4.1 Structural analyses

4.1.1 X-ray diffraction (XRD)

The X-ray diffraction (XRD) allows determining the crystallographic structure of mineral and metallic compounds. Combined with other characterization techniques, XRD is particularly helpful to differentiate products of the same chemical composition that present different crystal structures. The surfaces of the different samples of the study were analysed by XRD using a Bruker AXS D8 Advance with Cu Kα radiation (λ = 0.15406 nm). The XRD patterns were acquired for a 2θ range going from 10° to 90° with a step size of 0.02° for 2s of accumulation time. When a higher resolution was needed, e.g. phase quantification for zirconia, the step size was reduced to 0.01° at an accumulation time of 5s. Moreover, two different configurations could be used depending on the information needed. The asymmetrical mode at a 5° grazing incidence allowed to collect information relative to the uppermost surface, e.g. analysis of a thin layer. The symmetrical mode, also known as the Bragg-Brentano configuration (θ-2θ), allowed a deeper penetration of the X-rays into the sample, depending on the absorption coefficient of the materials analysed. The resulting data were processed using the DIFFRAC^{plus} EVA software and JCPDS database (Joint Committee of Powder Diffraction files System). Some peaks were also identified via comparison with literature data. Note that some diffraction peaks have not been indexed as they are due to tungsten pollution (W Lα radiation) of the support of the Cu target that duplicates the peaks at a different angle.

The phase structures were examined using Rietveld refinement technique. The mole percentages of monoclinic phase M_m, tetragonal phase $M_{t'/t}$ and cubic phase M_c were obtained from the following equations [7]:

$$\frac{M_m}{M_{t'/t,c}} = 0.82\frac{I_m(\bar{1}11) + I_m(111)}{I_{t'/t,c}(111)} \quad \text{(II.1)}$$

$$\frac{M_c}{M_{t'/t}} = 0.88\frac{I_c(400)}{I_{t'/t}(400) + I_{t'/t}(004)} \quad \text{(II.2)}$$

where $I_m(\bar{1}11)$ and $I_m(111)$ are the integral net intensities for monoclinic phase reflected from $(\bar{1}11)$ and (111) peaks; and $I_{t'/t,c}(111)$ is the intensity for tetragonal or cubic phase reflected from (111) plane. $I_c(400)$ is the intensity for cubic phase reflected from (400) plane. $I_{t'/t}(400)$ and $I_{t'/t}(004)$ are the intensities for tetragonal phase reflected from (400) and (004) plane, respectively. The yttria content in both tetragonal phases was quantified using the following equation [8]:

$$Y_2O_3\ (mol.\%) = \frac{(1.0225\ -\ c/a\sqrt{2})}{0.0016} \tag{II.3}$$

where *a* (Å) and *c* (Å) are the lattice parameters for each tetragonal phase. The yttria content of the cubic phase was also calculated using the following equation [9]:

$$Y_2O_3\ (mol.\%) = \frac{(a\ -\ 5.1159)}{0.001647} \tag{II.4}$$

where *a* (Å) is the lattice parameter of the cubic phase.

4.1.2 Raman micro-spectrometry

Raman micro-spectrometry is a non-destructive method used for local structural analyses (lateral resolution of approximately 1 µm [10]). This technique permitted the characterization of the molecular composition and of the crystalline structure of non-metallic compounds, from their vibrational transitions. The technique thus allowed local characterization of samples using surface and cross-section spots with a high-resolution micro-spectrometer Jobin Yvon Horiba (LabRam HR 8000 model) that uses a HeNe monochromatic laser (λ = 632.817 nm) as a source of excitation. An Olympus confocal microscope is coupled to the micro-spectrometer to visualize the sample and focus the laser beam (10x, 50x, 100x magnifications). The photons resulting from Raman scattering are collected with a CCD detector, cooled by Peltier effect, with a spectral resolution of approximately 0.5 cm^{-1}. Different filters can be used to adjust the intensity of the laser depending on the investigated products. The depth of the analyses is comprised between 1 and 5 µm according to the setup parameters and the sample. Since the wavelength of the laser and the experimental setup could result in different Raman shifts for the same compound, there is no reference database in the literature and comparison of the data is necessary to give reliable identifications.

4.2 Microscopy and elemental analysis

4.2.1 Surface preparation

When cross-sectional observations of the samples were needed, a smooth surface preparation had to be performed. The samples were cold mounted in an epoxy resin that offers a sufficiently slow polymerisation rate to avoid its contraction likely to provoke the degradation of brittle layers at the surface of the samples. The samples were progressively ground with SiC papers up to P4000 grade before polishing using 1 µm diamond paste DiaPro Nap R1 STRUERS, or colloidal silica suspension OP-S STRUERS, depending on the surface finish required. Special care was taken for grinding of ceramic samples or samples with an oxide layer to avoid pull-outs of the material.

4.2.2 Optical microscopy

Optical microscopy generally comes at the first stage of investigation after the visual inspection to get the elementary information of the surface and of the cross-sections like morphology, thickness of layers and differences of composition (by contrast) when proper metallographic preparation is used. A LEICA DMRM microscope coupled to a LEICA MC170 HD camera was used to characterize the samples. The images were processed with the LAS (Leica Application Suite) software.

4.2.3 Scanning Electron Microscopy (SEM) and Energy Dispersive Spectroscopy (EDS)

Electron microscopy provides grey-scale micrographs at a high resolution for which the contrast depends on the topography and/or the chemical composition of the sample studied. Thus, two imaging modes are usually considered in a SEM: Secondary Electrons Imaging (SEI) and Back-Scattered Electrons Imaging (BSEI). SEI uses the extracted electrons of the atoms of the samples surface, resulting from the inelastic interaction with electrons of the beam, to form a topographic representation of the scanned surface. BSEI uses the electrons resulting from the elastic reactions of the incident electrons with the atom nuclei, which are released with an energy that is a function of the atomic number, and forms images with chemical contrast (heavy elements appear brighter than lighter ones).

The analyses of the surface and of the cross-section were carried out with an environmental microscope FEI Quanta 200F equipped with a Schottky field emission gun (FEG). The energy of the electron beam was fixed at 20 kV at a working distance of 10 mm and a spot size of 3.6. With conductive samples, the analyses were performed under high vacuum mode ($P < 10^{-5}$ bar).

For low-conductive samples the analyses were performed under low-vacuum (0.9 mbar) and a thin sputtered gold layer was applied (especially for thick ceramic samples mounted in the epoxy resin) to avoid charge effects.

For elemental analyses, the SEM is coupled to an EDAX detector. Energy Dispersive X-ray Spectroscopy (EDS / EDX) allows the chemical analysis of the products by X-ray micro-diffraction. Depending on the energy of the emitted X photons, this technique can differentiate one element from the others. Spot, window (area) and map analyses were performed depending on the investigated sample. The EDS maps give the distribution of the elements in the scanned area by counting the probability to find a distinct element for a given position. This is particularly helpful for complex oxide scales or diffusion coatings that display a concentration gradient of the different elements.

4.2.4 Image Analysis (IA)

The microstructure of thermally sprayed coatings is characterized by the existence of various pores, micro-cracks, splat boundaries and un-melted particles due to the nature of the process. In order to characterize the microstructural evolution and to calculate the thermal conductivity of these ceramic coatings, the knowledge of the density is mandatory. As density is the ratio of mass to volume, finding out the actual volume of porous medium is consequently done through the determination of the porosity of the material.

Moreover, the shape of the pores is determinant to the thermal conduction as the scattering effect by pores is one of the major contributions of thermal insulation in addition to the fact that the different shapes and sizes of pores do not display the same contribution [11, 12]. In this way, the ability to separate cracks network and globular pores becomes essential for the overall microstructural characterization of plasma sprayed YSZ coatings.

Porosity can be quantitatively characterized using advanced techniques like computed micro-tomography (CMT) and small-angle neutron scattering (SANS), as well as simpler methods that measure the density of the coatings, such as gas sorption, e.g. He pycnometry and Brunauer-Emmett-Teller (BET), liquid intrusion, e.g. Archimede's method and mercury intrusion porosimetry (MIP), or image analysis (IA) [13, 14, 15, 16, 17, 18]. In the present study, image analysis (IA) has been used because it presents several advantages compared to the other techniques, like cost-effectiveness and easiness of use while allowing differentiating various types of pores and cracks.

The choice of the apparatus for the acquisition of images (SEM, TEM or optical) depends on the pore-size resolution required. For thermal sprayed YSZ, the images need to have significant contrast to distinguish the objects to be analysed (globular pores, inter-lamellar splats and cracks) from the rest of the matrix. In this way, high resolution back-scattered images from SEM are preferred over optical microscopy due to a better field depth (especially with higher magnification) and a higher resolution (0.1 µm) for SEM images [19]. Both BSEI and SEI can be used, but BSEI is recommended for a better contrast.

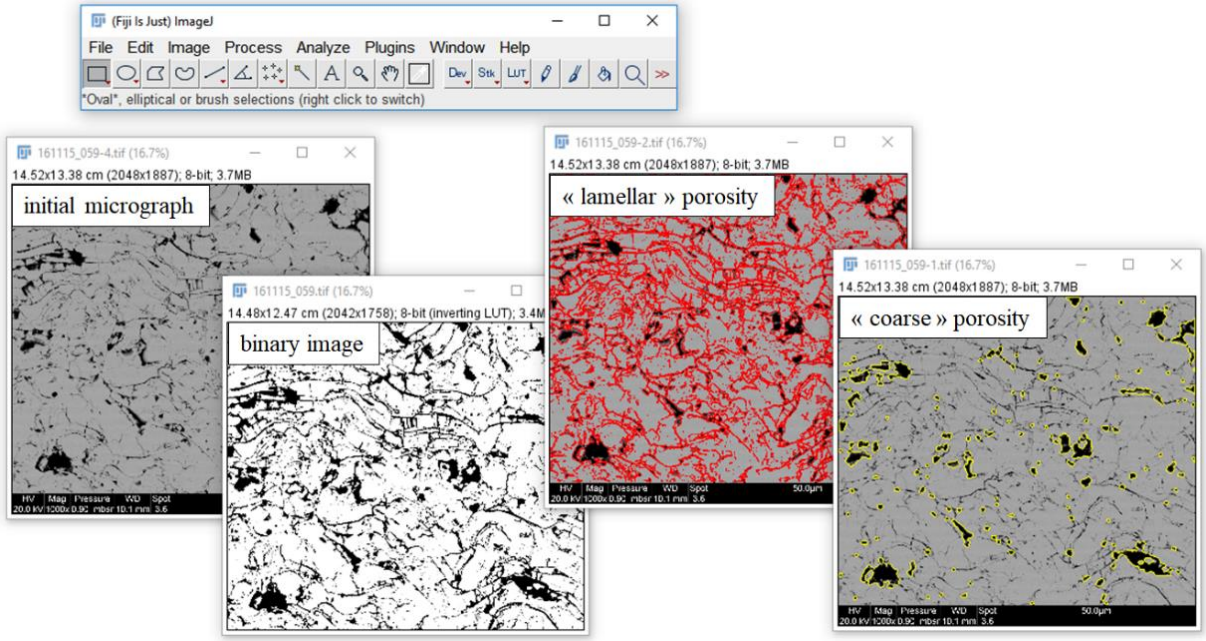

Figure II.6 *– ImageJ software on an example of image processing for porosity measurement.*

The threshold applied on the grey-scale image to separate the different phases or porosities by contrast is chosen from the critical value beyond which the calculated area of pores abruptly increases, allowing a good reproducibility of the computed analysis. For the accuracy of the measurement of the porosity, the magnification must be carefully chosen (to have a representative elementary volume) and needs to be in adequacy with a suitable resolution (as fine as possible for details). The number of fields of view will also be an important parameter as the heterogeneity of the coatings might vary and lead to important discrepancy of the values. Previous studies [20] and the standard method for porosity measurement of thermally sprayed coatings [21] reported that at least 15 images at x1000 magnification were enough to obtain reliable data on thermally sprayed YSZ coatings. As such, IA was statistically shown to give a 95 % confidence level regarding the specific experiments and metallographic preparation in the

study performed by Fowler and coll. [13]. Deshpande et al. also showed IA to be a reliable method for characterization of porosity in thermally sprayed coatings by comparing the results of IA with those obtained by CMT and SANS [16]. Several more images may be necessary when porosity or its size distribution is high. Processing of the images was made using ImageJ software and the porosity levels were calculated from the binary images obtained (***Figure II.6***).

4.3 Thermo-physical properties

Thermal conductivity is usually employed in the literature to describe the thermal insulation power of thermal barrier coatings and can be calculated from the thermal diffusivity (α), the density (ρ) and the specific heat capacity of the material (C_p) following equation (II.5):

$$\lambda(T) = \alpha(T) \times \rho(T) \times C_p(T) \quad \text{(II.5)}$$

where $\rho(T)$ was measured using precision density method and dilatometry while $C_p(T)$ and $\alpha(T)$ were measured using differential scanning calorimetry and the laser-flash method, respectively.

4.3.1 Precision density method and linear "push-rod" Dilatometer (DIL)

The linear "push-rod" dilatometer (DIL) allows the determination of the coefficient of linear thermal expansion (CTE) using a rigid solid material. The method is applicable to all materials whose absolute linear expansion is superior to 0.5 $\mu m.m^{-1}.K^{-1}$ on a 1000 K range [22]. The dilatometer measures the evolution of the length of a sample ($\Delta L/L_0$) as a function of the temperature and the CTE is deduced from the registered values. Specifics concerning the precautions and precision of the measurements are well described in the ASTM E228-11 standard [22]. In this study, measurements of 20 to 30 mm long cylindrical rods of 3 to 5 mm diameter were conducted from room temperature to 1100°C under air and Ar using a 2°C/min heating ramp. Five cycles of heating/cooling were performed to ensure reproducibility and the evolution of the length was measured on the heating stage only. Samples were weighed, and their dimensions measured before and after the measurements to ensure the validity of the results.

For the substrates, the densities at room temperature were measured using the "precision density" method which simply consists in the measurement of the mass of a given sample divided by its measured volume. Data were compared and found in agreement with the literature

(see **Table II.7**). For the ceramic coatings, the density at room temperature of the alumina and of the 7YSZ material of the literature were adjusted with the actual volume of the coatings by subtracting the volume of the pores measured via IA. Then, the evolution of ρ with the temperature was calculated using the densities at room temperature and the CTE values calculated from the DIL measurements (as well as the CTE of the literature data) for the different materials.

***Table II.7** – Density (ρ) of the different materials used in this study.*

Temperature (°C)	Density ρ (g.cm^{-3}) [reference values] *							
	AM1	Hastelloy X	Haynes 188	Inconel 600	Pure Ni	NiCrAlY	7YSZ	Alumina
25	[8.62]	[8.22]	[8.98]	8.34 [8.47]	8.91	[6.60]	[6.05]	[3.998]
100	8.60	8.20	8.96	8.315	8.77	6.58	-	-
200	8.57	8.16	8.92	8.28	8.74	6.56	-	-
300	8.54	8.13	8.88	8.24	8.70	6.53	-	-
400	8.50	8.09	8.85	8.20	8.67	6.50	-	-
500	8.47	8.05	8.81	8.16	8.64	6.47	-	-
600	8.43	8.01	8.76	8.12	8.60	6.44	-	-
700	8.39	7.97	8.72	8.08	8.57	6.41	-	-
800	8.35	7.94	8.67	8.03	8.53	6.37	-	-
900	8.30	7.90	8.62	7.99	8.50	6.34	-	-
1000	8.25	7.87	8.57	7.94	8.47	6.30	-	-
1100	8.19	7.83	8.52	7.88	-	6.27	-	-

**references: [23, 24, 25, 26, 27, 28]*

4.3.2 Differential Scanning Calorimetry (DSC)

The Differential Scanning Calorimeter (DSC) can detect small thermal events occurring in a system by comparison with a reference sample when a proper calibration has been made. By means of the "sapphire method", the DSC allows the measurement of the specific heat capacity of a material [29]. In this method, the heat released by the sample is measured and compared to a sapphire reference allowing the calculation of the specific heat capacity of the sample through three distinct measurements (blank, reference and sample). The analyses were carried out in a SETARAM Labsys Evo 1600 equipped with a 3D C_p detector unit. The samples were put in an alumina crucible (380 µL) and the measurements were performed in flowing Ar (20 mL.min^{-1}) to limit their oxidation. A stabilization dwell of 40 minutes was carried out prior to a

10°C.min^{-1} heating ramp for the C_p measurement. The samples were weighed before and after the DSC measurements to ensure the validity of the results.

Using this method, the C_p of Ni, AM1 and Inconel 600 substrates were successfully measured using bulk samples (**Table II.8**). For the material of the coatings (YSZ and NiCrAlY) the C_p values were measured from powders that were provided by SAFRAN Aircraft Engines. These powders were pre-sintered at 900 and 1300°C, for NiCrAlY and YSZ, respectively, in air for 24h to avoid the contribution of sintering during the C_p measurement. The C_p values of the other materials were taken from the literature because no samples were available for the measurement.

Table II.8 *– Specific heat capacity (Cp) of the different materials used in this study.*

Temperature (°C)	Specific heat capacity, C_p (J.g^{-1}.K^{-1}) [reference values]*							
	AM1	Hastelloy X	Haynes 188	Inconel 600	Pure Ni	NiCrAlY	7YSZ	Alumina
25	0.389 [0.422]	[0.486]	[0.402]	0.444 [0.444]	0.422 [0.449]	0.465 [0.469]	0.457 [0.469]	[0.775]
100	0.402	[0.490]	[0.432]	0.467 [0.465]	0.452 [0.474]	0.492 [0.495]	0.476 [0.510]	[0.889]
200	0.423	[0.494]	[0.444]	0.489 [0.486]	0.517 [0.514]	0.523 [0.524]	0.509 [0.544]	[0.986]
300	0.421	[0.497]	[0.465]	0.503 [0.502]	0.561 [0.574]	0.545 [0.546]	0.535 [0.566]	[1.051]
400	0.418	[0.511]	[0.486]	0.517 [0.519]	0.550 [0.590]	0.558 [0.560]	0.567 [0.586]	[1.107]
500	0.409	[0.534]	[0.502]	0.528 [0.536]	0.529 [0.527]	0.569 [0.563]	0.602 [0.603]	[1.155]
600	0.389	[0.565]	[0.523]	0.589 [0.578]	0.535 [0.535]	0.623 [0.608]	0.622 [0.616]	[1.200]
700	0.406	[0.605]	[0.540]	0.592 [0.595]	0.549 [0.545]	0.676 [0.638]	0.631 [0.631]	[1.243]
800	0.442	[0.656]	[0.557]	0.606 [0.611]	0.566 [0.557]	0.708	0.632 [0.642]	[1.283]
900	0.498	[0.725]	[0.573]	0.615 [0.628]	0.591 [0.570]	0.700	0.642 [0.6457	[1.323]
1000	0.598 [0.600]	[0.809]	[0.590]	0.638	0.623 [0.583]	0.650	0.682 [0.669]	[1.362]
1100	0.728	[0.861]	-	0.651	0.629	0.696	0.695 [0.670]	[1.401]

**references: [23, 24, 25, 26, 27, 28]*

4.3.3 Laser-Flash Analysis (LFA)

4.3.3.1 Principle of the technique

The laser-flash method allows the determination of the thermal diffusivity of primarily homogeneous isotropic solid materials [31]. Using this technique, it is possible to measure thermal diffusivity values ranging from 10^{-7} to 10^{-3} m^2.s^{-1} from about 75 K to 2800 K. The laser-flash apparatus used (LINSEIS LFA1600) and its principle are depicted on **Figure II.7**. The sample to measure is submitted to a high intensity laser pulse which is absorbed by the surface, while the heat increase is measured on the opposite surface using an infrared (IR) detector. The thermal diffusivity is then calculated from the time needed for the opposite surface to reach a

certain percentage of the maximum temperature reached after the laser pulse following equation (II.6):

$$\alpha = k_x \times L^2/t_x \qquad \text{(II.6)}$$

Where k_x is a constant that depends on the percentage x of the maximum temperature rise, L is the thickness of the sample and t_x is the time needed to reach the percentage x. Even though this technique is meant for the measurements of fully dense, homogeneous, and isotropic solid materials that are opaque to the applied energy pulse, experience shows that avoiding the deviations is possible when care and proper experimental design are followed. As a matter of fact, this technique has been previously used for the determination of the thermal diffusivity of ceramic freestanding coatings as well as ceramic coatings as part of a multilayer composite.

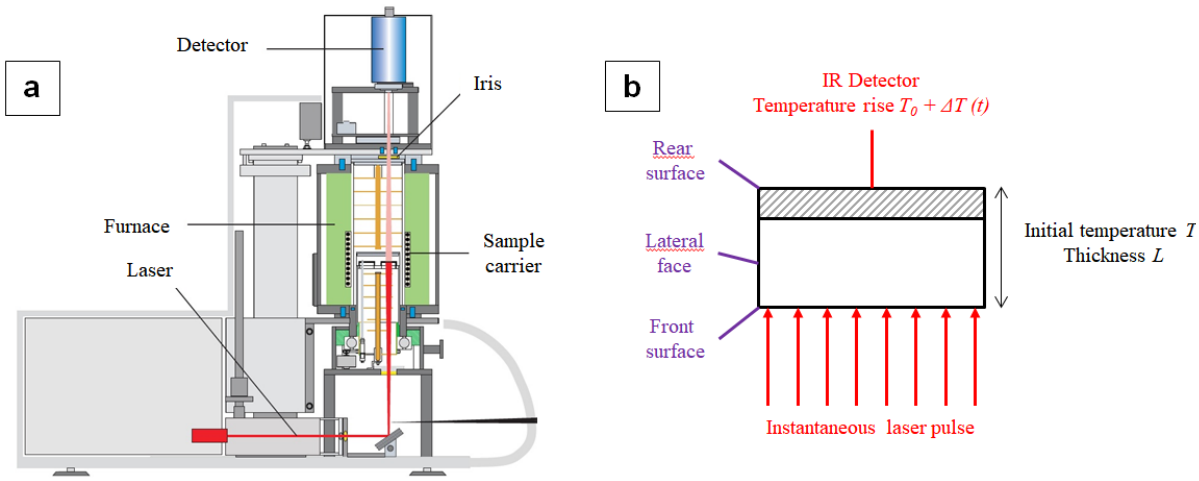

Figure II.7 *– Schematic representation of a) the laser-flash apparatus LINSEIS LFA1600 and b) the laser-flash principle [30].*

4.3.3.2 Laser-flash analysis for ceramic and composite samples

For the metallic substrates, a graphite layer was deposited on both surfaces of the samples to improve the homogeneity of the absorbed and emitted laser energy as recommended by the standard procedure [31]. However, for the measurements of the ceramic coatings (freestanding and full TBCs), additional preparation of the samples was needed because YSZ is transparent to the laser. Therefore, the deposition of a metallic layer is required for an adequate absorption and emission of the laser shot by the surfaces [31]. Thus, a layer of gold was applied by sputtering on the surfaces of the YSZ coatings in addition to the graphite one. Only the upper surface of the coating on a full TBC system was coated because the metal substrate naturally

absorbs the heat of the laser shot. Then, the laser-flash measurements were made using the Linseis LFA1600 apparatus under low vacuum (~1.10^{-2} mbar) from room temperature till 900-1100°C (depending on the samples) with five measurements by sample every 100°C step.

Laser-flash measurements give the thermal diffusivity of the whole sample thus, a calculation is needed when trying to investigate the thermal diffusivity of a single layer on a composite sample. This calculation requires the thermal properties (α, ρ and C_p) of each layer of the composite. Therefore, when investigating one layer on a 3-layered composite sample (substrate + bond coating + TBC), seven input parameters and the accurate thickness of each layer of the composite are needed for the calculation of the thermal diffusivity. A step-by-step procedure was used to determine the thermal diffusivity of the coating. At first, the thermal diffusivities of the different substrates were measured (see **Table II.9**).

Table II.9 *– Measured thermal diffusivities of the substrates of the study.*

Temperature (°C)	Thermal diffusivity (x10^{-3} $cm^2.s^{-1}$)				
	AM1	Hastelloy X	Haynes 188	Inconel 600	Pure Ni
25	22.7	27.4	28.3	36.4	173.7
100	24.6	30.7	31.8	39.3	149.7
200	27.1	34.2	35.2	42.7	124.0
300	29.6	37.1	38.2	45.4	100.4
400	31.9	39.9	40.6	48.0	117.3
500	34.4	42.8	43.3	50.8	120.3
600	36.7	44.7	45.8	53.1	122.0
700	39.4	47.4	48.5	55.3	123.7
800	41.0	51.1	51.7	55.6	125.3
900	41.8	49.8	50.4	57.2	125.3
1000	42.2	50.8	51.7	57.9	126.3
1100	43.2	52.1	52.9	58.7	-

Then, using the values of C_p and ρ of the substrates and of the MCrAlY material (**Table II.7** and **Table II.8**) and the thermal diffusivity of the substrates (**Table II.9**), the thermal diffusivity of the bond coating was calculated. However, the measured values of thermal diffusivity of the MCrAlY coatings were not consistent with those of the literature [32]. This discrepancy can be related to the MCrAlY layer, which is too thin compared to the substrate. Therefore, the heat transport properties cannot be sufficiently differentiated from those of the substrate via this technique. Thus, the thermal diffusivity values of the MCrAlY issued from the literature were employed to compare the calculated thermal diffusivities of a YSZ coating

using two different models (**Figure II.8**). The first model considered the MCrAlY layer (3-layer model: substrate + bond coating + TBC) and the second did not (2-layer model: substrate + TBC). As no significant differences were observed for thermal diffusivity using both models, the subsequent calculations of the thermal diffusivity of the different YSZ coatings were made using the 2-layer model, which also simplified the calculations.

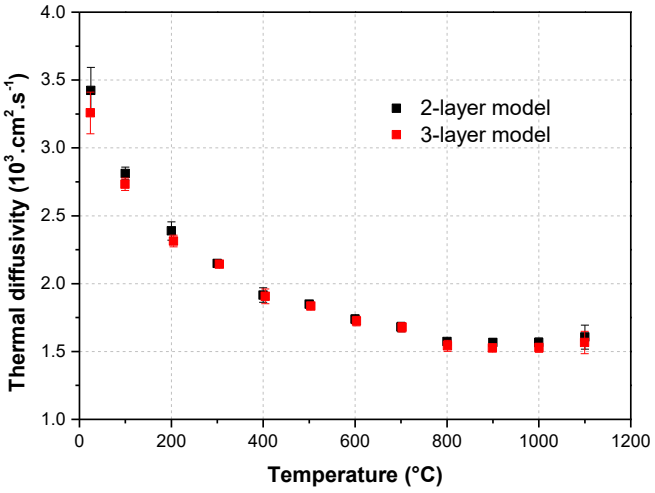

Figure II.8 *– Comparison between thermal diffusivity calculations using a 2-layer model (substrate + TBC) or a 3-layer model (substrate + BC + TBC).*

Although the laser-flash technique can be applied to determine the thermal diffusivity of both freestanding coatings and multi-layer samples, the values must be carefully considered. For instance, deviations in thermal diffusivity may arise from the method itself. This is due to the different input parameters required for its determination as well as inherent errors related to the intrinsic properties of the material or the complex geometries of some samples. In addition, the inaccurate values of density and of specific heat capacity as a function of the temperature can also increase the error in the calculated values of thermal diffusivity.

In the particular case of as-deposited coating samples, the measurements were carried out a second time because significant sintering occurred during the first measurement (till 1100°C). This phenomenon has been previously reported in the literature on similar YSZ TBCs [33, 34, 35].

Prior to the measurements with the laser flash and the deposition of the absorbing layers (gold and graphite), the thicknesses of the freestanding coatings and of the multilayer samples were accurately determined ($\pm 10^{-3}$ mm) with a digital calliper. The thicknesses of the layers of

the composite samples were measured after the laser-flash analyses by measuring the thicknesses on the cross-sections of the samples.

To assess the validity of the laser-flash measurements, reference samples were periodically measured. Moreover, the calculated thermal conductivity of the substrates using the measured values were compared with the literature data (**Table II.10**) and allowed to validate the reproducibility of the laser-flash technique for these materials.

Table II.10 *– Calculated thermal conductivity of the substrates of the study.*

Temperature (°C)	**Experimental thermal conductivity ($W.m^{-1}.K^{-1}$) [reference values]***				
	AM1	Hastelloy X	Haynes 188	Inconel 600	Pure Ni
25	6.2	11.4 [9.1]	10.2 [10.4]	13.4 [14.9]	69.0 [90]
100	8.5	12.9 [11]	12.0 [12.2]	15.3 [15.9]	62.1
200	9.8	14.4 [14.1]	14.0 [14.3]	17.3 [17.3]	55.6
300	10.6	15.4	15.8 [15.9]	18.8 [19.0]	50.2 [53.5]
400	11.3	16.7	17.5 [17.5]	20.3 [20.5]	60.0
500	11.9	18.4	19.2 [19.3]	21.9 [22.1]	54.8
600	12.0	20.2 [20.8]	21.0 [21.1]	25.4 [23.9]	56.0
700	13.4	22.7 [22.9]	22.8 [23.0]	26.2 [25.7]	57.7
800	15.2	26.1 [25.1]	25.0 [24.8]	27.1 [27.5]	59.6
900	17.2	28.1 [27.2]	24.9 [25.5]	28.0	60.7
1000	20.8	30.5	26.1 [27.6]	29.3	62.3 [63.1]
1100	25.8	-	-	30.7	-

**references: [23, 24, 25]*

4.4Adherence of the slurry coatings: the scratch tests

The adherence of the TBCs made from the slurry route was tested using the scratch test method. Scratching experiments were performed using an Anton-Parr STeP E400 scratch tester in which an acoustic emission (AE) sensor was coupled to the equipment. The top surfaces of the slurry TBCs were scratched with a Rockwell M-120 diamond indenter with 100 µm tip radius. **Table II.11** shows the experimental parameters of the scratch tests performed for the entire set of coatings. In addition, the normal force (F_N), the coefficient of friction (COF), and the residual depth (Rd) were measured with the aid of Scratch Software V. 4.52. One shall note that a pre-scan is realised at 0.03N on the sample prior to the scratch for the software to identify

the original surface of the sample. However, due to the low resistance of the porous coatings to measure, these pre-scans could already penetrate them and thus, the measured depth of penetration of the indent should be considered carefully. The worn tracks produced by the scratch tests were observed using optical microscopy (GX51 Olympus instrument) and scanning electron microscopy (SEM). With the scratch tester, the worn tracks are developed at constant speed rate, and linearly increasing load with automatic recording of an AE-normal force plot.

Table II.11 *– Experimental parameters employed during scratch tests.*

Range load (N)	0.03-10; 0.3-30
Speed rate ($mm.min^{-1}$)	2.5
Scratch length (mm)	5 and 7
Acquisition rate (Hz)	30

In addition to the scratch tests, micro-indentation was performed on the coatings in order to have another insight on the resistance of the coatings to penetration of the indent and to compare them with the results from the scratch tests. Therefore, the normal force applied (F_N) for the penetration of Vickers indents was recorded as a function of the depth of penetration till reaching 5 µm into the coatings. This depth was chosen in accordance with the different thickness of the slurry coatings.

5. References

1. Particoat - Homepage, web page visited on October 31st, 2018 at http://www.particoat.eu/
2. B. Rannou, F. Velasco, S. Guzmán, V. Kolarik, F. Pedraza, *Ageing and thermal behaviour of a PVA/Al microspheres slurry for aluminizing purposes*, Materials Chemistry and Physics, **2012**, 360-365.
3. F. Pedraza, B. Rannou, G. Boissonnet, B. Bouchaud, Z. Maache-Rezzoug, *Rheological behaviour, synthesis and performance of smart thermal barrier coating systems based on hollow alumina*, Journal of Material Sciences and Chemistry Engineering 3, **2015**, 17-22.
4. A. Gromov, A. Ilyin, U. Förter-Barth, U. Teipel, Propellants Explosives Pyrotechnics 31, **2006**, 401-409.

5. A. Aygun, A.L. Vasiliev, N.P. Padture, X. Ma, *Novel thermal barrier coatings that are resistant to high-temperature attack by glassy deposits*, Acta Materiala 55, **2007**, 6734-6745.
6. C.G. Levi, J.W. Hutchinson, M-H. Vidal-Sétif, C.A. Johnson, *Environmental degradation of thermal barrier coatings by molten deposits*, MRS Bulletin 37, **2012**, 932-941.
7. U. Schulz, *Phase Transformation in EB-PVD Yttria Partially Stabilized Zirconia Thermal Barrier Coatings during Annealing*, Journal of the American Ceramic Society 83, **2000**, 904-910.
8. J. Ilavsky, J.K. Stalick, *Phase composition and its changes during annealing of plasma-sprayed YSZ*, Surf. Coat. Technol. 127, **2000**, 120-129.
9. J. Ilavsky, J.K. Stalick, J.Wallace, *Thermal spray yttria-stabilized zirconia phase changes during annealing*, J. Therm. Spray Technol. 10, **2001**, 497-501.
10. Horiba, *What is Raman Spectroscopy*?, web page https://www.horiba.com/en_en/raman-imaging-and-spectroscopy/ visited on October 31st, **2018**.
11. I.O. Golosnoy, *Heat Transfer Through Plasma-Sprayed Thermal Barrier Coatings in Gas Turbines: A Review of Recent Work*, Journal of Thermal Spray Technology 18[5-6], **2009**, 809-821.
12. L. Pawlowski and P. Fauchais, *Thermal Transport Properties of Thermally Sprayed Coating*, International Materials Reviews 37[6], **1992**, 271-289.
13. D. B. Fowler, W. Rigg and J.C. Russ, *Inspecting thermal sprayed coatings*, Advanced Material Processing 11, **1990**, 41-52.
14. A. Kulkarni, S. Sampath, A. Goland, H. Herman and B. Dowd, *Computed microtomography studies to characterize microstructure-property correlations in thermal sprayed alumina deposits*, Scripta Materiala 43, **2000**, 471-476.
15. A. Kulkarni, Z. Wang, T. Nakamura, S. Sampath, A. Goland, H. Herman, J. Allen, J. Ilavsky, G. Long, J. Frahm and R.W. Steinbrech, *Comprehensive microstructural characterization and predictive property modeling of plasma-sprayed zirconia coatings*, Acta Materialia 51, **2003**, 2457-2475.
16. S. Deshpande, A. Kulkarni, S. Sampath and H. Herman, *Application of image analysis for characterization of porosity in thermal spray coatings and correlation with small angle neutron scattering*, Surface and Coatings Technology 187, **2004**, 6-16.
17. Y. Tan, V. Srinivasan, T. Nakamura, S. Sampath, P. Bertrand, *Optimizing Compliance and Thermal Conductivity of Plasma Sprayed Thermal Barrier Coatings via Controlled*

Powders and Processing Strategies, Journal of Thermal Spray Technology 21[5], **2012**, 950-962.

18. Y. Zhao, A. Shinmi, X. Zhao, P.J. Withers, S. Van Boxel, N. Markocsan, P. Nylen and P. Xiao, *Investigation of interfacial properties of atmospheric plasma sprayed thermal barrier coatings with four-point bending and computed tomography technique*, Surface and Coatings Technology 206, **2012**, 4922-4929.
19. A. Bacciochini, F. Ben-Ettouil, E. Brousse, J. Ilavsky, G. Montavon, A. Denoirjean, S. Valette, P. Fauchais, *Quantification of void networks of as-sprayed and annealed nanostructured yttria-stabilized zirconia (YSZ) deposits manufactured by suspension plasma spraying*, Surface and Coatings Technology 205, **2010**, 683-689.
20. O. Lavigne, Y. Renollet, M. Poulain, C. Rio, P. Moretto, P. Brannvall, J. Wigren, *Microstructural characterization of plasma sprayed thermal barrier coatings by quantitative analysis*, Quantitative microscopy of high temperature materials conference, Sheffield, UK, **1999**.
21. ISO Standard method, ISO-TR 26946, *Standard method for porosity measurement of thermally sprayed coating*, **2011**.
22. ASTM Standard method, ASTM E228-11, *Linear Thermal Expansion of Solid Materials with a Push-Rod Dilatometer*, **2011**.
23. Technical document, HAYNES International, High-Temperature Alloys, Haynes 188 alloy, H3001-C.
24. Technical document, HAYNES International, High-Temperature Alloys, Hastelloy X alloy, H3009-C.
25. Technical document, INCONEL alloy 600, High-Temperature Alloys, Hastelloy X alloy, at www.specialmetals.com
26. L. Pawlowski, Specific heat and thermal conductivity of plasma sprayed yttria-stabilized zirconia and NiAl, NiCr, NiCrAl, NiCrAlY..., High Temperatures-High Pressures 18, **1986**, 65-77.
27. T.A. Taylor and P.N. Walsh, *Thermal expansion of MCrAlY alloys*, Surface and Coatings Technology, 177-178, **2004**, 24-31.
28. R.E. Taylor, X. Wang, W. Xu, *Thermophysical properties of thermal barrier coatings*, Surface and Coatings Technology 120-121, **1999**, 89-95.
29. ASTM Standard method, ASTM E1269-05, *Determining Specific Heat Capacity by Differential Scanning Calorimetry*, **2005**.

30. Linseis, *Diffusivité Thermique & Conductivité Thermique – LFA 1000*, web page https://www.linseis.com/fr/nos-produits/diffusivite-thermique-conductivite-thermique/lfa-1000/ visited on October 31st, **2018**.
31. ASTM Standard method, ASTM E1461-13, *Thermal Diffusivity by the Flash Method*, **2013**.
32. M. Akoshima, T. Tanaka, S. Endo, T. Baba, Y. Harada, Y. Kojima, A. Kawasaki, and F. Ono, *Thermal Diffusivity Measurement for Thermal Spray Coating Attached to Substrate Using Laser Flash Method*, Japanese Journal of Applied Physics 50, **2011**, 11RE01-1-8.
33. F. Cernushi, L. Lorenzoni, S. Ahmaniemi, P. Vuoristo, T. Mäntylä, *Studies of the sintering kinetics of thick thermal barrier coatings by thermal diffusivity measurements*, Journal of European Ceramic Society 25, **2005**, 393-400.
34. Y. Tan, Jon P. Longtin, and Sanjay Sampath, *Effect of the Starting Microstructure on the Thermal Properties of As-Sprayed and Thermally Exposed Plasma-Sprayed YSZ Coatings*, Journal of the American Ceramic Society 92[3], **2009**, 710-716.
35. H.-J. Rätzer-Scheibe, U. Schulz, *The effects of heat treatment and gas atmosphere on the thermal conductivity of APS and EB-PVD PYSZ thermal barrier coatings*, Surface & Coatings Technology 201, **2007**, 7880-7888.

III. INFLUENCE OF AGEING ON THE THERMAL INSULATION OF APS COATINGS

Table of contents

1. Introduction

As exposed in the summary of the proposed strategy (see §I.4.2), this dissertation focuses at first on the current PS coatings made of YSZ in order to provide a better comprehension on the relationships between their intrinsic properties and their thermal insulation capacity. This chapter comprises two articles and intends to shed light on the exposure at high temperature in the presence or not of CMAS that results in microstructural and chemical degradations of these PS TBC systems.

As mentioned in §I.4.2.1, some studies have focused on the impacts of time and temperature that result in modifications of the structure of PS TBCs via sintering and oxidation, and on the associated relative changes of thermo-physical properties [1-4]. However, most of these studies only focused on the ceramic coating itself while the evolutions of the other components of the thermal barrier coating system have been neglected, e.g. TGO, thermally induced cracks. Therefore, **the first article** focuses on different PS thermal barrier coating systems to investigate the microstructure-heat insulation relationships through a systematic analysis of both the microstructure and the thermal diffusivity in their as-deposited state and when aged under various conditions.

Furthermore, the CMAS-related degradation mechanisms that are susceptible to increase heat transport through the TBCs by filling the pores or by chemical transformations have been only demonstrated in a few studies [5,6]. However, these studies generally focused only on a fully-infiltrated coating using an excess of CMAS. Thus, **the second article** focuses on finding the onset quantity of CMAS that could induce enough changes to alter the thermal conductivity of the coatings. Small amounts of CMAS are deposited on the surface of plasma-sprayed coatings followed with a high temperature heat treatment for infiltration to occur. This article investigates the sintering potential of minor calcium-magnesium-aluminium silicates (CMAS) deposits (from 0.25 to 3 $mg.cm^{-2}$) on freestanding yttria-stabilized zirconia (YSZ) plasma-sprayed thermal barrier coatings (TBCs) annealed at 1275°C for 1 h.

2. Article 1: *Evolution of Thermal Insulation of Plasma-Sprayed Thermal Barrier Coating Systems with Exposure to High Temperature*

Evolution of Thermal Insulation of Plasma-Sprayed Thermal Barrier Coating Systems with Exposure to High Temperature

G. Boissonnet[1]*, G. Bonnet[1], A. Pasquet[2], N. Bourhila[2], F. Pedraza[1]

1. Université de La Rochelle, Laboratoire des Sciences de l'Ingénieur pour l'Environnement (LaSIE UMR-7356 CNRS), Avenue Michel Crépeau, 17042 La Rochelle, cedex 01 – France.

2. SAFRAN Aircraft Engines. Site de Evry-Corbeil. Rue Henri-Auguste Desbruères. BP 81. 91003 Evry Cedex. France

*corresponding author: boissonnet.germain@gmail.com

Abstract. The thermal insulation potential of plasma-sprayed yttria-stabilized zirconia (YSZ) thermal barrier coating (TBC) system is generally assessed via the evaluation of the ceramic layer only. However, ageing of the complete system leads to microstructural transformations that may also play a role in the heat transport properties. This study thus investigated the microstructure-heat insulation relationships of different TBC systems in their as-deposited state and when aged under various conditions, through the systematic analysis of both microstructure and thermal diffusivity. The latter was measured from room temperature up to 1100°C using the laser-flash technique, while the porous microstructure was assessed using image analysis. The different coatings exhibited relatively similar thermal diffusivity values that were shown to be mostly influenced by the thin cracks and interlamellar porosities in contrast with larger defects. The thermal insulation of the TBC systems after exposure to high temperature was shown to be globally stable despite the microstructural variations introduced by cracks, oxidation and chemical degradations.

1. Introduction

Plasma-sprayed (PS) thermal barrier coatings (TBCs) made of yttria-stabilized zirconia (YSZ) are still the coatings of choice for the metallic components of the hottest part of aeronautical and utility gas turbines. These coating systems delay the onset of thermally induced failures by reducing the temperature and the oxidation rate of the metal substrate. However, the

YSZ may undergo significant microstructural changes with exposure to temperature. These changes include sintering of pores and cracks thereby decreasing the heat-scattering interfaces, hence the intrinsic thermal insulation of the coating. Plasma-sprayed YSZ coatings are particularly sensitive to these phenomena because they display a high anisotropy with a large number of pores and interfaces at the micro- and nano-scales. Since the low thermal conductivity of YSZ coatings depends on the scattering of phonons and photons by such defects, the understanding of the impact of microstructural changes on the insulating efficiency of thermal barrier systems becomes paramount.

A considerable number of researches has been conducted to determine the mechanisms of heat transport through the particular microstructure of PS TBCs [1-4]. For these coatings, the heat conduction is the result of a competition between that occurring through solid zirconia and that through gas-filled pores. While conductivity of fully dense YSZ at room temperature (RT) has been reported to be ~2.5 $W.m^{-1}.K^{-1}$ [5, 6], that of gas in a closed pore is a hundred times lower (λ_{air} ~ 0.025 $W.m^{-1}.K^{-1}$) considering the dimensions of the pores much larger that the molecular mean free path of the gas molecules [7]. However, when the pores are smaller (typically fine interlamellar pores ~1 µm), the heat conduction of the gas falls below the conduction of the free gas to ~0.01 $W.m^{-1}.K^{-1}$ due to gas molecule-wall collisions (Knudsen conduction) [8]. Even when considering very high temperature (1750°C) and high pressure (40 bar), the gas conduction in such small pores does not exceed ~0.01 $W.m^{-1}.K^{-1}$ [7], hence still providing a lower heat conduction than bulk zirconia (~2.0 $W.m^{-1}.K^{-1}$ [9]). Consequently, both the size and concentration of the pores in PS TBCs have a significant impact on the relative heat transport properties.

Porosity can be quantitatively characterized using advanced techniques like computed micro-tomography (CMT) and small-angle neutron scattering (SANS), as well as simpler methods that measure the density of the coatings, such as gas sorption, e.g. He pycnometry and Brunauer-Emmett-Teller (BET), liquid intrusion, e.g. Archimede's method and mercury intrusion porosimetry (MIP), or image analysis (IA) [10-15]. In the present study, image analysis (IA) has been employed because it presents several advantages compared to the other techniques, like cost-effectiveness and easiness of application while allowing differentiating various types of pores and cracks. Although it only requires a couple of images per coating, IA was statistically tested to give a 95 % confidence level regarding the specific experiments and metallographic preparation in the study performed by Fowler and coll. [13]. Desphande et al.

also showed IA to be a reliable method for characterization of porosity in thermally sprayed coatings by comparing the results of IA with those obtained by CMT and SANS [12].

In addition, numerous studies have focused on the impact of time and temperature that result in modifications of the structure of PS TBCs, and on the associated relative changes of thermo-physical properties [15-18]. For instance, Cernushi et al. examined the sintering kinetics of different coatings elaborated by varying the process parameters and measured the resulting changes in thermal diffusivity till 200°C [16]. Tan and coll. investigated the evolution of the starting microstructures as a function of different annealing conditions with the aim of finding a correlation between the sintering behavior and the thermal conductivity of these coatings [15, 17].

However, many of these studies have only focused on the ceramic coating itself while the evolutions of the other components of the thermal barrier coating system have been neglected. For instance, the development of the thermally grown oxide (TGO) and the growth of cracks in the ceramic due to thermal cycling may also play a role in the overall protection potential of TBCs. Therefore, the present study intends to unveil the relationships between the evolution of the microstructure of full thermal barrier coatings with temperature and the resulting thermal diffusivity. The work is focused on thermally-sprayed coatings in the as-deposited conditions, aged in the laboratory at high temperature and aged in service conditions (i.e. engine-run).

2. Experimental

2.1. Coatings of the study

The coatings considered in this study were produced by Safran Aircraft Engines (France) and by SR Technics Airfoil Services (Ireland) on different substrates (AM1, Haynes 188 or Inconel 600) by atmospheric plasma spray (APS) deposition technique and are listed in Table 1. For all the samples, MCrAlY bond coatings were deposited prior to YSZ ceramic coatings. The deflector-APS (DFL_APS), combustion chamber-APS (CC_APS) and injector-APS (INJ_APS) samples (10 x 10 mm^2) were cut from aeronautical engine parts while the laboratory samples were made using metallic plates as substrates for coating deposition and cut afterwards (DFL: deflectors, CC: combustion chamber, INJ: injectors). The CC_APS and INJ_APS samples were cut from serviced components of the combustion chamber and injectors, respectively.

Table 1 – *Samples of the study*

Sample	Type	Substrate	Bond coating	Ceramic coating
AM1_APS1	lab sample, as-deposited	AM1	NiCrAlY HVOF, 40 ±12 µm	APS YSZ; feedstock METCO 204 NS-G; 110 ±7 µm
AM1_APS2	lab sample, as-deposited	AM1	NiCrAlY HVOF, 15 ±5 µm	APS YSZ; feedstock METCO 204 NS-G; 430 ±15 µm
DFL_APS	*deflector*, as-deposited	Haynes 188	NiCoCrAlY HVOF, 130 ±9 µm	APS YSZ; feedstock METCO 204 NS-G; 330 ±12 µm
IN_APS	lab sample, as-deposited	Inconel 600	NiCrAlY HVOF, 72 ±5 µm	APS YSZ; feedstock PRAXAIR ZRO-113/114; 230 ±10 µm
AM1_APSmf	lab sample, as-deposited	AM1	NiCrAlY HVOF, 15 ±7 µm	APS YSZ; feedstock SPM 2000; 90 ±9 µm
CC_APS	*combustion chamber*, aged	Haynes 188	NiCoCrAlY, HVOF, 135 ±8 µm	APS YSZ; feedstock METCO 204 NS-G; 190 ±6 µm
INJ_APS	*Injectors*, aged	Haynes 188	NiCoCrAlY, HVOF, 70 ±11 µm	APS YSZ; feedstock METCO 204 NS-G; 450 ±8 µm

The IN_APS samples were used for the thermal ageing tests because of their greater availability. Isothermal heat treatments were performed in air at 1100°C on freestanding coatings and full samples for 50, 150, 250 and 500 h. The freestanding coatings were obtained by chemically dissolving the oxide interface between the bond coating and the YSZ TBC in a 20 vol.% HCl solution. Full IN_APS samples were also thermally cycled in a rig for 50, 100, 250 and 500 cycles of 1h at 1100°C in air followed by forced air cooling for 15 min. The cycling temperature of 1100°C was chosen as it is close to the working temperatures of most YSZ plasma coatings and because the phase change for YSZ is not significant below 1200°C [19].

2.2. Microstructural analysis of the coatings

The microstructural changes were investigated in polished cross-sections with 1 µm diamond paste. A FEI Quanta 200F scanning electron microscope (SEM) was employed to get backscattered electrons images at x1000 magnification. At least 15 images per coating were then processed using ImageJ software and porosity levels were calculated from the binary images obtained. IA additionally allows differentiating between coarse pores (often arising from the lack of complete filling due to harsh processing parameters [20]) and the thin porous network, composed of the microcracks (associated with the relief of quenching stresses) and interlamellar pores (result of the splat-based coating build-up), which is of major interest as these two types of categories exhibit different heat transport behaviors. In order to classify the different types of pores regarding their potential for heat transport reduction, discrimination

criteria that comprise the aspect ratio of the pores and their orientation with respect to the heat flux were generally employed [21, 22]. However, in this study, the thin pores (micro-cracks and interlamellar pores) were integrated as a single porosity level, regardless of their orientation. This "lamellar" porosity level was separated from the total porosity measured by a closing treatment on the binary image of the pores which dimensions fall below 1 µm.

The microstructure and the composition were also characterized using energy dispersive spectrometry (EDS/EDAX coupled to the SEM), Raman micro-spectrometry (Jobin Yvon LabRam HR800, λ_{laser} ~632nm) and X-ray diffraction (XRD, Brüker AXS D8 Advance) using the λ_{Cu} in θ-2θ mode. Note that some diffraction peaks have not been indexed as they are due to tungsten pollution (WLα radiation) of the support of the Cu target that duplicates the peaks at a different angle.

2.3. Determination of the thermal insulation ability

Thermal conductivity is usually employed in the literature to determine the thermal insulation power of thermal barrier coatings and can be calculated from the thermal diffusivity (α), the density (ρ) and the specific heat capacity of the material (C_p) following (eq. (1)):

$$\lambda = \alpha \times \rho \times C_p \qquad (1)$$

Although the laser-flash technique can be applied to determine the thermal conductivity of both freestanding coatings and multi-layer samples, the thermal conductivity values have to be carefully considered. As a matter of fact, deviations in thermal diffusivity may arise from the method itself due to the different input parameters required for its determination as well as errors inherent to the intrinsic properties of the material or the complexity of the measured samples. Additionally, imprecise knowledge of the density and specific heat capacity as a function of the temperature can also increase the error in the calculated thermal conductivity values. Therefore, it is more accurate to discuss the thermal properties (ρ, C_p and α) separately, thus the thermal diffusivity data will be preferred for the comparison of the thermal insulation properties of the different substrate and coating materials of this study.

The thermal diffusivity was determined using high-temperature laser-flash measurements with a Linseis LFA1600 apparatus at low pressure (~1.10^{-2} mbar) every 100°C between room temperature and 1100°C. Three samples per type of coating were analyzed with five separate

laser shots per sample at each temperature to increase accuracy of the results. In the particular case of as-deposited coating samples, the measurements were carried out a second time as significant sintering occurred during the first measurement. This phenomenon has been previously reported in the literature on similar YSZ TBCs [16, 17, 23]. After the second measurement, the thermal diffusivity was observed to be stable.

For multilayer calculation, the thermal diffusivities of the different substrates were measured. For the substrate of the samples aged in isothermal and cyclic conditions (Inconel 600), thermal diffusivities were compared before and after ageing at 1100°C in air for 500 h. Similarly, the thermal diffusivity of the MCrAlY bond coatings was measured via the laser-flash technique. Since the thickness of the MCrAlY coatings is smaller than that of the superalloy substrate and their thermal diffusivity values are equivalent, a 2-layer model (YSZ and bond coat + substrate) was employed rather than the 3-layer model (YSZ, bond coat and substrate) to assess the thermal diffusivity of the full thermal barrier coating systems.

Prior to the measurements with the laser flash, the thicknesses of the freestanding coatings and of the multilayer samples were accurately determined ($\pm 10^{-3}$ mm) with a digital caliper. All samples were then coated on both sides with a 4-5 µm graphite layer to increase the absorption of the laser pulse at the rear surface as well as the emissivity of the heat signal for the measurement by the InSb infrared detector on the front face of the sample. For multilayer calculations, thicknesses of the layers were measured on the cross-section images for a better accuracy of the computed values.

3. Results

3.1. Structure of as-received coatings

3.1.1. As-deposited coatings

The as-deposited coatings listed in Table 1 present a wide variety of microstructures according to the SEM cross-sections of Fig. 1. Three main layers (ceramic top coat, intermediate bond coating and substrate at the bottom) can be observed in Fig. 1a to 1e. The different thicknesses of the coating layers are given in Table 1. A large thickness range and huge differences of thickness ratios between the ceramic and the bond coating layers can be noted. For instance, the AM1_APS2 sample has a 430 µm ceramic layer with only 15 µm of NiCrAlY bond coating (Fig. 1b) while AM1_APS1 shows a 110 µm ceramic layer with 40 µm of NiCrAlY bond coating (Fig. 1a). It is also observed that due to the roughness of the plasma-

sprayed coatings, standard deviations to the measured thickness were significantly high compared to the thickness of the thinner coatings, i.e. 10 % error on the coating thickness for AM1_APS1 (Table 1).

At greater magnifications (Fig. 1f to 1j) the ceramic layers also exhibit significant differences of density, type of defects and pores. While DFL_APS ceramic coating shows a high level of interlamellar porosity (Fig. 1c), coatings from IN_APS samples (Fig. 1i) exhibit a more significant concentration of large defects (macro-pores). In contrast, the "micro-cracked" coating (AM1_APSmf) (Fig. 1e and j) possesses a very dense structure with very few pores and thinner interlamellar pores compared to the standard APS coatings.

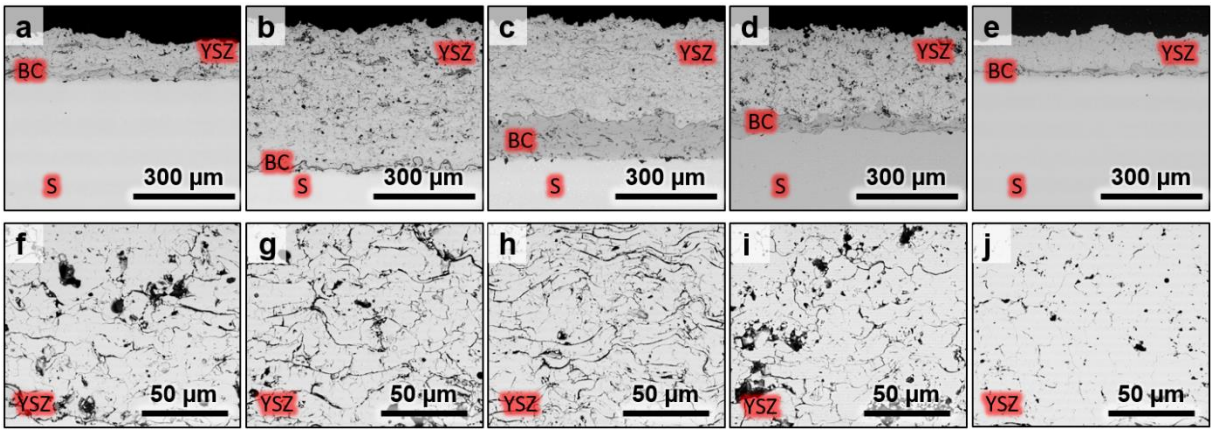

NB: YSZ = ceramic; BC = bond coating; S = substrate

***Figure 1** – **a**, **b**, **c**, **d** and **e** are SEM micrographs of the cross-sections of the as-deposited AM1_APS1, AM1_APS2, DFL_APS, IN_APS and AM1_APSmf samples respectively and **f**, **g**, **h**, **i** and **j** are the corresponding higher magnifications of the ceramic coatings.*

Fig. 2 gathers the porosity levels of the as-deposited ceramic coatings. The total porosity of the standard APS YSZ is comprised between 20 % and 25 % while that of the microcracked AM1_APSmf is of about 11 %. However, the level of the different types of porosity ("coarse" and "lamellar") is clearly different among the coatings as observed in Fig. 1. Indeed, although the total porosity of IN_APS and of DFL_APS is around 22 %, their lamellar porosity is, respectively, of 11 % and 16 %. In contrast, their coarse porosity is of 11 % and 6 %. The denser AM1_APSmf coatings exhibit a very small coarse porosity level of about 2 % and a lamellar porosity level of around 9 %.

The XRD of the coatings (Fig. 3) shows that all the as-deposited coatings exhibit the tetragonal structure of the zirconia. Only the IN_APS coatings additionally show some peaks of the monoclinic structure of the zirconia.

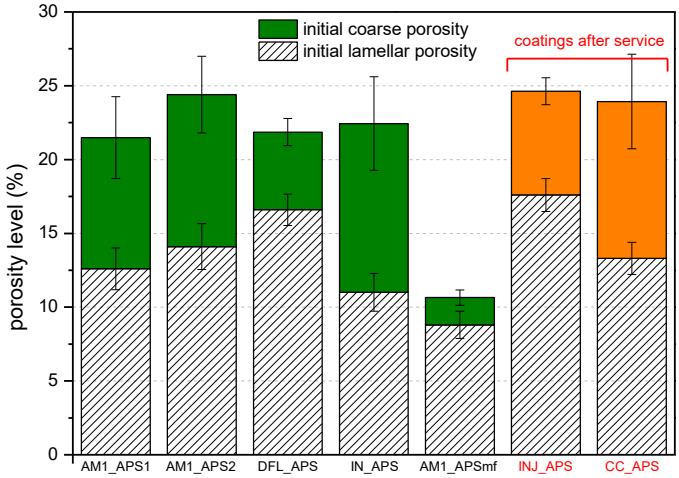

Figure 2 *– Initial porosity levels of the coatings of the study.*

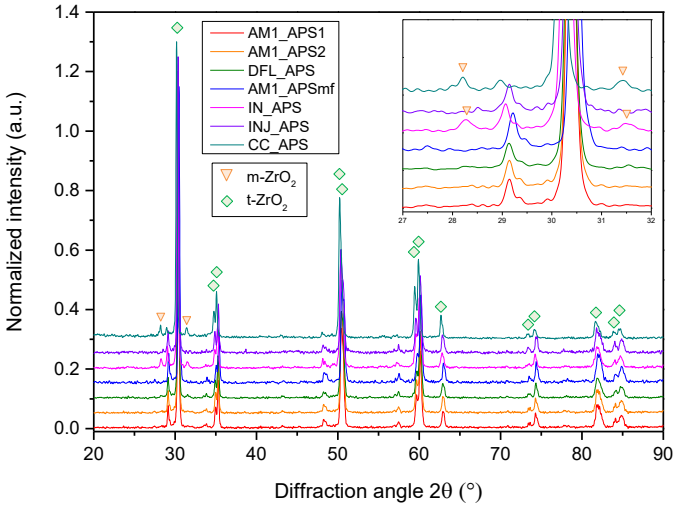

Figure 3 *– XRD patterns of the as-received plasma-sprayed coatings.*

3.1.2. Serviced coatings

Fig. 4 presents the SEM cross-section of a coating after service in the injectors of an aeronautical engine (INJ_APS). This thick coating does not seem significantly damaged apart from the oxidation of the bond coating Fig. 4b. The lamellar porosity of the ceramic layer appears quite large (17.5 %) compared to the coarse porosity level (7 %) and very few impurities can be observed (Fig. 2 and Fig. 4a). The diffraction pattern of Fig. 3 shows no monoclinic phase for this coating and only displays the peaks of the tetragonal phase of zirconia.

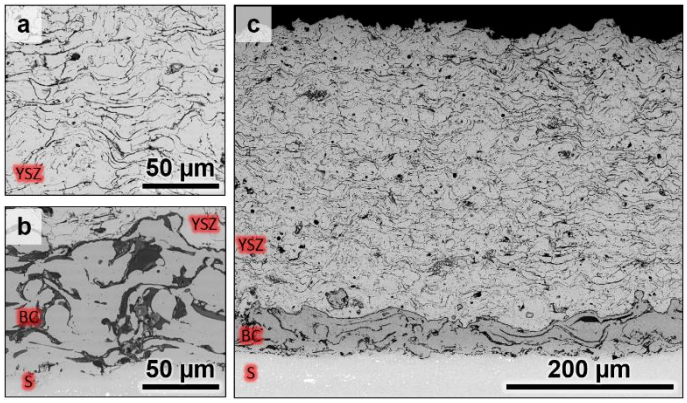

NB: YSZ = ceramic; BC = bond coating; S = substrate

Figure 4 *–Cross-sections of the INJ_APS sample with **a** and **b** being higher magnifications of the ceramic microstructure and the bond coating, respectively.*

The samples taken from a combustion chamber (CC_APS) (Fig. 5) appear more degraded than INJ-APS. In addition to the oxidation of the bond coating, Ni-Cr-Al mixed oxide particles are embedded in the YSZ ceramic layer (Fig. 5a). Also, corroded zones are observed where Si, Ca and Al were detected via EDS (Fig. 5b). The XRD pattern for this coating (Fig. 3) points out the monoclinic phase of zirconia along with the tetragonal one. Moreover, the different defects that can be seen on Fig. 5 were analyzed by Raman micro-spectrometry (Table 2). The zone of the Ni-Cr-Al mixed oxide of Fig. 5a exhibits some of the characteristic peaks of monoclinic phase of zirconia. The other missing peaks could not be clearly identified as the Raman signal was blurred by other species that could not be identified either. For the corroded zone of Fig. 5b, all the peaks correspond to the only monoclinic phase. The lamellar and the coarse porosity levels were measured to be of 13 % and 10 %, respectively (Fig. 2).

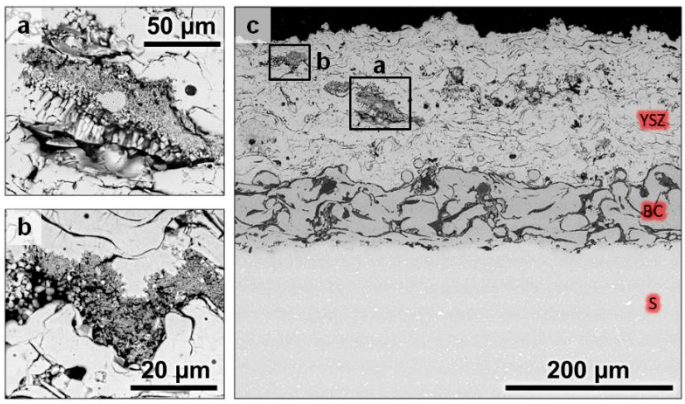

NB: YSZ = ceramic; BC = bond coating; S = substrate

Figure 5 *- Cross-sections of the CC_APS sample with **a** and **b** being higher magnifications of degradations of the ceramic by metal oxide inclusion and molten silicates corrosion, respectively.*

Table 2 *– Raman-tabulated peaks of tetragonal and monoclinic phases spotted in CC_APS sample. *[24]*

Phase	**Reference peaks***	**Experimental peaks**		
		YSZ *clean*	spot fig. 5a	spot fig. 5b
Tetragonal	~142	~146		
	~256	~257		
	~320	~321		
	~466	~465		
	~637	~636		
Monoclinic	~178		~176	~177
	~190		~188	~189
	~219		~220	~220
	~303		-	~304
	~331		~331	~332
	~345		~347	~346
	~379		~380	~380
	~474		~473	~473
	~500		-	~500
	~534		-	~536
	~559		-	~556
	~615		~612	~614
	~638		~636	~637

3.2. Thermal diffusivity of as-received coatings

The thermal diffusivity of the different coatings is plotted as a function of the temperature on Fig. 6. All the coatings follow a similar tendency with the evolution of the temperature. The coating from AM1_APSmf, which is the thinnest one (~90 µm, Table 1) with the smallest porosity level, presents the higher thermal diffusivity. At high temperature, this coating displays values of about ~3.10^{-3} $cm^2.s^{-1}$, while all the other standard coatings thermal diffusivities are comprised between 1.10^{-3} and 2.10^{-3} $cm^2.s^{-1}$. INJ_APS and DFL_APS have the highest levels of lamellar porosity and show the lowest values of thermal diffusivity.

To highlight the effect of the lamellar porosity level, the thermal diffusivity measured at room temperature and at 1100°C is plotted as a function of the porosity level of the different coatings on Fig. 7. The thermal diffusivity values for both temperatures are observed to decrease in a linear way with the increase of lamellar porosity. The slope of the linear relationship between the thermal diffusivity and porosity is smaller at 1100°C than at room temperature, which indicates that the dependence of thermal diffusivity on porosity is reduced at high temperature. In contrast, the CC-APS and AM1-APSmf coatings deviate from such linear relationship by exhibiting higher thermal diffusivity values.

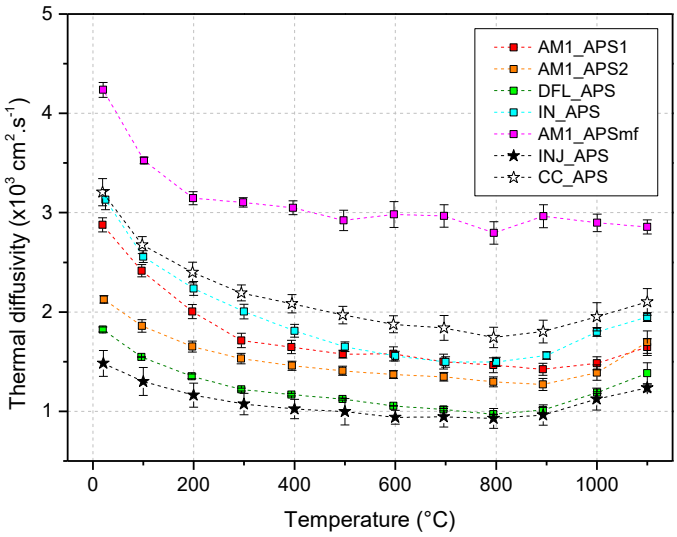

Figure 6 *–Initial thermal diffusivity as a function of temperature for the as-received coatings.*

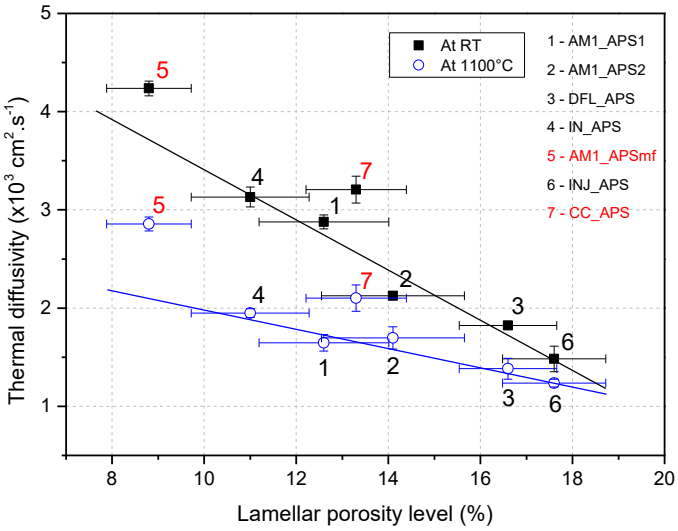

Figure 7 *– Thermal diffusivity at room temperature and 1100°C of the as-received coatings against lamellar porosity level*

3.3. Coatings aged in the laboratory

3.3.1. Microstructure

The microstructures of the thermal barrier systems of the IN-APS samples are respectively presented, after isothermal ageing at 1100°C for 50, 150, 250 and 500 h, on Fig. 8a, 8b, 8c and 8d. The oxide scale at the interface bond coat/ceramic layer significantly grew between 50 h and 150 h of exposure. After 250 h of exposure, the interface between the substrate and the

bond coating appeared oxidized. After 500 h, oxidation also occurred at the grain boundaries of the substrate. In addition, sintering of the lamellar pores of the ceramic increased with oxidation time, while long cracks had already developed after 50h of exposure only.

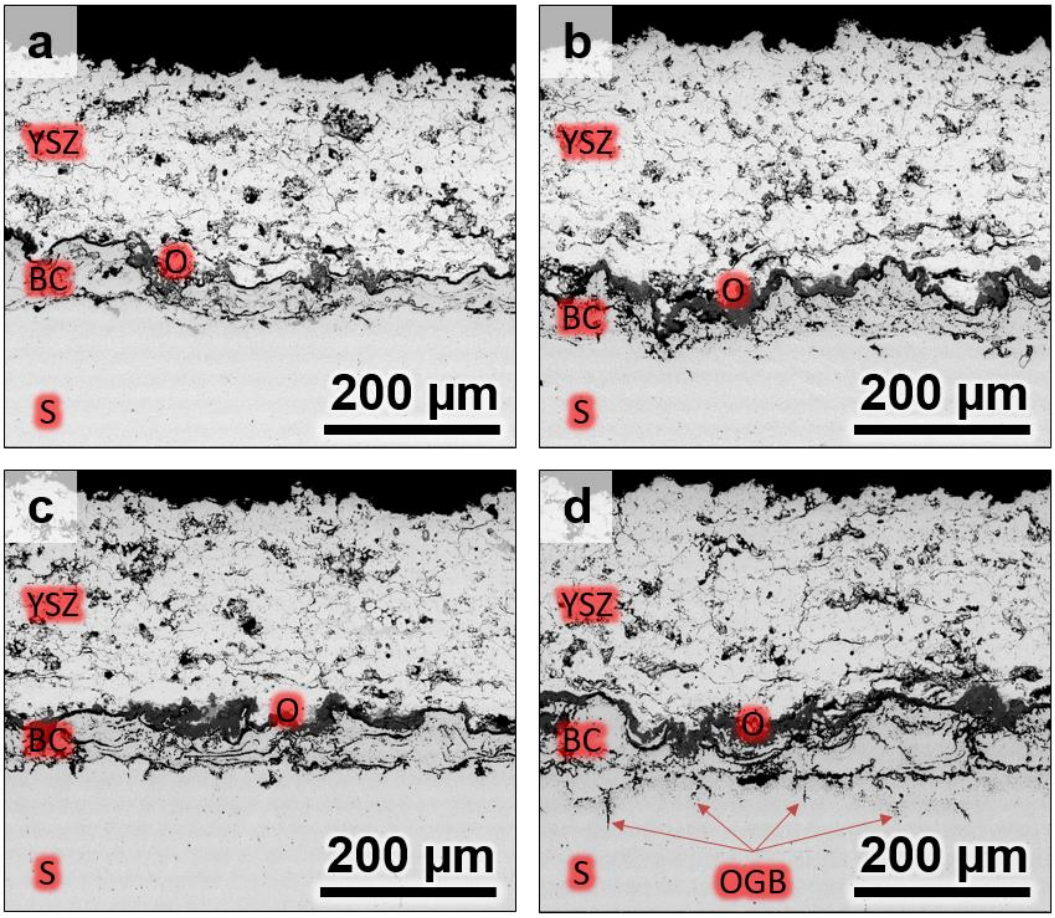

NB: YSZ = ceramic; BC = bond coating; S = substrate; O= oxides; OGB = oxidized grain boundaries

Figure 8 *– SEM micrographs of the cross-sections of the IN_APS samples isothermally treated at 1100°C in air for (a) 50, (b) 150, (c) 250 and (d) 500 h.*

Fig. 10 shows the same samples after thermal cycling in air at 1100°C for duration equivalent to those of isothermal exposure (50, 100, 250 and 500 cycles). Compared to the isothermal exposures, the oxide scale grew faster at the bond coat interface. Indeed, the oxide scale is after 50 cycles as thick as the one observed after 150h of isothermal exposure. Also, thick cracks have developed near the interface between the bond coating and the ceramic. After 250 cycles, delamination of the ceramic coating occurred and huge cracks going through the whole thickness were found.

Fig. 9a and 9b show the oxide scale developed at the interface between the bond coating and the YSZ of the samples after, respectively, 50 h of isothermal exposure and 50 cycles. In

both cases, a complex oxide layer (Ni, Cr, Al were detected via EDS) can be observed on top of an alumina scale. However, while a thick alumina scale is observed for the isothermally aged samples, the one of the cycled samples is rather thin and discontinuous.

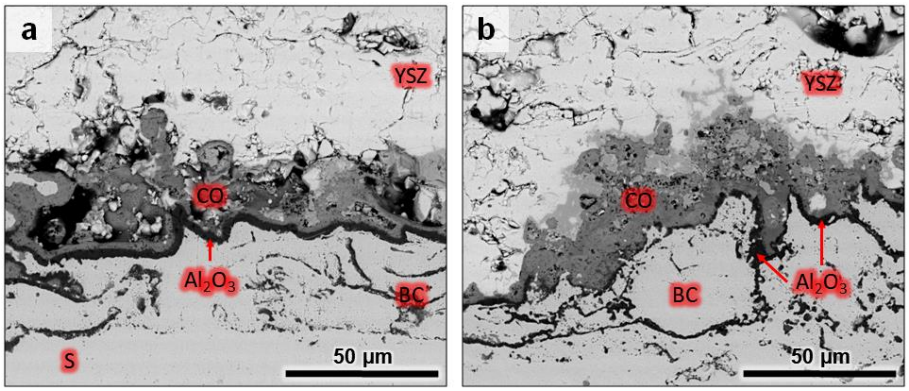

NB: YSZ = ceramic; BC = bond coating; S = substrate; CO= complex (Ni, Cr, Al) oxides;

Figure 9 *– SEM cross-section at the interface between the bond and ceramic coatings after exposure at 1100°C in air for (a) 150h in isothermal conditions and (b) 100 1-hour cycles.*

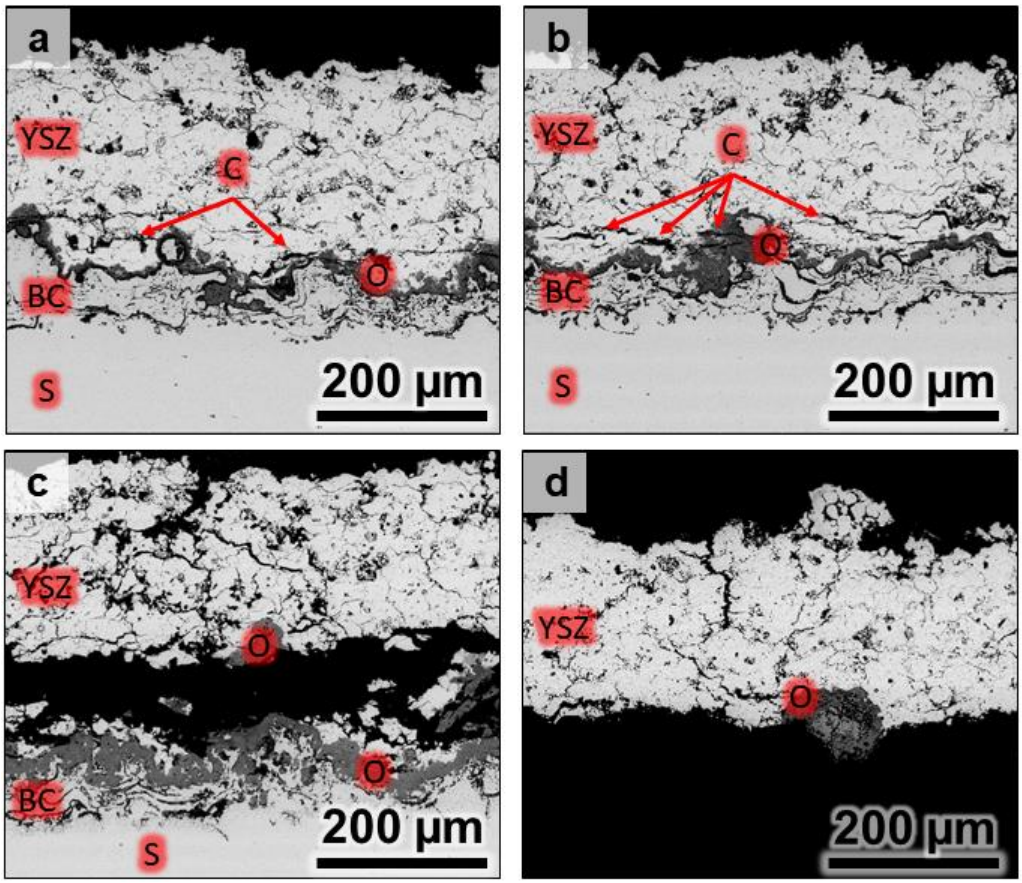

NB: YSZ = ceramic; BC = bond coating; S = substrate; O= oxides; OGB = oxidized grain boundaries; C= cracks

Figure 10 *- SEM micrographs of the cross-sections of the IN_APS samples after cyclic exposure (1h-cycles at 1100°C in air) for (a) 50, (b) 150, (c) 250 and (d) 500 h.*

The self-standing ceramic coatings were also isothermally exposed to 1100°C to substantiate their contribution to the thermal transport properties in the whole system. Fig. 11a gathers the lamellar and coarse porosities as a function of ageing condition while Fig. 11b displays the evolution of the relative lamellar porosity of the full systems and of the self-standing coatings with exposure time. The evolution of the total porosity could not be clearly defined due to significant variations of the coarse porosity levels. However, the lamellar porosity clearly decreased with exposure time at 1100°C irrespective of the isothermal or cyclic regime. The drop is more marked upon the first 100 h of exposure, then it tends to slow down to reach about 25 % and 30 % less lamellar porosity, compared to the initial coatings, after 500 h of isothermal and cyclic exposures, respectively. Sintering is more pronounced in the thermally cycled samples than in the isothermally exposed ones. The evolution of porosity of the self-standing coating with isothermal exposure is, however, not very even.

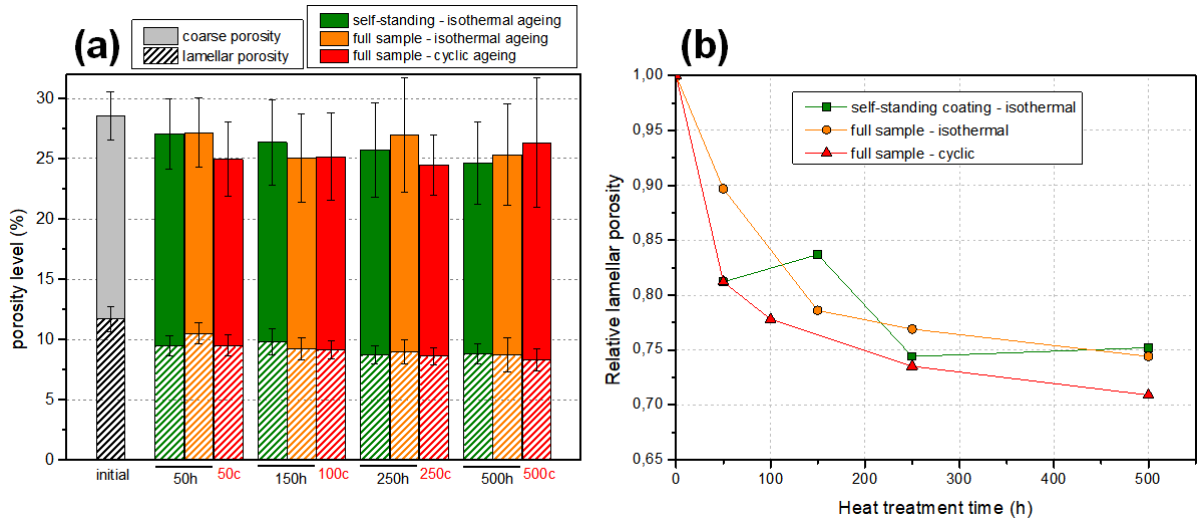

Figure 11 *– (a) Porosity levels measured for isothermally and cyclically aged IN_APS samples and (b) the associated relative lamellar porosity as a function of heat treatment time.*

3.3.2. Thermal diffusivity

Fig. 12 shows the evolution with temperature of the thermal diffusivity of the self-standing coatings in the as-deposited condition and after ageing at 1100°C for different times. At every temperature, all the aged coatings exhibit thermal diffusivities much greater than the as-deposited ones. With increasing ageing, the self-standing coatings exhibited slightly lower thermal diffusivity values than those observed after 50 h of exposure. This can be clearly observed (Fig. 13) when plotting the evolution of the relative thermal diffusivity with ageing time. The thermal diffusivity approximately increases of 40 % between the as-deposited and

the 50-h aged coatings. Then, the diffusivity slightly increases till 150h, drops (250 h) and finally stabilizes (500 h). The difference of thermal diffusivity between the as-deposited and the aged coatings tends to decrease at high temperature (above 800°C).

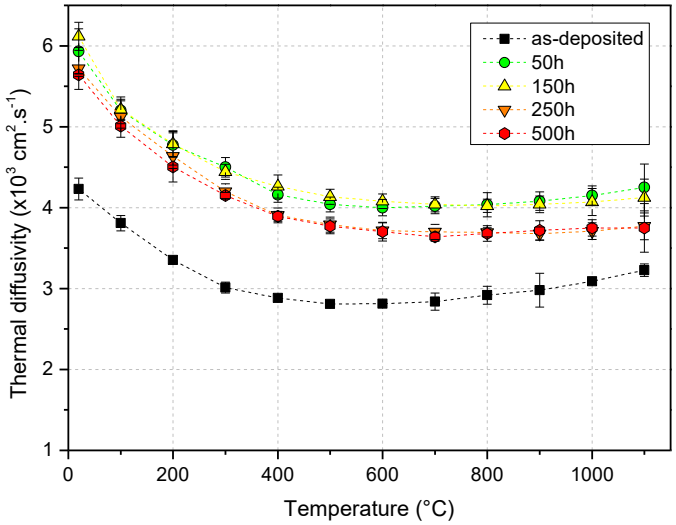

Figure 12 *– Thermal diffusivity as a function of the temperature for the self-standing coatings before and after isothermal ageing at 1100°C.*

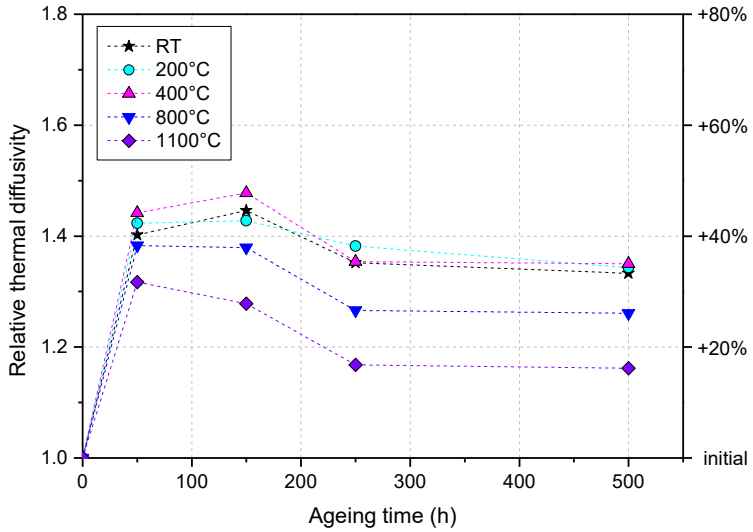

Figure 13 *– Relative thermal diffusivity as a function of heat treatment time for the isothermally aged freestanding coatings for different measurement temperatures.*

The evolution of thermal diffusivity of the as-deposited and the aged full TBCs with temperature is shown on Fig. 14. Like with the self-standing coatings and irrespective of the temperature of measurement, the thermal diffusivity increases between the as-deposited and the aged coatings, in particular under isothermal exposures. However, the full TBCs exhibit lower thermal diffusivity values (~3.10^{-3} cm^{2}.s^{-1}) than the self-standing coatings (~4.10^{-3} cm^{2}.s^{-1}). The thermal diffusivity values are greater for the coatings aged under cyclic conditions than for the

as-deposited ones but are lower than the ones for isothermally oxidized coatings. Also, the cycled coatings exhibit similar values either after 50 cycles or 100 cycles.

The rise of thermal diffusivity with isothermal ageing time is also depicted in Fig. 15. At 1100°C the thermal diffusivity reaches a maximum of approximately 40 %, which represents twice the increase observed for the self-standing coating at the same temperature. However, when measured at room temperature, the thermal diffusivity reaches an increase of 70 % after 500 h of isothermal exposure.

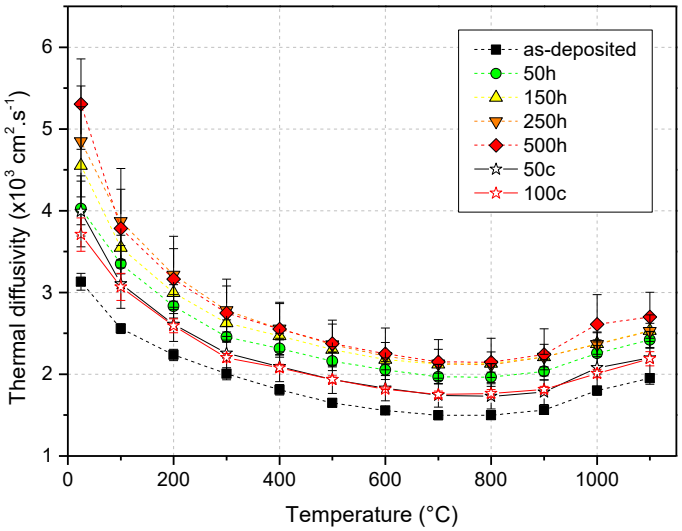

Figure 14 *- Thermal diffusivity as a function of temperature of the full TBC systems on IN_APS samples before and after ageing at 1100°C in air under isothermal and cyclic conditions.*

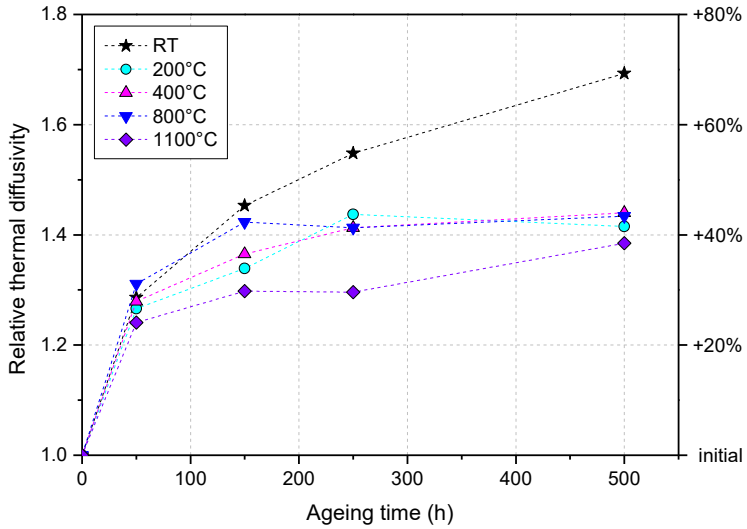

Figure 15 *- Relative thermal diffusivity as a function of heat treatment time for the isothermally aged full TBC systems on IN_APS samples for different measurement temperatures.*

4. Discussion

4.1. Effect of starting microstructure on thermal transport properties

The microstructures of the as-deposited ceramic coatings elaborated by the same manufacturer and with the same "standard" designation (AM1_APS1, AM1_APS2 and DFL_APS) exhibit significant differences. This can be related to the APS parameters for which small variations have been demonstrated to vary the coarse and lamellar porosities [15, 17, 18, 23]. In the one hand, harsh spray parameters increase the number of stacking faults between the splats, resulting in the growth of the coarse porosity level (e.g. IN_APS samples exhibit a coarse porosity level equal to the half of its total porosity). On the other hand, a good combination of the parameters leads to the building of thin splats that hence raise the concentration of inter-lamellar interfaces through the whole coating (e.g. DFL_APS which lamellar porosity level represents more than 75 % of its total porosity). Regarding the literature, the different measured levels of total porosity of plasma-sprayed coatings are in agreement with the one observed in this work. However, due to differences in the criterion that differentiate globular voids and lamellar pores, the lamellar levels in this work (~12-15%) are quite higher than the one found in the literature (~7-8%) [26, 27]. One shall note that the levels of porosity may depend on the image threshold limit fixed by the operator as well as the discrimination criteria used to separate the different types pores. Thus, the given values must be considered carefully when trying to compare with the ones found in the literature. In addition, inclusions of metallic impurities (that may result from the removal of the upper MCrAlY splats of the bond coat upon collision of the YSZ particles) have been found in some ceramic coatings (especially in IN_APS coatings). Therefore the coarse porosity level of polluted coatings may be slightly overestimated as such impurities may be included in the calculation.

Interlamellar pores are reported in the literature as the major microstructural feature that reduces the thermal transport properties of PS TBCs. Indeed, Lu and coll. showed via finite element model that splat interfaces were responsible for ~45 % of the reduction of the thermal conductivity in through-thickness direction while pores were responsible for ~24 % [28]. Experimental studies also showed a linear relationship between porosity and thermal conductivity [25, 29]. A similar dependence between thermal diffusivity and lamellar porosity was found in this study (Fig. 7). However, this linearity is only observed because the microstructures of the coatings studied are similar, other studies demonstrated that when different porosity range and aspect are considered, the linearity could not be observed [25].

When looking at models for thermal diffusivity estimation, the relation between the microstructure and the heat transport properties is significantly more complex and do take into account the orientation and shape factors, e.g. Bruggeman model [26, 30]. Therefore, the slight variations to the linearity of the different coatings could also be explained by the fact that the porosity levels in this study did not consider those details. Also, the impact of lamellar porosity on the thermal diffusivity of the coatings is more pronounced at room temperature than at 1100°C. This can be explained by the fact that, when temperature increases, the impact of the scattering by the micro-defects becomes less significant, hence leading to the flattening of the evolution at 1100°C [2, 7].

Moreover, the fact that the AM1_APSmf microcracked coatings exhibit thermal diffusivities slightly above the observed trend may be attributed to the very low level of coarse porosity, as it was shown that larger pores also have an impact on the reduction of thermal transport. In addition, the inter-lamellar interfaces of the "micro-cracked" coating are thinner than the ones of other standard coatings (see Fig. 1), which would lead to a better contact between the splats and hence to a relatively higher heat conduction through the ceramic.

However, although CC_APS coating exhibits lamellar and coarse porosity levels similar to that of the as-deposited AM1_APS1 and AM1_APS2 coatings, its thermal diffusivity is slightly above the expected trend. This means that the transformations that occurred upon ageing are to be considered in addition to the porosity, which will be discussed in the next section.

4.2. Effect of ageing

4.2.1. Effect of impurities in the ceramic coating

The degradation of the ceramic YSZ coating may be responsible for the high thermal diffusivity values of the engine-run CC_APS samples displayed in Fig. 6. Since the level of lamellar and coarse porosity is equivalent between the as-received and the engine-run coatings, the increase of thermal diffusivity can be ascribed to the impurities observed in Fig. 5. On the one hand, the mixed Ni, Al and Cr oxides of (Fig. 5a), resulting from the oxidation of the bond coat particles incorporated in the ceramic coating, are believed to fill in gaps and pores of the YSZ coating. On the other hand, the corroded zone (Fig. 5b) associated with the siliceous composition identified by EDS and the full monoclinic phase identified via Raman (Table 2) indicates that CMAS (calcium, magnesium, aluminum silicates) corrosion occurred. This phenomenon starts at temperatures above 1200°C and leads to a destabilization of the YSZ

material via a dissolution-reprecipitation process [31-33] which usually comes with the sintering of the surrounding porous network. The destabilization of the so-called non-transformable tetragonal phase of the YSZ material results in the formation of a mix of Y-depleted monoclinic phased zirconia together with an amorphous Y-enriched siliceous glass. The monoclinic phase of zirconia has a higher thermal conductivity (5.4 $W.m^{-1}.K^{-1}$) than its tetragonal counterpart (2.8 $W.m^{-1}.K^{-1}$) [34]. Therefore, the combination of the YSZ transformation with local sintering of the coating due to the glassy melt can also contribute to the observed increase of heat transport. Compared to the oxide impurities, the CMAS corrosion mechanism may be the main factor leading to the high values of thermal diffusivity observed for CC_APS samples. This hypothesis might be in agreement with the work of Levi and coll. who showed that fully CMAS infiltrated PS YSZ TBCs exhibit about 110 % increase of the thermal conductivity compared to the initial coating [35, 36].

4.2.2. Sintering and bond coating oxidation

The evolution of microstructure in the free-standing YSZ and full TBCs differs with the annealing conditions (isothermal and cyclic exposure) in air at 1100°C. Compared to the as-received conditions, the free-standing coatings developed many cracks associated with the thermal shocks when the samples were removed from the isothermal hot furnace. Although such cracks may contribute to the experimental error in the determination of the porosity, it clearly appeared that sintering of the pores upon the first exposure times had a predominant effect in the decrease of the relative lamellar porosity (Fig. 11).

The ageing of the full TBC systems resulted in the significant oxidation of the bond coating material to form a complex oxide scale (Fig. 9) as well as in the formation of multiple cracks parallel to the surface near the bond coating interface (Figs. 8 and 10). The formation of such oxide scale is well-described by Hu et al. who showed that Al_2O_3, $Y_3Al_5O_{12}$ (YAG), $NiCr_2O_4$ and NiO were successively formed at the YSZ/NiCrAlY interface at 1050°C in air [37]. Moreover, the formation of the cracks that led to spallation of the YSZ coating (Fig. 10) was also reported when TBC systems with HVOF bond coatings were aged under similar cyclic exposure at 1100°C [18]. This failure mechanism was described by Evans and was observed for similar rough and wavy surfaces of the bond coatings [38]. Moreover, the drop of the lamellar porosity that is more pronounced in the cycled samples than in the isothermally aged ones (Fig. 11) was ascribed to compression stresses generated upon cycling that accelerate the rates of sintering and stiffening [39, 40]. Despite the different microstructural evolution with

the two types of ageing on the full and self-standing coatings, the decrease of the lamellar porosity is initially sharper then tends to decrease with the annealing time (Fig. 11). This behavior is well-known for PS-YSZ ceramics and is related to the closure of interlamellar pores and cracks, healing of intra-splats micro-cracks and transformation of cracks into globular pores [34, 41-44].

The ageing at such high temperature usually provokes necking and connections are formed between the splats, enhancing the heat flow via bridge funneling from splat to splat that should result in increased thermal diffusivity [7]. This is indeed observed in our self-standing (Fig. 13) and full TBCs (Fig. 15). The resulting ~40% increase in the relative thermal diffusivity of both types of coatings was also presented by Cernushi et al. with an equivalent 40.3% relative thermal diffusivity increase for laser-flash measurements at 200°C of thick PS YSZ self-standing coatings after isothermal exposure at 1100°C in air for 94h [16]. Similar raises in thermal conductivity were observed in previous works for PS YSZ self-standing coatings aged in the same conditions [17, 25]. The increase of thermal diffusivity is lower for the cycled full TBC samples than for the isothermally aged samples (see Fig. 14) despite the fewer lamellar porosity in the former (Fig. 11). As indicated above, cycling introduces competitive oxidation and cracking [18, 38] with sintering [39, 40]. The thick cracks (see Fig. 9) may contribute to reduce the thermal conductivity by generating new pores in which gas conduction will lead heat transport [7], while a thick oxide scale may add significant thermal transport resistance because the thermal conductivity of the oxides is much lower than that of the MCrAlY bond coat [45, 46] and the pores or micro-cracks in the oxide layer perpendicular to the heat flow further reduce the heat transport. However, the oxide scale was not computed for the calculation of the thermal diffusivity in the multilayer model. Consequently, the thermal diffusivity values of the cycled samples may be underestimated compared to the isothermally aged ones whose oxide layer was thinner and displayed less cracks. However, the role of the TGO may be disregarded when considering the similar increasing trend of the thermal diffusivity with annealing time of the self-standing coatings and the full TBCs. Indeed, there was barely any oxidation in the former and only the competitive cracking and sintering of the ceramic can be responsible for such evolution of the thermal diffusivity.

4.3. Crossed comparison of thermal diffusivity results

Significant differences have been observed between the thermal diffusivity values of the self-standing coatings and those of the full TBCs (Figs. 12 and 14). The self-standing coatings

possess about 30 % higher values of thermal diffusivity than the coatings of the full TBC systems. In addition, the evolution of thermal diffusivity with annealing time and temperature of the laser-flash measurement differs between the two types of coatings (Figs. 13 and 15). At room temperature, the thermal conductivity of the full TBCs tended to increase continuously with time while it increased and then stabilized in the free-standing ceramic coatings. Similar phenomena occurred for the high temperature aged coatings but the differences with respect ageing time were less marked. Since the thermal diffusivity of the substrate was not modified with the annealing time and temperature (see 2.3), the reasons for the differences in increased thermal diffusivity can be explained on the basis of different aspects including the evolution of main defects (pores and cracks), oxidation and the inherent method of laser flash. The effects of the defects and of oxidation have been discussed above. As for the laser-flash method, it is known that the thin ceramic coatings are more subject to deviations due to radiation, whereas thicker samples are more subject to heat loss effects [47], which also contribute to the difference of thermal diffusivity between the free-standing and the full TBCs.

5. Conclusions

The effect of the microstructure of the insulating ceramic, as well as the role of the transformations that plasma-sprayed thermal barrier coating systems can endure through ageing, have been correlated with the changes in thermal transport properties through the measurement of thermal diffusivity by the laser-flash technique. Thin cracks and lamellar porosities were confirmed to be the main contributors to the reduction of thermal conduction in studied coatings. Nevertheless, the role of coarse porosity was also shown to be significant regarding the “micro-cracked” coating and the effect of cracks in the case of cycled samples. The transformations related to CMAS corrosion found in the aged coatings of the combustion chamber also increased the thermal diffusivity.

Sintering of the coatings during thermal exposure (ageing and laser flash measurements) was also confirmed to reduce the lamellar porosity rate, hence leading to an increase in heat conduction. However, due to the oxidation of the bond coating and the formation of cracks, a compensation of the sintering effect was observed when studying the complete thermal barrier coating system through multilayer calculation of the thermal diffusivity.

ACKNOWLEDGEMENTS

The authors gratefully acknowledge Safran Aircraft Engines (France) & SR Technics Airfoils Services, Ltd. (Ireland) for providing the samples of this study. Part of this work was funded by the Région Poitou-Charentes.

REFERENCES

1. R. McPherson, *A Model for the Thermal Conductivity of Plasma-Sprayed Ceramic Coatings*, Thin Solid Films 112 (1984) 89-95.
2. L. Pawlowski and P. Fauchais, *Thermal Transport Properties of Thermally Sprayed Coating*, International Materials Reviews 37[6] (1992) 271-289.
3. F. Cernuschi, P. Bianchi, M. Leoni, and P. Scardi, *Thermal Diffusivity/Microstructure Relationship in Y-PSZ Thermal Barrier Coatings*, Journal of Thermal Spray Technology 8[1] (1999) 102-109.
4. I.O. Golosnoy, S.A. Tsipas, and T.W. Clyne, *An Analytical Model for Simulation of Heat Flow in Plasma Sprayed Thermal Barrier Coatings*, Journal of Thermal Spray Technology 14[2] (2005) 205-214.
5. S. Raghavan, H. Wang, R.B. Dinwiddie, W.D. Porter, and M.J. Mayo, *The Effect of Grain Size, Porosity and Yttria Content on the Thermal Conductivity of Nanocrystalline Zirconia*, Scripta Materiala 39[8] (1998) 1119-1125.
6. D. Zhu, N.P. Bansal, K.N. Lee, and R.A. Miller, *Thermal Conductivity of Ceramic Thermal Barrier and Environmental Barrier Coating Materials*, NASA TM-2001-211122, NASA Lewis Research Center, Cleveland, OH, (2001).
7. I.O. Golosnoy, A. Cipitria, and T.W. Clyne, *Heat Transfer Through Plasma-Sprayed Thermal Barrier Coatings in Gas Turbines: A Review of Recent Work*, Journal of Thermal Spray Technology 18[5-6] (2009) 809-821.
8. L.B. Loeb, *The Kinetic Theory of Gases*, McGraw-Hill, New York, (1934).
9. R. Mevrel, J.-C. Laizet, A. Azzopardi, B. Leclercq, M. Poulain, O. Lavigne, and D. Demange, *Thermal Diffusivity and Conductivity of* $Zr_{1-x}Y_xO_{2-x/2}$ *(x = 0, 0.084 and 0.179) Single Crystals*, Journal of the European Ceramic Society 24 (2004) 3081-3089.
10. A. Kulkarni, S. Sampath, A. Goland, H. Herman, and B. Dowd, *Computed microtomography studies to characterize microstructure-property correlations in thermal sprayed alumina deposits*, Scripta Materiala 43 (2000) 471-476.

11. A. Kulkarni, Z. Wang, T. Nakamura, S. Sampath, A. Goland, H. Herman, J. Allen, J. Ilavsky, G. Long, J. Frahm, and R.W. Steinbrech, *Comprehensive microstructural characterization and predictive property modeling of plasma-sprayed zirconia coatings*, Acta Materiala 51 (2003) 2457-2475.
12. S. Deshpande, A. Kulkarni, S. Sampath, and H. Herman, *Application of image analysis for characterization of porosity in thermal spray coatings and correlation with small angle neutron scattering*, Surface and Coating Technology 187 (2004) 6-16.
13. D. B. Fowler, W. Rigg, and J.C. Russ, *Inspecting thermal sprayed coatings*, Advanced Material Processing 11 (1990) 41-52.
14. Y. Zhao, A. Shinmi, X.Zhao, P.J. Withers, S. Van Boxel, N. Markocsan, P. Nylen, and P. Xiao, *Investigation of interfacial properties of atmospheric plasma sprayed thermal barrier coatings with four-point bending and computed tomography technique*, Surface and Coating Technology 206 (2012) 4922-4929.
15. Y. Tan, V. Srinivasan, T. Nakamura, S. Sampath, and P. Bertrand, *Optimizing Compliance and Thermal Conductivity of Plasma Sprayed Thermal Barrier Coatings via Controlled Powders and Processing Strategies*, Journal of Thermal Spray Technology 21[5] (2012) 950-962.
16. F. Cernushi, L. Lorenzoni, S. Ahmaniemi, P. Vuoristo, and T. Mäntylä, *Studies of the sintering kinetics of thick thermal barrier coatings by thermal diffusivity measurements*, Journal of European Ceramic Society 25 (2005) 393-400.
17. Y. Tan, J.P. Longtin, and S. Sampath, *Effect of the Starting Microstructure on the Thermal Properties of As-Sprayed and Thermally Exposed Plasma-Sprayed YSZ Coatings*, Journal of the American Ceramic Society 92[3] (2009) 710-716.
18. N. Curry, N. Markocsan, L. Ostergren, X-H. Li, and M. Dorfman, *Evaluation of the Lifetime and Thermal Conductivity of Dysprosia-Stabilized Thermal Barrier Coating Systems*, Journal of Thermal Spray Technology 22[6] (2013) 864-872.
19. R.A. Miller, J.L. Smialek, and R.G. Garlic, *Phase stability in plasma-sprayed, partially stabilized zirconia-yttria*, Journal of the American Ceramic Society 3 (1981) 241-254.
20. K. Bobzin, N. Bagcivan, D. Parkot, M. Schäfer, and I. Petkovic, *Modeling and simulation of microstructure formation for porosity prediction in thermal barrier coatings under air plasma spraying condition*, Journal of Thermal Spray Technology 18[5-6] (2009) 975-980.

21. F. Cernuschi, P.G. Bison, S. Martinetti, and P. Scardi, *Thermophysical, mechanical and microstructural characterization of aged free-standing plasma sprayed zirconia coatings*, Acta Materiala 56 (2008) 4477-4488.
22. Y. Tan, J. P. Longtin, and S. Sampath, *Modeling Thermal Conductivity of Thermal Spray Coatings: Comparing Predictions to Experiments*, Journal of Thermal Spray Technology 15[4] (2006) 545-552.
23. H.-J. Rätzer-Scheibe, U. Schulz, *The effects of heat treatment and gas atmosphere on the thermal conductivity of APS and EB-PVD PYSZ thermal barrier coatings*, Surface & Coatings Technology 201 (2007) 7880-7888.
24. C.M. Ramos, A.S. Tabata, P.F. Cesar, J.H. Rubo, P.A. Silveira Fracisconi, and A.F. Sanches Borges, *Application of Micro-Raman Spectroscopy to the Study of Yttria-Stabilized Tetragonal Zirconia Polycrystal (Y-TZP) Phase Transformation*, Applied Spectroscopy 69[7] (2015) 810-814.
25. W. Chi, S. Sampath, and H. Wang, *Microstructure-Thermal Conductivity Relationships for Plasma-Sprayed Yttria-Stabilized Zirconia Coatings*, Journal of the American Ceramic Society 91[8] (2008) 2636-2645.
26. F. Cernuschi, I.G. Golosnoy, P. Bison, A. Moscatelli, R. Vassen, H-P Bossmann, and S. Capelli, *Microstructural Characterization of Porous Thermal Barrier Coatings by IR gas porosimetry and sintering forecasts*, Acta Materiala 61 (2013) 248-262.
27. F. Cernuschi, P. Bison, D.E. Mack, M. Merlini, S. Boldrini, S. Marchionna, S. Capelli, S. Concari, A.Famengo, A. Moscatelli and W. Stamm, *Thermo-physical properties of as deposited and aged Thermal Barrier Coatings (TBC) for Gas turbines: state-of-the art and advanced TBCs*, Journal of the European Ceramic Society 38[11] (2018) 3945-3961.
28. L. Lu, F-C. Wang, Z. Ma, and Q-B. Fan, *Anisotropic effect of splat interface on thermal conductivity of plasma sprayed YSZ coating*, Surface & Coatings Technology 235 (2013) 596-602.
29. K. Torkashvand, E. Poursaeidi, and J. Ghazanfarian, *Experimental and numerical study of thermal conductivity of plasma-sprayed thermal barrier coatings with random distributions of pores*, Applied Thermal Engineering 137 (2018) 494-503.
30. B. Schulz, *Thermal conductivity of porous and highly porous materials*, High Temperatures - High Pressures 13[6] (1981) 649-660.

31. C.G. Levi, J.W. Hutchinson, M-H. Vidal Sétif, and C.A. Johnson, *Environmental degradation of thermal-barrier coatings by molten deposits*, MRS Bulletin 37 (2012) 932-940.
32. F.H. Stott, D.J. de Wet, and R.Taylor, *Degradation of thermal-barrier coatings at very high temperatures*, MRS Bulletin (1994) 46-49.
33. S. Krämer, J. Yang, and C.G. Levi, *Thermochemical interaction of thermal barrier coatings with molten CaO-MgO-Al2O3-SiO2 (CMAS) deposits*, Journal of the American Ceramic Society 89[10] (2006) 3167-3175.
34. R.W. Trice, Y. Jennifer Su, J.R. Mawdsley, K.T. Faber, A.R. De Arellano-Lopez, H.Wang, and W.D. Porter, *Effect of heat treatment on phase stability, microstructure, and thermal conductivity of plasma-sprayed YSZ*, Journal of Materials Science 37 (2002) 2359-2365.
35. T.R. Kakuda, C.G. Levi, and T.D. Bennett, *The thermal behavior of CMAS-infiltrated thermal barrier coatings*, Surface & Coatings Technology 201 (2007) 7880-7888.
36. J. Wu, H. Guo, Y. Gao, and S. Gong, *Microstructure and thermo-physical properties of yttria stabilized zirconia coatings with CMAS deposits*, Journal of the European Ceramic Society 31 (2011) 1881-1888.
37. Y. Hua, C. Caia, Y. Wanga, H. Yuc, Y. Zhoua, and G. Zhou, *YSZ/NiCrAlY interface oxidation of APS thermal barrier coatings*, Corrosion Science (2018) https://doi.org/10.1016/j.corsci.2018.06.035.
38. H.E. Evans, *Oxidation Failure of TBC Systems: An Assessment of Mechanisms*, Surface and Coating Technology 206[7] (2011) 1512-1521.
39. J.A. Thompson and T.W. Clyne, *The Effect of Heat Treatment on the Stiffness of Zirconia Top Coats in Plasma-Sprayed TBCs*, Acta Materiala 49 (2001) 1565-1575.
40. S.A. Tsipas, I. O. Golosnoy, T. W. Clyne, and R. Damani, *The Effect of a High Thermal Gradient on Sintering and Stiffening in the Top Coat of a Thermal Barrier Coating System*, Journal of Thermal Spray Technology 13[3] (2004) 370-376.
41. J. Ilavsky, G.G. Long, A.J. Allen, and C.C. Berndt, *Evolution of the Void Structure in Plasma-Sprayed YSZ Deposits During Heating*, Materials Science and Engineering A 272[1] (1999) 215-221.
42. A.J. Allen, J. Ilavsky, G.G. Long, J.S. Wallace, C.C. Berndt, and H. Herman, *Microstructural Characterization of Yttria-stabilized Zirconia Plasma-Sprayed Deposits Using Multiple Small-Angle Neutron Scattering*, Acta materiala 49 (2001) 1661-1675.

43. P.S. Anderson, X. Wang, and P. Xiao, *Effect of Isothermal Heat Treatment on Plasma-Sprayed Yttria-Stabilized Zirconia Studied by Impedance Spectroscopy*, Journal of the American Ceramic Society 88[2] (2005) 324-330.
44. S. Paul, A. Cipitria, I.O. Golosnoy, L. Xie, M.R. Dorfman, and T.W. Clyne, *Effects of Impurity Content on the Sintering Characteristics of Plasma-Sprayed Zirconia*, Journal of Thermal Spray Technology 16[5-6] (2007) 798-803.
45. W.D. Kingery, J. Francl, R.L. Coble, and T. Vasilos, *Thermal Conductivity: X, Data for Several Pure Oxide Materials Corrected to Zero Porosity*, Journal of the American Ceramic Society 37[2] (1954) 107-110.
46. G. Moskal and A. Jasik, *Thermal Diffusivity Characterization of Bond-Coat Materials Used for Thermal Barrier Coatings*, Journal of Thermal Analysis and Calorimetry 126 (2016) 9-17.
47. ASTM standard E1461 - 13, 2013, *Standard Test Method for Thermal Diffusivity by the Flash Method*, ASTM international, West Conshohocken, PA, DOI: 10.1520/E1461-13.

3. Article 2: *Thermal insulation of CMAS (Calcium-Magnesium-Alumino-Silicates)- attacked plasma-sprayed thermal barrier coatings*

Thermal insulation of CMAS (Calcium-Magnesium-Alumino-Silicates)-attacked plasma-sprayed thermal barrier coatings

G. Boissonnet*[1], C. Chalk[2], J. Nicholls[2], G. Bonnet[1], F. Pedraza[1]

1. Université de La Rochelle, Laboratoire des Sciences de l'Ingénieur pour l'Environnement (LaSIE UMR-7356 CNRS), Avenue Michel Crépeau, 17042 La Rochelle, cedex 01 – France.

2. Cranfield University, Surface Engineering and Nanotechnology Institute (SENTi), College Rd, Wharley End, Bedford MK43 0AL – United Kingdom.

*corresponding author: boissonnet.germain@gmail.com

Abstract. The impact of the penetration of small quantities of calcium-magnesium-aluminium silicates (CMAS) glassy melt in the porous plasma-sprayed (PS) thermal barrier coatings (TBCs) is often neglected even though it might play a non-negligible role on the sintering and hence on the thermal insulation potential of TBCs. In this study, the sintering potential of small CMAS deposits (from 0.25 to 3 mg.cm^{-2}) on freestanding yttria-stabilized zirconia (YSZ) PS TBCs annealed at 1250°C for 1 h was investigated. The results showed a gradual in-depth sintering with increasing CMAS deposits. This sintering was concomitant with local transformations of the tetragonal YSZ and resulted in an increase in the thermal diffusivity of the coatings that reached a maximum of ~110 % for the fully penetrated coating.

1. Introduction

Among the different sources of identified failures of yttria-stabilized zirconia (YSZ) -based thermal barrier coatings (TBCs) of fuel-fired engines [1], the infiltration of siliceous molten deposits, also known as Calcium-Magnesium-Alumino-Silicates (CMAS) is of growing concern [2]. In the hot-gas path and at peak temperatures, CMAS deposits yields a glassy melt that can penetrate the porous structure of ceramic coatings due to their low viscosity [3, 4]. Infiltration of the CMAS melt in the void spaces of the coating leads to sintering of this porous structure. Sintering of the ceramic is known to reduce the TBC mechanical performances [5, 6, 7] but may also contribute to a decrease in thermal resistance due to the loss of phonon-scattering defects, i.e. microcracks or lamellar interspaces of plasma sprayed TBCs [8, 9, 10].

However, only few studies proved this CMAS-sintering to result in a decline of the insulation capacity of TBCs [11, 12]. In addition to sintering, the penetrated melt can chemically attack the insulating oxide through a dissolution-reprecipitation mechanism that induces the destabilization of the t' phase desirable for toughness [13, 14]. Such destabilization results from depletion of Y in the ceramic matrix, which may generate an increase in heat transport since the thermal conductivity of YSZ is dependent of the Y content [15].

The low-melting temperature of these silicate deposits (around 1200°C [2]) is therefore becoming a fundamental barrier to the increase of the gas temperature and reduction of fuel consumption, hence on the engine efficiency. Thus, a full understanding of the impact that CMAS can exert on the insulating properties of TBCs is of crucial importance.

Kakuda et al. investigated the effect of amorphous CMAS infiltration on the thermal properties and heat transport of plasma-sprayed (APS) coatings using photothermal emission analysis (PopTea) and observed a rise in both volumetric heat capacity and thermal conductivity of the coating upon infiltration [12]. However, the study focused only on a fully-infiltrated coating using an excess of one composition of CMAS. Previous studies have demonstrated the importance of the CMAS composition on the characteristics and severity of the attack due to the basicity of the oxide melt [16]. For instance, the presence of iron oxide Fe_2O_3 led to a decrease of the melting point via the formation of eutectics [17], hence reducing the viscosity of the melt, which in turn induced a faster penetration of the CMAS [18].

Therefore, this investigation intended to shed light on the influence of the amount of CMAS on the thermal conductivity of YSZ TBCs. The study focused on finding the onset quantity of CMAS likely to induce enough changes to alter the thermal conductivity of the coatings. Small amounts of CMAS were deposited on the surface of plasma-sprayed coatings followed with a high temperature heat treatment for infiltration to occur. Laser-flash analysis (LFA), differential scanning calorimetry (DSC) and density measurements were conducted to measure the changes in the thermal properties of the coatings induced by CMAS infiltrations.

2. Experimental methods

The coatings considered in this study were produced by SR Technics Airfoil Services, Ltd. (Ireland) on Inconel 600 (15.5 Cr, 8.0 Fe, 0.5 Mn, < 0.5 Cu, < 0.5 Si, wt. %, bal. Ni) substrates. The thermal barrier coating systems comprised a ~300 µm plasma-sprayed YSZ coating

deposited on top of a ~70 µm plasma-sprayed NiCrAlY bond coating (***Figure 1***). The samples were prepared with a square shape (10 x 10 mm^2) for the laser flash measurements.

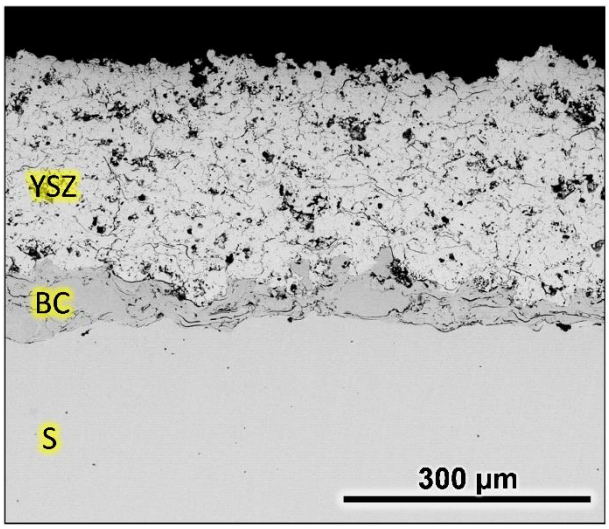

Figure 1 *– BSE micrographs of the as-deposited plasma-sprayed YSZ coating.*

The CMAS mixture, which composition is given in ***Table*** was used for the corrosion tests. This composition was drawn from previous studies conducted by Aygun et al. [124] and is close to the model CMAS composition used in other studies [2]. The individual oxide powders were mixed in deionized water to form a thick paste which was put into Pt-10Rh crucibles and heated a first time at 1400°C for 4 h. The resulting glassy melt was crushed in a mortar, re-melted for 4 h at 1400°C to improve the glass homogeneity and crushed again.

Table 1 *– Average composition of the model CMAS measured via EDS (mol. %).*

CaO	MgO	Al_2O_3	SiO_2	Fe_2O_3
36	6	5	52	1

The resulting powders were mixed with milliQ water to a 50/50 weight ratio before spraying on the samples using an air brush. The samples to coat were weighed using a 10^{-5} g precision balance prior to CMAS deposition. Then, the samples were pre-heated at 80°C to help the adhesion of the CMAS by evaporating the water once the spray in contact with the surface of the sample. Thus, short spray pulses were successively applied with intermediate re-heating and weighing of the samples till the desired mass of deposited CMAS was obtained.

First, tests were conducted to investigate the kinetics of penetration of the CMAS melt into the coatings. Therefore, thick deposits of ~20 mg.cm^{-2} were applied on the surface of plasma-sprayed TBC and different durations of heat treatment were investigated. The samples were placed in a furnace at room temperature and heated till 1250°C (above the melting point of the mixture as observed by DSC), and removed after 15 and 30 min, 1 and 2 h. ***Figure 2*** shows that after only 15 minutes, and despite a non-homogeneous front, the CMAS has almost sintered 200 µm of the YSZ coating (till the red line) by infiltration through the pores. Moreover, the CMAS melt started to saturate the TBC (blue region) through the dissolution of the YSZ material, hence resulting in the loss of the initial microstructure of the coating. Therefore, smaller quantities were investigated using the 1 h heat treatment to isolate the sintering effect of the CMAS from this type of exaggerated degradation.

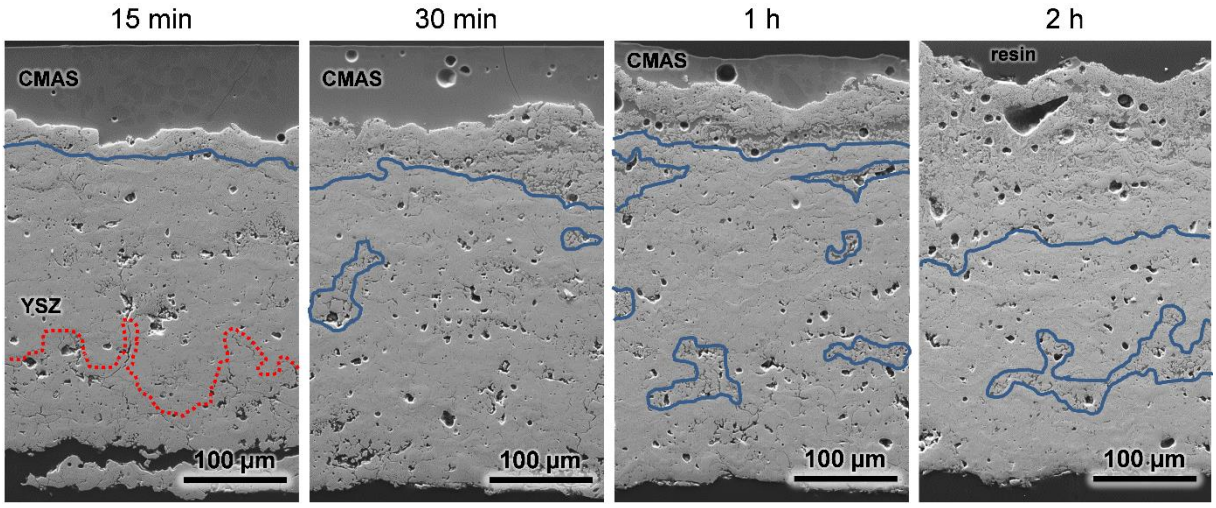

Figure 2 *– BSE micrographs of plasma-sprayed YSZ coatings annealed at 1250°C for different time with CMAS deposits of 20 mg.cm^{-2}.*

Freestanding coatings were used in this study to isolate their contribution to the heat transport from the whole system. The freestanding coatings were obtained by chemically dissolving the oxide interface between the bond coating and the YSZ TBC in a 20 vol. % HCl aqueous solution. CMAS deposits of 0.25, 0.50, 1 and 3 mg.cm^{-2} were applied on the freestanding coatings which were then placed in a muffle furnace pre-heated at 1250°C. After 1 h of annealing, the samples were removed from the furnace and quenched in air at room temperature.

The microstructural changes were investigated in polished cross-sections with a FEI Quanta 200F scanning electron microscope (SEM) coupled to an EDAX detector for local analysis of the composition using energy dispersive spectrometry (EDS). X-ray diffraction

(XRD, Brüker AXS D8 Advance) using the λ_{Cu} in θ-2θ mode and Raman micro-spectrometry (Jobin Yvon LabRam HR800, λ_{laser} ~632nm) were employed to follow the change in structure of the ceramic coatings, respectively, on the surface and on the cross-section of the coatings.

The phase structures were examined by X-ray diffraction technique using Rietveld refinement technique. The mole percentages of monoclinic phase M_m, tetragonal phase $M_{t'/t}$ and cubic phase M_c were obtained from the following equations [20]:

$$\frac{M_m}{M_{t'/t,c}} = 0.82\frac{I_m(\bar{1}11) + I_m(111)}{I_{t'/t,c}(111)} \quad (1)$$

$$\frac{M_c}{M_{t'/t}} = 0.88\frac{I_c(400)}{I_{t'/t}(400) + I_{t'/t}(004)} \quad (2)$$

Where $I_m(\bar{1}11)$ and $I_m(111)$ are the integral net intensities for monoclinic phase reflected from $(\bar{1}11)$ and (111) peaks; and $I_{t'/t,c}(111)$ is the intensity for tetragonal or cubic phase reflected from (111) plane. $I_c(400)$ is the intensity for cubic phase reflected from (400) plane. $I_{t'/t}(400)$ and $I_{t'/t}(004)$ are the intensities for tetragonal phase reflected from (400) and (004) plane, respectively.

To assess the evolution of the thermal insulation potential of the TBCs, thermal diffusivity was determined using high-temperature laser-flash measurements with a Linseis LFA1600 apparatus at low pressure (~1.10^{-2} mbar) every 100°C between room temperature and 1100°C. Three samples for the same deposited quantity of CMAS were analyzed with five separate laser shots per sample at each temperature step to increase the accuracy of the results.

The thicknesses of the multilayer samples were determined (±10^{-3} mm) with a digital caliper prior to the laser flash measurements. All samples were also coated on both sides with graphite (4-5 µm) to increase the absorption and the emissivity of the laser shot through the sample.

3. Results

3.1. Transformations due to CMAS penetration

3.1.1. With 20 mg.cm^{-2} deposits

Figure 2 shows the depth of penetration of the CMAS melt for different times of annealing at 1250°C. The CMAS melt penetrated quite rapidly with a non-homogeneous front into the porous network of the PS coatings as it was observed that after only 15 minutes, almost 200 µm were completely sintered (till the red line). Moreover, it is observed that significant transformations of the initial microstructure occurred by the appearance of round-shaped pores and CMAS-saturated zones (blue region).

The evolution of the different phases was evaluated at local scale by Raman spot analyses (***Figure 3***). The tetragonal (t+t') and the monoclinic phases of zirconia were unambiguously differentiated in the as-deposited and upon exposure to CMAS. While the distribution of the tetragonal phases is quite even across the coatings' thickness, the appearance of the monoclinic phase appears more random and more intense. However, the occurrence and intensity of the monoclinic doublets (175 and 200 cm^{-1} A_g vibrational modes) increase with exposure time, in particular in the upper zone of the coatings which is saturated with CMAS. This clearly indicates that either the amount or the time of exposure to CMAS may induce phase transformations of the YSZ.

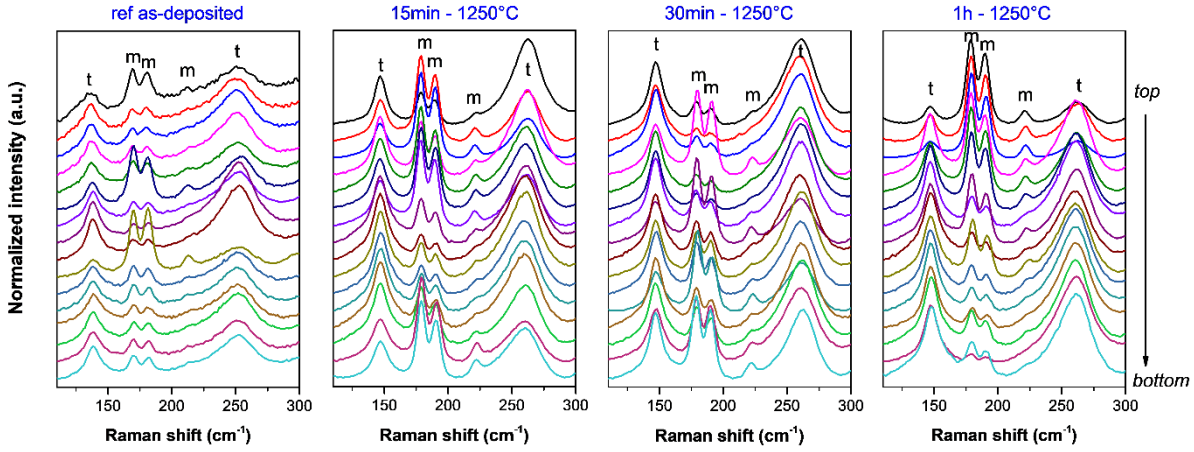

Figure 3 *– Raman local spot analysis of plasma-sprayed YSZ coatings annealed at 1250°C for different times with CMAS deposits of 20 mg.cm^{-2}.*

3.1.2. With 0.25, 0.50, 1 and 3 mg.cm^{-2}

Figure 4 shows the microstructure of the freestanding plasma sprayed coatings with CMAS deposits of 0.25, 0.5, 1 and 3 mg.cm^{-2} after annealing at 1250°C for 1h. With increasing the quantity of CMAS, the depth of the sintering of the porous microstructure increases (red line). The thin lamellar pores appear to be sintered to a depth of ~40, ~70, ~130 and ~250 µm (full depth) for, respectively, 0.25, 0.5, 1 and 3 mg.cm^{-2} of CMAS deposits. The thicker cracks and the "globular" pores remain the only porosity observed in the sintered zone affected by the CMAS. ***Figure 5*** shows details of the microstructure of the upper (***Figure 5***a) and lower (***Figure 5***b) zone of the plasma coating that have been transformed by a deposit of 1 mg.cm^{-2} of CMAS and annealed at 1250°C for 1 h. The microstructure of the upper part of the coating that has been exposed to the major part of the CMAS melt was completely transformed. This transformed zone appears as a mixture of round shaped grains surrounded by a darker phase that comprises small bright grains in a dark matrix. The EDS spot analyses in the dark phase allowed the identification of zirconia, which is slightly depleted in Y (~8 wt.% compared to the ~9 wt.% of the measurements made on the lower part of the coating, ***Figure 5***a), and an average of ~3 wt.% of the combined CMAS compounds. The round shaped grains were identified as zirconia with a slightly higher rate of Y (~10 wt.%). The microstructure below the red line is quite similar to the one of the as-deposited coating (***Figure 1***) and presents thin cracks and globular pores.

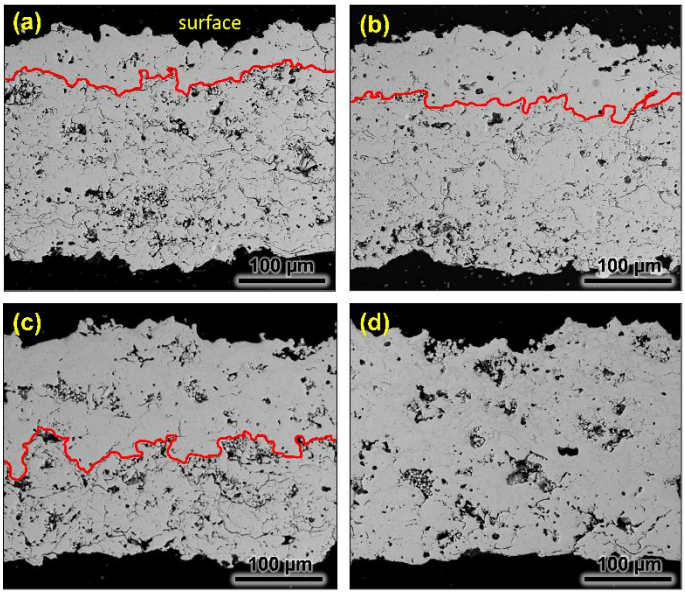

Figure 4 – *BSE micrographs of freestanding YSZ coatings annealed at 1250°C for 1h with CMAS deposits of* ***(a)*** *0.25,* ***(b)*** *0.50,* ***(c)*** *1.0 and* ***(d)*** *3.0 mg.cm^{-2}.*

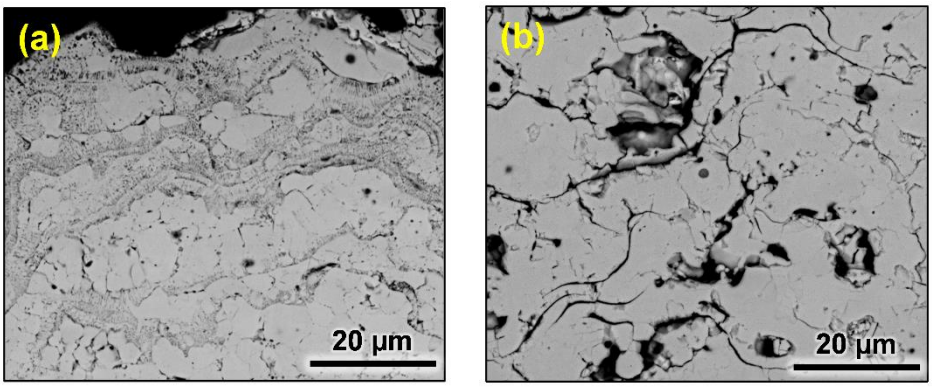

Figure 5 *– SEM micrographs showing the microstructural differences between* ***(a)*** *the CMAS affected zone above the red line (see* ***Figure 3****) and* ***(b)*** *the unaffected zone below the red line on the YSZ coating with CMAS deposit of 1 mg.cm^{-2} after annealing at 1250°C–1h.*

The penetration depth of CMAS elements in the coatings as a function of initial deposited mass is given in ***Figure 6***. These results show that the concentration of the CMAS elements into the coating decrease with increasing depth and that most of the CMAS is retained in the transformed zone above the red line of ***Figure 4***. Moreover, the greater the amount of CMAS deposited, the higher the concentration of the CMAS compounds. It can also be noted that the concentrations of Si and of Ca decrease more rapidly than the ones of Mg, Al and Fe with depth in the coating. This suggests that the CMAS viscosity is sufficiently low to allow the percolation through the coating and that Si and Ca are likely more reactive with YSZ than Mg, Al and Fe.

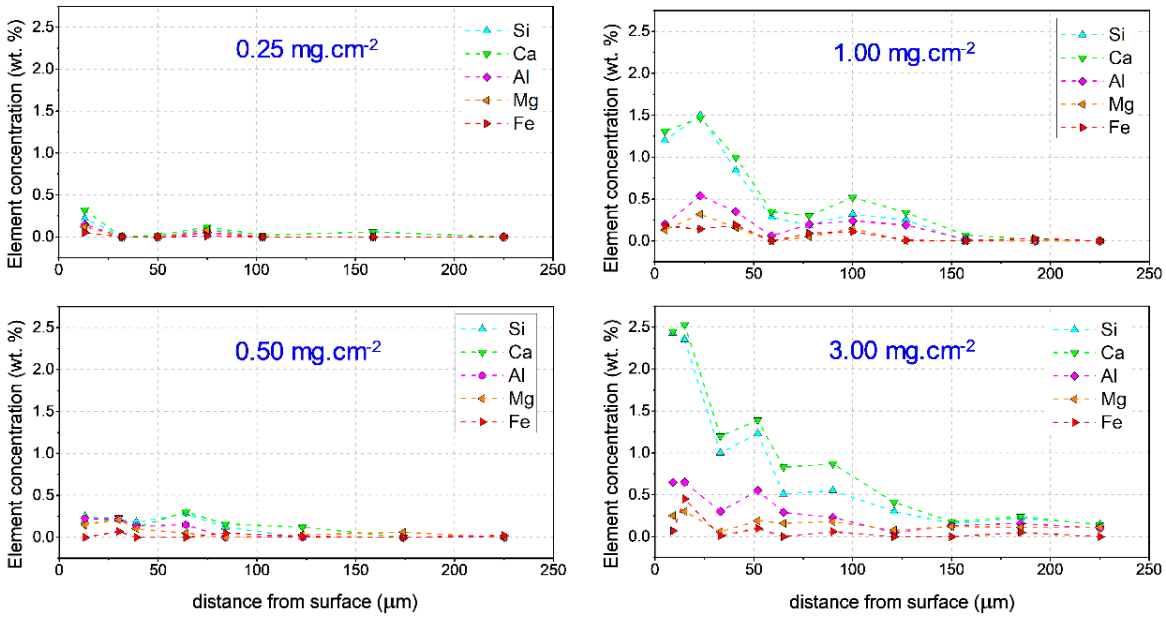

Figure 6 *– Evolution of CMAS content with depth in the YSZ freestanding coatings for different deposited amounts.*

Figure 7 presents the X-ray diffraction patterns for the as-deposited coating and the samples annealed at 1250°C with the different CMAS deposits. The as-deposited coating already displays the monoclinic structure of zirconia with the two peaks around 28°5 and 31°5. Quantitative analysis using Rietveld refinement were conducted in the 27°-32° and 72°-76° ranges to identify more accurately the phase changes occurring by reaction of the YSZ with the CMAS. The results are gathered in ***Table 2***. The phase analysis shows that only the Y-rich stabilized *t'*-ZrO_2 (93.1 wt.%) and the *m*-ZrO_2 (6.9 wt.%) are present in the as-deposited coating. The evolution of the different phases with increasing the CMAS deposits is presented on ***Figure 8*** for a better overview. The content of *t'*-ZrO_2 tends to decrease while that of the low-yttria *t*-ZrO_2 increases with the amount of CMAS. Also, the initial *m*-ZrO_2 phase decreases with annealing irrespective the deposited amount of CMAS. In contrast, the rate of *c*-ZrO_2 phases remains approximately constant with CMAS. These results indicate that yttria is depleted from the zirconia with increasing CMAS content.

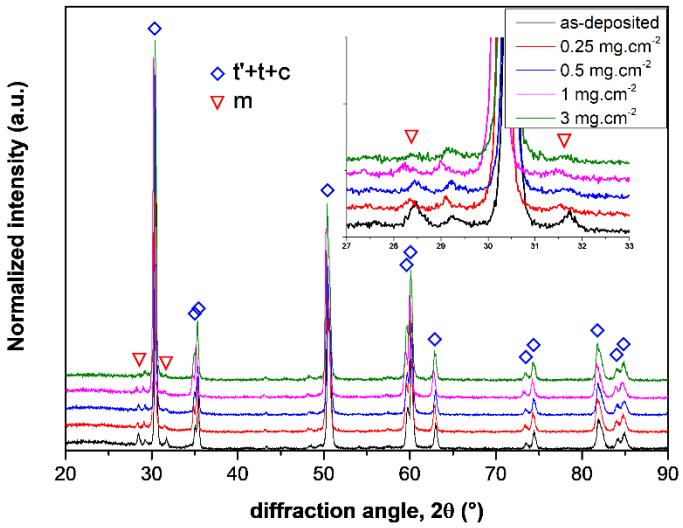

Figure 7 *– XRD patterns of the CMAS-attacked freestanding YSZ coatings compared with the as-deposited one.*

Table 2 *- Relative percentages and yttria contents for zirconia phases in as-sprayed and in CMAS-attacked YSZ coatings (Rietveld analysis).*

Sample	***c*-ZrO_2** (wt.%)	**Yttria content** (wt.%)	***t'*-ZrO_2** (wt.%)	**Yttria content** (wt.%)	***t*-ZrO_2** (wt.%)	**Yttria content** (wt.%)	***m*-ZrO_2** (wt.%)
as-deposited	-	-	93.1	7.3	-	-	6.9
0.25	1.8	9.1	82.9	7.4	12.3	5.6	3.0
0.50	1.3	9.0	81.8	7.3	13.7	5.6	3.2
1	1.0	10.8	77.9	7.5	18.0	5.3	3.1
3	1.7	10.9	67.8	8.2	29.8	6.3	0.7

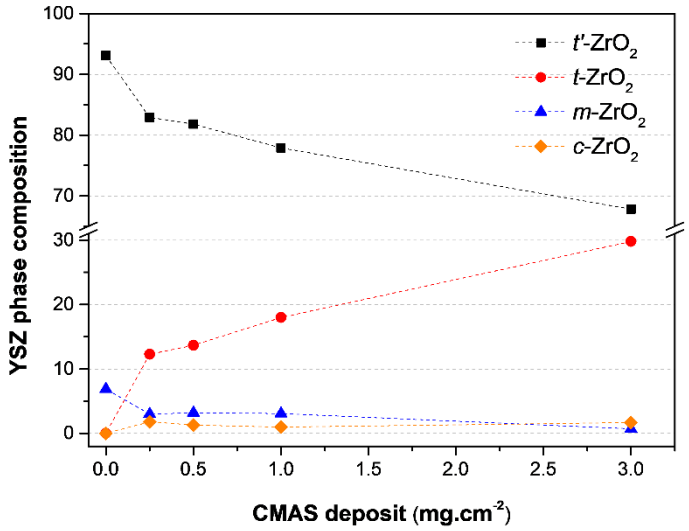

Figure 8 *– Evolution of the different phase percentage in CMAS-attacked YSZ coatings.*

The evolution of the different phases was also evaluated at local scale by Raman spot analyses. The results are presented in ***Figure 9***. In contrast with the results obtained with the 20 mg.cm^{-2} of CMAS deposit, the Raman spectra highlight the progressive disappearance of the *m*-ZrO_2 phase with increasing CMAS content, results being consistent with the one of XRD (***Figure 8***).

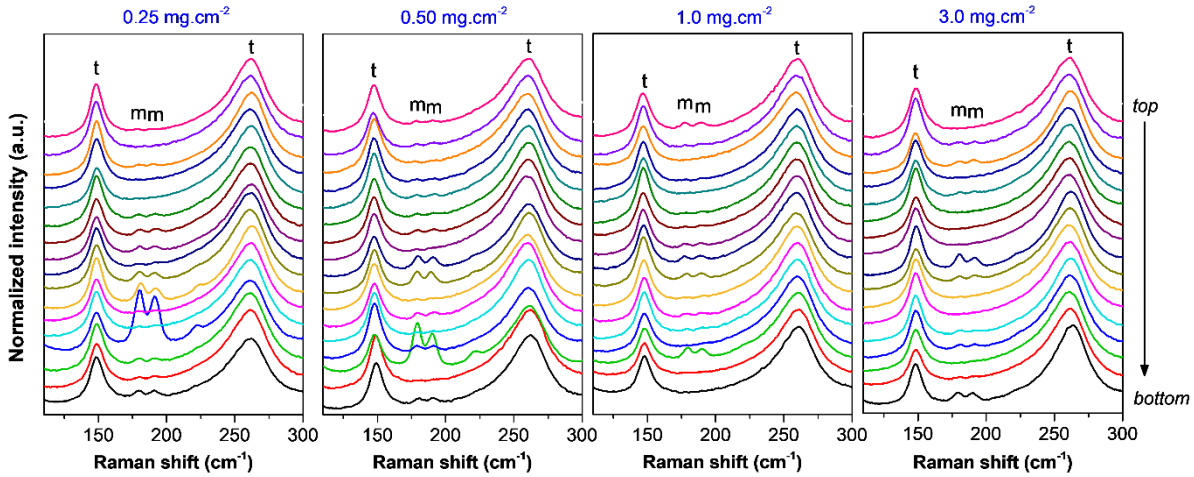

Figure 9 *– Local Raman spot analysis of the CMAS-attacked freestanding YSZ coatings.*

3.2. Thermal diffusivity

The thermal diffusivity as a function of the temperature for the as-deposited coatings and for the annealed samples (with and without CMAS deposits) is presented on ***Figure 10***. The as-deposited coating displays a thermal diffusivity comprised between 4.10^{-7} (at RT) and 3.10^{-7} $m^2.s^{-1}$ (at 1000°C) with a minimum observed at 600°C. The values raise to 6.10^{-7} (RT) and 4.10^{-7} $m^2.s^{-1}$ (1000°C) when annealed at 1250°C for 1 h without CMAS. In the presence of CMAS, the thermal diffusivity increases gradually with increasing the amount of CMAS. The effect of the deposited amount of CMAS on the thermal diffusivity is plotted in ***Figure 11***. With respect to the annealed and CMAS-free coatings, the thermal diffusivity of the CMAS-attacked layers increases by ~15, ~30, ~50 and 110 % for, respectively, the 0.25, 0.5, 1 and 3 $mg.cm^{-2}$ amounts of CMAS. One can assume a quasi-linear relationship between the CMAS deposited quantity and the observed rise in thermal diffusivity.

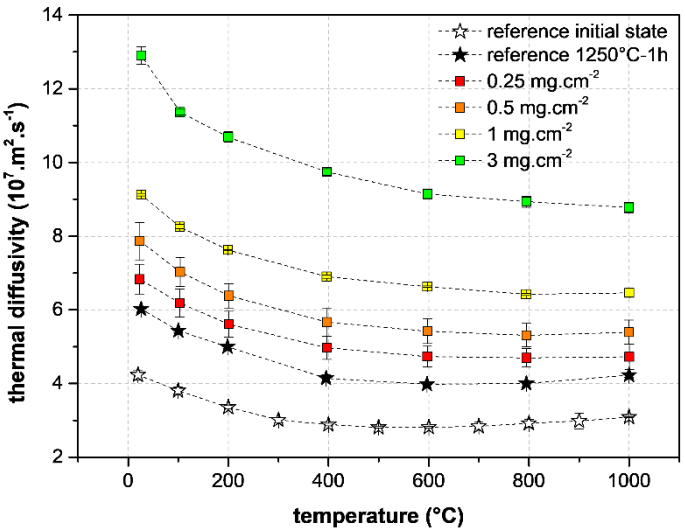

Figure 10 *– Thermal diffusivity of the of the of the CMAS-attacked freestanding YSZ coatings compared with the as-deposited reference with and without annealing at 1250°C for 1h.*

Figure 12 gives the lamellar porosity level as well as the thermal diffusivity at room temperature of the freestanding coatings in the as-deposited and in the annealed conditions. The data are compared with other similar freestanding coatings measured in a previous study [21]. The as-deposited coatings display a lamellar porosity rate of ~11.7% for a thermal diffusivity at room temperature of ~$4.2.10^{-7}$ $m^2.s^{-1}$. After a pre-heating at 1150°C for 1 h, the lamellar porosity level decreases till ~11% and is associated with an increase of the thermal diffusivity to ~$4.6 .10^{-7}$ $m^2.s^{-1}$. The annealing treatment of 1 h at 1250°C performed in this study leads to a lamellar porosity rate of ~9.5%, which is similar to the one obtained in a previous study after

50h at 1150°C [21]. The resulting thermal diffusivity at RT for both of these annealed coatings is also observed to be similar (~6 .10^{-7} $m^2.s^{-1}$). Finally, one shall note that the lamellar porosity level measured in the unaffected zone of the coatings annealed with 1 $mg.cm^{-2}$ CMAS (see ***Figure 5***b) is close to the one of the annealed coating without CMAS (~9.6%). In the CMAS-attacked zone, the thin lamellar porosity disappeared and only the larger cracks and globular pores are still visible.

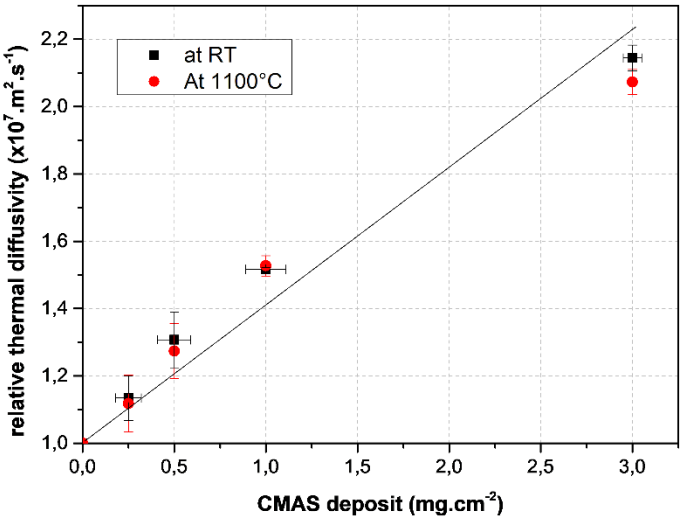

Figure 11 *– Relative thermal diffusivity of the freestanding YSZ coatings annealed at 1250°C for 1h with CMAS deposits of 0.25, 0.50, 1.0 and 3.0 $mg.cm^{-2}$.*

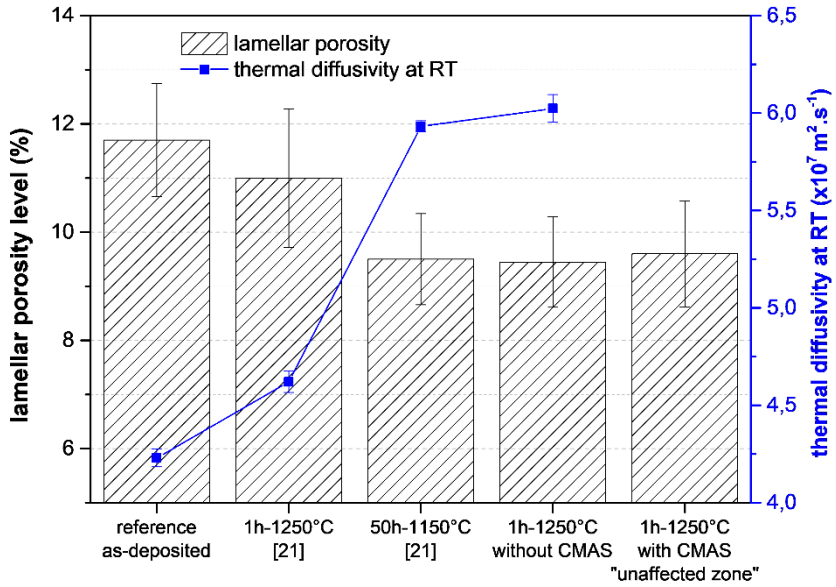

Figure 12 *– Lamellar porosity levels of the PS coatings of the study compared with the one of the same coatings measured in [21] versus the thermal diffusivity measured at room temperature.*

4. Discussion

The penetration of the CMAS melt has been shown to be associated with the loss of the initial microstructure of the coatings that resulted in closure of the thin pores and appearance of round-shaped pores (***Figure 2***). This transformation results from the dissolution-reprecipitation mechanism described in numerous studies [2, 14, 3]. The appearance of round shaped pores, once reported by Borom et al. [3], is a frothing phenomenon which origin is still under debate. Li et al. ascribed the froth to the fact that the air within the porous coating structure tries to escape from it and is trapped within the molten phase [22]. This phenomenon was observed for the substantial deposits of 20 $mg.cm^{-2}$ and in other studies that employed large amount of CMAS deposits [3, 22, 11]. However, no evidence of frothing was observed with the smaller deposits of 0.25 to 3 $mg.cm^{-2}$ (***Figure 4***). This means that, when using smaller amounts of deposited CMAS, the melt is not significant enough to create a large melted zone via dissolution of the YSZ material.

The microstructure of the "affected" zone in the case of the small deposits (***Figure 5a***) looks like the one observed in other studies [13, 3, 11]. After the dissolution of the *t'*-ZrO_2 in the CMAS melt, the zirconia reprecipitates into round-shaped grains that are either depleted in yttria and transformed to monoclinic on cooling, or enriched in Y and fully stabilised into *c*-ZrO_2 [14]. The Y-depletion was ascribed to the higher solubility of Y^{3+} in the glassy melt compared to Zr^{4+} ions that leads to further reprecipitation of *m*-ZrO_2 [14]. The higher content of Y that was measured via EDS in the round shaped grains of zirconia (see ***Figure 5a***) could be linked to a possible enrichment in Y during reprecipitation, leading to a partial transformation of the *t'*-ZrO_2 into a *c*-ZrO_2 [14], which is also in line with our XRD results (see ***Table 2***). For instance, Kramer et al. identified via TEM and EDS analysis the globular grains to be made of *c*-ZrO_2 surrounded by a mixture of crystallized aluminium silicates and residual glassy CMAS (the dark matrix of ***Figure 5a***) in which small grains of zirconia were embedded [24, 14]. The darker phase in the "affected" zone of ***Figure 5a*** would thus be composed of reprecipitated small grains of Y-lean zirconia in the anorthite ($Ca_2ZrSi_4O_{12}$) matrix often reported in other studies with similar CMAS compositions [2, 19]. One shall note that, in this study, the deposited amounts of CMAS are very small compared to those of other works. Therefore, the CMAS becomes the limiting reagent in our case and different reaction products than those reported may also form. In addition, as opposed to the increase of the *m*-ZrO_2 observed for the substantial CMAS deposits of 20 $mg.cm^{-2}$ (***Figure 3***), the X-ray analysis and

the Raman spectra of the coatings with the small deposits (***Table 2*** and ***Figure 9***) show a decrease of the *t'*-ZrO_2 and of the *m*-ZrO_2 and an increase of the *t*-ZrO_2. The formation of the *m*-ZrO_2 may be impeded upon quenching (see the $YO_{1.5}$–ZrO_2 phase diagram ***Figure 13***), which would agree with the opinion of Aygun et al. [19]. However, as the deposit of 20 $mg.cm^{-2}$ led to the formation of *m*-ZrO_2, it appears more likely that the amount of deposited CMAS was not sufficient to further destabilize the *t'*-ZrO_2 into the *m*-ZrO_2 by dissolution of Y and thus resulted only in the formation of the Y-lean *t*-ZrO_2 instead of *m*-ZrO_2. In this sense, we have also disregarded the relatively short annealing time (1h) because we have demonstrated that, when larger quantities of CMAS were employed, transformations into *m*-ZrO_2 were possible.

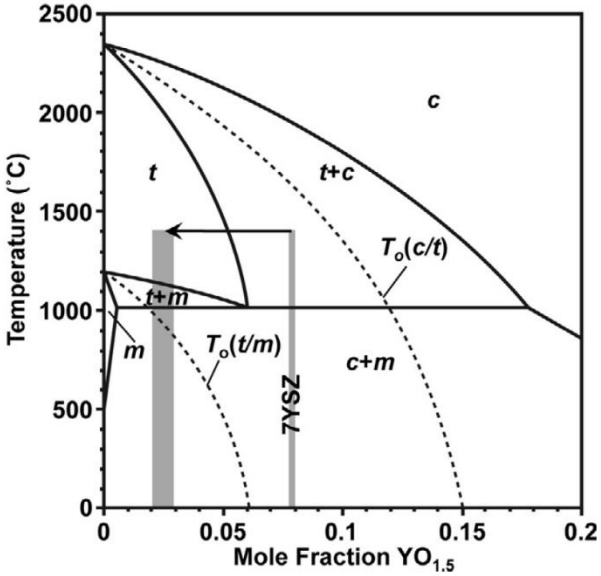

Figure 13 *– Portion of the $YO_{1.5}$–ZrO_2 phase diagram [25]. The arrow indicates Y-depletion due to interaction with CMAS.*

Considering the thermal diffusivity measurements (see ***Figure 10***), it was observed that the annealing treatment at 1250°C for 1 h was already responsible for a decrease of the thermal insulation potential of the coating. This 50% rise in thermal diffusivity is very likely due to the significant sintering of the lamellar porosity of the coating that is depicted on ***Figure 12*** and which was previously reported in similar works [21,10]. With the addition of CMAS, the thermal diffusivity is observed to increase further. In view of the different transformations observed, the rise in the thermal diffusivity could be due to (i) the sintering of the porous structure in the "affected zone", (ii) the phase transformations described above, and (iii) the thermal properties of the CMAS itself or of the reaction products issued from the interaction between the glassy melt and the YSZ coating.

It is well-known that the reduction of the heat transport through the YSZ coating, and especially for the plasma-sprayed coatings, is mainly due to their porous network [26, 27, 28, 29]. Previous works demonstrated that sintering is a major contributor of the loss of thermal insulation potential of such coatings [30, 31, 10]. In a previous study that concerned the same freestanding coating, a reduction of the lamellar porosity rate of ~20 % led to a ~40 % raise in thermal diffusivity [21]. This means that the complete filling of the thin pores by the CMAS will result in a sintering that will increase the heat transport through the coating.

The different phase contents measured using XRD (***Table 2***) showed a significant decreasing tendency of the *t'*-ZrO_2 in favour of *t*-ZrO_2 compared with a small increase of *c*-ZrO_2 and a small decrease of *m*-ZrO_2 (see also ***Figure 8***). Previous works also demonstrated that decreasing the Y_2O_3 content in YSZ single crystals contributed to an increase in the thermal diffusivity, i.e. a decrease from 10.6 to 7.7 wt. % resulted in an increase of the thermal diffusivity of 10% [15]. Thus, the important decrease of *t'*-ZrO_2 in favour of *t*-ZrO_2 could be responsible for further increasing the thermal diffusivity when compared to the less significant variations of the *m*-ZrO_2 and *c*-ZrO_2 phases. In addition, the phase changes measured via XRD associated with the increasing CMAS amount (***Table 2***) depend on the limited depth of penetration of the X-ray. Thus, the phase transformations depicted in ***Table 2*** relate only to a fraction of the affected depth. This would imply that the actual amount of transformed YSZ material into the less-insulating *t*-ZrO_2 might be significantly higher with increasing the deposited quantity of CMAS.

Considering the CMAS thermal properties, Kakuda et al. determined the thermal properties of amorphous and crystallized CMAS via local PopTea analysis and showed that crystallized CMAS led to very close thermal diffusivity values to that of the fully dense 7YSZ [12]. However, in the case of amorphous CMAS, the thermal diffusivity appeared to be half of the one of its crystallized form. Thus, the addition of CMAS in the coating could lead by itself to a decrease of the thermal diffusivity. However, in the coatings of this study, the CMAS retained within the coatings were estimated by EDS to be in a very small amount (see ***Figure 6***). Even in the case of the highest amount of CMAS (~3 $mg.cm^{-2}$), this mass would represent less than ~3% of the total mass of the sample and thus, the contribution of the CMAS to the thermal properties of the sample can be disregarded.

5. Conclusions

In this study, small quantities of CMAS were put in order to assess the impact that the resulting partial transformation of the YSZ plasma-sprayed coating could exert on the coating thermal insulation potential. The experimental results showed a gradual increase of the sintered depth with increasing CMAS deposits accompanied by phase transformations of the YSZ. The CMAS-induced sintering and the destabilization of the *t'*-ZrO_2 were found to be the major contributors of the raise in the thermal diffusivity of the coatings that reached a maximum of ~110 % for the fully penetrated coating.

ACKNOWLEDGEMENTS

The authors gratefully acknowledge SR Technics Airfoils Services, Ltd. (Ireland) for providing the samples of this study and the University of La Rochelle for supporting the collaboration with the Cranfield University.

REFERENCES

1. D.R. Clarke, M. Oechsner, N.P. Padture, *Thermal-barrier coatings for more efficient gas-turbine engines*, MRS Bulletin 37, **2012**, pp. 891-898.
2. C.G. Levi, J.W. Hutchinson, M.-H. Vidal Sétif, C.A. Johnson, *Environmental degradation of thermal-barrier coatings by molten deposits*, MRS Bulletin 37, **2012**, pp. 932-940.
3. M.P. Borom, C.A. Johnson, L.A. Peluso, *Role of environmental deposits and operating surface temperature in spallation of air plasma sprayed thermal barrier coatings*, Surface and Coatings Technology 86-87, **1996**, pp. 116-126.
4. C. Mercer, S. Faulhaber, A.G. Evans, R. Darolia, *A delamination mechanism for thermal barrier coatings subject to calcium–magnesium–alumino-silicate (CMAS) infiltration*, Acta Materialia 53, **2005**, pp. 1029-1039.
5. R.G. Wellman, J.R. Nicholls, *On the effect of ageing on the erosion of EB-PVD TBCs*, Surface and Coatings Technology 177-178, **2004**, pp. 80-88.

6. X. Zhao, X. Wang, P. Xiao, *Sintering and failure behaviour of EB-PVD thermal barrier coating after isothermal treatment*, Surface and Coatings Technology 200, **2006**, pp. 5946-5955.

7. A.C.F. Cocks, N.A. Fleck, *Constrained sintering of an air-plasma-sprayed thermal barrier coating*, Acta Materialia 58, **2010**, pp. 4233-4244.

8. I.O. Golosnoy, A. Cipitria, T.W. Clyne, *Heat transfer through plasma-sprayed thermal barrier coatings in gas turbine: a review of recent work*, Journal of Thermal Spray Technology 18, **2009**, pp. 809821.

9. L. Lu, F.-C. Wang, Z. Ma, Q.-B. Fan, *Anisotropic effect of splat interface on thermal conductivity of plasma sprayed YSZ coating*, Surface and Coatings Technology 235, **2013**, pp. 596-602.

10. H.-J. Rätzer-Scheibe, U. Schulz, *The effects of heat treatment and gas atmosphere on the thermal conductivity of APS and EB-PVD PYSZ thermal barrier coatings*, Surface and Coatings Technology 201, **2007**, pp. 7880-7888.

11. J. Wu, H.-B. Guo, Y.-Z. Gao, S.-K. Gong, *Microstructure and thermo-physical properties of yttria stabilized zirconia coatings with CMAS deposits*, Journal of the European Ceramic Society 31, **2011**, pp. 1881-1888.

12. T.R. Kakuda, C.G. Levi, T.D. Bennett, *The thermal behavior of CMAS-infiltrated thermal barrier coatings*, Surface and Coatings Technology 272, **2015**, pp. 350-356.

13. F.H. Stott, D.J. de Wet, R. Taylor, *Degradation of thermal-barrier coatings at very high temperatures*, MRS Bulletin, **1994**, pp. 46-49.

14. S. Krämer, J. Yang, C.G. Levi, *Thermochemical interaction of thermal barrier coatings with molten CaO–MgO–Al_2O_3–SiO_2 (CMAS) deposits*, Journal of the American Ceramic Society 89[10], **2006**, pp. 3167-3175.

15. J.-F. Bisson, D. Fournier, M. Poulain, O. Lavigne, R. Mévrel, *Thermal conductivity of yttria–zirconia single crystals, determined with spatially resolved infrared thermography*, Journal of the American Ceramic Society 83[8], **2000**, pp. 1993-1998.

16. M. Craig, N.L. Ndamka, R.G. Wellman, J.R. Nicholls, *CMAS degradation of EB-PVD TBCs: The effect of basicity*, Surface and Coatings Technology 270, **2015**, pp. 145-153.

17. W. Braue, P. Mechnich, Recession of an EB-PVD YSZ coated turbine blade by CaSO4 and Fe, Ti-rich CMAS-type deposits, Journal of the American Ceramic Society 94[12], **2011**, pp. 4483-4489.

18. V.L. Wiesner, U.K. Vempati, N.P. Bansal, *High temperature viscosity of calcium-magnesium-aluminosilicate glass from synthetic sand*, Scripta Materialia 124, **2016**, pp. 189-192.

19. A. Aygun, A.L. Vasiliev, N.P. Padture, X. Ma, *Novel thermal barrier coatings that are resistant to high-temperature attack by glassy deposits*, Acta Materiala 55, **2007**, pp. 6734-6745.

20. U. Schulz, *Phase Transformation in EB-PVD Yttria Partially Stabilized Zirconia Thermal Barrier Coatings during Annealing*, Journal of the American Ceramic Society 83, **2000**, pp. 904-910.

21. G. Boissonnet, G. Bonnet, A. Pasquet, N. Bourhila, F. Pedraza, *Evolution of Thermal Insulation of Plasma-Sprayed Thermal Barrier Coating Systems with Exposure to High Temperature*, accepted in Journal of the European Ceramic Society on January 14th.

22. L. Li, N. Hitchman, and J. Knapp, *Failure of Thermal Barrier Coatings Subjected to CMAS Attack*, Journal of Thermal Spray Technology 19, **2010**, pp. 148-155.

23. A.G. Evans, J.W. Hutchinson, *The mechanics of coating delamination in thermal gradients*, Surface and Coatings Technology 201, **2007**, pp. 7905-7916.

24. S. Krämer, S. Faulhaber, M. Chambers, D.R. Clarke, C.G. Levi, J.W. Hutchinson, A.G. Evans, *Mechanisms of cracking and delamination within thick thermal barrier systems in aero-engines subject to calcium-magnesium-alumino-silicate (CMAS) penetration,* Materials Science and Engineering A 490, **2008**, pp. 26-35.

25. H.F. Garces, B.S. Senturk, N.P. Padture, *In situ Raman spectroscopy studies of high-temperature degradation of thermal barrier coatings by molten silicate deposits*, Scripta Materialia 76, **2014**, pp. 29-32.

26. L.P.H. Jeurgens, W.G. Sloof, F.D. Tichelaar, E.J. Mittemeijer, *Structure and morphology of aluminium-oxide films formed by thermal oxidation of aluminium*, Thin Solid Films 418, **2002**, pp. 89-101.

27. L. Pawlowski and P. Fauchais, *Thermal Transport Properties of Thermally Sprayed Coating*, International Materials Reviews 37[6], **1992**, pp. 271-289.

28. F. Cernuschi, P. Bianchi, M. Leoni, and P. Scardi, *Thermal Diffusivity/Microstructure Relationship in Y-PSZ Thermal Barrier Coatings*, Journal of Thermal Spray Technology 8[1], **1999**, pp. 102-109.

29. I.O. Golosnoy, S.A. Tsipas, and T.W. Clyne, *An Analytical Model for Simulation of Heat Flow in Plasma Sprayed Thermal Barrier Coatings*, Journal of Thermal Spray Technology 14[2], **2005**, pp. 205-214.

30. F. Cernushi, L. Lorenzoni, S. Ahmaniemi, P. Vuoristo, and T. Mäntylä, *Studies of the sintering kinetics of thick thermal barrier coatings by thermal diffusivity measurements*, Journal of European Ceramic Society 25, **2005**, pp. 393-400.

31. Y. Tan, J.P. Longtin, and S. Sampath, *Effect of the Starting Microstructure on the Thermal Properties of As-Sprayed and Thermally Exposed Plasma-Sprayed YSZ Coatings*, Journal of the American Ceramic Society 92[3], **2009**, pp. 710-716.

4. References introduction chapter III

1. F. Cernushi, L. Lorenzoni, S. Ahmaniemi, P. Vuoristo, and T. Mäntylä, *Studies of the sintering kinetics of thick thermal barrier coatings by thermal diffusivity measurements*, Journal of European Ceramic Society 25, **2005**, 393-400.

2. Y. Tan, J.P. Longtin, and S. Sampath, *Effect of the Starting Microstructure on the Thermal Properties of As-Sprayed and Thermally Exposed Plasma-Sprayed YSZ Coatings*, Journal of the American Ceramic Society 92[3], **2009**, 710-716.

3. Y. Tan, V. Srinivasan, T. Nakamura, S. Sampath, and P. Bertrand, *Optimizing Compliance and Thermal Conductivity of Plasma Sprayed Thermal Barrier Coatings via Controlled Powders and Processing Strategies*, Journal of Thermal Spray Technology 21[5], **2012**, 950-962.

4. N. Curry, N. Markocsan, L. Ostergren, X-H. Li, and M. Dorfman, *Evaluation of the Lifetime and Thermal Conductivity of Dysprosia-Stabilized Thermal Barrier Coating Systems*, Journal of Thermal Spray Technology 22[6], **2013**, 864-872.

5. J. Wu, H. Guo, Y. Gao, and S. Gong, *Microstructure and thermo-physical properties of yttria stabilized zirconia coatings with CMAS deposits*, Journal of the European Ceramic Society 31, **2011**, 1881-1888.

6. T.R. Kakuda, C.G. Levi, T.D. Bennett, *The thermal behavior of CMAS-infiltrated thermal barrier coatings*, Surface and Coatings Technology 272, **2015**, 350-356.

IV. INFLUENCE OF AGEING ON THE THERMAL INSULATION OF EB-PVD COATINGS

Table of contents

1. Introduction

After focusing on PS TBC systems, this chapter intends to provide a better understanding on the relationships between the intrinsic properties and the thermal insulation potential of EB-PVD TBC systems. In addition to the currently employed YSZ material, yttria-erbia (Y_2O_3-Er_2O_3) stabilized zirconia EB-PVD TBCs were investigated in this study. As a matter of fact, doping with several other additives such as Nd_2O_3, Er_2O_3, Yb_2O_3 and Gd_2O_3 has been of particular interest as they allow to lower the thermal conductivity of YSZ ceramic [1]. Likewise, rare-earth (RE) elements are known to be effective to mitigate Calcium-Magnesium-Aluminum-Silicates (CMAS) corrosion [2]. Thus, studying their microstructural and chemical stability for long term exposure at high temperature with and without CMAS is of major interest. Like for the PS TBCs, this chapter is divided in two different articles.

For these EB-PVD coatings, some studies dealt with the impact of the thickness and the columnar morphology of the coatings on the associated heat transport properties [3] [4]. However, very few investigations were conducted to understand the influence of ageing on the heat conduction of these coatings [5] [6] [7] and none can be found on the particular Y_2O_3-Er_2O_3 TBC systems. Thus, the first article (**article 3**) focuses on YSZ and Y_2O_3-Er_2O_3 stabilized zirconia (ErYSZ) TBC systems to investigate the microstructure-heat insulation relationships through systematical analysis of both microstructure and thermal diffusivity in their as-deposited state and isothermally aged.

For the interaction of these columnar coatings with molten CMAS, the studies were mostly conducted to understand the degradation mechanisms [8] [9] [10] and none can be found on the impact on the thermal transport properties in the presence of Er_2O_3. Thus, using the same approach as with the PS TBC systems presented in chapter 3, the second article (**article 4**) focuses on finding the onset quantity of CMAS that could induce enough changes to alter the thermal conductivity of the coatings. Small amounts of CMAS are deposited on the surface of YSZ and ErYSZ EB-PVD TBCs followed with a high temperature heat treatment for infiltration to occur.

2. Article 3: Phase Stability and Thermal Insulation of YSZ and Erbia-Yttria stabilized Zirconia EB-PVD Thermal Barrier Coating Systems

Phase Stability and Thermal Insulation of YSZ and Erbia-Yttria stabilized Zirconia EB-PVD Thermal Barrier Coating Systems

G. Boissonnet[1], C. Chalk[2], J. R. Nicholls[2], G. Bonnet[1], F. Pedraza[1]

1. Laboratoire des Sciences de l'Ingénieur pour l'Environnement, (LaSIE, UMR-CNRS 7356), Université de La Rochelle, Avenue Michel Crépeau, 17042 La Rochelle, cedex 01 – France.

2. Cranfield University, Surface Engineering and Nanotechnology Institute (SENTi), College Rd., Wharley End, Bedford MK43 0AL – United Kingdom.

*corresponding author: boissonnet.germain@gmail.com

Keywords: Thermal barrier coatings (TBCs); Electron-beam physical vapour deposition (EB-PVD); Yttria stabilized zirconia (YSZ); Erbia doping; thermal diffusivity

Abstract. In order to cope with the ever-increasing operating temperature of aero gas turbines, new thermal barrier coatings are being investigated. Among the different solutions, erbia-yttria stabilized zirconia coatings made by electron-beam physical vapour deposition (EB-PVD) show promising results in terms of thermal insulation enhancement. Annealing of these coatings was performed at 1100°C in air in order to investigate their stability in comparison with that of standard 8 mol.% yttria stabilized zirconia (8YSZ). Their thermal transport properties were measured using the laser-flash technique. The results show that, in the as-deposited conditions, the Y_2O_3-Er_2O_3 stabilized zirconia (ErYSZ) coatings offered lower heat conduction than the standard ones in the studied temperature range (from room temperature to 1100°C). However, the microstructural and phase transformations of the ErYSZ coatings after annealing were significantly greater than those of the standard coatings, hence strongly modifying their thermal insulation potential.

1. Introduction

The application of thermal barrier coatings (TBCs) on the metallic structures of the hottest sections of aero gas turbines offers many benefits like the increase in operating temperatures hence the engine efficiency, while enhancing component durability [1,2]. TBCs comprise two layers: (i) a bond coating (BC), which is an oxidation-resistant metallic layer carrying the

structural load and (ii) a top coating (TC), which is a porous ceramic layer that acts as a thermal insulator between the substrate and the surrounding environment. The conventional material used for the TC in TBCs is zirconia (ZrO_2) stabilized with 6-9 wt. % yttria (Y_2O_3) [3]. Electron-beam physical vapour deposited (EB-PVD) thermal barrier coatings (TBCs) are widely used to protect the turbine blades of aircraft engines because their segmented columnar structure allows high strain compliance, resulting in superior thermal shock resistance [4]. Their continued development is essential for improving the efficiency and performance of gas turbines by allowing the inlet gas temperature to be increased further. For this reason, there is considerable interest in developing top coatings with even lower thermal conductivities [5].

Phase stability of the TC is of great importance for the durability and reliability of TBCs. Zirconia exists as three crystalline phases that are stable at different temperatures [6]. Up to 1200°C, the monoclinic phase (m) is the stable one. Then, zirconia transforms from the monoclinic to the tetragonal phase (t) above 1200°C and to the cubic phase (c) above 2370°C. The m to t-phase transformation is associated to a volume decrease of ~4 % [7]. Zirconia-based TBCs must consequently be doped with trivalent or tetravalent cations in order to stabilize the tetragonal zirconia polymorph and prevent catastrophic cracking resulting from the volume changes accompanying the t→m transformation, occurring at temperatures within the range of the working environment in gas turbines. The polymorphism of zirconia has led to the investigation of various stabilized zirconia alloys [8]. Among the different solutions investigated, doping with several other additives such as NiO, Nd_2O_3, Er_2O_3, Yb_2O_3 and Gd_2O_3 has been of particular interest as they also allow to lower the thermal conductivity of YSZ ceramic [9]. ZrO_2-Er_2O_3, ZrO_2-Sm_2O_3 and ZrO_2-Nd_2O_3 TBCs have been reported to consist of non-transformable t' tetragonal phase up to compositions of 6 mol. % of stabilizer above which only the cubic structure occurs [10,11,12]. Erbia (Er_2O_3)-stabilized coatings showed better thermal phase stability than samaria (Sm_2O_3)- and neodymia (Nd_2O_3)-stabilized coatings, which decomposed into the monoclinic and tetragonal phases after heat treatment [10,11,12]. The phase stability of the top coating constitutes an important factor for determining the thermomechanical properties of TBCs. Likewise, rare-earth (RE) elements are known to be effective to mitigate Calcium-Magnesium-Aluminum-Silicates (CMAS) corrosion [13]. This is because RE elements allow the precipitation of stable apatite silicate and fluorite as soon as the dissolution of the TBC material starts, hence stopping the penetration of the molten silicates. Thus, studying their stability for long term exposure at high temperature is of major interest.

Therefore, in this work, the phase stability and thermal insulation potential of 8YSZ and ErYSZ EB-PVD coatings have been compared to those of the state-of-the-art yttria-stabilized zirconia (8YSZ). Both coatings were synthesized on Ni-based alloys and exposed to high temperature in order to evaluate the impact of the microstructural transformations on the thermal insulation properties.

2. Experimental

The EB-PVD coatings were produced at the Surface Engineering and Nanotechnology Institute (SENTi) in Cranfield University (UK) on Inconel 600 substrates (15.5 Cr, 8.0 Fe, 0.5 Mn, < 0.5 Cu, < 0.5 Si, wt. %, bal. Ni). Prior to the deposition of the ceramic, the Inconel 600 plates were cut into 10 x 10 mm^2 coupons and aluminized via Chemical Vapour Deposition (CVD). Two different rods were used to perform the elaboration of the 8YSZ coatings (ZrO_2 - 8 mol. % Y_2O_3) and the ErYSZ ones (ZrO_2 – 4 mol.% Y_2O_3 – 4 mol.% Er_2O_3). The obtained coatings showed slight differences in columnar orientation (0-10°) and thicknesses (120-160 µm) since they were individually fixed on sample holders and were not all located at the same distance from the deposition source. Several samples were exposed for 500 h in air at 1100°C in a muffle furnace to induce microstructural changes in the ceramic coating as well as oxidation and transformations of the complete system (substrate + BC + TC).

The microstructural changes were investigated from polished cross-sections with a FEI Quanta 200F scanning electron microscope (SEM) coupled to an EDAX detector for local analysis of the composition using energy dispersive spectrometry (EDS). X-ray diffraction (XRD, Brüker AXS D8 Advance) using the λ_{Cu} in θ-2θ mode and Raman micro-spectrometry (Jobin Yvon LabRam HR800, λ_{laser} ~632nm) were employed to follow the structural changes of the ceramic coatings on the surface and on the cross-section respectively. The weight fractions of tetragonal, monoclinic and cubic phases were calculated from the peak intensities of slow scans (step size of 0.01° at a dwell time of 10 s per step) on the ranges of interest, i.e. 2θ = 27 to 32° for the $(\bar{1}11)$ and (111) peaks of the monoclinic phase and 2θ = 72 to 76° for the (400) and (004) peaks of the cubic and tetragonal phases. The integrated intensities were calculated after peak deconvolution and profile fitting, performed with the Rietveld method using MAUD software.

To assess the evolution of the thermal insulation potential of the TBCs, thermal diffusivity was determined using high-temperature laser-flash measurements with a Linseis LFA1600 apparatus at low pressure (~1.10^{-2} mbar), every 100°C between room temperature and 1100°C. Three to five samples per type of coating were analyzed with five separate laser shots per sample at each temperature to increase accuracy of the results. In the case of as-deposited coating samples, the measurements were carried out a second time as significant sintering occurred along the first measurement. This phenomenon has been previously reported in the literature on similar YSZ TBCs [14]. After the second measurement, the thermal diffusivity was observed to remain stable.

The calculations were performed using a 2-layer model – (i) YSZ and (ii) substrate + aluminide layer – to assess the thermal diffusivity of the full thermal barrier coating systems. Thus, the thermal diffusivity of the substrate was measured before and after ageing at 1100°C in air for 500 h and with or without the Al diffusion coating. Prior to the measurements with the laser flash, the thicknesses of the multilayer samples were accurately determined (± 10^{-3} mm) with a digital caliper. The surfaces of the samples were coated with a graphite spray to foster absorption of the laser and heat emissivity. Heat is collected with an infrared detector situated at the front of the specimens. The thicknesses of the coatings to be used in the multilayer calculations were measured from the cross-sectional images.

3. Results and Discussion

3.1. Microstructure of the coatings

Fig. 1 presents the microstructures of the different coatings in their as-deposited state and after annealing at 1100°C in air. Both the standard 8YSZ and ErYSZ coatings exhibited similar microstructural features. Therefore, only the ErYSZ coating is presented in its as-deposited conditions (**Fig. 1a**, **1b** and **1c**). The full TBC displays the typical ceramic top coatings with a feather like morphology attached to a thin (~ 0.6 µm) α-Al_2O_3 grown on a β-NiAl bond coating layer of about 30 µm (**Fig. 1a**). The bond coat also contains Al-Cr precipitates and residual alumina particles introduced via grit blasting at the interface with the substrate. One can also note that the ceramic layer displays thin lamellar pores trapped in between the "feather arms" of each column (**Fig. 1b** and **1c**). This porous microstructure is reported in the literature to be responsible for the reduction of the heat transport [15,16].

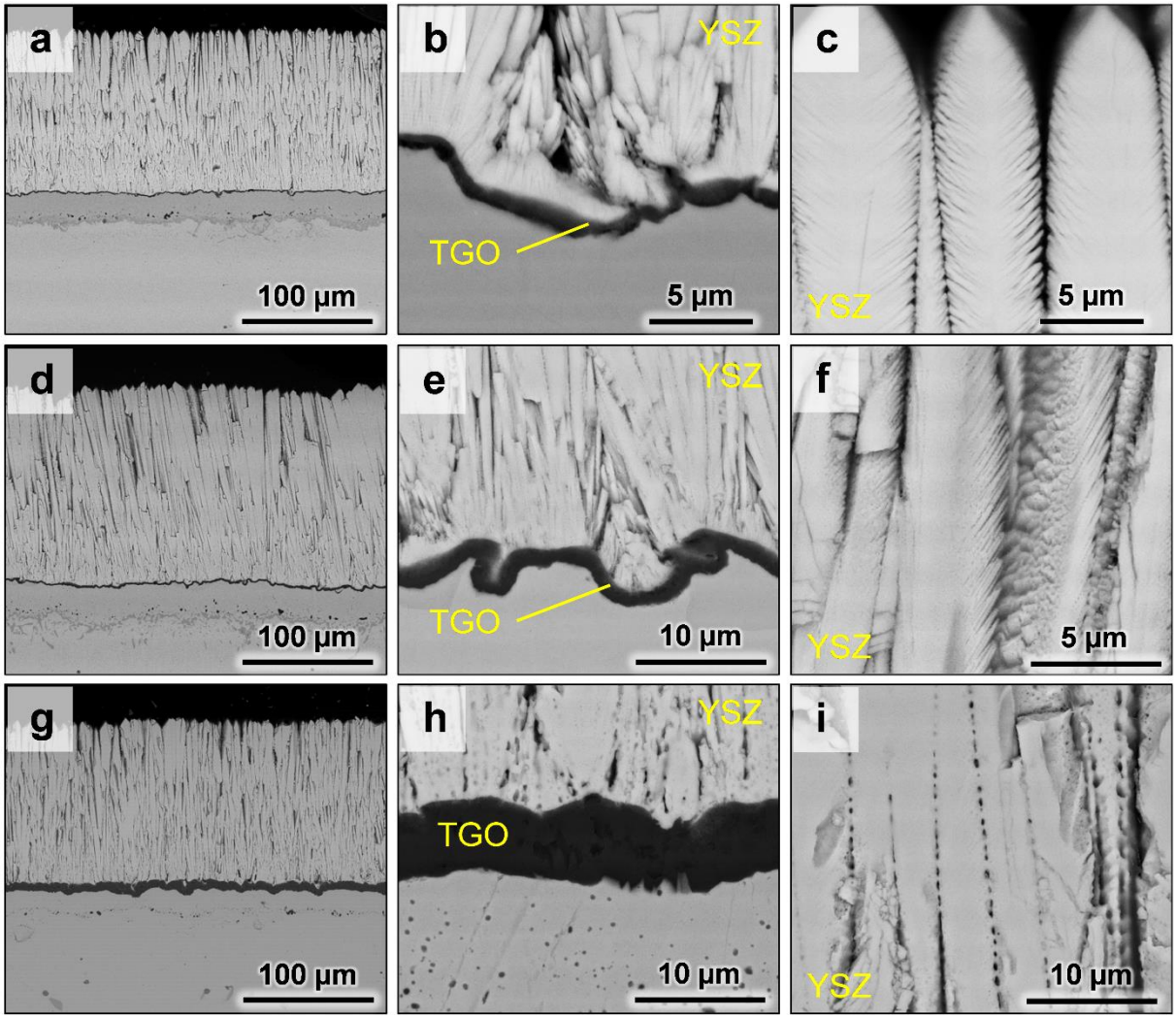

***Fig. 1** – SEM micrographs of the EB-PVD coatings in the as-deposited conditions with **a**, **b** and **c** (similar for both standard and Er-doped coatings) and after ageing* in air at 1100°C for 500h *with (**d**, **e** and **f**) for the standard 8YSZ coating and (**g**, **h** and **i**) for the ErYSZ coating.*

After isothermal exposure at 1100°C for 500 h, the standard 8YSZ coated sample exhibits few microstructural transformations of the TBC system (**Fig. 1d**, **1e** and **1f**). The additive layer was depleted in Al and formed γ'-Ni_3Al phases within the β-NiAl layer. The associated bond coating oxidation resulted in the growth of the α-Al_2O_3 TGO till a thickness of ~1.2 µm (**Fig. 1e**). **Fig. 1f** shows that the intra-columnar gaps started to sinter, closing the thin lamellar pores of the feathery-like columns. However, the sintering of the ceramic appears rather weak as compared with similar coatings aged in analogous conditions [16,17,18]. This probably indicates a higher stability of the coatings in this study at the considered temperature. The Raman spectra of **Fig. 2** show that the stabilized tetragonal phase of zirconia (t'-ZrO_2) is the only one detected for both as-deposited and aged coatings, with the characteristic bands of

tetragonal ZrO_2 at ~150, 260, 330, 470, 615 and 643 cm^{-1} [7,19]. The phase compositions were calculated using Rietveld refinement from the X-ray data in the 72-76° range (for tetragonal and cubic phases), (**Fig. 4a**). No significant difference was observed for the 8YSZ standard coating and only tetragonal (t') phase was detected (**Fig. 4c**), confirming the observations made by Raman spectroscopy.

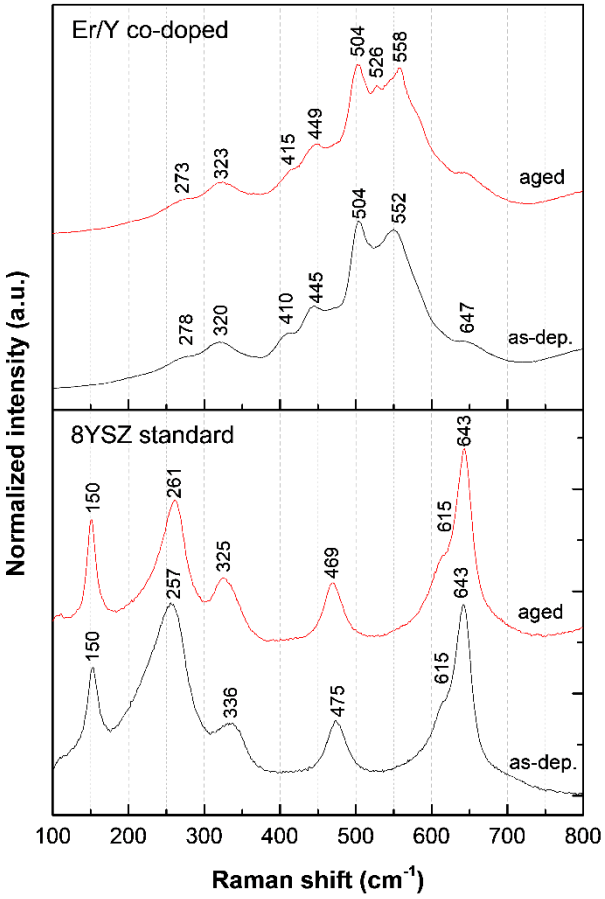

Fig. 2 *– Raman spectra of the 8YSZ standard and ErYSZ coatings in their as-deposited conditions and after ageing in air at 1100°C for 500h.*

In the case of the ErYSZ coating, the sintering and bond coating oxidation is more pronounced (**Fig. 1g**, **1h** and **1i**). The contrast of the bond coating layer disappeared almost completely in the BSE micrographs of **Fig. 1g**, indicating that Al was mostly consumed to form a thick TGO at the interface with the ceramic layer (<5 wt.% Al via EDS). As a matter of fact, the α-Al_2O_3 TGO reached a thickness of ~6 µm which is five times the thickness observed for the standard 8YSZ coating aged in the same conditions (**Fig. 1h**). One shall note that, unlike the standard YSZ coatings, the five aged samples used in the LFA measurements displayed different TGO thicknesses, ranging from 5.2 to 6.5 µm (the thicker the ceramic coating, the

thinner the TGO scale). Thickening of the alumina scale might be attributed to an increase of the oxidation kinetics of the aluminide triggered by the presence of Er_2O_3. For instance, Hou et al. also observed an acceleration of the initial growth kinetics of FeCrAl alloy when coated with RE (Ce, La) oxides [20]. The reactive element oxides (REO) are known to be oxygen-deficient oxides and Chevalier et al. proposed that oxygen transport could be accelerated around these particles [21]. By studying the impact of Nd_2O_3 and Y_2O_3 coatings on top of alumina forming alloys on the oxidation at high temperature (1050°C, 1100°C and 1200°C), they also observed an increase of the mass gain and higher oxidation rates for both types of coatings compared with the uncoated substrate. In addition, different reaction products between the REO and alumina could be formed depending on the oxidation temperature [21]. Although we have not observed such reaction compounds in our system, it appears that the doping effect of Er effectively affects the growth of the TGO compared to the standard YSZ coating.

The ErYSZ ceramic coating exhibits a more sintered microstructure than the standard one as closure of the inter-columnar gaps started via the formation of sintering bridges between the columns (**Fig. 1h** and **1i**). This enhanced sintering could also be explained by the increased affinity of erbium to oxygen with respect Y [21]. Also, the increased anionic diffusion in the presence of Er fosters sintering because the latter depends on ionic diffusion. The Raman spectra for the ErYSZ coatings (**Fig. 2**) show that the same bands are observed for both as-deposited and aged conditions. The bands observed at ~275, 320, 410, 445, 504, 552 and 650 cm^{-1} have also been observed for ErYSZ powders in the work of He et al. [22]. These authors explained that the Raman bands of zirconia overlap with the fluorescence bands of Er^{3+}, thus preventing a clear identification of the phases of ZrO_2. However, the XRD of ErYSZ coatings shows that the tetragonal t'-phase of ZrO_2 is the main phase of the coatings in the as-deposited and aged conditions (**Fig. 3**). The phase composition of the ErYSZ coating (**Fig. 4**) indicates that the coating also contains cubic (c-ZrO_2) and a second tetragonal phase (t-ZrO_2). The existence of a second tetragonal phase was highlighted by several other authors and is related to the lower content of Y in the tetragonal phase than in the t'-ZrO_2 [23,24]. With annealing at 1100°C, the ErYSZ coating destabilizes. The t'-ZrO_2 content decreases with annealing at 1100°C at the expense of c-ZrO_2 and t-ZrO_2. This could indicate that diffusion of the stabilizing species (Er and/or Y) occurs during annealing that leave the t'-ZrO_2 to form the Y-depleted t-ZrO_2 and the Y-enriched c-ZrO_2. Such diffusion of the species could also explain the high sinterability of the coating.

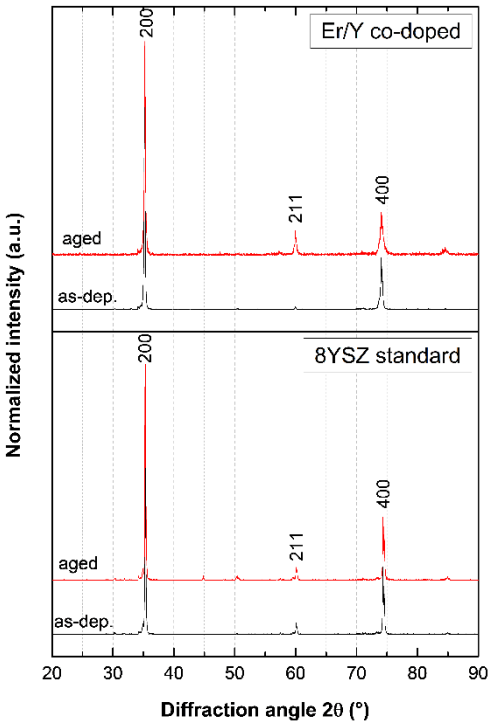

Fig. 3 *– Diffraction patterns of the 8YSZ standard and ErYSZ coatings in their as-deposited conditions and after ageing in air at 1100°C for 500h.*

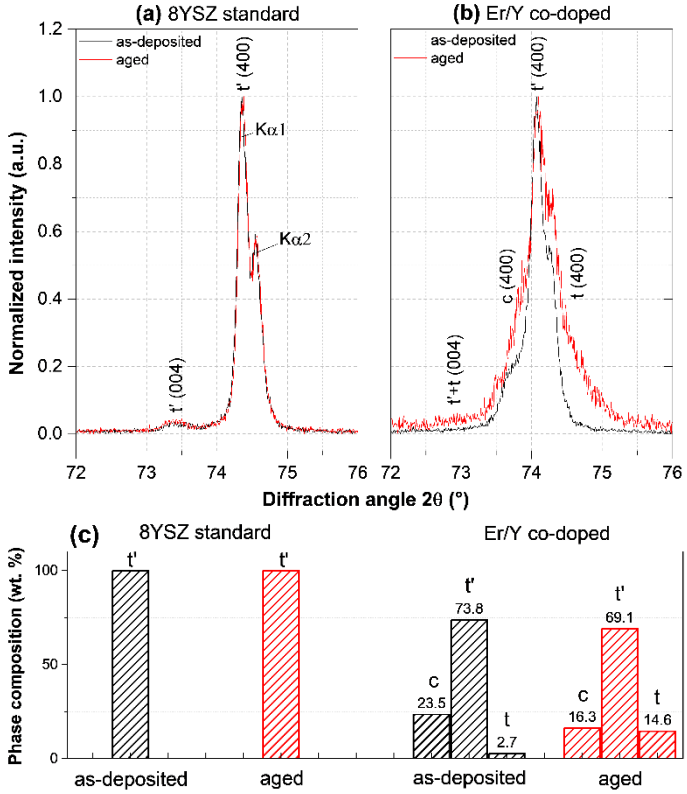

Fig. 4 *– Diffraction patterns of the 72-76° range for* ***a)*** *8YSZ standard and* ***b)*** *ErYSZ coatings in their as-deposited conditions and after ageing in air at 1100°C for 500 h and* ***c)*** *the corresponding phase composition measured using Rietveld refinement.*

3.2. Thermal diffusivity

The thermal diffusivities as a function of temperature for the 8YSZ standard coatings in their as-deposited state, pre-sintered after the first laser-flash measurement, and after 500 h of annealing in air are presented in **Fig. 5a**. The thermal diffusivity follows the same decreasing tendency for the three different states of the coating, followed by an increase above 900°C. This temperature dependence is typical for zirconia, as phonon-phonon scattering is the dominant mechanism responsible for thermal transport, and is consistent with the experimental results for YSZ described in the literature [25,26]. In the as-deposited state, the 8YSZ standard coating exhibits a maximum of the thermal diffusivity of ~6.3×10^{-7} $m^2.s^{-1}$ at room temperature and a minimum of ~3.7×10^{-7} $m^2.s^{-1}$ at 900°C. When measured a second time, after the pre-sintering of the first laser-flash measurement, the coatings exhibit approximately the same thermal diffusivity values than the as-deposited ones with only a slight increase after 500°C. This slight increase might be attributed to the sintering of the smallest pores of the coatings. It has been noticed that the thermal conductivity increase is usually more significant at the beginning of any annealing. Such behavior has been extensively demonstrated in previous studies. For instance, an increase in thermal conductivity was already observed when the as-deposited EB-PVD YSZ coatings were measured on the cooling stage of the laser-flash measurement from 1100°C [17] or after only 1 h at 1100°C [16]. After ageing at 1100°C in air for 500 h, the thermal diffusivity of the coatings remained barely the same, which is thus in agreement with the observed absence of significant microstructural transformation or phase change. However, the thermal diffusivity values varied from one sample to the other (**Fig. 5b**). This discrepancy between the different samples is also observed to increase with temperature. This was observed to be related to the variations in thickness of the coatings: the thinner the coating, the lower the thermal diffusivity. However, the thickness of the coatings is used in the multilayer calculations and thus should not significantly contribute to such variations in thermal diffusivity. In the other hand, the performed multilayer calculations did not consider the growth of the α-Al_2O_3 TGO. Since alumina presents a thermal conductivity significantly lower than that of the metal substrate, it likely increases the resistance to heat transport with the TGO thickening. The impact of the alumina scale on the thermal diffusivity values would thus be more significant for the thin coatings than for the thick ones. In addition, as the thermal conductivity of the alumina decreases with increasing temperature [27], its impact would become greater at high temperature, hence enhancing the differences between the samples. Therefore, the thermal diffusivity values might be slightly underestimated in the aged samples.

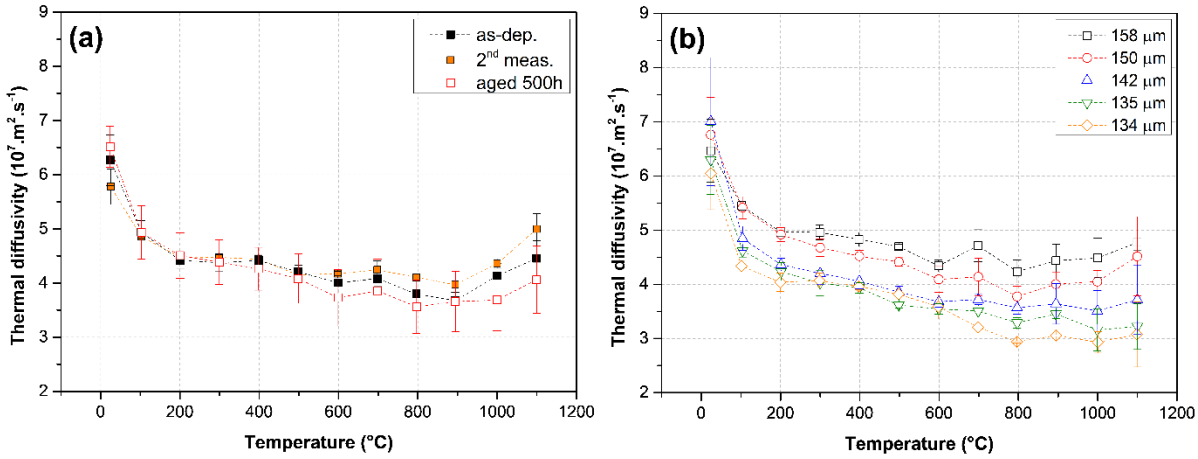

Fig. 5 – a) *Thermal diffusivity as a function of the temperature for the 8YSZ standard coatings in the as-deposited conditions, pre-sintered during the first measurement and aged in air at 1100°C for 500h and* ***b)*** *details of the 5 samples after ageing.*

The evolution of thermal diffusivities as a function of temperature is shown in **Fig. 6a** for the ErYSZ coatings in the three different conditions. The coatings display lower thermal diffusivity in the as-deposited condition than the 8YSZ standard coatings with a maximum of ~4.8×10^{-7} $m^2.s^{-1}$ at room temperature and a minimum of ~3.5×10^{-7} $m^2.s^{-1}$ at 600°C. Therefore, co-doping with 4 mol.% Er_2O_3 - 4 mol.% Y_2O_3 brings about a ~20% reduction in the thermal diffusivity compared to the standard 8YSZ composition while a ~30 % reduction was reported when the thermal barrier was doped with 8 mol.% Er_2O_3 [9]. The second measurement of the thermal diffusivity of the same coatings gave higher values (~10 % rise) than the as-deposited ones. This indicates a significant sintering of the coating during the first laser-flash measurement, which did not occur in the 8YSZ standard coatings. With ageing in air at 1100°C for 500 h, the thermal diffusivity of the ErYSZ coatings in the low temperature range (RT to 500°C) was observed to be higher than the one of the coatings in their initial state. With increasing temperature, the thermal diffusivity values remained below the ones of the coatings in their initial state. This peculiar trend could be attributed to the impact of two opposed factors: (i) the sintering of the coatings that is meant to ease heat conduction, as the number of phonon scattering interfaces is reduced [16], and (ii) the TGO, that was previously shown to decrease the thermal diffusivity by adding a non-negligible resistance to heat transport (especially at high temperature). One shall note that the phase transformations are not supposed to take a significant part in the modification of the heat transport compared with the sintering effect. Previous works that estimated the phase fraction by XRD and the thermal conductivity values as a function of Y_2O_3 concentration demonstrated that the phase transformation contributes to

less than 10 % to the evolution of the thermal conductivity of ceramic coating [18,28]. The sintering was observed to be quite significant in the case of the ErYSZ coatings (**Fig. 1i**) and thus could explain the rise of the thermal diffusivity in the low temperature range. Several other authors reported a similar increase of the heat conduction when ageing of EB-PVD YSZ coatings at 1100°C [18, 16,17]. Then, as the temperature of the measurement increased, the thermal diffusivity of the coatings decreased due to the increasing heat resistance of the α-Al_2O_3 TGO, as previously observed for the aged YSZ standard coatings. The greater reduction of the thermal diffusivity of the ErYSZ aged coatings compared with the one of the standard YSZ aged coatings could be explained by the evolution of the TGO, which is five times thicker in the Er-doped systems after ageing. Thus, underestimation of the thermal diffusivity values for these aged samples could also be even greater than in the case of the aged YSZ standard coatings.

Fig. 6b shows the dispersion of the thermal diffusivity values for the different aged ErYSZ coatings. Clearly, the evolution of the thermal diffusivity was also markedly dependent on the coating thickness. However, as opposed with the aged 8YSZ standard coatings, the dispersion of the values is more pronounced at room temperature. The greater dispersion observed at room temperature could be explained by the fact that the thicknesses of the measured TGO were slightly different between the samples. Also, the microstructural transformations observed for the aged coatings are more significant for these ErYSZ coatings. Therefore, the effect of microstructural transformations and the greater evolution of the TGO thickness could induce a greater dependence of the thermal diffusivity to the coating thickness.

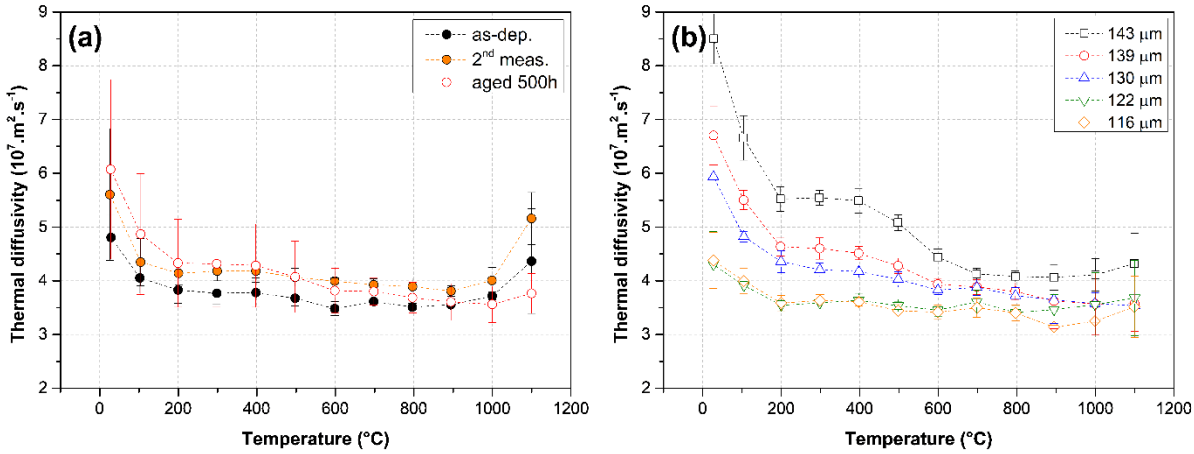

***Fig. 6** – **a)** Thermal diffusivity as a function of the temperature for the 8YSZ standard coatings in the as-deposited conditions, pre-sintered during the first measurement and aged in air at 1100°C for 500h and **b)** details of the 5 samples after ageing.*

4. Conclusions

Erbia-yttria stabilized zirconia coatings made by electron-beam physical vapour deposition (EB-PVD) were compared with the standard 8YSZ coatings. At room temperature, the co-doped coatings showed better thermal insulation than the standard ones. However, after annealing at 1100°C in air, the co-doped coating exhibited greater microstructural and phase transformations than its standard counterpart, which led to important thermal insulation changes. Thus, despite a better initial thermal insulation potential, the ErYSZ coating was shown to be less stable than the 8YSZ standard coating due to a faster degradation of the TBC system that could further lead to a poor lifespan.

ACKNOWLEDGEMENTS

The authors gratefully acknowledge SR Technics Airfoils Services, Ltd. (Ireland) for providing the samples of this study. G. Boissonnet thanks also the Région Poitou-Charentes for funding his PhD and the Université de La Rochelle for supporting his stay at Cranfield University.

REFERENCES

1. A.G. Evans , D.R. Clarke , C.G. Levi , *The influence of oxides on the performance of advanced gas turbines*, J. Eur. Ceram. Soc. 28 (2008) 1405-1419.
2. R. Vaßen , M. Ophelia-Jarligo , T. Steinke , D. Emil-Mack , D. Stöver , *Overview on advanced thermal barrier coatings*, Surf. Coat. Technol. 205 (2010) 938-942.
3. D. R. Clarke, M. Oechsner, and N. P. Padture, *Thermal-barrier coatings for more efficient gas-turbine engines*, MRS Bulletin 37 (2012) 891-898.
4. U. Schulz , C. Leyens , K. Fritscher , M. Peters , B. Saruhan-Brings , O. Lavigne , J.M. Dorvaux , M. Poulain , R. Mevrel , M.L. Caliez, *Some recent trends in research and technology of advanced thermal barrier coatings, Aerosp. Sci. Technol. 7 (2003) 73-80.*
5. M.R. Winter, D.R. Clarke, *Oxide Materials with Low Thermal Conductivity*, J. Am. Ceram. Soc. 90 (2007) 533-540.
6. H. Herman and N. R. Shankar, *Survivability of thermal barrier coatings*. Mater. Sci. Eng. 88 (1987) 69-74.

7. C. Viazzi, J-P. Bonino, F. Ansart, A. Barnabé, *Structural study of metastable tetragonal YSZ powders produced via a sol-gel route*, Journal of Alloys and Compounds 452 (2008) 377-383.
8. P. A. Langjahr, R. Oberacker, and M. J. Hoffmann, *Long-term behavior and application limits of plasma-sprayed zirconia thermal barrier coatings*. J. Am. Ceram. Soc., 84 (2001) 1301-1308.
9. J. R. Nicholls, K. J. Lawson, A. Johnstone and D. S. Rickerby, *Methods to reduce the thermal conductivity of EB-PVD TBCs,* Surf. Coat. Technol. 151-152 (2002) 383-391.
10. K. A. Khor and J. Yang, *Lattice parameters, tetragonality (c/a) and transformability of tetragonal zirconia phase in plasma-sprayed ZrO_2–Er_2O_3 coatings.* Mater. Lett. 31 (1997) 23-27.
11. K. A. Khor and J. Yang, *Plasma sprayed ZrO_2–Sm_2O_3 coatings: lattice parameters, tetragonality (c/a) and transformability of tetragonal zirconia phase.* J. Mater. Sci. Lett. 16 (1997) 1002-1004.
12. K. A. Khor and J. Yang, *Transformability of t-ZrO_2 and lattice parameters in plasma sprayed rare-earth oxides stabilized zirconia coatings.* Scripta Mater. 37 (1997) 1279-1286.
13. C.G. Levi, J.W. Hutchinson, M-H. Vidal-Sétif and C.A. Johnson, *Environmental degradation of thermal barrier coatings by molten deposits*, MRS Bulletin 37 (2012) 932-941.
14. H.-J. Rätzer-Scheibe, U. Schulz, *The effects of heat treatment and gas atmosphere on the thermal conductivity of APS and EB-PVD PYSZ thermal barrier coatings*, Surf. Coat. Technol. 201 (2007) 7880-7888.
15. S. Sampath, U. Schulz, M.O. Jarligo and S. Kuroda, *Processing science of advanced thermal-barrier systems*, MRS Bulletin 37 (2012) 903-910.
16. A.F. Renteria, B. Saruhan, U. Schulz, H.-J. Raetzer-Scheibe, J. Haug, A. Wiedenmann, *Effect of morphology on thermal conductivity of EB-PVD PYSZ TBCs*, Surf. Coat. Technol. 201 (2006) 2611-2620.
17. H.-J. Rätzer-Scheibe, U. Schulz, *The effects of heat treatment and gas atmosphere on the thermal conductivity of APS and EB-PVD PYSZ thermal barrier coatings*, Surf. Coat. Technol. 201 (2007) 7880-7888.

18. A. Azzopardi, R. Mévrel, B. Saint-Ramonda, E. Olson, K. Stiller, *Influence of aging on structure and thermal conductivity of Y-PSZ and Y-FSZ EB-PVD coatings*, Surf. Coat. Technol. 177-178 (2004) 131-139.
19. C. M. Ramos, A. S. Tabata, P. F. Cesar, J. H. Rubo, P. A. Silveira Fracisconi, A. F. Sanches Borges, *Application of Micro-Raman Spectroscopy to the Study of Yttria-Stabilized Tetragonal Zirconia Polycrystal (Y-TZP) Phase Transformation*, Applied Spectroscopy 69 (2015) 810-814.
20. P. Y. Hou, Z. R. Shui, G. Y. Chuang, and J. Stringer, *Effect of Reactive Element Oxide Coatings on the High Temperature Oxidation Behavior of a FeCrAl Alloy*, J. Electrochem. Soc. 139 (1992) 1119-1126.
21. S. Chevalier, C. Nivot and J.P. Larpin, *Influence of Reactive Element Oxide Coatings on the High Temperature Oxidation Behavior of Alumina-Forming Alloys*, Oxidation of Metals 61 (2004) 195-217.
22. J. He, M. Luo, L. Jin, M. He, P. Fang, Y. Xie, *Raman Spectrum of Er-Y-codoped ZrO_2 and Fluorescence Properties of Er^{3+}*, Chinese Journal of Chemical Physics 20 (2006) 90-94.
23. U. Schulz, *Phase Transformation in EB-PVD Yttria Partially Stabilized Zirconia Thermal Barrier Coatings during Annealing*, J. Am. Ceram. Soc., 83 (2000) 904-910.
24. G. Di Girolamo, C. Blasi, L. Pagnotta, M. Schioppa, *Phase evolution and thermophysical properties of plasma sprayed thick zirconia coatings after annealing*, Ceramics International 36 (2010) 2273-2280.
25. S. Raghavan, H. Wang, R.B. Dinwiddie, W.D. Porter, and M.J. Mayo, *The Effect of Grain Size, Porosity and Yttria Content on the Thermal Conductivity of Nanocrystalline Zirconia*, Scripta Mat. 39 (1998) 1119-1125.
26. P.K. Schelling, S.R. Phillpot, *Mechanism of Thermal Transport in Zirconia and Yttria-Stabilized Zirconia by Molecular-Dynamics Simulation*, J. Am. Ceram. Soc. 84 (2001) 2997-3007.
27. D.G. Cahill, S-M. Lee and T.I. Selinder, *Thermal conductivity of κ-Al_2O_3 and α-Al_2O_3 wear-resistant coatings*, Journal of Applied Physics 83 (1998) 5783-5786.
28. J.-F. Bisson, D. Fournier, M. Poulain, O. Lavigne, R. Mévrel, *Thermal conductivity of yttria–zirconia single crystals, determined with spatially resolved infrared thermography*, J. Am. Ceram. Soc. 83 (2000) 1993-1998.

3. Article 4: Thermal Insulation of YSZ and Erbia-Yttria stabilized Zirconia EB-PVD Thermal Barrier Coating Systems after CMAS attack

Thermal Insulation of YSZ and Erbia doped Yttria-stabilized Zirconia EB-PVD Thermal Barrier Coating Systems after CMAS attack

G. Boissonnet[1], C. Chalk[2], J. R. Nicholls[2], G. Bonnet[1], F. Pedraza[1]

1. Université de La Rochelle, Laboratoire des Sciences de l'Ingénieur pour l'Environnement (LaSIE UMR-7356 CNRS), Avenue Michel Crépeau, 17042 La Rochelle, cedex 01 – France.

2. Cranfield University, Surface Engineering and Nanotechnology Institute (SENTi), College Rd., Wharley End, Bedford MK43 0AL – United Kingdom.

*corresponding author: boissonnet.germain@gmail.com

Keywords: Thermal barrier coatings (TBCs); Electron-beam physical vapour deposition (EB-PVD); Yttria stabilized zirconia (YSZ); Erbia doping; thermal diffusivity

Abstract. The impact of the adhesion of small deposits of calcium-magnesium-aluminium silicates (CMAS) on the top of electron-beam physical vapour deposition (EB-PVD) thermal barrier coatings (TBCs) made of yttria-stabilized zirconia (YSZ) is often neglected in most of the studies even though it might play a non-negligible role on the microstructural and chemical stability, hence on the thermal insulation potential of TBCs. Therefore, the present work investigates the degradation potential of minor CMAS deposits (from 0.25 to 5 $mg.cm^{-2}$) annealed at 1250°C for 1 h on a novel Er_2O_3-doped YSZ EB-PVD TBC, which is compared to the standard 8YSZ coating. Due to the high reactivity of Er_2O_3-doped coatings, CMAS penetration is limited in comparison with the standard YSZ coatings, hence resulting in a better thermal insulation of the former after ageing.

1. Introduction

The application of thermal barrier coatings (TBCs) on the metallic structures of the hottest sections of aero gas turbines offers many benefits like the increase in operating temperatures hence the engine efficiency, while enhancing component durability [1, 2]. TBCs comprise two layers: (i) a bond coating (BC), which is an oxidation-resistant metallic layer carrying the

structural load and (ii) a top coating (TC), which is a porous ceramic layer that acts as a thermal insulator between the substrate and the surrounding environment. The conventional material used for the TC in TBCs is zirconia (ZrO_2) stabilized with 6-9 wt. % yttria (Y_2O_3) [3]. Electron-beam physical vapour deposited (EB-PVD) thermal barrier coatings (TBCs) are widely used to protect the turbine blades of aircraft engines because their segmented columnar structure allows high strain compliance, resulting in superior thermal shock resistance [4]. Their continued development is essential for improving the efficiency and performance of gas turbines by allowing the inlet gas temperature to be increased further. For this reason, there is considerable interest in developing top coatings with even lower thermal conductivities [5].

The polymorphism of zirconia has led to the investigation of various stabilized zirconia alloys [6]. Among the different solutions investigated, doping with several other additives such as NiO, Nd_2O_3, Er_2O_3, Yb_2O_3 and Gd_2O_3 has been of interest as they allow to lower the thermal conductivity of YSZ ceramic [7]. ZrO_2-Er_2O_3, ZrO_2-Sm_2O_3 and ZrO_2-Nd_2O_3 TBCs have been reported to consist of non-transformable t' tetragonal phase up to compositions of 6 mol. % of stabilizer above which only the cubic structure occurs [8, 9, 10]. Erbia (Er_2O_3)-stabilized coatings showed better thermal phase stability than samaria (Sm_2O_3)- and neodymia (Nd_2O_3)-stabilized coatings, which decomposed into the monoclinic and tetragonal phases after heat treatment [8, 9, 10].

However, with the rise of the gas temperature for reduction of fuel consumption, the infiltration of siliceous molten deposits, also known as Calcium-Magnesium-Alumino-Silicates (CMAS) is of great concern [11]. In the hot-gas path and at peak temperatures, CMAS deposits yields a glassy melt that can penetrate the porous structure of ceramic coatings due to its low viscosity [12, 13]. Infiltration of the CMAS melt within the coating is slowed due to the inherent temperature gradient across the coating thickness and degrades the in-plane compliance of the structured ceramic that further leads to delamination processes upon thermal cycling. The progressive delamination of the ceramic leads to a loss in the insulating capacity of the TBC. As a result, the temperature at the metallic interface increases, which enhances the oxidation rate and causes the activation of other modes of failure, e.g. rumpling, cavitation [3], thus reducing the lifetime of the system. However, other CMAS-related failure mechanisms are susceptible to increase heat transport through the TBCs. Sintering of the ceramic is known to reduce the TBC mechanical performances [14] [15] [16] but may also contribute to a decrease in thermal resistance due to the loss of phonon-scattering defects, i.e. fine porosities of feather-like EB-PVD coatings [17]. The low-melting temperature of these silicate deposits (around

1200°C [11]) is therefore becoming a fundamental barrier to the increase of the gas temperature and reduction of fuel consumption, hence on the engine efficiency. Thus, a full understanding of the impact of CMAS on the insulating properties is crucial.

In parallel, researches are conducted to find mitigation solution to the CMAS corrosion issue, and the most recent strategies are based on the chemical reactivity of the TBC material in contact with the CMAS melt. For instance, Aygun et al. showed that co-doping of Al_2O_3 and TiO_2 with YSZ promoted the crystallization of the anorthite phase $CaAl_2Si_2O_8$ via local enrichment of Al_2O_3 into the CMAS melt [18]. More recently, rare-earth (RE) zirconates, used as TBC material (RE = Gd [19], Y [20, 21], Yb [21], Sm [22, 23], Nd [24], La [25]), were shown to foster the rapid crystallization of stable apatite and fluorite phases as soon as the CMAS melt starts to dissolve the ceramic coating [11].

Therefore, in this work, the thermal insulation potential and the resistance to CMAS attack of yttria and erbia stabilised zirconia EB-PVD coatings have been compared to those of the state-of-the-art yttria-stabilised zirconia (8YSZ). Both coatings were synthesized on Ni-based alloys and exposed to high temperature in order to evaluate the impact of the microstructural transformations on the thermal insulation properties.

2. Experimental

The EB-PVD coatings were produced at the Surface Engineering and Nanotechnology Institute (SENTi) in Cranfield University (UK) on Inconel 600 substrates (15.5 Cr, 8.0 Fe, 0.5 Mn, < 0.5 Cu, < 0.5 Si, wt. %, bal. Ni). Prior to the deposition of the ceramic, the Inconel 600 plates were cut into 10 x 10 mm^2 coupons and aluminized via Chemical Vapour Deposition (CVD). Two different rods were used to perform the elaboration of the 8YSZ coatings (ZrO_2 - 8 mol. % Y_2O_3) and the Er/Y co-stabilised ones (ZrO_2 – 4 mol.% Y_2O_3 – 4 mol.% Er_2O_3).

The CMAS mixture, whose composition is given in ***Table 1*** was used for the corrosion tests. This composition was drawn from previous studies conducted by Aygun et al. [18] and is close to the model CMAS composition used in other studies [11]. The individual oxide powders were mixed in deionized water to form a thick paste which was put into Pt-10Rh crucibles and heated a first time at 1400°C for 4 h. The resulting glassy melt was crushed in a mortar, re-melted for 4 h at 1400°C to improve the glass homogeneity and crushed again.

Table 1 *– Average composition of the model CMAS measured via EDS (mol. %).*

CaO	MgO	Al_2O_3	SiO_2	Fe_2O_3
36	6	5	52	1

CMAS deposits of 0.25, 1 and 5 mg.cm^{-2} were applied on both types of coatings (see samples characteristics in **Table 2**). After an annealing treatment at 1250°C for 1h, the samples were slowly cooled down till RT to avoid spallation.

Table 2 *– Samples of the study.*

Sample ID	**Initial coating**	**TBC thickness (µm)**	**CMAS deposit (mg.cm^{-2})**
As-deposited	*8YSZ standard* (ZrO_2 - 8 mol. % Y_2O_3)	202.0 ± 5.6	-
Std025		209.1 ± 1.5	0.26 ± 0.1
Std1		203.0 ± 1.1	1.03 ± 0.1
Std5		194.4 ± 1.7	5.07 ± 0.1
As-deposited	*ErYSZ* (ZrO_2 - 4 mol.% Y_2O_3 - 4 mol.% Er_2O_3)	148.3 ± 8.3	-
Er025		145.7 ± 1.9	0.25 ± 0.1
Er1		155.9 ± 2.4	0.98 ± 0.1
Er5		158.2 ± 1.2	5.02 ± 0.1

The microstructural changes were investigated from polished cross-sections with a FEI Quanta 200F scanning electron microscope (SEM) coupled to an EDAX detector for local analysis of the composition using energy dispersive spectrometry (EDS). Raman micro-spectrometry (Jobin Yvon LabRam HR800, λ_{laser} ~632nm) was employed to follow the structural changes of the ceramic coatings on the surface and on the cross-section. To assess the evolution of the thermal insulation potential of the TBCs, thermal diffusivity was determined using high-temperature laser-flash measurements with a Linseis LFA1600 apparatus at low pressure (~1.10^{-2} mbar), every 100°C between room temperature and 1100°C. The calculations were performed using a 2-layer model – (i) YSZ and (ii) substrate + aluminide layer – to assess the thermal diffusivity of the full thermal barrier coating systems. Prior to the measurements with the laser flash, the thicknesses of the multilayer samples were accurately determined (± 10^{-3} mm) with a digital calliper. The surfaces of the samples were coated with a graphite spray to foster absorption of the laser and heat emissivity. Heat is collected with an infrared detector situated at the front of the specimens. The thicknesses of the coatings to be used in the multilayer calculations were measured from the cross-sectional images.

3. Results

3.1. EB-PVD coatings without CMAS

Fig. 1 presents the microstructural features of the as-deposited coatings (**Fig. 1a**, **b** and **c**) compared with the ones of the standard 8YSZ (**Fig. 1d**, **e** and **f**) and ErYSZ coatings (**Fig. 1g**, **h** and **i**) annealed at 1250°C for 1h. Both the standard 8YSZ and the ErYSZ coatings present the typical columnar morphology of EB-PVD ceramic top coatings attached to a thin (~ 0.6 µm) α-Al_2O_3 grown oxide layer on a β-NiAl bond coating of about 30 µm in the as-deposited conditions (**Fig. 1a**). With the annealing at 1250°C for 1h, the α-Al_2O_3 layer grows till ~2 µm in both coatings (**Fig. 1e** and **Fig. 1h**). With annealing, the feather-like morphology of the columns in which small pores were trapped in the as-deposited conditions (**Fig. 1c**) tend to sinter. For the 8YSZ coating (**Fig. 1f**) the intra-lamellar gaps started to close. In the case of the ErYSZ ceramic (**Fig. 1i**), the stiffening that may have occurred during ageing resulted in the appearance of cracks in the columns.

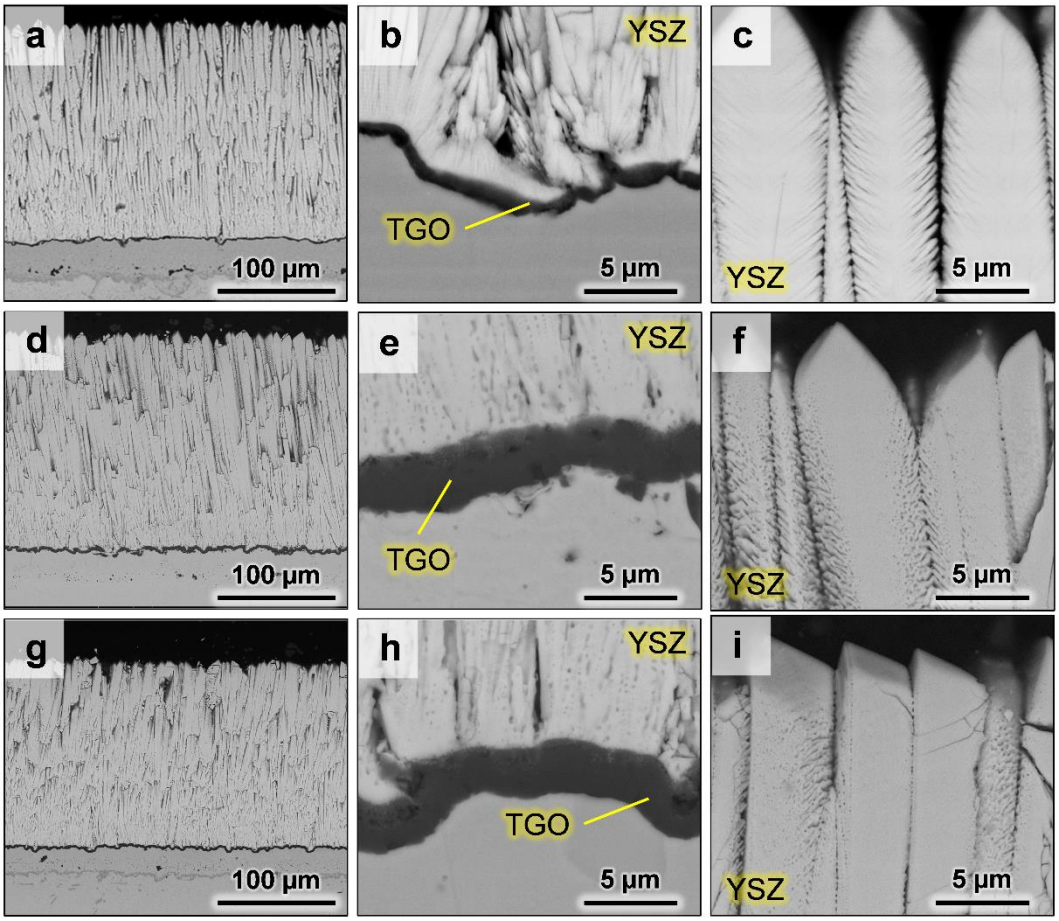

***Fig. 1** – SEM micrographs of the EB-PVD coatings in the as-deposited conditions with **a**, **b** and **c** (similar for both 8YSZ and* ErYSZ *coatings) and after ageing in air at 1250°C for 1h with **d**, **e** and **f** for the standard 8YSZ coating and **g**, **h** and **i** for the ErYSZ coating.*

Fig. 2 shows the phase composition along the cross-section of both coatings in the as-deposited conditions and after annealing in air at 1250°C for 1h measured by Raman micro-spectrometry. For the standard 8YSZ coating, the Raman spectra show that the stabilized tetragonal phase of zirconia (*t'*-ZrO_2) is the only one detected for both as-deposited and annealed coatings, with the characteristic bands of tetragonal ZrO_2 at ~153, 255, 335, 475, 615 and 642 cm^{-1} [26, 27]. After annealing, the Raman bands tend to sharpen and are slightly shifted compared to the as-deposited coating. For the ErYSZ coatings, the same bands are observed for both as-deposited and annealed conditions. The bands observed at ~275, 320, 410, 445, 505, 550 and 650 cm^{-1} have also been observed for Er-doped YSZ powders in previous studies [28, 29]. He et al. explained that the Raman bands of ZrO_2 overlap with the fluorescence bands of Er^{3+}, thus preventing a clear identification of the phases of zirconia [28].

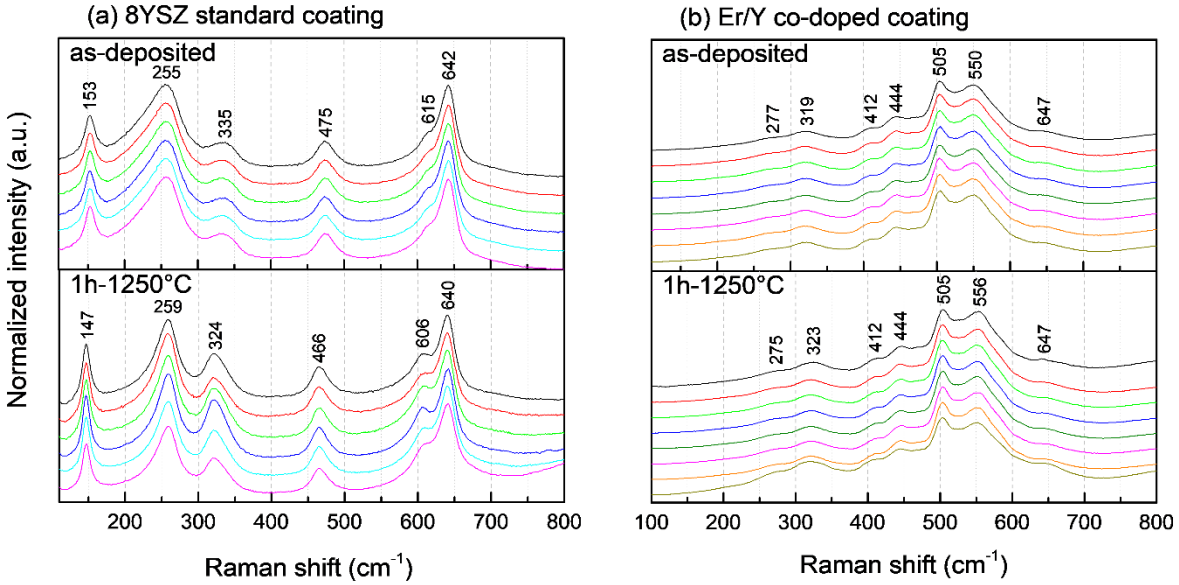

***Fig. 2** – Raman spectra of the 8YSZ standard and ErYSZ coatings in their as-deposited conditions and after annealing in air at 1250°C for 1h.*

3.2. EB-PVD coatings corroded by CMAS

On the surface of the 8YSZ standard coatings annealed at 1250°C with CMAS in **Fig. 3a**, **b** and **c**, a dark phase associated with melted CMAS covers an increasing surface of the coating with increasing the amount of deposited CMAS. These residual CMAS means that the melt did not fully penetrate the ceramic coatings. On the associated cross-sections (**Fig. 3d**, **e** and **f**), the microstructure of the upper part of the columns looks corroded along with an apparent sintering between the columns, whose depth and homogeneity increases with the amount of CMAS. This

penetration thus led to transformations of the edges of the columns as well as sintering due to the sealing of the inter-columnar gap by the CMAS. For the ErYSZ coatings, a similar distribution of the residual CMAS is observed on the surface of the coatings **Fig. 4a**, **b** and **c**. However, the microstructure of the cross-section of the coatings (**Fig. 4d**, **e** and **f**) appears less corroded than the one of the standard 8YSZ. Indeed, the CMAS seem to have reacted with a smaller depth of the co-stabilised coatings compared with the standard ones. The coatings also look brittle with several cracks of the columns irrespective of the amount of deposited CMAS since the cracks were also observed in the annealed coatings without CMAS.

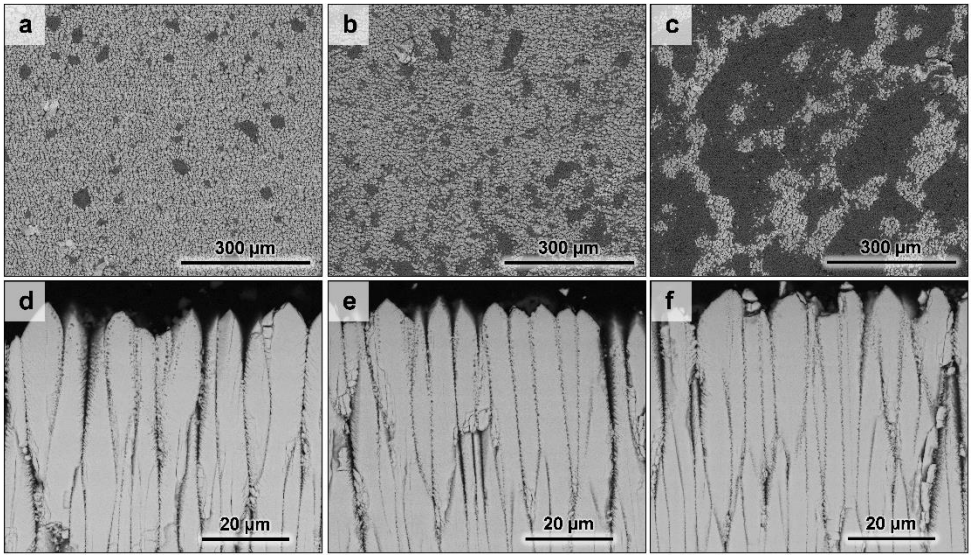

Fig. 3 *– SEM micrographs of the standard 8YSZ coating with CMAS deposits of (**a**, **d**) 0.25, (**b**, **e**) 1 and (**c**, **f**) 5 mg.cm^{-2} annealed in air at 1250°C for 1h.*

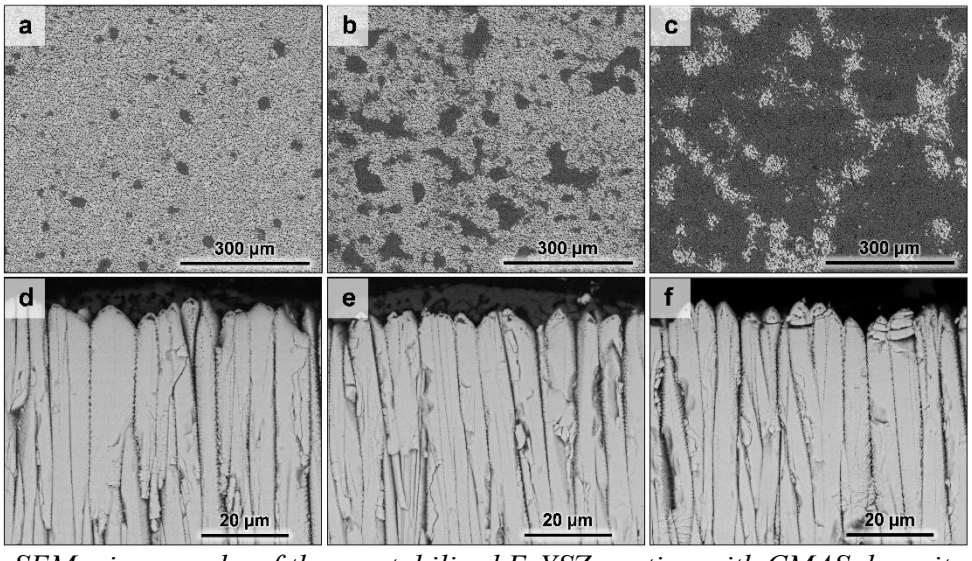

Fig. 4 *– SEM micrographs of the co-stabilised ErYSZ coating with CMAS deposits of (**a**, **d**) 0.25, (**b**, **e**) 1 and (**c**, **f**) 5 mg.cm^{-2} annealed in air at 1250°C for 1h.*

The EDS elemental analysis of the cross-sections of the 8YSZ and ErYSZ coatings (**Fig. 5**) shows that the high concentration of the CMAS elements in the upper part of the coatings decreases with increasing depth. In the case of the 8YSZ standard coatings, the CMAS penetrated fully the coatings (**Fig. 5a**, **b** and **c**). On the opposite, very low contents of the CMAS elements were detected deep in the ErYSZ coatings (**Fig. 5d**, **e** and **f**) even when the maximum amount of 5 mg.cm^{-2} of CMAS had been deposited. This means that the penetration of the CMAS melt was hampered in the ErYSZ coating.

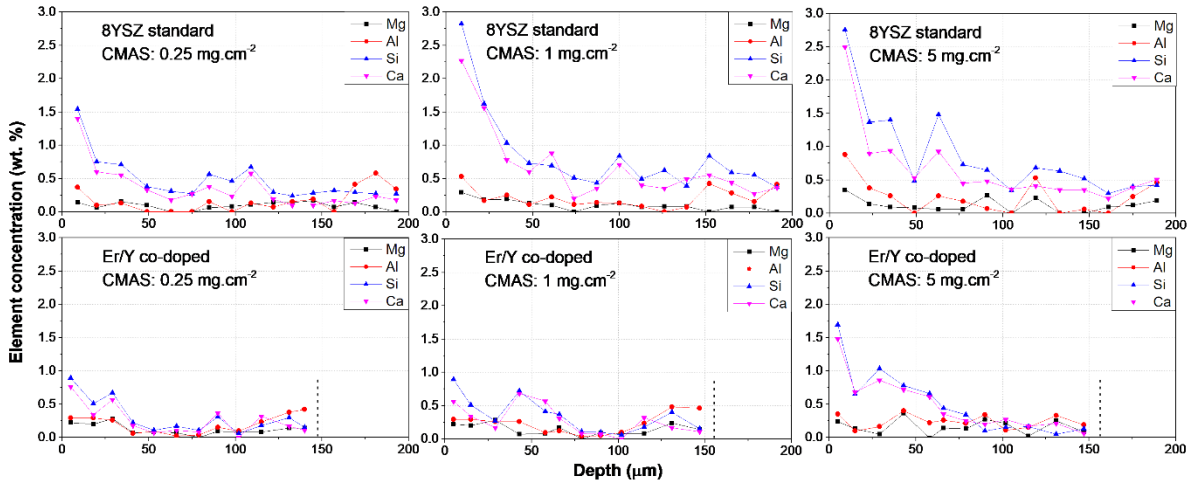

***Fig. 5** – EDS elemental analysis of the CMAS compounds present in* the cross sections of *the standard 8YSZ and co-stabilised ErYSZ after annealing with the different CMAS deposits.*

Fig. 6 shows the phase transformations of zirconia of the 8YSZ standard coatings exposed to different amounts of CMAS. The Raman spectra along the cross-section indicate little transformation of the initial tetragonal phase of zirconia (*t'*-ZrO_2) into the Y-lean monoclinic phase (*m*-ZrO_2). Also, the transformation does not seem to depend on the amount of deposited CMAS and only very minor presence of the *m*-ZrO_2 occurred randomly when increasing the CMAS deposit. In contrast, no particular phase transformations occurred in any of the ErYSZ coatings attacked by CMAS since all the Raman spectra were identical to as-deposited one (see **Fig. 7**).

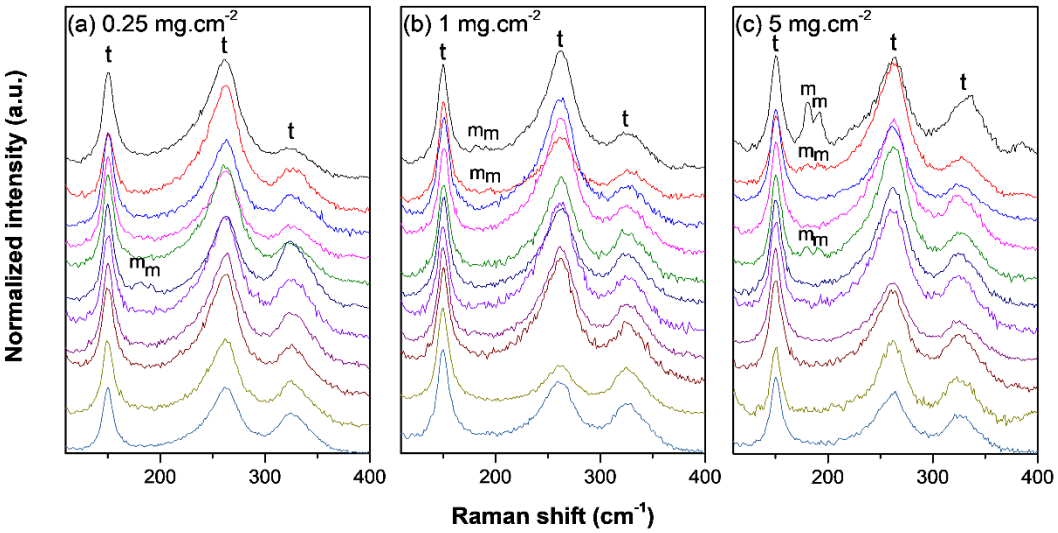

Fig. 6 *– Raman spectra in* the cross sections *of the standard 8YSZ coatings with CMAS deposits of* ***(a)*** *0.25,* ***(b)*** *1 and* ***(d)*** *5 mg.cm^{-2} annealed in air at 1250°C for 1h.*

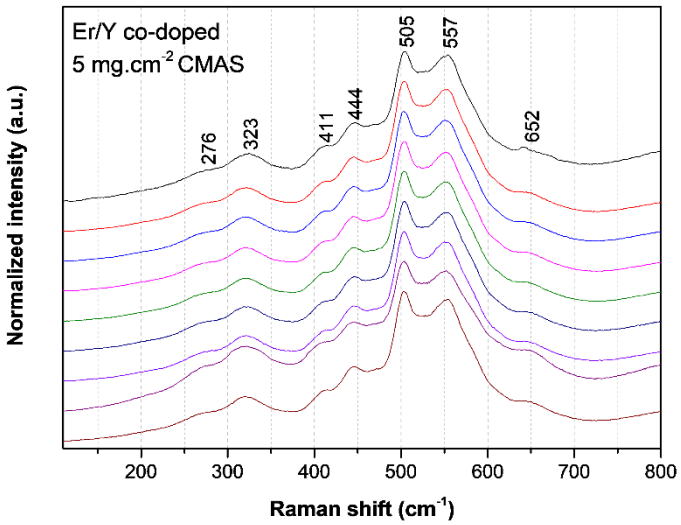

Fig. 7 *– Raman spectra in* the cross sections *of the ErYSZ coating annealed in air at 1250°C for 1h with 5 mg.cm^{-2} CMAS deposit.*

3.3. Thermal diffusivity measurements

In the as-deposited conditions, the thermal diffusivity of 8YSZ standard coating displays a maximum of ~5.8×10^{-7} m^2.s^{-1} at room temperature (RT) and a minimum of ~4×10^{-7} m^2.s^{-1} at high temperature (**Fig. 8a**). After the annealing in air at 1250°C with the CMAS deposits, the thermal diffusivity of the 8YSZ standard coatings increases. With 0.25 and 1 mg.cm^{-2} of CMAS, the thermal diffusivities are equivalent with a maximum of ~8×10^{-7} m^2.s^{-1} at room temperature and a minimum of ~5.2×10^{-7} m^2.s^{-1} at high temperature. However, the thermal diffusivity of the coating with 5 mg.cm^{-2} of CMAS is slightly inferior than with 0.25 and 1

mg.cm^{-2} deposits. The thermal diffusivity falls to ~7.5×10^{-7} m^2.s^{-1} and to ~4.6×10^{-7} m^2.s^{-1} at room and high temperature, respectively.

For the as-deposited ErYSZ coatings (**Fig. 8b**), the thermal diffusivity is lower than the 8YSZ standard one with a maximum of ~5.5×10^{-7} m^2.s^{-1} at RT and a minimum of ~3.8×10^{-7} m^2.s^{-1} at high temperature. However, the thermal diffusivity decreases after the reaction of the coatings with the CMAS deposits. The thermal diffusivity of Er025 is the lowest and ranges between ~2.8 and ~4.5×10^{-7} m^2.s^{-1}. The coating exposed to 5 mg.cm^{-2} of CMAS (Er5) displays intermediate values between ~5×10^{-7} m^2.s^{-1} and ~3×10^{-7} m^2.s^{-1} while the Er1 coating exhibit values ranging between ~4.6 and ~3.6×10^{-7} m^2.s^{-1}, which are close to the ones of the as-deposited conditions.

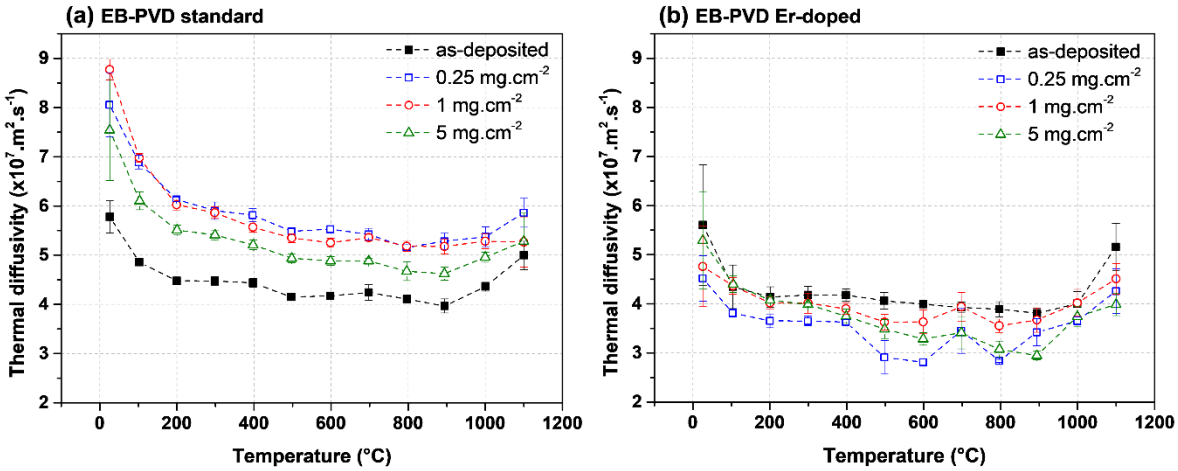

***Fig. 8** – Thermal diffusivity of **(a)** 8YSZ standard and **(b)** ErYSZ TBC systems in the as-deposited condition and after CMAS attack.*

4. Discussion

With the annealing at 1250°C in air for 1h, both the 8YSZ standard and the ErYSZ coatings exhibited microstructural transformations with the sintering of the small intra-columnar pores and the closing of the pores trapped in the feather-like structure associated with the growth of the α-Al_2O_3 TGO (see **Fig. 1**). Similar transformations were observed in previous works for standard EB-PVD YSZ coatings [30, 31, 32] and ErYSZ coatings [29]. However, no phase transformation was highlighted during the annealing treatment as only the tetragonal phase of zirconia was detected in the Raman analysis (see **Fig. 2**).

After the exposure of the coatings to the CMAS deposits for 1h at 1250°C, some residues of the glassy melt were found at the surface of the coatings (see **Fig. 3**). This suggests that either

the whole amount of CMAS deposited did not melt completely or that they were too viscous to penetrate fully in the coatings. The first hypothesis can probably be disregarded because of the glassy appearance of the residues. Nevertheless, the capillaries formed by the columnar structure of the EB-PVD coatings allowed the CMAS to penetrate the standard YSZ coatings (see **Fig. 5a**, **b** and **c**) and to sinter the columns (see **Fig. 3d**, **e** and **f**). Sintering is a well-known factor that reduce the thermal insulation of EB-PVD coatings [31, 32] and can therefore explain the increase of the thermal diffusivity of the coatings exposed to CMAS. In a previous work, similar CMAS deposits (0.25 to 3 $mg.cm^{-2}$) where used on freestanding plasma-sprayed YSZ coatings and an increasing trend of the thermal diffusivity was observed with increasing CMAS deposits [33]. However, such increase was not observed for the EB-PVD coatings. In contrast, even lower thermal diffusivities were observed for the higher amounts of CMAS, i.e. the lowest thermal diffusivity occurred with the densest CMAS deposit of 5 $mg.cm^{-2}$ (**Fig. 8a**). Thus, the thermal diffusivity in this case does not seem to be directly related to the amount of deposited CMAS

This suggests that other factors than sintering could be responsible for the change in the heat transport properties of the TBCs exposed to CMAS. These include (i) the phase transformations of zirconia [34, 35, 32], (ii) the thermal transport properties of the CMAS and its reaction products [36] and (iii) the increase of interfacial resistance that was not considered in the multilayer calculation such as the growth of the TGO [29, 37].

The phase transformations of YSZ in contact with CMAS have been shown to result from the depletion of Y in the YSZ via the dissolution-reprecipitation mechanism of corrosion by molten CMAS [11, 12, 38]. Bisson et al. showed that decreasing the Y_2O_3 content in YSZ single crystals contributed to an increase in the thermal diffusivity [34]. However, no significant phase transformations of the zirconia have been observed in our study via Raman analysis (**Fig. 6**). Thus, the increase in thermal diffusivity due to phase transformations should be negligible.

Considering the thermal transport properties of CMAS itself, Kakuda et al. showed that the thermal diffusivity of crystallized CMAS was very close to that of the fully dense 7YSZ and that the one of amorphous CMAS was half the one of its crystallized form [36]. Therefore, the addition of CMAS in the coating could lead to a decrease of the thermal diffusivity, and the presence of residual CMAS on top of the coatings would also hamper the heat transport. This would thus explain the smaller thermal diffusivity values of the Std5 coating which was almost entirely covered by CMAS.

The growth of the TGO observed in the case of the annealed coatings (see **Fig. 1**) might also add a non-negligible resistance to the thermal transport that would lead to an underestimation of the coating's thermal diffusivity because the TGO growth has not been considered in the multilayer calculation. The influence of the TGO was observed in previous works when measuring the thermal diffusivity of plasma-sprayed coatings as part of a complete TBC system (substrate + bond coating + top coating) [37]. In addition, after 500h annealing at 1150°C of the same standard YSZ EB-PVD coating, the increase in TGO thickness from 0.6 to 1.2 µm already led to a discrepancy between the thermal diffusivity of coatings of different thicknesses, i.e. a 5% decrease of the top coating thickness was linked to a 10% decrease of the calculated thermal diffusivity values [29]. Thus, the underestimation of the thermal diffusivity would be greater for the thinner coatings.

As a matter of fact, the Std1 coating that is 3% thinner than the Std025 one (**Table 1**) display a slightly lower thermal diffusivity than the latter (**Fig. 8a**) despite the higher sintering observed in **Fig. 3**. Moreover, the Std5 sample, which is 15% thinner than the Std025 shows a significantly lower thermal diffusivity (**Fig. 8a**). The lower calculated thermal diffusivity values could be thus assigned to both the smaller thickness of the top coating that exacerbate the TGO influence and the remaining CMAS on top of the coatings.

In the case of the ErYSZ coatings, the thermal diffusivity in the as-deposited conditions was observed to be smaller than the one of the standard 8YSZ coating (**Fig. 8b**) which agrees with the effect of erbia doping that was demonstrated to be responsible for thermal diffusivity reduction [7, 29]. When considering the CMAS attacked coatings, the penetration of the CMAS was limited to the upper part of the coatings (see **Fig. 4** and **Fig. 5d**, **e** and **f**) and only a limited transformation of the microstructure of the top of the columns was observed irrespective of the amount of deposited CMAS. This behaviour was ascribed to the high reactivity of the RE oxide that could mitigate CMAS penetration [11]. Therefore, as the CMAS penetration was hampered, the impact of the sintering by the melt is limited in the ErYSZ coatings. In comparison with the 8YSZ standard TBC, the calculated thermal diffusivity of this ErYSZ coating should thus mostly be affected by (i) the coverage of the surface by CMAS, (ii) the TGO growth whose impact depend on the TBC thickness and (iii) on the phase transformations. The calculated thermal diffusivity of the CMAS attacked ErYSZ coatings was not significantly different from the one in the as-deposited condition (**Fig. 8b**). This means that the possible contribution to the increase of the thermal diffusivity by sintering and phase transformations was compensated by the combination of the insulating potential of the residual CMAS and the

TGO growth. This hypothesis is supported by the results of Figures 4 and 7 where neither the sintering nor the phase transformations appear significant for all the ErYSZ coatings.

Therefore, the slight decrease of the thermal diffusivity observed for the CMAS attacked coatings could be ascribed to the insulative potential of both the TGO growth and the residual CMAS. As the coverage by the CMAS melt was observed similar for both ErYSZ and YSZ coatings (see **Fig. 3** and **Fig. 4**), the insulative potential should be similar. However, its impact might be even slightly higher in the case of the ErYSZ as CMAS penetration was observed to be negligible and would thus mean that a thicker CMAS coat could be covering the ErYSZ top coatings (this was not measured due to the heterogeneity of the coverage). In addition, the TGO growth was observed to be similar for both the ErYSZ coatings and the standard YSZ one (from ~0.6 µm in the as-deposited conditions to ~2 µm; see **Fig. 1**) and should thus bring about a similar impact on the calculated thermal diffusivity. Nevertheless, the top coating thicknesses of the ErYSZ were significantly lower than those of the standard YSZ, e.g. there is a ~36 µm gap between the thinner standard top coating (Std5) and the thicker ErYSZ one (Er5) (see **Table 2**). Thus, the impact of the TGO growth on the calculated values of the thermal diffusivity of the ErYSZ coatings should be more pronounced compared to the ones of the standard coatings.

5. Conclusions

This study investigated the degradation potential of minor CMAS deposits (0.25, 1, and 5 $mg.cm^{-2}$) on ErYSZ and standard 8YSZ EB-PVD TBCs annealed at 1250°C for 1h. The CMAS was not allowed to fully penetrate the coatings, which resulted in the partial coverage of the surface of the coatings. Irrespective of the CMAS amount, the melt that penetrated the ceramic layer reached the full thickness of the standard YSZ coatings but was limited for the ErYSZ coatings. The associated microstructural and chemical transformations were thus less important for the ErYSZ coatings, hence, resulting in a better thermal insulation after ageing in the presence of CMAS.

ACKNOWLEDGEMENTS

The authors gratefully acknowledge SR Technics Airfoils Services, Ltd. (Ireland) for providing the substrates of this study.

REFERENCES

1. A.G. Evans, D.R. Clarke, C.G. Levi, *The influence of oxides on the performance of advanced gas turbines*, J. Eur. Ceram. Soc. 28, **2008**, 1405-1419.
2. R. Vaßen, M. Ophelia-Jarligo, T. Steinke, D. Emil-Mack, D. Stöver, *Overview on advanced thermal barrier coatings*, Surf. Coat. Technol. 205, **2010**, 938-942.
3. D.R. Clarke, M. Oechsner, N.P. Padture, *Thermal-barrier coatings for more efficient gas-turbine engines*, MRS Bull. 37, **2012**, 891-898.
4. U. Schulz, C. Leyens, K. Fritscher, M. Peters, B. Saruhan-Brings, O. Lavigne, J.M. Dorvaux, M. Poulain, R. Mevrel, M.L. Caliez, *Some recent trends in research and technology of advanced thermal barrier coatings,* Aerosp. Sci. Technol. 7, **2003**, 73-80.
5. M.R. Winter, D.R. Clarke, *Oxide materials with low thermal conductivity*, J. Am. Ceram. Soc. 90, **2007**, 533-540.
6. P. A. Langjahr, R. Oberacker, and M. J. Hoffmann, *Long-term behavior and application limits of plasma-sprayed zirconia thermal barrier coatings*. J. Am. Ceram. Soc., 84, **2001**, 1301-1308.
7. J. R. Nicholls, K. J. Lawson, A. Johnstone and D. S. Rickerby, *Methods to reduce the thermal conductivity of EB-PVD TBCs,* Surf. Coat. Technol. 151-152, **2002**, 383-391.
8. K. A. Khor and J. Yang, *Lattice parameters, tetragonality (c/a) and transformability of tetragonal zirconia phase in plasma-sprayed ZrO_2–Er_2O_3 coatings.* Mater. Lett. 31, **1997**, 23-27.
9. K. A. Khor and J. Yang, *Plasma sprayed ZrO_2–Sm_2O_3 coatings: lattice parameters, tetragonality (c/a) and transformability of tetragonal zirconia phase.* J. Mater. Sci. Lett. 16, **1997**, 1002-1004.
10. K. A. Khor and J. Yang, *Transformability of t-ZrO_2 and lattice parameters in plasma sprayed rare-earth oxides stabilized zirconia coatings.* Scripta Mater. 37, **1997,** 1279-1286.
11. C.G. Levi, J.W. Hutchinson, M.-H. Vidal Sétif, C.A. Johnson, *Environmental degradation of thermal-barrier coatings by molten deposits*, MRS Bull. 37, **2012**, 932-940.
12. M.P. Borom, C.A. Johnson, L.A. Peluso, *Role of environmental deposits and operating surface temperature in spallation of air plasma sprayed thermal barrier coatings*, Surf. Coat. Technol. 86-87, **1996**, 116-126.

13. C. Mercer, S. Faulhaber, A.G. Evans, R. Darolia, *A delamination mechanism for thermal barrier coatings subject to calcium–magnesium–alumino-silicate (CMAS) infiltration*, Acta Mater. 53, **2005**, 1029-1039.

14. R.G. Wellman, J.R. Nicholls, *On the effect of ageing on the erosion of EB-PVD TBCs*, Surf. Coat. Technol. 177-178, **2004**, 80-88.

15. X. Zhao, X. Wang, P. Xiao, *Sintering and failure behaviour of EB-PVD thermal barrier coating after isothermal treatment*, Surf. Coat. Technol. 200, **2006**, 5946-5955.

16. A.C.F. Cocks, N.A. Fleck, *Constrained sintering of an air-plasma-sprayed thermal barrier coating*, Acta Mater.58, **2010**, 4233-4244.

17. I.O. Golosnoy, A. Cipitria, T.W. Clyne, *Heat transfer through plasma-sprayed thermal barrier coatings in gas turbine: a review of recent work*, J. Therm. Spray Technol. 18, **2009**, 809-821.

18. A. Aygun, A.L. Vasiliev, N.P. Padture, X. Ma, *Novel thermal barrier coatings that are resistant to high-temperature attack by glassy deposits*, Acta Mater. 55, **2007**, 6734-6745.

19. S. Krämer, J. Yang, C.G. Levi, *Infiltration-inhibiting reaction of gadolinium zirconate thermal barrier coatings with CMAS melts*, J. Am. Ceram. Soc. 91, **2008**, 576-583.

20. A.R. Krause, X. Li, N.P. Padture, *Interaction between ceramic powder and molten calcia-magnesia-alumino-silicate (CMAS) glass, and its implication on CMAS-resistant thermal barrier coatings*, Scripta Mater. 112, **2016**, 118-122.

21. J.M. Drexler, A.L. Ortiz, N.P. Padture, *Composition effects of thermal barrier coating ceramics on their interaction with molten Ca-Mg-Al-silicate (CMAS) glass*, Acta Mater. 60, **2012**, 5437-5447.

22. H. Wang, A. Bakal, X. Zhang, E. Tarwater, Z. Sheng, J.W. Fergus, *CaO-MgO-Al_2O_3-SiO_2 (CMAS) corrosion of $Gd_2Zr_2O_7$ and $Sm_2Zr_2O_7$*, J. Electrochem. Soc. 163, **2016**, C643-C648.

23. H.B. Zhao, C.G. Levi, H.N.G. Wadle, Molten silicate interactions with thermal barrier coatings, Surf. Coat. Technol. 251, **2014**, 74-86.

24. N. Chellah, *Contribution à la compréhension de la dégradation chimique de barrières thermiques en zircone yttriée par les CMAS en vue de proposer une nouvelle composition*

céramique résistante dans le système ZrO_2-Nd_2O_3, thesis of the University of Lorraine, France, **2016**.

25. U. Schulz, W. Braue, Degradation of $La_2Zr_2O_7$ and other novel EB-PVD thermal barrier coatings by CMAS (CaO-MgO-Al_2O_3-SiO_2) and volcanic ash deposits, Surf. Coat. Technol. 235, **2013**, 165-173.

26. C. Viazzi, J-P. Bonino, F. Ansart, A. Barnabé, *Structural study of metastable tetragonal YSZ powders produced via a sol-gel route*, J. Alloys Compd. 452, **2008**, 377-383.

27. C.M. Ramos, A.S. Tabata, P.F. Cesar, J.H. Rubo, P.A. Silveira Fracisconi, A.F. Sanches Borges, *Application of Micro-Raman Spectroscopy to the Study of Yttria-Stabilized Tetragonal Zirconia Polycrystal (Y-TZP) Phase Transformation*, Appl. Spectrosc. 69, **2015**, 810-814.

28. J. He, M. Luo, L. Jin, M. He, P. Fang, Y. Xie, *Raman Spectrum of Er-Y-codoped ZrO_2 and Fluorescence Properties of Er^{3+}*, Chin. J. Chem. Phys. 20, **2006**, 90-94.

29. G. Boissonnet, C. Chalk, J. R. Nicholls, G. Bonnet, F. Pedraza, *Phase stability and thermal insulation of YSZ and erbia-yttria stabilized zirconia EB-PVD thermal barrier coating systems*, in preparation.

30. A.F. Renteria, B. Saruhan, U. Schulz, H.-J. Raetzer-Scheibe, J. Haug, A. Wiedenmann, *Effect of morphology on thermal conductivity of EB-PVD PYSZ TBCs*, Surf. Coat. Technol. 201, **2006**, 2611-2620.

31. H.-J. Rätzer-Scheibe, U. Schulz, *The effects of heat treatment and gas atmosphere on the thermal conductivity of APS and EB-PVD PYSZ thermal barrier coatings*, Surf. Coat. Technol. 201, **2007**, 7880-7888.

32. A. Azzopardi, R. Mévrel, B. Saint-Ramonda, E. Olson, K. Stiller, *Influence of aging on structure and thermal conductivity of Y-PSZ and Y-FSZ EB-PVD coatings*, Surf. Coat. Technol. 177-178, **2004**, 131-139.

33. G. Boissonnet, C. Chalk, J. Nicholls, G. Bonnet, F. Pedraza, *Thermal insulation of CMAS (Calcium-Magnesium-Alumino-Silicates)-attacked plasma-sprayed thermal barrier coatings*, in preparation.

34. J.-F. Bisson, D. Fournier, M. Poulain, O. Lavigne, R. Mévrel, Thermal conductivity of yttria–zirconia single crystals, determined with spatially resolved infrared thermography, J. Am. Ceram. Soc. 83, **2000**, 1993-1998.

35. G. Di Girolamo, C. Blasi, L. Pagnotta, M. Schioppa, *Phase evolution and thermophysical properties of plasma sprayed thick zirconia coatings after annealing*, Ceram. Int. 36, **2010**, 2273-2280.

36. T.R. Kakuda, C.G. Levi, T.D. Bennett, *The thermal behavior of CMAS-infiltrated thermal barrier coatings*, Surf. Coat. Technol. 272, **2015**, 350-356.

37. G. Boissonnet, G. Bonnet, A. Pasquet, N. Bourhila, F. Pedraza, *Evolution of thermal insulation of plasma-sprayed thermal barrier coating systems with exposure to high temperature*, J. Eur. Ceram. Soc., **2019**, doi: 10.1016/j.jeurceramsoc.2019.01.026.

38. S. Krämer, J. Yang, C.G. Levi, *Thermochemical interaction of thermal barrier coatings with molten CaO–MgO–Al_2O_3–SiO_2 (CMAS) deposits*, J. Am. Ceram. Soc. 89, **2006**, 3167-3175.

4. References introduction chapter IV

1. . R. Nicholls, K. J. Lawson, A. Johnstone and D. S. Rickerby, *Methods to reduce the thermal conductivity of EB-PVD TBCs,* Surf. Coat. Technol. 151-152, **2002**, 383-391.

2. C.G. Levi, J.W. Hutchinson, M-H. Vidal-Sétif and C.A. Johnson, *Environmental degradation of thermal barrier coatings by molten deposits*, MRS Bulletin 37 (2012) 932-941.

3. A.F. Renteria, B. Saruhan, U. Schulz, H.-J. Raetzer-Scheibe, J. Haug, A. Wiedenmann, *Effect of morphology on thermal conductivity of EB-PVD PYSZ TBCs*, Surf. Coat. Technol. 201 (2006) 2611-2620.

4. H.-J. Rätzer-Scheibe, U. Schulz, T. Krell, *The effect of coating thickness on the thermal conductivity of EB-PVD PYSZ thermal barrier coatings*, Surface and Coatings Technology 200, **2006**, 5636-5644.

5. H.-J. Rätzer-Scheibe, U. Schulz, *The effects of heat treatment and gas atmosphere on the thermal conductivity of APS and EB-PVD PYSZ thermal barrier coatings*, Surf. Coat. Technol. 201, **2007**, 7880-7888.

6. A. Azzopardi, R. Mévrel, B. Saint-Ramonda, E. Olson, K. Stiller, *Influence of aging on structure and thermal conductivity of Y-PSZ and Y-FSZ EB-PVD coatings*, Surf. Coat. Technol. 177-178, **2004**, 131-139.

7. T.R. Kakuda, A.M. Limarga, T.D. Bennett, D.R. Clarke, *Evolution of thermal properties of EB-PVD 7YSZ thermal barrier coatings with thermal cycling*, Acta Materialia 57, **2009**, 2583-2591.

8. S. Krämer, J. Yang, C.G. Levi, *Thermochemical interaction of thermal barrier coatings with molten CaO–MgO–Al_2O_3–SiO_2 (CMAS) deposits*, J. Am. Ceram. Soc. 89, **2006**, 3167-3175.

9. W. Braue, *Environmental stability of the YSZ layer and the YSZ/TGO interface of an in-service EB-PVD coated high-pressure turbine blade*, Journal of Material Sciences, **2009**, 1664-1675.

10. H.B. Zhao, C.G. Levi, H.N.G. Wadle, Molten silicate interactions with thermal barrier coatings, Surf. Coat. Technol. 251, **2014**, 74-86.

V. ELABORATION AND CHARACTERISATION OF THERMAL BARRIER COATINGS MADE FROM A SLURRY CONTAINING ALUMINIUM MICROPARTICLES

Table of contents

1. Introduction

As explained in §I.1.3.2.2, the formation of a complete thermal barrier coating using the slurry technique appears to be a convincing alternative for protection of materials of the low-pressure turbine (LPT) section due to its relative low cost and ease of application. The principal challenges and strategy to obtain a TBC system from a slurry containing Al microparticles were already exposed in §I.4.2.2. This chapter is comprised of two articles.

The mechanisms of formation of the coatings using the hybrid-atmosphere heat treatment described in §I.4.2.2.3 were developed on a pure Ni model substrate and will be discussed in **the first article** (article 5) of this chapter. Then, in a **second part**, the resulting coatings will be mechanically tested, and their thermal insulation capacity measured via the laser-flash technique and compared with the state-of-the-art PS and EB-PVD YSZ TBCs.

2. Article 5: Development of thermal barrier coating systems from Al microparticles. Part I: Influence of processing conditions on the mechanisms of formation

Development of thermal barrier coating systems from Al microparticles. Part I: Influence of processing conditions on the mechanisms of formation

Germain Boissonnet*, Benjamin Grégoire, Gilles Bonnet, Fernando Pedraza

Laboratoire des Sciences de l'Ingénieur pour l'Environnement, (LaSIE, UMR-CNRS 7356), Université de La Rochelle, Avenue Michel Crépeau, 17042 La Rochelle Cedex 1, France

* corresponding author: boissonnet.germain@gmail.com

Keywords: aluminizing; thermal barrier coating; nickel; oxidation; diffusion

Abstract. This work presents the mechanisms of formation of full thermal barrier coating systems (aluminide coating, thermally grown oxide and thermal barrier top coating) on pure nickel from micro-sized Al particles dispersed in a slurry annealed in different atmospheres (Ar, air, water vapour and mixtures thereof). The simultaneous formation of nickel aluminides and of a thermal barrier made of sintered hollow alumina spheres involved self-propagating high-temperature synthesis in all cases. However, the microstructures and adherence of the top coats changed markedly with either a diffusion step (700°C-2 h) or a complete heat treatment (700°C-2 h + 1100°C-2 h) depending on the atmosphere. Whereas fast consumption of Al occurred in Ar to form the nickel aluminides, synthetic air and water vapour fostered the peripheral oxidation of Al micro-sized particles that impeded the release of Al and its diffusion towards the substrate. This resulted in heterogeneous diffusion layers but thicker top coatings with better sintering and thicker alumina shells.

1. Introduction

Current processes of fabrication of thermal barrier coatings (TBCs) for the hottest sections of aeronautical engines are very complex and quite expensive. Therefore, they cannot be applied to other sections that now require thermal insulation due to the increase of the turbine inlet temperatures. Among the alternative coating techniques, slurries containing Al microspheres appear particularly attractive as they can form, in addition to a diffusion aluminide

coating, a top foam of hollow alumina spheres [1, 2, 3, 4, 5]. It has been demonstrated by laser flash that just a 40 µm -thick top foam indeed confer insulation properties between 400°C and 900°C equivalent to those of conventional 400 µm thick APS YSZ coatings [6]. However, this light alumina foam is not sufficiently mechanically resistant and can be easily removed, for example by grit blasting [7]. Recently, Pedraza and Podor investigated the influence of annealing conditions on the formation of hollow alumina spheres from micro-sized Al particles [8]. The release of Al from the particles was associated with two simultaneous mechanisms: i) peripheral oxidation of the spheres and ii) volume expansion of the Al core upon heating [8, 9]. Their findings agreed with the pioneer works of Levitas et al. for micro-sized particles [10, 11, 12]. They reported that the initial amorphous alumina shell surrounding the microparticles grows upon heating until it reaches a critical thickness of 4 to 5 nm [13,14]. At about 550°C, the amorphous alumina shell therefore crystallizes into γ-Al_2O_3 [13,15,16]. Since the density of γ-Al_2O_3 is greater than that of the amorphous alumina layer [9,17], tensile stresses develop in the newly formed γ-Al_2O_3 layer, inducing nano-cracks in the alumina shell. Depending on the p_{O_2} and on the heating ramp, healing of the non-continuous alumina shell may occur by oxidation of the exposed Al core [12]. When the temperature approaches the Al melting point, additional tensile stresses develop on the γ-Al_2O_3 layer since the solid-liquid transformation of Al is accompanied with a volume expansion of 12 % [18]. The release of Al from the particles is therefore controlled by the simultaneous healing of the alumina shell and the diffusion of Al through the cracks because of the pressure build-up in the molten Al core [9, 10,12]. The thickness of the oxide shell exerts a tremendous effect on the amount of Al flowing out from the microspheres. The size of the micro-particles also has a considerable influence on the kinetics of oxidation (i.e. growth of the peripheral alumina layer) and on the release of Al [13,19]. This can be attributed to the higher specific surface area of the smaller particles, which simultaneously enhance their peripheral oxidation and lessen the expansion of the Al melt [13,21]. The peripheral oxide layer of the smaller particles tend to resist more to the pressure build-up induced by the thermal expansion of the Al melt upon heating [9,18] and could provide a significant source to thicken the particles walls and to enhance the sintering of the top coating when a sufficient p_{O_2} or p_{H_2O} is employed for the heat treatment. In contrast, large particles would tend to be better Al donor for the formation of the diffusion coating as the release of Al would be faster. Indeed, the larger the Al core, the higher the pressure build-up on the oxide

shell [OxM179, OxM209]. In this view, Kolarik et al. found that the optimal particle size was in the range of 2-5 µm to simultaneously obtain continuous diffusion zones and adherent ceramic top coatings from organic-based slurries [4].

The mechanisms of formation of water-based Al-containing slurry coatings have already been discussed under inert atmosphere (Ar) [2, 3, 20] and in air [1] on pure nickel and on nickel-based superalloys. However, none of such studies investigated the influence of the atmosphere on the simultaneous aluminizing of the substrate and the sintering of the hollow alumina spheres. Therefore, the present study aims at elucidating the influence of the atmosphere on the mechanisms of formation of the complete thermal barrier systems. Pure nickel was used as a model material for nickel-based superalloys. One inert atmosphere (Ar) and two oxidizing atmospheres (synthetic air and Ar-10 % H_2O) were investigated.

2. Experimental method

Approximately 2 mm-thick coupon samples were prepared from a 12.7 mm diameter nickel rod (99.98 % purity, GoodFellow). After machining, the samples were ground with SiC paper to P180 grade, rinsed with deionized water and ultrasonically cleaned in ethanol. The water-based slurries were prepared with deionized water (solvent), polyvinyl alcohol (organic binder) and micro-sized Al particles. Two different types of Al powders were used in this study: i) micro-particles of homogeneous sizes (**Al_HS**), provided by Sibthermochim (Russia), and ii) micro-particles of dispersed sizes (**Al_DS**), provided by Hermillon (France). Approximately 9±1 mg.cm^{-2} of slurry were deposited on the samples by air brush. The samples were coated on both sides and dried in a fume cupboard for 1 h after slurry deposition. A SETARAM TGA 92 thermobalance with a 10^{-6} g accuracy was used for the heat treatment in Ar and in synthetic air, while a SETARAM Setsys Evo 1750 (10^{-7} g accuracy) was used for the heat treatment under wet air (10 vol.% water vapour). The water vapour was created using the SETARAM Wetsys module and transferred to the bottom of the thermal enclosure of the thermobalance via a heated transfer pipe. Three different atmospheres were investigated in this study: one inert (Ar) and two oxidizing atmospheres (synthetic air and Ar-10 vol. % H_2O). For the sake of clarity, the latter will be noted Ar-10%H_2O. Since the heating ramp has a strong influence on the simultaneous peripheral oxidation and opening of the Al microparticles [8,15], all the heating

ramps were fixed at 5°C/min (***Fig. 1*a and *Fig. 1*b**). The samples were systematically cured at 400°C for 1 h to remove the organic binder prior to any further step. For a better understanding of the mechanisms of formation, one or two additional steps were then performed based on previous works done in our group [2,3]. The diffusion step (700°C-2 h) to aluminize the substrate by major inward diffusion of Al and the annealing step (1100°C-2 h) to stabilize the nickel aluminide coating (i.e. to promote the outward diffusion of nickel) and to stabilize the α-Al_2O_3. For the diffusion heat treatment (***Fig. 1*a**), a quench at 50°C/min was performed to freeze the microstructure. **Table 1** summarizes the different experimental conditions tested for the diffusion heat treatment **(*Fig. 1*a**) and the complete heat treatment (***Fig. 1*b**). For both heat treatments, the coated samples were exposed to three different atmospheres (Ar, synthetic air and Ar-10%H_2O). Additional samples were first treated in Ar before the introduction of the oxidizing atmosphere upon heat treatment (**Table 1**). Here, the objective was to propose a single heat treatment to elaborate a complete thermal barrier system (diffusion coating + thermally grown oxide + ceramic top coating) by switching the composition of the atmosphere during the heat treatment. The corresponding switch between the inert and the oxidizing atmosphere is indicated with the arrow marks (1 to 4) in ***Fig. 1*b**

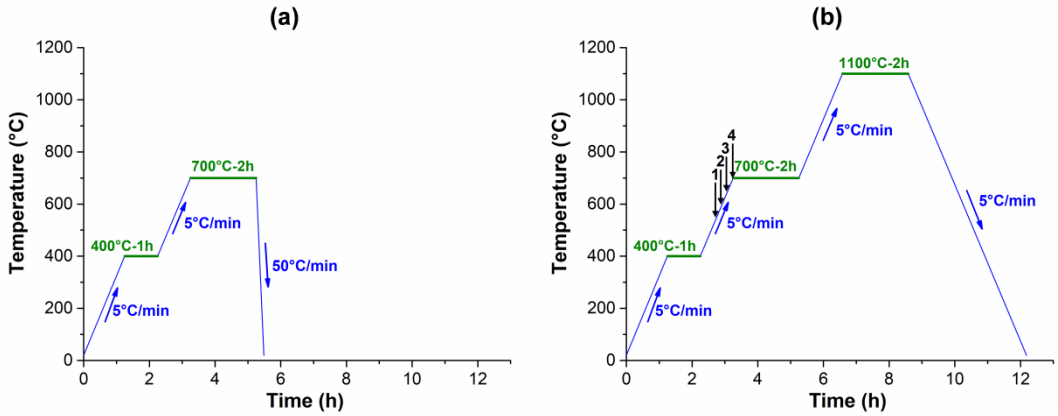

***Fig. 1** – Temperature profiles of **(a)** the diffusion heat treatment and **(b)** the complete heat treatment performed in TGA to form the thermal barrier systems on pure nickel. The arrow marks (1 to 4) in **Fig. 1b** indicate the introduction of the oxidizing atmosphere at the expense of Ar.*

The observations of the surface and of the cross-sections were performed with a FEI Quanta 200F environmental scanning electron microscope equipped with Schottky Field Emission Gun (FEG) at 0.9 mbar. The chemical analysis by Energy Dispersive Spectrometry (EDS) were

obtained through an EDAX detector coupled to the SEM. X-ray diffraction (XRD) was conducted in the Bragg-Brentano configuration with a Bruker AXS D8 Advance diffractometer using Cu $K_{\alpha 1}$ radiation (λ = 0.15406 nm) to characterize the oxide and the intermetallic crystal structures.

***Table 1** – Summary of the different heat treatments performed in TGA (see **Fig. 1**).*

Heat Treatment	Starting atmosphere	Introduction of the oxidizing atmosphere	Mark in *Fig. 1*b
400°C-1 h + 700°C-2 h	Ar Synthetic air Ar-10%H_2O	-	-
400°C-1 h + 700°C-2 h + 1100°C-2 h	Ar Synthetic air Ar-10%H_2O	-	-
	Ar	550°C	1
		600°C	2
		650°C	3
		700°C	4

3. Results

3.1. Microstructure of the TBC systems after the diffusion heat treatment (700°C-2 h)

Fig. 2 presents the macrographs and the morphologies of the two different types of Al micro-particles (Al_HS and Al_DS) from the slurry coated pure nickel samples exposed to the diffusion heat treatment in the three different atmospheres (Ar, synthetic air and Ar-10%H_2O). The corresponding XRD patterns of the different surfaces are presented in **Fig. 3**. **Fig. 4** shows the cross-sections of the coatings.

Under Ar flow (**Fig. 2a**), the surface of the sample coated with Al_HS slurry is composed of hollow spheres featuring thin transparent shells. No X-ray peak related to Al can be observed in the patterns (**Fig. 3a**) suggesting that the whole Al reacted with nickel upon the diffusion heat treatment. This is also confirmed by the fact that no metallic Al was observed in the cross-section of the top coating (**Fig. 4a**). Al_HS particles led to a ceramic top layer of ~50 µm with hollow spheres that are observed on top of a continuous diffusion layer of ~50 µm. Whereas the δ-Ni_2Al_3 phase represents most of the diffusion layer for both types of slurry (identified via XRD **Fig. 3a**), β-NiAl and γ'-Ni_3Al were successively identified at the interface with the nickel substrate (**Fig. 4a**). In the case of the Al_DS slurry, the smallest particles (appearing bright in

BSE mode) kept their Al core (**Fig. 2d** and **Fig. 4d**) and a small diffraction peak of Al was observed on the corresponding XRD pattern (**Fig. 3b)**. However, the identification of the δ-Ni_2Al_3 crystal structure indicates that most of the Al (i.e. the largest particles) had reacted with the Ni substrate. The hollow particles that were close to the substrate did not keep their spherical shape and started to collapse, hence leading to a thinner top coating of ~30 µm (**Fig. 4d**).

For the samples exposed to synthetic air, a large quantity of metallic Al is still present in the top coating for both the HS and the DS slurries (**Fig. 3**). From the SEM observations (**Fig. 2b** and **Fig. 2e**), it appears that the larger microparticles are broken whereas the smaller ones are still filled with Al. These plain microparticles were also identified on the cross-sections of the Al_HS (**Fig. 4**b) and the Al_DS (**Fig. 4**e). The crystal structure of δ-Ni_2Al_3 was also observed on the XRD pattern confirming that the reaction between Al and Ni occurred in synthetic air too. The bright spots observed on the smaller micro-particles (**Fig. 2b, Fig. 2e, Fig. 4**b and **Fig. 4**e) correspond to nickel enrichment according to the EDS spot analyses and to the XRD analyses from which the crystal structure of $NiAl_3$ was identified. In addition, the crystal structure of NiO (**Fig. 3**), indicates that the Ni from the substrate coated with the two slurries was oxidized during this 2 h step at 700°C. Due to the exposure to synthetic air, the supply of Al toward the substrate was also disturbed hence resulting in a thinner diffusion layer of the Al_HS sample (**Fig. 4**b and **Fig. 4**e) and diffusion islands for the Al_DS one. Moreover, NiO started to develop in locations where the Al did not form the aluminide coating.

The samples exposed to Ar-10%H_2O (**Fig. 2**c, **Fig. 2f, Fig. 4**c, **Fig. 4**f) exhibit less emptied particles than when exposed to synthetic air, hence a larger ratio of large particles still contains Al (**Fig. 3**). However, in these conditions, the Al_HS top coating spalled almost completely from the substrate and remained adherent only to the edges (**Fig. 2**c). The XRD pattern for this Al_HS sample (**Fig. 3a**) shows a high intensity for the peaks of the Ni and of the Al while smaller intensities of the δ-Ni_2Al_3 peaks are observed. In contrast, no detachment is observed in the Al_DS sample for which Ni and Al are also observed along with the $NiAl_3$ and δ-Ni_2Al_3 phases (**Fig. 3b**). The diffusion layers of the two types of samples appear very heterogeneous due to the insufficient release of Al from the particles (**Fig. 4**c and **Fig. 4**f). Moreover, the bright spots that resulted from the Ni enrichment of the Al top particles in Ar and in synthetic air are less observed on the samples exposed to water vapour. For both types of particles, the top coating shows a poor contact with the substrate in comparison with the heat treatments

conducted in the two other atmospheres. This probably explains the spallation of the Al_HS top coating observed on **Fig. 2c**. Unlike the samples exposed to synthetic air, NiO did not grow in the uncoated regions, confirmed by the lower intensity of the diffraction peaks of NiO that are less intense than for the samples exposed to air.

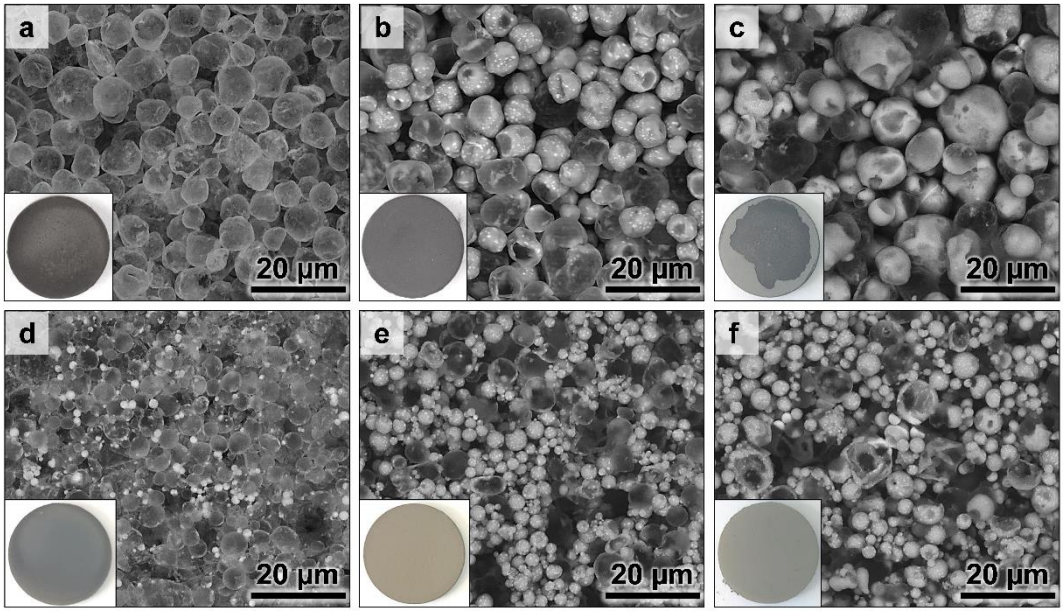

***Fig. 2** – Surface morphology of the thermal barrier systems elaborated from **(a, b, c)** Al_HS and **(d, e, f)** Al_DS micro-particles on pure nickel after the diffusion heat treatment (700°C-2 h) in **(a, d)** Ar, **(b, e)** synthetic air and **(c, f)** Ar-10%H_2O. The main features of the surfaces are shown in the insets.*

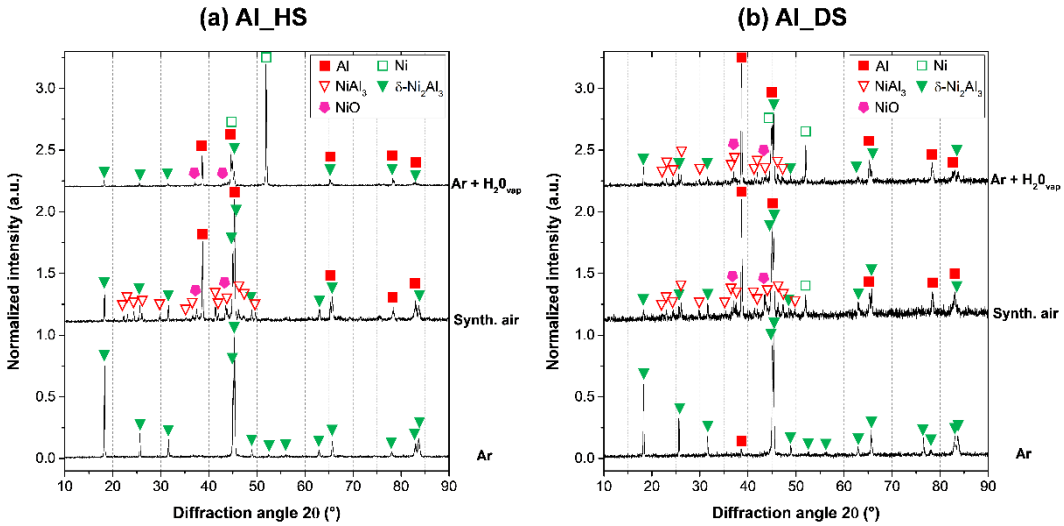

***Fig. 3** – X-ray diffraction patterns of the slurry coated samples after the diffusion heat treatment (700°C-2 h) in the three different atmospheres for **(a)** Al_HS and **(b)** Al_DS microparticles.*

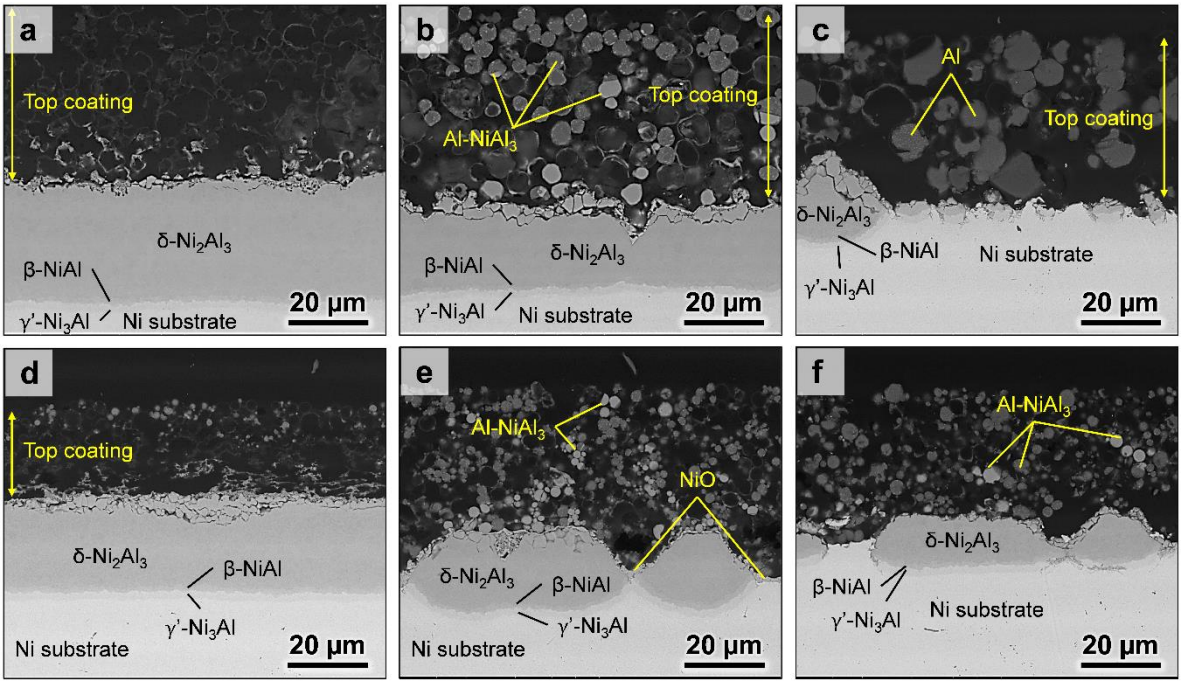

***Fig. 4** – BSE cross-section images of the thermal barrier systems elaborated from **(a, b, c)** Al_HS and **(d, e, f)** Al_DS micro-particles on pure nickel after the diffusion heat treatment (700°C-2 h) in **(a, d)** Ar, **(b, e)** synthetic air and **(c, f)** Ar-10%H_2O.*

In order to assess the impact of the particle size on the aluminizing of the pure Ni substrate, the particle size distribution of emptied particles for both Al_HS and Al_DS micro-particles in the three different atmospheres after the diffusion heat treatment (700°C-2 h) is plotted in **Fig. 5**. The particle size values corresponding to 0%, 50% and 100% of emptied particles for the different conditions are given in **Table 2**. Regardless the atmosphere composition and the type of Al micro-particles, the larger particles generally broke more rapidly than the smaller ones (i.e. higher fraction of emptied particles). For the Al_HS micro-particles, the whole Al reservoir reacted with nickel after the diffusion heat treatment in Ar (**Fig. 5**a). This was also observed for Al_DS micro-particles except for the particles smaller than 3 µm that kept their Al core (**Fig. 2**d and **Fig. 5**b). By performing the heat treatment in Ar, the major Al supply from the microspheres therefore led to the formation of relatively thick and homogeneous diffusion layers on pure nickel substrate (**Fig. 4**a and **Fig. 4**d).

By performing the diffusion heat treatment in synthetic air or in Ar-10%H_2O, fewer particles released their Al and the threshold for the opening of the microspheres shifted towards

larger-sized particles for both Al_HS (**Fig. 5**a) and Al_DS slurries (**Fig. 5**b), in particular for the Al_HS micro-particles (**Table 2**).

When the Al_HS particles are exposed to Ar-10%H_2O, a significant fraction of the larger micro-particles did not release their Al after the diffusion heat treatment as observed on the surface (**Fig. 2**c) and in the cross-section (**Fig. 4**c). Since fewer particles released their Al source in both synthetic air and Ar-10%H_2O, fewer interactions between Al and Ni were made possible leading to the discontinuous diffusion layers observed previously.

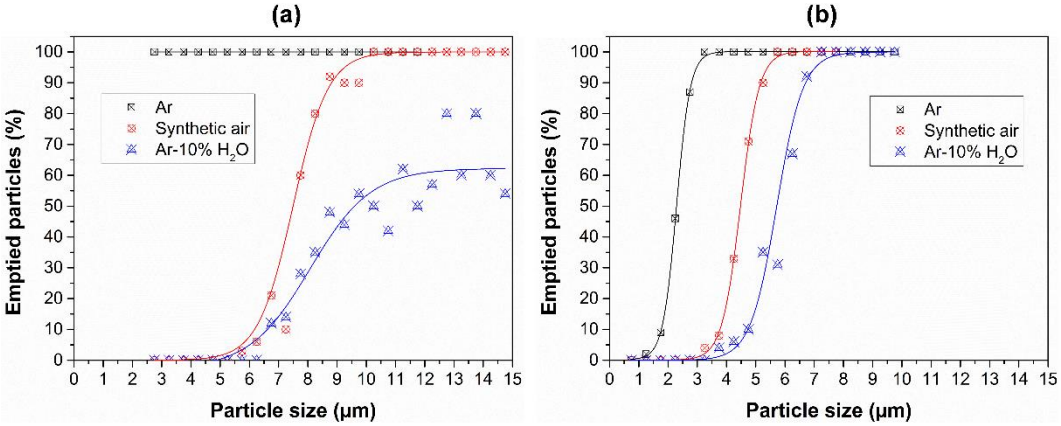

***Fig. 5** – Particle size distribution of the emptied particles after the diffusion heat treatment (700°C-2 h) in the three different atmospheres for **(a)** Al_HS and **(b)** Al_DS microparticles.*

***Table 2** – Determination of the particle size (µm) for 0, 50 and 100% of emptied particles for the two types of Al microparticles after the diffusion heat treatment (700°C-2 h) in the three different atmospheres.*

Atmosphere	Al_HS			Al_DS		
	0%	50%	100%	0%	50%	100%
Ar	-	-	> 2.5	< 1.5	2.3	> 3
Synthetic air	< 4.5	7.5	> 10.5	< 3.0	4.5	> 6
Ar-10%H_2O	< 5.0	9.6	-	< 3.5	5.7	> 7.5

3.2. Microstructure of the TBC systems after the complete heat treatment (700°C-2 h + 1100°C-2 h)

The surfaces and the morphologies of the samples coated with the Al_HS and Al_DS slurries after the complete heat treatment in the different atmospheres are given in **Fig. 6**. The corresponding XRD patterns are presented in **Fig. 7**. Cross-sectional micrographs of the coatings are presented in **Fig. 8**.

Under Ar flow, the hollow spheres from the Al_HS slurry shrunk and lost their initial shape (**Fig. 6a**) whereas the Al_DS microparticles completely lost their spherical shape and collapsed to form a thin layer through which the metallic sub-layer is visible (**Fig. 6d**). The corresponding macrograph of the latter shows a "dry-mud" like morphology in which the top coating is broken by multiple micro-cracks. The diffusion coatings are similar for both samples and constituted of two different layers: an external layer composed of both β-NiAl and γ'-Ni_3Al phases and an internal layer that corresponds to the γ'-Ni_3Al composition at the interface with the nickel substrate (**Fig. 8a** and **Fig. 8d)** while neither Al nor δ-Ni_2Al_3 could be identified via XRD (**Fig. 7**). By contrast, the microstructure of the top coating composed of α-Al_2O_3 (see XRD in **Fig. 7**) is significantly different for the two types of microparticles. Whereas the broken spheres from the top coating collapsed in the case of Al_DS particles (**Fig. 8d**) to give a very thin top coating (~10 µm), the Al_HS particles maintained a quasi-spherical shape with a thin oxide shell for a resulting top coating of ~30 µm (**Fig. 8a**).

For the samples heat treated in synthetic air (**Fig. 6b** and **Fig. 6e**), the microspheres are less deformed and appear more sintered than the ones obtained in Ar. Moreover, the oxide crusts highlight a stronger thickening of the alumina shells. This thickening led to thicker top coating made of spherical hollow spheres (**Fig. 8b** and **Fig. 8e**) and is in good agreement with the XRD patterns since the characteristic diffraction peaks of α-Al_2O_3 are unambiguously observed (**Fig. 7**). In addition, the crystal structures of Al and δ-Ni_2Al_3 were no longer identified on the XRD pattern of both samples whereas both β-NiAl and γ'-Ni_3Al ones were detected after the complete heat treatment (**Fig. 7**). This indicates that the diffusion islands formed upon the diffusion heat treatment (**Fig.4e**) were transformed into β-NiAl and γ'-Ni_3Al phases after the additional step at 1100°C. The bright spots (BSE mode) observed on the surface of Al_HS particles (**Fig. 6b**) and of Al_DS particles (**Fig. 6e**) correspond to unemptied Al microparticles enriched in Ni, confirmed by the top coatings cross-sections (**Fig. 8b** and **Fig. 8e**) and the detection of $NiAl_3$ in addition to β-NiAl and γ'-Ni_3Al (**Fig. 7b**). Also, the annealing at 1100°C in synthetic air brings about the formation of a relatively thick thermally grown oxide (TGO). Between the diffusion spots, the substrate was vulnerable to oxidation and gave thick NiO oxide scale while an alumina layer started to internally develop around the diffusion islands (**Fig. 8b** and **Fig. 8e**).

The top coatings of both Al_HS and Al_DS samples heat treated in Ar-10%H_2O spalled. One shall note that the observations of the microspheres of the surfaces (**Fig. 6c** and **Fig. 8c**) and of the cross-sections (**Fig. 8c** and **Fig. 8f**) were made on the edges of the samples where the top coatings remained adherent. The microparticles of the Al_HS slurry exhibit various oxide morphologies and appear more oxidized than after the heat treatment under synthetic air. As a matter of fact, none of the large particles of the surface seems to have broken to release Al from the core. Unlike with synthetic air, Ni, Al and $NiAl_3$ were identified by XRD for the Al_HS sample (**Fig. 7a**), indicating that some Al remained trapped in the top coating. Like with synthetic air, the surface of both coatings displays brighter contrasted areas rich in Ni (**Fig. 6**). Moreover, no NiO was detected by XRD for both Al_HS and Al_DS and only the structure of α-Al_2O_3 was observed. The heat treatment in water vapour resulted in a more heterogeneous diffusion of Al that gave smaller and dispersed diffusion islands composed of β-NiAl which were also surrounded by an α-Al_2O_3 oxide layer.

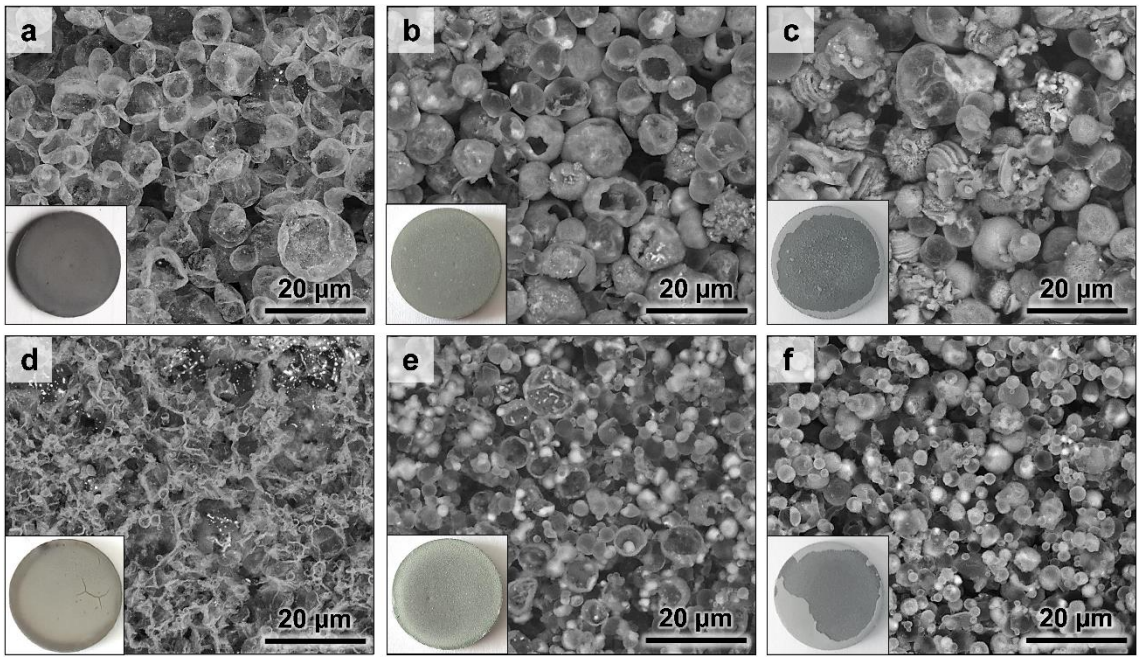

Fig. 6 – *Surface morphology of the thermal barrier systems elaborated from* ***(a, b, c)*** *Al_HS and* ***(d, e, f)*** *Al_DS microparticles on pure nickel after the complete heat treatment (700°C-2 h + 1100°C-2 h) in* ***(a, d)*** *Ar,* ***(b, e)*** *synthetic air and* ***(c, f)*** *Ar-10%H_2O. The main features of the surfaces are shown in the insets.*

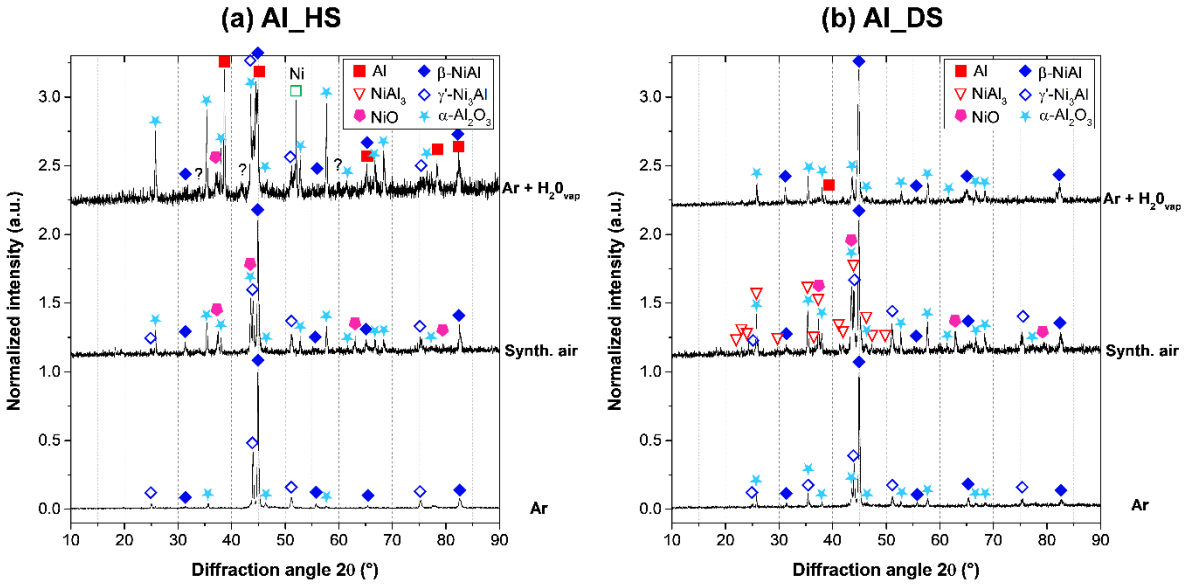

Fig. 7 *– X-ray diffraction patterns of the slurry coated samples after the complete heat treatment (700°C-2 h + 1100°C-2 h) in the three different atmospheres for* ***(a)*** *Al_HS and* ***(b)*** *Al_DS microparticles.*

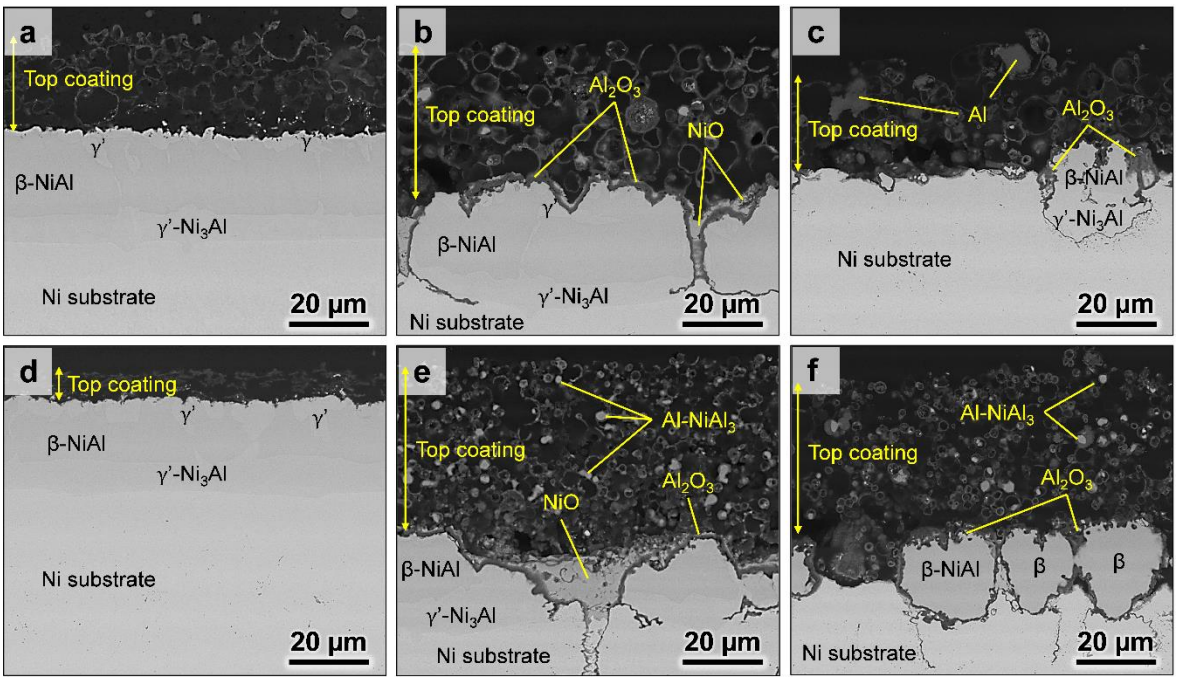

Fig. 8 *– BSE cross-section images of the thermal barrier systems elaborated from* ***(a, b, c)*** *Al_HS and* ***(d, e, f)*** *Al_DS microparticles on pure nickel after the complete heat treatment (700°C-2 h + 1100°C-2 h) in* ***(a, d)*** *Ar,* ***(b, e)*** *synthetic air and* ***(c, f)*** *Ar-10%H_2O.*

The evolution of the mass gain with the annealing time in the different atmospheres is depicted in **Fig. 9**. Clearly, the very small mass gain observed in Ar (~0.5 mg) is in line with

the poor oxidation of the Al microparticles and of the substrate observed. However, the use of air or of Ar-10%H_2O brings about an overall mass gain much greater (~7.5 mg) than in Ar at the end of the experiment. This agrees with the thick oxide crusts observed for the particles in the top coatings. One can also note that synthetic air generated more oxidation of the coated samples than Ar-10%H_2O during the diffusion treatment at 700°C. As a result, an oxide layer already develops at 700°C in air and disturb the Al diffusion while preventing the formation of an even front of Ni_xAl_y intermetallic phases. In contrast, no NiO was observed with Ar-10%H_2O and the mass gain is related to the oxidation of Al according to Fig. 8(c) and (d).

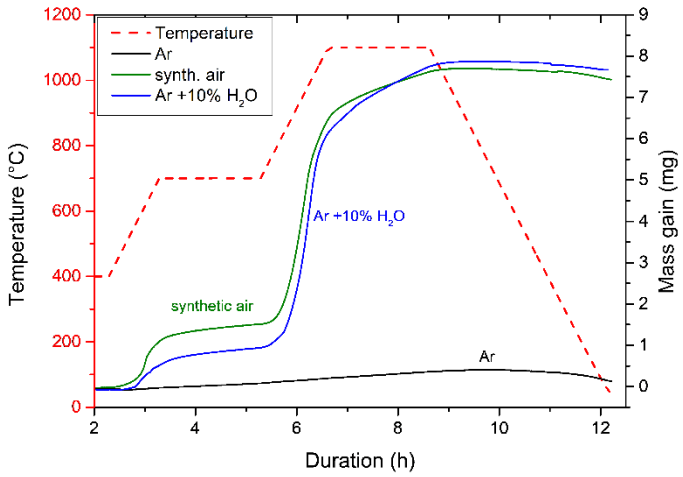

Fig. 9 *– Mass gain measured via TGA of the samples (Al_HS on one face and Al_DS on the other) heat treated in Ar, synthetic air and Ar-10%H_2O.*

3.3. Microstructure of the TBC systems with switch of atmospheres upon heating

The replacement of the inert Ar atmosphere by an oxidizing atmosphere was performed at different times along the heat treatment (see **Table 1)**. Thus, synthetic air was introduced at 550°C, 600°C, 650°C and 700°C during the heating ramp from 400°C to 700°C while the Ar-10%H_2O atmosphere was introduced only at 600°C and 650°C.

The introduction of air at 550°C or 600°C results in coatings similar to the ones obtained with a full heat treatment under synthetic air regardless of the type of microparticles (**Fig. 10a** and **Fig. 10d**). The mass gain for the samples during the heat treatment are also observed to be similar for both temperature of the switch (~7.5 mg) and also equivalent to the one that was fully heat treated in air (**Fig. 11**). Thus, a similar morphology of the coatings is observed. Diffusion islands composed of β-NiAl and of γ'-Ni_3Al grew over a continuous γ'-Ni_3Al

diffusion layer. NiO also formed between the diffusion islands and at the interface with the top coating and a thick α-Al_2O_3 TGO developed on top of the diffusion islands. The top coatings achieved with the switch at 550°C and 600°C are composed of sintered hollow alumina spheres with thick oxide shells, whose thicknesses are comparable with the ones of the samples fully treated in synthetic air. In the same way as the full heat treatment in synthetic air, a poor interface between the top layer and the aluminide coating is observed for both Al_DS and Al_HS samples that resulted in spallation of the top coating for the Al_HS one (**Fig. 10a**).

When synthetic air was introduced at 650°C (**Fig. 10b** and **Fig. 10e**), the diffusion coatings obtained from both types of micro-particles were more homogeneous and similar to the ones fabricated with the full treatment in the inert Ar atmosphere (**Fig. 8**a and **Fig. 8**d). However, as opposed to the latter, the top coatings exhibit thicker shells and a thicker α-Al_2O_3 TGO at the interface between the aluminide and the top coating. This is confirmed by the mass gain observed in **Fig. 11** (~3 mg) that is lower than the ones of the samples with air introduced at 550°C and 600°C, but that is also significantly higher than the one of the sample heat-treated in Ar.

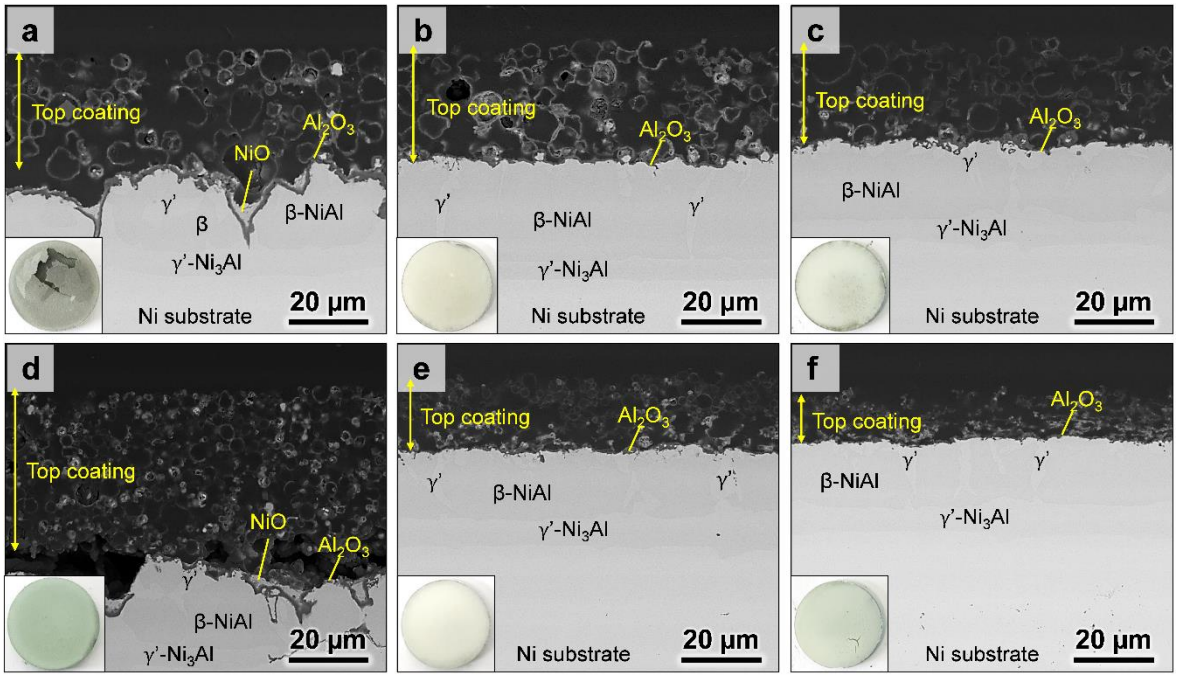

Fig. 10 *– BSE cross-section images and corresponding surface macrographs of the thermal barrier systems elaborated from* ***(a, b, c)*** *Al_HS and* ***(d, e, f)*** *Al_DS microparticles on pure nickel after introduction of synthetic air at* ***(a, d)*** *600°C,* ***(b, e)*** *650°C and* ***(c, f)*** *700°C, and subsequent annealing (700°C-2 h + 1100°C-2 h).*

The introduction of synthetic air at 700°C also resulted in coatings similar to the ones obtained with the full heat treatment in Ar and therefore, the diffusion layers are very homogeneous for both types of micro-particles. In contrast, the shells of the top coating are very thin, resulting in shrunk top coatings, with collapsed microspheres for Al_DS micro-particles (**Fig. 10f**). However, a slight oxidation is to be highlighted as the resulting mass gain during the heat treatment (~2 mg) was observed to be significantly higher than the sample heat-treated in Ar (**Fig. 11**).

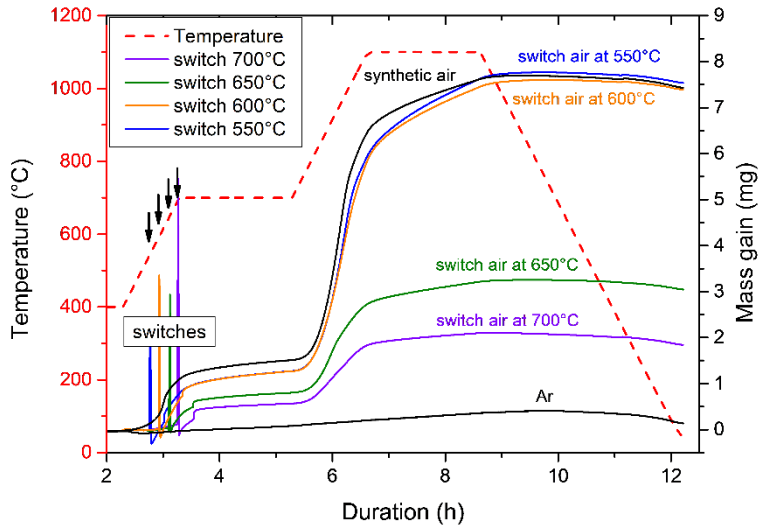

***Fig. 11** – Mass gain measured via TGA of the samples (Al_HS on one face and Al_DS on the other) heat treated in different atmospheres – switch from Ar to synthetic air.*

Fig. 12 shows the cross-section of the coatings with the introduction of Ar-10%H_2O at 650°C (**Fig. 12a** and **Fig. 12c**) and at 700°C (**Fig. 12b** and **Fig. 12d**). The top coatings were not fully adherent to the surface when Ar-10%H_2O was introduced at 650°C (**Fig. 12a** and **Fig. 12c**) while at 700°C they spalled off completely with the Al_HS or remained adhered with the Al-DS particles. All the diffusion layers had approximately the same thickness and comprised β-NiAl as the main phase and γ-Ni_3Al at the grain boundaries. However, the diffusion layers were very uneven and internally oxidized with the switch to Ar-10%H_2O in the Al_DS at 650°C and in the Al_HS at 700°C (**Fig. 12b** and **Fig. 12c**). Contrarily, the introduction of water vapour at 650°C and at 700°C respectively, in the Al_HS and Al_DS coatings resulted in homogeneous diffusion coatings (**Fig. 12a** and **Fig. 12d**).

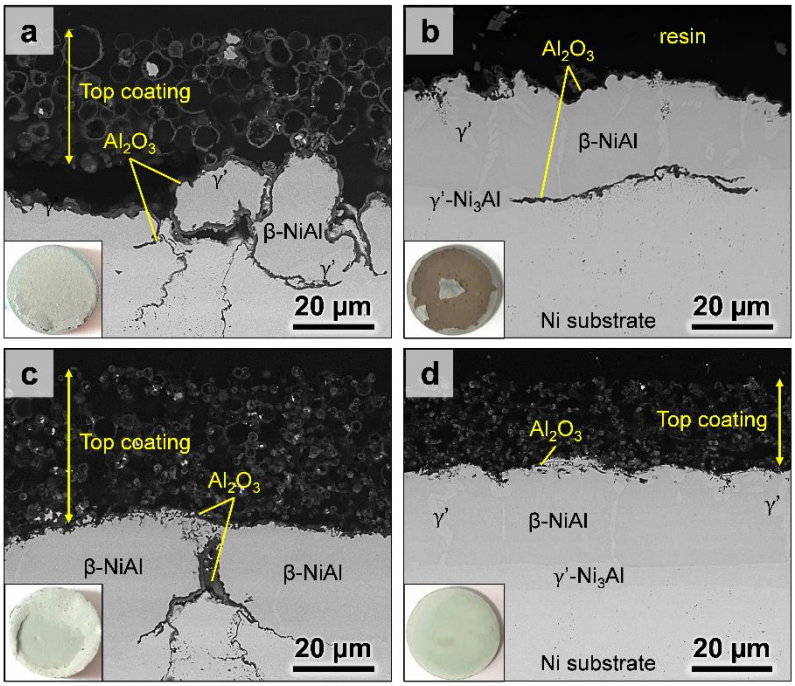

***Fig. 12** – BSE cross-section images and corresponding surface macrographs of the thermal barrier systems elaborated from **(a, b)** Al_HS and **(c, d)** Al_DS microparticles on pure nickel after introduction of Ar-10%H_2O at **(a, c)** 650°C and **(b, d)** 700°C, and subsequent annealing (700°C-2 h + 1100°C-2 h).*

Fig. 13 compares the mass gains of the samples with the introduction of Ar-10%H_2O at different temperatures. At 700°C, the mass differences fall within the uncertainty of the TGA device. In contrast, the mass gains changed markedly after the final annealing step at 1100°C. As a matter of fact, the major changes occur upon heating and very interesting differences are observed as a function of the annealing atmosphere. When Ar+10%H_2O is introduced at 700°C, the mass gain increases markedly upon heating to 1100°C but slows down when this temperature is reached. A similar effect is observed when the wet Ar is introduced at 650°C but the overall mass gain is greater than at 700°C. Therefore, quite thick oxide shells around the particles are observed at 650°C. In contrast, oxidation continues at 1100°C in Ar till it slows down. On the one hand, this implies that there is little matter left to be oxidized with late introduction of Ar+10%H_2O at 700°C compared to the introduction at 650°C. This would explain the thinner walls of the particles of the top coat and its subsequent shrinkage and the less oxidation of the diffusion coating compared to the coatings obtained with the introduction of Ar-10%H_2O at 650°C. On the other hand, the higher mass gains clearly indicate that it can

only be attributed to the oxidation of Al since Ni cannot oxidize in Ar. Similarly, only Al can get oxidized in the presence of Ar-10%H_2O because of the low P_{O2} (0.005 atm).

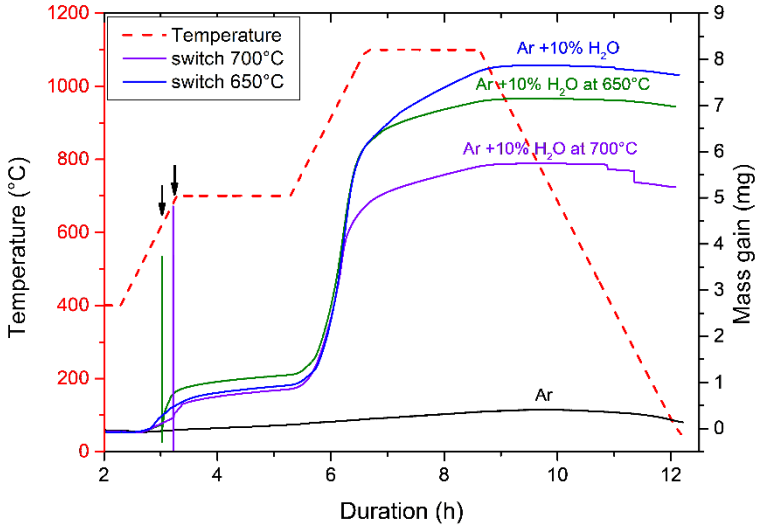

Fig. 13 *– Mass gain measured via TGA of the samples (Al_HS on one face and Al_DS on the other) heat treated in different atmospheres – switch from Ar to Ar-10%H_2O.*

4. Discussion

4.1. Single atmosphere for the formation of TBC systems

Under Ar atmosphere, the Al microspheres tend to release their Al core rapidly while limited oxidation occurs due to the low oxygen and water partial pressures contained in the commercial gas (2 vpm O_2 + 3 vpm H_2O according to the supplier). Although some Al was still trapped in the smallest particles of the Al_DS slurry (<3 µm) after the diffusion heat treatment step (see **Fig. 5**), most of the Al of both Al_HS and Al_DS was released towards the substrate and reacted with Ni to form an aluminides coating of ~30 µm following a SHS reaction [3,20]. The δ-Ni_2Al_3 phase that represented most of the diffusion layer for both types of slurry after the diffusion step (see **Fig. 4a** and **d**) transformed into β-NiAl and γ'-Ni_3Al phases after the 1100°C-2h annealing step (see **Fig. 8a** and **d**) due to solid-state interdiffusion between Al and Ni as commonly observed for high-activity Al coatings [22,23,24]. Similar microstructures on pure nickel were reported when slurry coated with relatively similar Al microparticles annealed in Ar [2]. Concerning the top coating, after the diffusion heat treatment, both types of micro-particles led to alumina hollow spheres with thin transparent shells as observed by Pedraza and

Podor in Ar and in 120 Pa He-4%H_2 [8]. With the annealing step at 1100°C for 2h, the top coatings got thinner (~7 µm and ~20 µm for Al_DS and Al_HS, respectively – see **Fig. 8a** and **Fig. 8d**) and micro-craks appeared for the Al_DS sample (see **Fig. 6a** and **Fig. *6*d**), but were still observed to be adherent on the samples. The thinning and cracking of the coatings was attributed to the volume shrinkage of the thin alumina shells that occurs during the γ-Al_2O_3 to α-Al_2O_3 transition [9,21,25]. The same morphology was reported by Pedraza and Podor after exposure to 1150°C in He-4%H_2 atmosphere [8].

When increasing the oxidizing ability of the atmosphere using synthetic air (p_{O_2} = 0.20 atm), the microspheres tend to keep more Al (see **Fig. 5**). In contrast with the Ar atmosphere, the diffusion coatings were more heterogeneous after exposure in synthetic air (ranging from 0 to 30 µm – see **Fig. 8b**, **Fig. 8e**). This was attributed to the greater oxidation of both the Al microparticles and of the interface between the particles and the substrate (see **Fig. 9**). Indeed, a thick NiO was observed on top of the uncoated region of the substrate (**Fig. 4e** and **Fig. 8e**). Moreover, the peripheral oxidation of the particles could hamper the release of Al towards the substrate as the Al melt that is released through the cracks of the shells might be quickly oxidized. The presence of the $NiAl_3$ structure for the Al_DS sample (**Fig. 7**) and the bright particles observed in the cross-section in **Fig. 8e** indicate that some Al remained trapped in the particles and could thus not diffuse towards the substrate. A thick α-Al_2O_3 TGO also developed on top and on the edges of the diffusion islands. The oxide crusts around the particles of the top coatings thickened significantly (**Fig. 6b** and **Fig. 6e**) compared to the ones observed in Ar [9,26], resulting in significantly thicker top coatings (~60 µm and ~50 µm for Al_DS and Al_HS, respectively – see **Fig. 8b** and **Fig. 8e**) than the one obtained in Ar. This is probably due to the further oxidation of the microspheres that, thus, hampered the shrinkage of the hollow alumina spheres and the subsequent collapsing of the top coating.

The differences between the heat treatment in synthetic air and in Ar-10%H_2O mostly lie in the oxidation behaviour of the particles and of the substrate. After the diffusion step in Ar-10%H_2O, more Al remained in the top coatings and fewer diffusion islands were observed (**Fig. 4c** and **4f**). This can be ascribed to less Al being released from the particles. As a matter of fact, fewer particles were observed to be broken after diffusion heat treatment in Ar-10%H_2O than in Ar or in synthetic air (**Fig. 2**, **Fig. 4** and **Table 2**). The diffusion coatings observed on the cross-sections were also observed to be more heterogeneous than the ones obtained in synthetic

air (**Fig. 4**). These phenomena probably arose because water vapour delays the opening of the microparticles like Pedraza and Podor demonstrated by in situ SEM in 120 Pa of H_2O and 120 Pa of synthetic air [8]. However, after the complete heat treatment till 1100°C, the quantity of Al that diffused towards the substrate did not significantly increase and the derived top coatings spalled from the substrates. The fact that Al did not reach the substrate could be explained by a selective oxidation of the Al from the microspheres and of the substrate. Indeed, the oxide shells after the complete heat treatment in water vapour were shown to be as thick as the ones obtained in air (**Fig. 8**) and the diffusion islands were surrounded by a thick α-Al_2O_3 TGO although the substrate remained unoxidized. The reasons why NiO grew under synthetic air and not in Ar-10%H_2O are still not fully understood since Rudolphi and Schütze have shown very minor differences between NiO grown at 800°C under dry and wet (10 and 30%H_2O) air [29]. Probably, the differences relate to the faster growth of the NiO scales in water vapour. This would induce further defects in the microstructure according to the SEM in situ observations at 700°C [30] through which Al can diffuse and react following thermite reactions [31].

Therefore, using a single atmosphere for the heat treatment did not allow to obtain both a homogeneous aluminide coating and a thick and adherent top coating. The purpose of the hybrid atmosphere was to procure enough diffusion of Al to form a homogeneous diffusion coating while promoting the oxidation of the shells of the Al micro-particles in order to increase the strength of the top coatings. Thus, inert atmosphere was employed during the first part of the heat treatment to allow the initiation of the Al-Ni reaction. Then, the introduction of an oxidizing atmosphere was realized to oxidize the Al left in the micro-particles hence, to thicken the alumina shells while simultaneously promoting the formation of α-Al_2O_3 TGO.

4.2. Hybrid atmosphere: optimizing the formation of TBC systems in a single heat treatment

When synthetic air is introduced at 550 or 600°C, the heterogeneous diffusion coatings were similar to the ones obtained in air with NiO at the interface between the diffusion coating and the top coating (**Fig. 10**). Like with the treatment conducted in air, the micro-particles shells were thickened prematurely, and the release of Al was thus hindered as explained in section 4.1. This heterogeneous diffusion resulted in a poor adherence of the top coating from both types of micro-particles which was even shown to spall from the substrate for the Al_HS sample (**Fig. 10a**).

By further delaying the introduction of air at 650°C, a homogeneous diffusion coating was achieved (**Fig. 10**a and **Fig. 10e**), similar to the one obtained in Ar. It appeared that the micro-particles were allowed to release sufficient Al towards the substrate to form the diffusion coating. However, unlike the heat treatment performed in Ar, the introduction of air before the complete emptying of the microparticles was shown to trigger the thickening of the shells of the microspheres which were observed to be thicker for both types of particles. Also, a relatively thick α-Al_2O_3 TGO was also achieved and both top coatings were adherent to the substrate.

Finally, when synthetic air was introduced at 700°C, the resulting diffusion coatings were homogeneous and similar to the ones obtained in Ar. However, the top coatings were also similar to the ones in Ar. This means that when the introduction of the oxidizing atmosphere is performed too late, the quantity of Al remaining in the top coating is not enough to thicken the microspheres which shrunk and collapsed. The only difference with the heat treatment performed in Ar is that the introduction of air allowed the thickening of the α-Al_2O_3 TGO.

The changes in the formation of the coatings with the introduction of Ar+10%H_2O at 650 and 700°C can be explained with the results of **Fig. 13**. On the one hand, the late introduction of Ar+10%H_2O at 700°C allows Al to be supplied from the particles and react with the substrate. Therefore, there is little matter left to get oxidized compared to the introduction at 650°C. This would explain the thinner walls of the particles of the top coat and its subsequent shrinkage and the less oxidation of the diffusion coating compared to the coatings obtained with the introduction of Ar-10%H_2O at 650°C. As such, the shell of the particles of the top coating appear thicker and the top coating itself is thicker (~30 and ~50 µm) than at 700°C (~20 µm). On the other hand, the higher mass gains recorded in Ar clearly indicate that the mass gains recorded can only be attributed to the oxidation of Al since Ni cannot oxidize in Ar. Similarly, only Al can get oxidized in the presence of Ar-10%H_2O because of the low P_{O2} (0.005 atm). Therefore, no NiO formed could be detected in Ar-10%H_2O as opposed to the switch of the atmosphere with synthetic air (P_{O2} ~ 0.02 atm).

5. Conclusions

This work presented the mechanisms of formation of full thermal barrier coating systems (aluminide coating, thermally grown oxide and thermal barrier top coating) from micro-sized

Al particles on pure nickel. Depending on the atmosphere composition, different microstructures were obtained after a diffusion step (700°C-2 h) or a complete heat treatment (700°C-2 h + 1100°C-2 h). Whereas fast consumption of Al occurred in Ar to form the nickel aluminides, synthetic air and water vapour fostered the peripheral oxidation of Al micro-sized particles that impeded the release of Al and its diffusion towards the substrate. This resulted in heterogeneous diffusion layers but thicker top coatings with better sintering and thicker alumina shells. By using hybrid atmospheres, a good compromise for thickening the alumina shells and having a homogeneous aluminide coating was found when the oxidizing atmosphere was introduced at 650°C for the synthetic air and at 700°C for the Ar-10%H_2O atmosphere. Further work will be conducted in order to assess the mechanical resistance and thermal insulation of the different top coatings achieved.

ACKNOWLEDGEMENTS

The authors gratefully acknowledge the French Ministry of Armed Forces (Direction Générale de l'Armement, Grant no. 2014.60.0059) and the Région Poitou-Charentes for partially funding this research.

REFERENCES

1. X. Montero, M.C. Galetz, M. Schütze, Surf. Coat. Technol. 206 (2011) 1586-1594.
2. F. Pedraza, M. Mollard, B. Rannou, J. Balmain, B. Bouchaud, G. Bonnet, Mater. Chem. Phys. 134 (2012) 700-705.
3. B. Bouchaud, B. Rannou, F. Pedraza, Mater. Chem. Phys. 143 (2013) 416-424.
4. V. Kolarik, R. Roussel, M. Juez Lorenzo, H. Fietzek, Mater. High Temp. 29 (2012) 89-94.
5. F. Pedraza, M. Mollard, B. Rannou, B. Bouchaud, J. Balmain, G. Bonnet, Oxid. Met. 85 (2016) 231-244.
6. F. Pedraza, B. Rannou, G. Boissonnet, B. Bouchaud, Z. Maache-Rezzoug, J. Mat. Sci. Chem. Eng. 3 (2015) 17-22.
7. F. Pedraza, G. Boissonnet, B. Fernandez, B. Bouchaud, R. Podor, Int. Conference on Metallurgical Coatings and Thin Films, San Diego, USA, April 25-28, 2016.
8. F. Pedraza, R. Podor, Mater. Charact. 113 (2016) 198-206.

9. S. Hasani, M. Panjepour, M. Shamanian, Oxid. Met. 78 (2012) 179-195.
10. V.I. Levitas, B.W. Asay, S.F. Son, M. Pantoya, J. Appl. Phys. 101 (2007) 083524-1-20.
11. V.I. Levitas, M. Pantoya, K.W. Watson, Appl. Phys. Lett. 92 (2008) 201917-1-3.
12. V.I. Levitas, Phil. Trans. R. Soc. A 371 (2013) 1-14.
13. B. Rufino, F. Boulc'h, M.V. Coulet, G. Lacroix, R. Denoyel, Acta Materialia 55 (2007) 2815-2827.
14. L.P.H. Jeurgens, W.G. Sloof, F.D. Tichelaar, E.J. Mittemeijer, Thin Solid Films 418 (2002) 89-101.
15. M.A. Trunov, M. Schoenitz, X. Zun, E.L. Dreizin, Combust. Flame 140 (2005) 310-318.
16. B. Rufino, M.V. Coulet, R. Bouchet, O. Isnard, R. Denoyel, Acta Materialia 58 (2010) 4224-4232.
17. I. Levin, D. Brandon, J. Am. Ceram. Soc. 81 (1998) 1995-2012.
18. A. Rai, D. Lee, K. Park, M.R. Zachariah, J. Phys. Chem. B 108 (2004) 14793-14795.
19. M.A. Trunov, M. Schoenitz, E.L. Dreizin, Combust. Theory Model. 10 (2006) 603-623.
20. M.C. Galetz, X. Montero, M. Mollard, M. Gunthner, F. Pedraza, M. Schütze, Intermetallics 44 (2014) 8-17.
21. S. Hasani, A.P. Soleymani, M. Panjepour, A. Ghaei, Oxid. Met. 82 (2014) 209-224.
22. G.W. Goward, D.H. Boone, Oxid. Met. 3 (1971) 475-495.
23. D.K. Das, V. Singh, S.V. Joshi, Metall. Mater. Trans. A 29 (1998) 2173-2188.
24. J. Angenete, K. Stiller, Surf. Coat. Technol. 150 (2002) 107-118.
25. V. Kolarik, M. Juez Lorenzo, H. Fietzek, Mater. Sci. Forum 696 (2011) 290-295.
26. F. Velasco, S. Guzman, C. Moral, A. Bautista, Oxid. Met. 80 (2013) 403-422.
27. S. Shankar, L.L. Seigle, Metall. Mater. Trans. A 9 (1978) 1467-1476.
28. J.M. Brossard, B. Panicaud, J. Balmain, G. Bonnet, Acta Materialia (2007) 6586-6595.
29. M. Rudolphi, M. Schütze, *Moisture Induced Damage in Oxide Scales*, https://gfkorr.de/kwi_media/Downloads/hochtemperaturwerkstoffe/Projekte/high_temperature_materials_poster_moisture_damage.pdf, accessed to 31/01/2019
30. B. Schmid, N. Aas, Ø. Grong, R. Ødegaard, Scanning 23 (2001) 255-266.
31. D. Vrel, A. Hendaoui, P. Langlois, S. Dubois, V. Gauthier, B. Cochepin, Intnal. J. Self-Propag. High-Temp. Synth. 16 (2007) 62-69.

3. Development of thermal barrier coating systems from Al microparticles. Part II: Characterisation of mechanical and thermal transport properties

3.1. Microstructure of the thermal barrier systems

After the production of the different thermal barrier coatings systems from the slurry route presented in the previous section (article 5 §V.2), preliminary investigations to assess the adherence and mechanical resistance of the coatings using scratch tests and micro-indentation were realized. The evaluation of their thermal insulation potential is discussed in a separate paragraph. **Table V.1** provides the main features of the different samples studied hereafter. Two different types of aluminium particles were employed for the slurry coatings. Al_DS and Al_HS microparticles are referred to as "dispersed size" and "homogeneous size" particles (see chapter II). For both types of Al slurry, different heat treatments were performed in order to produce the coatings. Such heat treatments are also detailed in the previous section (article 5 §V.2). Full heat treatments in Ar and synthetic air were carried out to synthesize baseline coatings. The heat treatments in the hybrid atmosphere were performed by introducing synthetic air at different temperatures of the annealing. In all hybrid coatings, the first stages were conducted in Ar. As expected, the different atmospheres resulted in a relatively large variety of coatings due to the difference of in their oxidation potential that depends on the duration of exposition to the synthetic air (Ar < s700 < s650 < s600 < air).

The different samples surfaces are gathered in **Figure V.1** while the cross-sections of the coatings are shown in **Figure V.2**. The different oxidation potential of the atmospheres led to significant changes in the coatings as a function of the type of particle. In Ar atmosphere, both Al_DS and Al_HS samples resulted in thin top coatings made of the collapsed hollow particles, i.e. ~8 µm for Al_DS-Ar and ~20 µm for Al_HS-Ar (**Figure V.2a** and **V.2f**). The dark grey aspect of the coating heat treated under Ar in **Figure V.1** results from the poor oxidation of the top coatings, i.e. the hollow microparticles have such thin walls that it is possible to see the substrate colour through [1]. In synthetic air, the aspect is also grey due to the presence of metallic Al trapped in some of the particles (see **Figure V.2e** and **V.2j**). Such grey surfaces were observed in some of our previous works [1, 2]. In air, the resulting top coatings are thick due to the early oxidation of the particles, i.e. ~60 µm for Al_DS-air and ~50 µm for Al_HS-air, but the diffusion coatings obtained are heterogeneous and display a NiO layer on top of a

thick alumina layer. By modifying the temperature of introduction of synthetic air as a replacement of the Ar atmosphere during the heat treatment, various structures were achieved (see paper 5). With the atmosphere switch at 600°C, the coatings were observed to be quite oxidized as well. However, in contrast with the complete heat treatment under synthetic air, the switch led to spallation of the top coating for the Al_HS-s600 sample and to cracks and voids at the interface between the diffusion coating and the top coating for the Al_DS-s600 sample (**Figure V.2d** and **V.2i**). With further delaying of the introduction of air, homogeneous diffusion coatings were achieved with thicker top coatings than the one obtained with pure Ar atmosphere, i.e. ~40, ~35, ~30 and ~15 µm for Al_HS-s650, Al_HS-s700, Al_DS-s650, and Al_DS-s700, respectively (**Figure V.2b**, **V.2c**, **V.2g** and **V.2h**).

Table V.1 *– Main features of the different samples (Diffusion coating: β–NiAl and γ'– Ni_3Al).*

Sample	Atmosphere	Thickness TC (µm)	Thickness DC (µm)
Al_DS-Ar	Pure Ar	7-10	24 (β) + 12 (γ)
Al_DS-s700	Ar + air at 700°C	15-20	24 (β) + 12 (γ)
Al_DS-s650	Ar + air at 650°C	25-30	24 (β) + 12 (γ)
Al_DS-s600	Ar + air at 600°C	60-70	0-35 (β+γ)
Al_DS-air	Synthetic air	60-70	0-35 (β+γ)
Al_HS-Ar	Pure Ar	15-25	30 (β) + 15 (γ)
Al_HS-s700	Ar + air at 700°C	30-40	30 (β) + 15 (γ)
Al_HS-s650	Ar + air at 650°C	35-45	30 (β) + 15 (γ)
Al_HS-s600	Ar + air at 600°C	*spallation*	0-35 (β+γ)
Al_HS-air	Synthetic air	40-50	0-35 (β+γ)

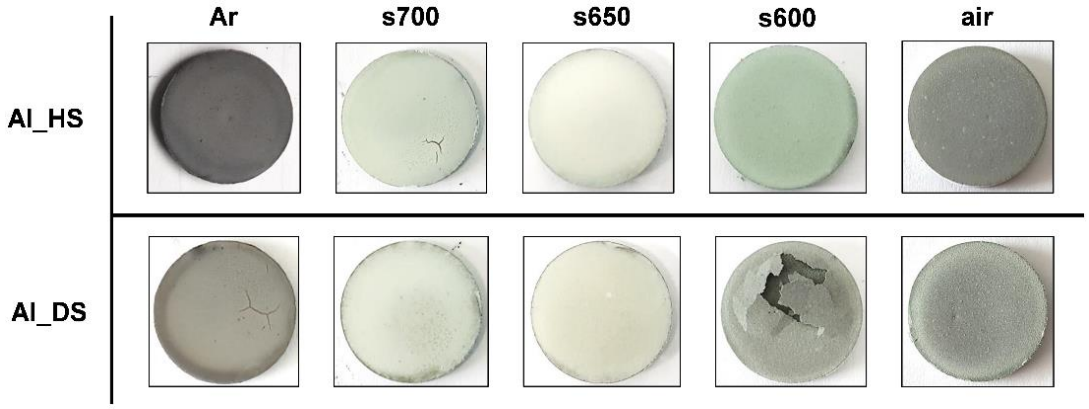

Figure V.1 *– Macrographs of the surface of the different samples after heat treatment.*

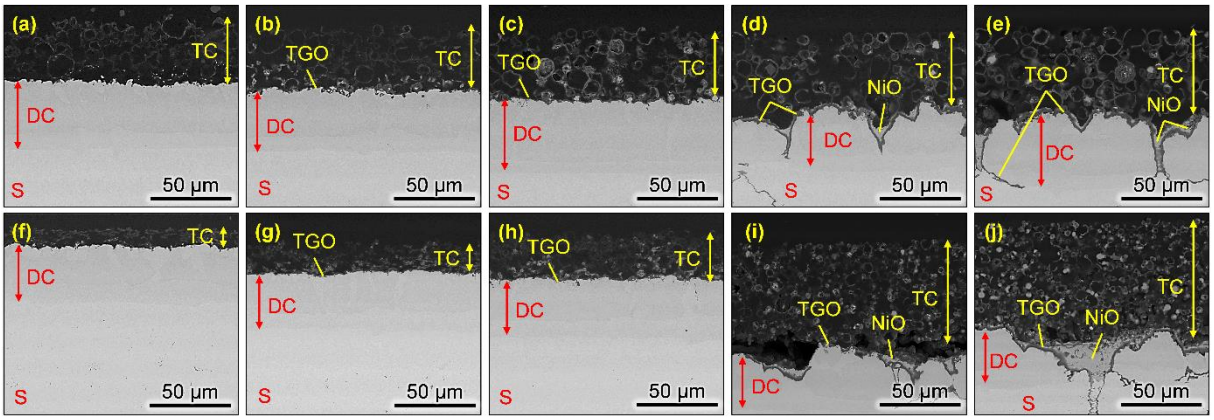

***TC**: Top Coating; **DC**: Diffusion Coating; **TGO**: Thermally Grown Oxide (alumina)*

***Figure V.2** – SEM cross-sections of the coatings of the study; a) Al_HS-Ar, b) Al_HS-s700, c) Al_HS-s650, d) Al_HS-s600, e) Al_HS-air, f) Al_DS-Ar, g) Al_DS-s700, h) Al_DS-s650, i) Al_DS-s600 and j) Al_DS-air.*

Then, the adherence of all the coatings was assessed via preliminary scratch tests except for the Al_DS-s600 samples whose top coat had spalled off.

3.2. Mechanical tests

Figure V.3 shows the penetration depth of the indent as a function of the applied force along the length of the scratch while **Table V.2** gathers the penetration depth measured in different locations. The details of the conditions employed for the scratch tests are presented in chapter II. One shall note that pre-scans were realised at 0.03N on the sample prior to the scratch for the software to identify the original surface of the sample that thus, may already penetrate the porous coatings.

It was observed that spallation of the top coating only occurred in the case of Al_DS-s600 sample (**Figure V.4**). As a matter of fact, it is observed a sharp drop of the penetration depth in the early stage of the scratch as spallation occurred (**Figure V.3a**). All the other coatings remained adherent to the underlying coating after the scratch tests. The recorded depths against the applied load in **Figure V.3** follows a two-stage sequence. Over the first microns of the scratch, the indent tends to penetrate the whole thickness of the coatings (see **Figure V.4**) leading to a quick drop of the measured depth. Afterwards, the penetration of the indent tends to stabilize and increases more steadily as it starts to scratch and to reach the diffusion coating. The maximum penetrated depth (D_{max} in **Table V.2**) appears to be consistent with the thickness of the top coatings of the different samples (**Table V.1**). As the surface of the diffusion coating is rapidly reached, the measured depth at 0.5N ($D_{0.5N}$ in **Table V.2**) should be similar to the

total thickness of the top coatings. However, the penetrated depths $D_{0.5N}$ are smaller than the coating thicknesses presented in **Table V.1**. This is because the scratch starts with a relatively small applied force of 0.03N (see **Figure V.4b**). Indentations were performed in order to measure the depth penetrated at this small force and are gathered in **Table V.2** as $D_{0.03N}$. It is observed that the depth of penetration at 0.03N is already significant (see also the pre-scan print at 0.03N in **Figure V.4b**) and tends to decrease as the oxidation potential of the heat treatment increases (Ar < s700 < s650 < s600 < air). In contrast, the coatings annealed in Ar exhibit smaller penetration at 0.03N as coating thicknesses are in the same range as the penetrated depth. In addition, some peculiar trends of the penetrated depth are observed in the early stage of the scratch for the most oxidized and thickest coatings (Al_DS-air, Al_DS-s650, Al_HS-air and Al_HS-s650). The measured depth seems to be stable after the drop until a given value of applied force is reached. This can be attributed to the fact that the microparticles of the top coatings are crushed under the indent (see **Figure V.4a**) and act as a lubricant which prevents the penetration of the indent at some point. This hypothesis is based on previous work that showed that alumina could act as a lubricant that limits friction [3].

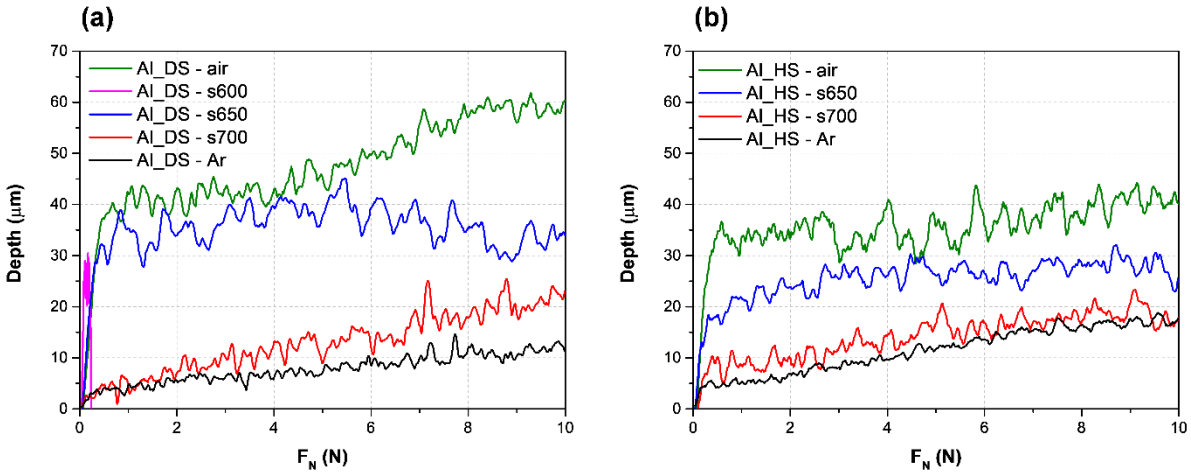

Figure V.3 *– Scratch tests. Depth of penetration of the indent as a function of the load applied for a) Al_DS and b) Al_HS coatings.*

To further assess the difference in terms of mechanical strength, micro-indentation tests were performed on the different top coatings produced. The force needed to penetrate the first 5 µm of the different coatings is gathered in **Table V.3**. Except for the top coatings performed in Ar atmosphere, the force required to penetrate the 5 µm increases with increasing the oxidation potential of the heat treatment. With the coatings produced under Ar, the small

coatings thickness is rapidly reached and, thus, the contribution of the underlying substrate increases the force needed to reach the 5 µm.

Table V.2 *– Scratch tests. Depth of penetration measured after the scratch tests.*

Atmosphere of heat treatment	D_{max} (µm)		$D_{0.5N}$ (µm)		$D_{0.03N}$ (µm)	
	Al_HS	Al_DS	Al_HS	Al_DS	Al_HS	Al_DS
Ar	19.0	14.7	4.5	3.9	5.9 ± 1.4	6.5 ± 2.4
Switch 700°C	23.4	25.7	10.2	4.8	11.0 ± 5.0	8.1 ± 1.1
Switch 650°C	32.2	45.2	18.6	32.4	9.3 ± 6.3	4.8 ± 0.9
Switch 600°C	-	30.6	-	-	-	-
Synthetic air	44.5	61.9	36.8	40.3	5.5 ± 2.2	5.9 ± 3.4

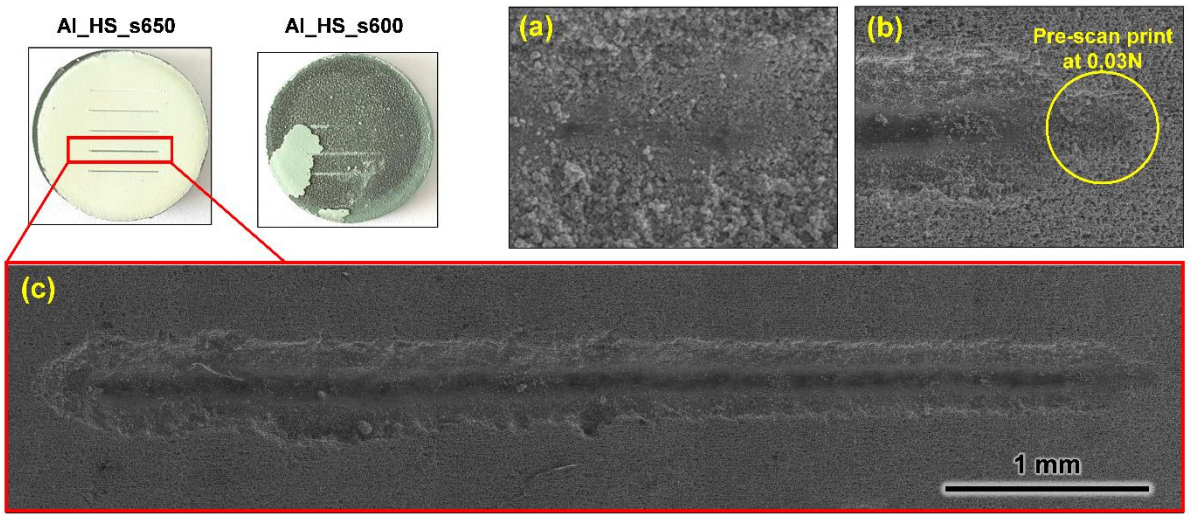

Figure V.4 *– Macrographs of Al_DS-s650 and s600 after the scratch tests and corresponding SEM micrographs in SE mode of a) the bottom of the scratch, b) the beginning of the scratch and c) the scratch in full length.*

Table V.3 *– Micro-indentation. Load applied to penetrate 5 microns into the different coatings.*

Atmosphere of heat treatment	$F_{N,mean}$ (mN)	
	Al_HS	Al_DS
Ar	19.6 ± 5.1	21.3 ± 9.3
Switch 700°C	8.5 ± 0.7	9.6 ± 2.3
Switch 650°C	12.0 ± 1.7	12.6 ± 4.5
Synthetic air	17.6 ± 7.4	27.3 ± 4.5
APS YSZ	201.3 ± 22.0	
EB-PVD YSZ	897.3 ± 229.0	

However, the micro-indentation performed on the APS and EB-PVD YSZ coatings shows that there is a significant difference between the mechanical strength of the standard TBCs and the Al slurry ones. As a matter of fact, the indentations in the plasma-sprayed coatings resulted in a mean load that was 10 times higher (~200 mN) than the Al slurry coatings performed in synthetic air. The indentations performed on the EB-PVD coatings were even higher but showed a wide dispersion of the values due to the inherent heterogeneity of the surface of these columnar coatings. Despite alumina microhardness is slightly higher than YSZ (HV = 16 GPa for α-Al_2O_3 and 11.5 GPa for *t*-ZrO_2 [4,5]), the comparison is not straightforward because the YSZ coatings are much denser and thicker than the hollow Al_2O_3 microspheres and also because of differences of the underlying substrates (superalloys vs. pure Ni).

3.3. Thermal diffusivity

The thermal diffusivity of the top coatings was then calculated via laser-flash measurements of the complete system (substrate + aluminide + top coating) and the results are presented in **Figure V.5**. All the coatings present thermal diffusivity values ranging between 0.8 to 5.0 $x10^{-7}$ $m^2.s^{-1}$ that are in the same range than the thermal diffusivity of YSZ APS coatings (chapter 3) and even lower than the one of YSZ EB-PVD coatings (chapter 4). The coatings heat treated in Ar present the lower thermal diffusivities since the shell of the microparticles that trap air is very thin. As a matter of fact, heat conduction is greater in alumina (λ_{air} 5-35 $W.m^{-1}.K^{-1}$ at RT) than in the gas filled pores (λ_{air} ~0.025 $W.m^{-1}.K^{-1}$ at RT) and could decrease even further when the pores are smaller than the gas mean free path (typically pores ~1 µm) where the heat conduction of the gas falls below the conduction of the free gas to ~0.01 $W.m^{-1}.K^{-1}$ due to gas molecule-wall collisions (Knudsen conduction) [6-8]. However, the top coatings that were heat treated in air present lower thermal diffusivities than the one heat treated in Ar + air-650°C despite the thicker shells of the former. This could be explained by the fact that a thick thermal oxide grew at the interface between the top coating and the diffusion coating for the samples heat treated in synthetic air. As a matter of fact, the contribution of the oxide layer that was not considered in the multilayer calculation via the laser-flash technique was previously shown in chapters 3 and 4 to be responsible for adding a non-negligible resistance to heat transport and hence, leading to an underestimation of the thermal diffusivity. Moreover, the Al_HS coatings exhibit higher thermal diffusivity values than the Al_DS ones. This can be attributed to several factors that derive from the initial differences in particle size. Indeed, for the same coating

thickness, the number of interfaces increases with decreasing the size of the particles. Therefore, and because interfaces are known to scatter the heat through ceramic coatings [9-11], the greater the number of interfaces, the lower the thermal diffusivity. In addition, since the heat flow could also be enhanced when the ratio of material vs. void is more significant, the Al_HS particles whose particle shells are thicker than those of the Al_DS will lead to higher heat conduction.

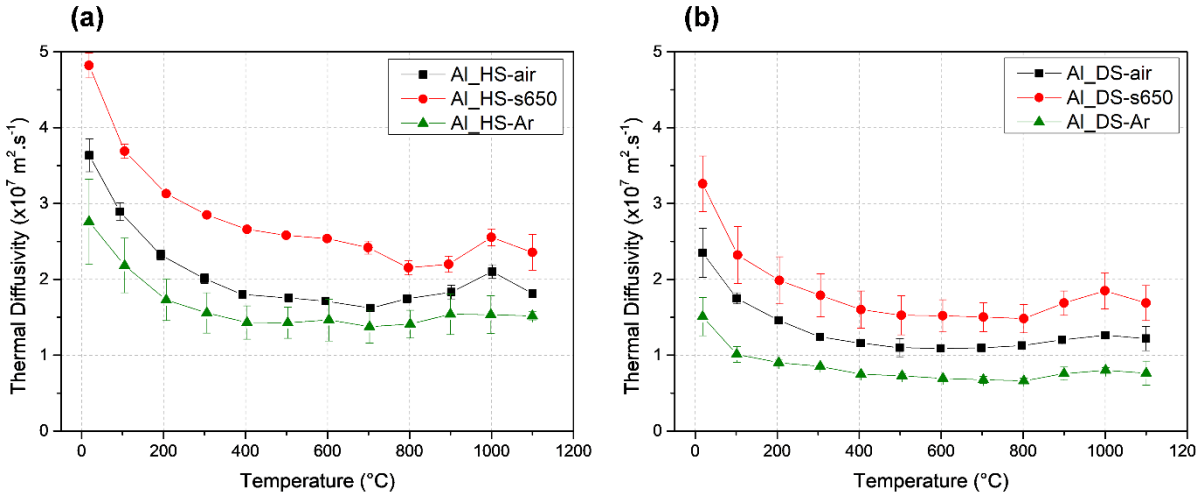

Figure V.5 *– Thermal diffusivity as a function of the temperature of a) Al_HS and b) Al_DS coatings.*

3.4. Conclusions

The adherence and the mechanical strength of different Al-slurry thermal barrier coating systems were assessed via scratch and micro-indentation tests while their thermal insulation potential was evaluated via the measurement of the thermal diffusivity of the top coatings using the laser-flash technique. The top coatings made from the slurry route were observed to be adherent to their substrate for most of the different conditions employed to produce them. The micro-indentation tests have pointed out the superior strength of the standard YSZ APS and EB-PVD coatings probably because the coatings were made on superalloy substrates. However, it appears that significant improvements have been made using hybrid atmosphere in order to obtain homogeneous diffusion coatings with stronger top coatings than when performed under pure Ar atmosphere. Moreover, the laser-flash measurements have shown that the insulation potential of such coatings is equivalent to that of the standard YSZ APS and EB-PVD coatings measured in previous chapters.

4. References Chapter V

1. G. Boissonnet, B. Grégoire, G. Bonnet, F. Pedraza, *Development of thermal barrier coating systems from Al microparticles. Part I: Influence of processing conditions on the mechanisms of formation*, in preparation.
2. M. Brossard, B. Bouchaud, F. Pedraza, *Influence of water vapour on the oxidation behaviour of a conventional aluminide and a new thermal barrier coating system sintered from a slurry*, Materials and Corrosion 65, **2014**, 161-168.
3. Y. Depierre, S. Albaladejo, P. Latge, J. Raffailhac, P. Mazars, *Résistance à l'Usure et à la corrosion dans le sodium liquide de revêtements d'aluminiures sur Aciers inoxydables austénitiques*, Materials Science and Engineering 88, **1987**, 287-293.
4. K.A. Habib, J.J. Saura, C. Ferrer, M.S. Damra, E. Gimenez, L. Cabedo, *Comparison of flame sprayed Al_2O_3/TiO_2 coatings: Their microstructure, mechanical properties and tribology behavior*," Surface and Coatings Technology 201, **2006**,1436-1443.
5. J. Lin and J. Duh, *Fracture toughness and hardness of ceria-and yttria-doped tetragonal zirconia ceramics*, Material Chemistry and Physics 78, **2003**, 253-261.
6. C. J. M. Lasance, *The thermal conductivity of ceramics*, Electronics Cooling 5, **1999**, 12-16.
7. I.O. Golosnoy, A. Cipitria, and T.W. Clyne, *Heat Transfer Through Plasma-Sprayed Thermal Barrier Coatings in Gas Turbines: A Review of Recent Work*, Journal of Thermal Spray Technology 18, **2009**, 809-821.
8. L.B. Loeb, The Kinetic Theory of Gases, McGraw-Hill, New York, (1934).
9. R. McPherson, A Model for the Thermal Conductivity of Plasma-Sprayed Ceramic Coatings, Thin Solid Films 112 (1984) 89-95.
10. L. Pawlowski and P. Fauchais, Thermal Transport Properties of Thermally Sprayed Coating, International Materials Reviews 37 (1992) 271-289.
11. I.O. Golosnoy, S.A. Tsipas, and T.W. Clyne, An Analytical Model for Simulation of Heat Flow in Plasma Sprayed Thermal Barrier Coatings, Journal of Thermal Spray Technology 14 (2005) 205-214.

VI. CONCLUSIONS AND PERSPECTIVES

Table of contents

1. Conclusions

1.1 PS and EB-PVD TBC systems

The first aim of this work was to provide a better comprehension on the relationships between the intrinsic properties of the current thermal barrier coatings (TBCs) and their thermal insulation capacity in order to give reliable tools for the development of future coatings. In all cases, the insulating capacity has been established by measuring the thermal diffusivity (α) through the laser flash technique. As a reminder, the thermal conductivity (λ) requires to determine also the heat capacity (C_p) and the density (ρ) that we have shown to vary very slightly in the temperature range studied here.

In Chapter III, our studies have focused on plasma-sprayed (PS) YSZ TBCs. Firstly, we investigated appropriate characterization techniques to evaluate both the intrinsic properties of the TBC system and their thermal transport properties. It is known that the APS deposition process parameters can significantly influence the microstructure of the APS as-deposited coatings, in particular in porosity. It is also known that the inherent porosity of these PS coatings lowers the thermal conductivity. Therefore, the microstructures of the different APS coatings of this study were evaluated using image analysis (IA) using ImageJ software from binary SEM images. This IA technique allowed differentiating between coarse pores and the thin porous network, which is of major interest as these two types of categories exhibit different heat transport behaviors. In this study, the thin pores (micro-cracks and interlamellar pores) were integrated as a single porosity level, regardless of their orientation. This “lamellar” porosity level was separated from the total porosity measured by an opening/closing computed image treatment on the binary image of the pores whose dimensions fall below 1 µm. As a result, a strong relationship between the thermal diffusivity and the lamellar porosity level has been found in this study. In agreement with the literature, the interlamellar pores of the coatings are the major microstructural feature that reduces the thermal transport properties of PS TBCs. Even if we employed simple criteria on the calculation of the thermal diffusivity (two-layers model) and on the binary image analysis (instead of 3D), we have provided a fairly adequate estimation of the potential thermal insulation of the plasma-sprayed coatings studied using simple, fast and low-cost approaches.

Therefore, the same methods were employed to assess the thermal insulating potential of the thermally aged coatings (ageing tests and laser flash measurements). We have shown that ageing makes the microstructure to evolve. Sintering of the coatings occurred and brings about a reduction of the overall lamellar porosity, hence an increase in heat conduction. Ageing at high temperature (here 1100°C) provokes necking and forms connections between the splats that compose the PS coatings, which enhances the heat flow via bridge funneling from splat to splat, resulting in increased thermal diffusivity. However, due to the oxidation of the bond coating and the formation of cracks, a compensation of the sintering effect was observed when studying the complete thermal barrier coating system through multilayer calculation of the thermal diffusivity. The thick cracks may contribute to reduce the thermal conductivity by generating new pores in which gas conduction will lead heat transport. Also, a thick oxide scale may add significant thermal transport resistance because the thermal conductivity of the oxides is much lower than that of the metallic MCrAlY bond coating. In addition, the pores or micro-cracks in the oxide layer perpendicular to the heat flow further reduce the heat transport.

Thereafter, the PS TBCs were exposed to calcium-magnesium-alumino-silicates (CMAS) to study the potential effect of such a corrosive attack. In this work, small quantities of CMAS were applied onto the surface of the coatings in order to assess the impact that the resulting partial transformation of the YSZ plasma-sprayed coating could exert on the coating thermal insulation potential. SEM imaging coupled to elemental analysis (EDS) were employed to measure the extent of the microstructural degradation caused by the CMAS attack. Additionally, X-ray diffraction (XRD) and Raman micro-spectrometry were used to follow the changes in crystal structure of the ceramic coatings, respectively, on the surface and on the cross-section of the coatings. The experimental results have shown a gradual increase of the sintered depth with increasing the amount of CMAS accompanied by phase transformations of the YSZ. The CMAS-induced sintering and the destabilization of the *t'*-ZrO_2 have been found to be the major contributors to the raise in the thermal diffusivity of the coatings that reached a maximum of ~110 % when the coating was fully penetrated with CMAS.

Overall, in YSZ PS coatings the maintenance of the interlamellar porosity ensures a low thermal conductivity. Therefore, in Chapter IV, we aimed at understanding the relationships between the heat transport and a columnar feather-like microstructure of YSZ fabricated by electron-beam physical vapour deposited (EB-PVD). In this type of coating, the heat flow is mainly

parallel to the columns, in contrast to the PS coatings for which the heat transport is normal to the interlamellar splats and porosities. The same X-ray diffraction (XRD) and Raman micro-spectrometry analyses were successfully employed to assess the phase stability of the ceramic coatings. However, due to the particular columnar microstructure of such coatings, the IA method turned out to be inadequate to differentiate the coatings or evaluate the porosity-heat transport relationship. Therefore, only qualitative interpretations of the microstructural features were made to evaluate the evolution and the differences between the coatings.

In addition to the currently employed YSZ material, yttria-erbia (Y_2O_3-Er_2O_3) co-doped EB-PVD TBCs were also investigated, as rare-earth (RE) doped coatings are of interest for their potential to further increase the heat insulation and mitigate CMAS corrosion. In their as-deposited state, although both coatings presented similar microstructures, co-doped coatings showed better thermal insulation than the standard ones. After isothermal annealing at 1100°C in air, the co-doped coating exhibited greater microstructural and phase transformations than its standard counterpart. The sintering and oxidation of the bond coating were more pronounced on the former due to the presence of Er_2O_3, whose enhanced affinity to oxygen led to an increase of the oxidation kinetics of the aluminide and increased sintering. Simultaneously, the phase stability of the Er/Y co-doped coating appeared to be also poorer than the standard YSZ coating when annealed in air at 1100°C for 500h. Thus, despite a better initial thermal insulation potential, the co-doped Er/Y coating was shown to be less stable than the 8YSZ standard coating due to a faster degradation of the TBC system that could further lead to a poor lifespan.

When exposed to CMAS at high-temperature, the EB-PVD coatings did not interact in the same manner as that of the PS TBCs. Despite the 1h-annealing at 1250°C, the small CMAS deposits did not fully penetrate the coatings. This resulted in a greater coverage of the surface of the coatings by the residual glassy melt with increasing the deposited amount. However, the standard YSZ coatings were fully impregnated with a small concentration of CMAS. This resulted in an increased in-depth sintering by the glassy melt, hence in a poorer thermal insulation than the co-doped ones. In the presence of CMAS, the lower thermal diffusivity of the Er/Y as compared to the standard YSZ can be attributed to the presence of Er_2O_3 that impeded the penetration of CMAS.

In summary, the first section of this study (chapters III and IV) related to conventional PS and EB-PVD YSZ (and less conventional Er/YSZ) TBCs allowed to establish the relationship

between the intrinsic properties of the as-deposited coatings, their evolutions upon ageing and the heat transport properties of each type of YSZ TBCs. However, we have noticed some limitations to the analyses employed when trying to evaluate the true properties of the different coatings studied. For instance, when measuring the thermal diffusivity via the laser-flash technique, deviations between free-standing coatings and complete systems were found due to the very own limitations of the technique. The thin ceramic coatings are more subject to deviations due to radiation, whereas thicker samples are more subject to heat loss effects, which also contribute to the difference of thermal diffusivity between the free-standing and the coatings measured on their substrate. Moreover, uncertainties in the determination of the specific heat capacity (C_p) and the density (ρ) of very thin layers cannot be excluded. Therefore, the heat transport properties were compared through the measurement of each separate heat transport properties (α, C_p and ρ) rather than by using thermal conductivity calculations.

1.2 Al slurry TBC systems

The main challenge of this work was to investigate an alternative solution to create a TBC from a cost-effective and environmentally friendly process through the slurry route. This study was motivated because previous works in our research group showed the possibility of synthesizing TBCs from a slurry containing Al microparticles in a single step process. With just 50 µm of top coating composed of hollow alumina spheres, the thermal insulation potential was equivalent to 300 µm of PS YSZ. However, the mechanical strength appeared very poor. Therefore, in the thesis, we have first focused on the influence of different types of Al particles and atmospheres of the thermal treatment on the mechanisms of formation of the coatings on a pure Ni substrate. Then, their properties of heat transport and mechanical resistance were assessed and compared to the ones of the PS and EB-PVD TBCs. One must notice however that the PS and EB-PVD coatings contain by far more matter and that the coatings were applied on nickel-based superalloy substrates instead of pure Ni.

Firstly, both aluminizing of the nickel substrate and oxidation of the Al particles were shown to be dependent on the type of Al micro-particles (homogeneous HS vs. dispersed DS sizes). The release of Al from the particles was associated with the peripheral oxidation of the spheres and the volume expansion of the Al core upon heating. Therefore, larger particles were found to be particularly interesting for aluminizing purposes while the smaller particles, that kept Al in their core, were able to provide a significant source to thicken the surrounding shells and to

enhance the sintering of the top coating when a sufficient p_{O_2} or p_{H_2O} was employed for the heat treatment.

Then, the impacts of the oxidizing potential of different atmospheres (Ar, air and Ar/$H_2O_{(g)}$) were compared. When using synthetic air (p_{O_2} = 0.20 atm), the shells of the Al microspheres were observed to be thicker and more sintered as they tended to keep more Al in comparison with the inert Ar atmosphere. However, the diffusion coatings were more heterogeneous and thinner. This was attributed to the oxidation of both the Al microparticles and of the interface between the top coating and the diffusion layer. Indeed, the combination of a thick NiO formed on top of uncoated regions of the substrate and the peripheral oxidation of the particles were shown to impede the aluminizing of the substrate. With the use of the Ar-10%H_2O atmosphere, the shells of the Al microparticles were observed to be as thick as the ones obtained in air but the aluminizing was limited despite that no evidence of significant oxidation of the substrate was observed, which suggests oxide shells denser than the ones grown in air.

Hybrid atmospheres were thus introduced to find a compromise between aluminizing of the substrate and thickening of the shells in order to increase the mechanical strength of the top coatings. The inert Ar atmosphere was employed during the first part of the heat treatment to allow the initiation of the Al-Ni reaction and the oxidizing atmosphere was subsequently introduced to oxidize the Al left in the micro-particles. The oxidizing atmosphere was shown to be optimal when introduced at 650°C for the synthetic air and at 700°C for the Ar-10%H_2O atmosphere.

The adherence and mechanical strength of the top hollow alumina spheres coatings were also investigated via scratch and micro-indentation tests. It was shown that the best adherence was achieved with the coatings elaborated in air and in the hybrid atmosphere with the introduction of air at different temperatures. Also, the coatings made from the Al_DS particles gave higher mechanical strength than the ones made with the Al_HS particles. However, this strength is still much lower than that of the YSZ PS and EB-PVD coatings for which the coating thickness and density are much higher, and the substrate was not nickel but a nickel-based superalloy. In contrast, the heat transport properties assessed via the laser-flash technique have been shown to be in the same range than the PS and EB-PVD YSZ TBCs ones. Still, some improvements can be considered as it seems that the slurry route offers plenty of possibilities of investigation in future works.

1.3 Generalities on the measurements of the thermal properties of TBCs

Concerning the measurements of the thermal properties, thermal conductivity calculations of the thin layers studied appeared difficult in terms of accuracy of the results as precise density and specific heat capacity of the coatings are difficult to attain using the techniques employed. For instance, the image analysis method used for the determination of the porosity and hence, the density, was shown to give slightly higher values than the one observed in the literature. Moreover, due to the sensitivity of the DSC technique for the measurement of the specific heat capacity, some deviations of the heat signal were generally observed at high temperature that thus led to non-negligible differences in comparison with the reference values. Considering the thermal diffusivity, some deviations could also be found at high temperature due to the transparency of the YSZ ceramic material to the laser pulse and the loss of the conductive layers during the laser-flash test that was applied to prevent the errors due to this transparency. Therefore, it is generally preferred to discuss the measured values independently than trying to calculate the thermal conductivity. Thus, in this study, despite that specific heat capacities and densities were measured for the different materials studied, no thermal conductivity values were presented.

2. Outlooks

For the measurement of heat transport properties, several perspectives could be drawn from the present study. Firstly, to assess the thermal conductivity of the coatings, further investigations on the measurement of the thermal diffusivity, specific heat capacity, and density values could be interesting to compare the results obtained. For instance, advanced techniques for porosity determination like X-ray and Neutron Scattering (Computed MicroTomography CMT or Small Angle Neutron Scattering SANS) could be used for the different coatings to obtain precise knowledge of the microstructure. Similarly, photothermal emission analysis (PopTea) might be used in order to compare the different thermal properties measured. To reduce deviations of the laser-flash measurement at high temperature, a sputtered conductive layer of Pt could also be employed in combination with the graphite layer.

In more general terms, it would be interesting to compare the experimental results with computed calculations and heat transport models in order to ascertain the hypothesis made on the impact of the evolution of each compound of the TBC systems on the thermal transport properties (TGO growth, cracks opening…).

To deepen our understanding on the impact of the CMAS on the thermal transport properties, it would be of interest to measure the properties of the different compounds that could result from the interaction between the CMAS and the YSZ material. For instance, by mixing YSZ powders with CMAS in different proportions to form the desired compounds, it would be easier to measure the thermal properties of the different possible reaction products that form during CMAS attack.

For the TBC made by the slurry route, several improvements could be investigated in future works. First, a better knowledge of the oxidation behaviour of the Al powders could be obtained through in situ detectors of the partial pressure of oxygen or of the humidity during thermal treatments. It would also allow a better understanding of the mechanisms of thickening of the microspheres of the coating. In this way, the impact of the atmosphere would be better mastered and different combinations of atmospheres might thus be investigated for comparison purposes.

Due to the simplicity of the slurry coating technique, a lot of different powder combinations could be investigated. In the same way that different sizes and heterogeneity of the Al powders were tested in this work, mixing Al with other elements could be of major interest to extend the performances or the range of practical applications for such coatings. For instance, control of the Al activity to obtain low-activity aluminide coating was also investigated in different studies by blending the Al powders with Cr or Al_2O_3 particles.

Also, the extrapolation of the mechanisms of formation of slurry TBCs on the alloys of interest would be required to validate those coatings and to further investigate their performances. The aluminizing, as well as the formation of top coatings, were shown in previous works to be quite different when using Ni and Fe-based alloys and superalloys. Then, the enhancement of top coating adherence and resistance to erosion could be further investigated on these other substrates as the mechanisms would be different. For instance, increasing the microspheres sintering using aluminothermic reaction with NiO or Cr_2O_3 oxides, or promoting the thickening of the microsphere shells using pre-oxidizing treatment in various atmospheres would be interesting to enhance the mechanical resistance of such slurry top coatings. Finally, testing the resistance to long-term thermal exposure of the different coatings achieved on those alloys would be another step to go further for concerning these coatings.